

Tuning the superconducting properties of magnesium diboride

by

Rudeger Heinrich Theoderich Wilke

A dissertation submitted to the graduate faculty
in partial fulfillment of the requirements for the degree of
DOCTOR OF PHILOSOPHY

Major: Condensed Matter Physics

Program of Study Committee:
Paul C. Canfield, Major Professor
Alan I. Goldman
John Lajoie
R. William McCallum
Vladimir Kogan

Iowa State University

Ames, Iowa

2005

Copyright © Rudeger Heinrich Theoderich Wilke, 2005. All rights reserved.

Graduate College
Iowa State University

This is to certify that the doctoral dissertation of
Rudeger Heinrich Theoderich Wilke
has met the dissertation requirements of Iowa State University

Major Professor

For the Major Program

TABLE OF CONTENTS

List of Tables	vi
List of Figures	vii
1. Introduction	1
2. Physics Review	6
2.1 Properties of Superconductors	6
2.2 Ginzburg-Landau Theory	10
2.3 Two Gap Superconductivity	13
2.4 Critical Current Densities	17
2.5 Bean Critical State Model	20
3. Basic Properties of MgB₂	23
3.1 Crystal Structure and Bonding	23
3.2 Pairing Mechanism	23
3.3 Thermodynamic Properties and Two Gap Nature	26
4. Sample Preparation and Characterization	33
4.1 Sample Preparation	33
4.1.1 Production of Boron Filaments	33
4.1.2 Conversion to MgB ₂	34
4.1.3 Carbon Doped MgB ₂ Filaments	36
4.1.4 Neutron Irradiation	37
4.2 Sample Characterization	39
4.2.1 Powder X-ray diffraction (XRD)	39

4.2.2	Magnetic Measurements	39
4.2.3	Transport Measurements	40
5.	Superconducting and Normal State Properties of $\text{Mg}(\text{B}_{1-x}\text{C}_x)_2$	42
5.1	Optimization of Reaction	43
5.2	Thermodynamic and Transport Properties	51
5.3	Discussion	62
6.	Enhancing Critical Current Densities in $\text{Mg}(\text{B}_{1-x}\text{C}_x)_2$	65
6.1	Titanium Additions to MgB_2	65
6.2	Titanium Additions to Carbon Doped MgB_2	75
7.	Synthesis of $\text{Mg}(\text{B}_{1-x}\text{C}_x)_2$ Powders	81
7.1	Sample Synthesis	81
7.2	Results and Discussion	82
8.	Plasma Spray Synthesized Doped Boron Powders	97
8.1	Powder Synthesis	97
8.1.1	Superconducting and Normal State Properties	99
8.2	Powder In Tube Fabrication	107
8.2.1	Sample Synthesis	108
8.2.2	Results and Discussion	108
9.	Superconducting and Normal State Properties of Neutron Irradiated MgB_2	121
9.1	Fluence and Annealing Studies	123
9.1.1	Structural Studies of As Damaged Samples	123
9.1.2	24 Hour Anneals of Samples Exposed to a Fluence of 4.75×10^{18} n/cm ²	126
9.1.3	Variable Time Anneals on Samples Exposed to a Fluence of 4.75×10^{18} n/cm ²	133
9.1.4	Variable Fluence Levels, 24 Hour Anneal	138
9.1.5	Long Time Annealing Studies	140
9.2	Discussion	144

10. Effects of Neutron Irradiation on Carbon Doped MgB₂ Wire Segments .	154
10.1 Structural Properties	154
10.2 Thermodynamic and Transport Measurements	160
10.3 Discussion	168
11. Conclusions and Future Work	173
Bibliography	177
Acknowledgements	186

LIST OF TABLES

Table 4.1	Gas flow rates for synthesizing carbon doped boron fibers	37
Table 4.2	Exposure times and fluence levels for neutron irradiation of MgB_2 . . .	38
Table 5.1	Calculated x in $\text{Mg}(\text{B}_{1-x}\text{C}_x)_2$	50
Table 8.1	Gas flow rates for powder synthesis	98

LIST OF FIGURES

Figure 2.1	Magnetization of Type I and Type II Superconductors	8
Figure 2.2	Vortex and Vortex Lattice	9
Figure 2.3	Superconducting coherence length in dirty superconductors	13
Figure 2.4	H_{c2} for Ta doped Nb	14
Figure 2.5	Influence of scattering rates on $H_{c2}(T)$ in MgB_2	16
Figure 2.6	Development of resistance in superconductors	19
Figure 2.7	Magnetic field profiles in the Bean Critical State Model	21
Figure 3.1	Crystal structure and Fermi surface of MgB_2	24
Figure 3.2	Isotope effect in MgB_2	25
Figure 3.3	Upper critical field of MgB_2	27
Figure 3.4	Measurements of the two superconducting gaps in MgB_2	29
Figure 3.5	Theoretical temperature dependence of superconducting gaps	30
Figure 4.1	CVD reaction chamber	34
Figure 4.2	Mg/B phase diagram	35
Figure 4.3	Sample platform for transport measurements at NHMFL	41
Figure 5.1	Carbon doped wires reacted for 4 hours at 950 °C	44
Figure 5.2	Comparison of completeness of reaction for carbon doped filaments re- acted for different amounts of time and at temperatures	45
Figure 5.3	Carbon doped filaments reacted at 1200 °C	46
Figure 5.4	Optical images of fibers reacted using ramped temperature profiles . . .	47

Figure 5.5	X-ray peaks for $\text{Mg}(\text{B}_{1-x}\text{C}_x)_2$ using ramped and isothermal temperature profiles	48
Figure 5.6	Comparison of the a-lattice parameter in $\text{Mg}(\text{B}_{1-x}\text{C}_x)_2$ using ramped and isothermal temperature profiles	49
Figure 5.7	X-ray peaks for a series of $\text{Mg}(\text{B}_{1-x}\text{C}_x)_2$ samples	51
Figure 5.8	Transport measurements on $\text{Mg}(\text{B}_{1-x}\text{C}_x)_2$ wires	52
Figure 5.9	Magnetization curves for $\text{Mg}(\text{B}_{1-x}\text{C}_x)_2$ wires	53
Figure 5.10	Comparison of in-field transitions for $\text{Mg}(\text{B}_{1-x}\text{C}_x)_2$ wires reacted using different temperature profiles	54
Figure 5.11	Resistivity versus field measurements in $\text{Mg}(\text{B}_{.962}\text{C}_{.038})_2$	55
Figure 5.12	H_{c2} values for $\text{Mg}(\text{B}_{.962}\text{C}_{.038})_2$	56
Figure 5.13	Transport measurements on $\text{Mg}(\text{B}_{.948}\text{C}_{.052})_2$	57
Figure 5.14	$H_{c2}(T)$ for $\text{Mg}(\text{B}_{1-x}\text{C}_x)_2$ up to $x=0.052$	59
Figure 5.15	Flux flow resistivity in carbon doped MgB_2 filaments	60
Figure 5.16	Critical current densities in $\text{Mg}(\text{B}_{1-x}\text{C}_x)_2$	61
Figure 5.17	T_c and H_{c2} in $\text{Mg}(\text{B}_{1-x}\text{C}_x)_2$	63
Figure 6.1	Ti levels in doped B fibers made by CVD	67
Figure 6.2	Magnetization curves for MgB_2 with Ti additions reacted at different temperatures	68
Figure 6.3	Lattice parameters for MgB_2 with Ti additions	69
Figure 6.4	Upper critical fields for MgB_2 with Ti additions	70
Figure 6.5	Critical current densities for MgB_2 wires with Ti additions	71
Figure 6.6	Optical images of wires containing various Ti levels	73
Figure 6.7	TEM micrographs of precipitates in MgB_2 samples with various levels of Ti additions	74
Figure 6.8	X-ray peaks in MgB_2 samples with various levels of Ti and C additions	76
Figure 6.9	Magnetization curves for MgB_2 samples with various levels of Ti and C additions	77

Figure 6.10	$H_{c2}(T)$ curves for $Mg(B_{1-x}C_x)_2$ with various levels of Ti additions . . .	78
Figure 6.11	TEM micrographs of precipitates in carbon doped MgB_2 with Ti additions	79
Figure 6.12	Critical current densities in $Mg(B_{1-x}C_x)_2$ wires with various levels of Ti additions	80
Figure 7.1	X-ray peaks for pure and nominal $Mg(B_{.95}C_{.05})_2$ made with B_4C . . .	83
Figure 7.2	Magnetization curves for nominal $Mg(B_{.95}C_{.05})_2$ samples	84
Figure 7.3	X-ray peaks for nominal $Mg(B_{.95}C_{.05})_2$ reacted using differing number of sintering steps	85
Figure 7.4	Comparison of 2-step reactions with and without excess Mg	86
Figure 7.5	X-ray peaks for a series of $Mg(B_{1-x}C_x)_2$ powders	87
Figure 7.6	Magnetic transitions for a series of $Mg(B_{1-x}C_x)_2$ powders	88
Figure 7.7	X-ray peaks for nominal 20% carbon doped samples after 1, 2, and 3 step reactions	90
Figure 7.8	Transport measurements on a pellet of $Mg(B_{0.931}C_{0.069})_2$	91
Figure 7.9	Comparison of $H_{c2}(T)$ for carbon doped wires and pellets	93
Figure 7.10	Effects of purity on T_c for $Mg(B_{1-x}C_x)_2$ powders	94
Figure 7.11	Effects of purity on x-ray peak positions in $Mg(B_{1-x}C_x)_2$ powders . .	95
Figure 7.12	Effects of purity on $H_{c2}(T=0)$ values in $Mg(B_{1-x}C_x)_2$	96
Figure 8.1	Tekna PL-50 RF Induction Plasma Torch	98
Figure 8.2	SEM images of as-synthesized plasma spray powders	99
Figure 8.3	X-ray peaks for powders reacted for 48 hours at 1200 °C	100
Figure 8.4	Magnetization curves for powders reacted for 48 hours at 1200 °C . . .	101
Figure 8.5	Evolution of T_c as a function of the $ \Delta a $ in carbon doped powders . .	102
Figure 8.6	X-ray spectra for powders reacted for 4 hours at 950 °C	103
Figure 8.7	Magnetization curves for pellets reacted for 4 hours at 950 °C	104
Figure 8.8	Critical current densities in pellets reacted for 4 hours at 950 °C	105
Figure 8.9	Grain sizes in pellets reacted for 4 hours at 950 °C	106

Figure 8.10	PIT wires made using the CTFF process	109
Figure 8.11	X-ray peaks for PIT processed wires	111
Figure 8.12	X-ray spectra for pure and carbon doped PIT wires	112
Figure 8.13	Magnetization curves for PIT wires	113
Figure 8.14	T_c vs. $ \Delta a $ for PIT wires	115
Figure 8.15	SEM images of PIT wires	116
Figure 8.16	Reaction profiles for PIT wires reacted in a HIP	117
Figure 8.17	Magnetization curves for HIPed PIT wires	118
Figure 8.18	Critical current densities in PIT wires	119
Figure 9.1	X-ray peaks for as-damaged neutron irradiated samples	122
Figure 9.2	Evolution of x-ray peaks as a function of annealing temperature	125
Figure 9.3	Magnetization and resistivity curves for 24 hour annealed samples	127
Figure 9.4	Restoration of T_c as a function of annealing temperature	128
Figure 9.5	In-field transport measurements used to determine $H_{c2}(T)$ for a sample annealed for 24 hours at 500 °C	129
Figure 9.6	$H_{c2}(T)$ for 24 hour annealed samples	131
Figure 9.7	Critical current densities for samples annealed for 24 hours	132
Figure 9.8	Magnetization curves for samples annealed at 300 °C for various times	134
Figure 9.9	Evolution of ΔT_c as a function of annealing time at different annealing temperatures	135
Figure 9.10	Critical current densities for samples annealed at 300 °C for various times	137
Figure 9.11	X-ray peaks for samples exposed to different fluences and all annealed for 24 hours at 300 °C	138
Figure 9.12	X-ray peaks for samples exposed to fluences of 1.43×10^{19} and 1.90×10^{19} n/cm^2 and annealed for 24 hours at temperatures between 300 °C and 500 °C	139
Figure 9.13	Calculated lattice parameter shifts for all four damage levels annealed at temperatures up to 500 °C	140

Figure 9.14	Magnetization curves and corresponding T_c values for all four damage levels annealed for 24 hours at various temperatures	141
Figure 9.15	Transition temperatures for samples annealed for 1000 hours at 500 °C	143
Figure 9.16	$H_{c2}(T)$ for samples annealed for 1000 hours at 500 °C	144
Figure 9.17	Comparison of the evolution of T_c with unit cell dimensions for neutron irradiated MgB_2 and MgB_2 under pressure	146
Figure 9.18	Evolution of T_c as a function of unit cell dimensions in different neutron irradiation studies	148
Figure 9.19	Comparisons of T_c , H_{c2} and ρ_0 for carbon doped, aluminum doped and neutron irradiated MgB_2	151
Figure 10.1	X-ray peaks for the series of neutron irradiated $Mg(B_{0.962}C_{0.038})_2$ samples annealed for 24 hours at various temperatures.	155
Figure 10.2	Evolution of the x-ray (002) peak as a function of annealing temperature for 24 hour anneals.	156
Figure 10.3	Lattice parameters as a function of annealing temperature for 24 hour anneals.	157
Figure 10.4	X-ray peaks and resultant shift of the a- lattice parameter for samples annealed at 500 °C.	158
Figure 10.5	Magnetization and zero field resistivity curves for samples annealed at various temperatures for 24 hours.	159
Figure 10.6	Magnetization zero field resistivity curves for samples annealed at various times at 500 °C.	161
Figure 10.7	ΔT_c as a function of time for 500 °C anneals.	163
Figure 10.8	Transport measurements on samples annealed at 500 °C for 1000 hours.	165
Figure 10.9	$H_{c2}(T)$ for annealed samples of neutron irradiated carbon doped MgB_2	166
Figure 10.10	Critical current densities in neutron irradiated carbon doped MgB_2 . .	167
Figure 10.11	Normal state resistivity in neutron irradiated pure and carbon doped MgB_2	170

CHAPTER 1. Introduction

The discovery of superconductivity in MgB_2 near 40 K (1) has opened the door for the development a myriad of superconducting devices operating near 20 K. Although the transition temperature for MgB_2 lies far below those of the superconducting cuprates at 90 K, it has several material advantages that make it a viable choice for many niche technologies. Unlike high temperature superconductors MgB_2 can carry a large amount of current across high angle grain boundaries (2) and therefore does not require highly sophisticated synthesis processes to ensure grain alignment. Many groups have fabricated round superconducting MgB_2 wires using conventional powder-in-tube processing and already companies have begun developing this material for applications ranging from magnetic resonance imaging (MRI) to microwave devices.

Although bulk synthesis of pure MgB_2 is relatively straight forward, critical current densities fall off rapidly in the presence of externally applied magnetic fields. In order to make MgB_2 a useful material for power applications, the field range in which it can carry large amounts of current, in excess of 10^4 A/cm^2 , needs to be extended to higher magnetic fields. There are several contributing factors which lead to this poor in-field performance. First, pure MgB_2 has a fairly low and highly anisotropic upper critical field. At $T=0$, $H_{c2}^{\parallel ab} \sim 16 \text{ T}$ and $H_{c2}^{\perp ab} \sim 2.5 \text{ T}$ (3; 4), which should be compared to the near 25 T for pure Nb_3Sn (5). The low magnitude of $H_{c2}^{\perp ab}$ contributes to the degradation of J_c in low fields (6; 7), presumably due to a reduction in the superconducting volume fraction causing a decrease in the percolative network. Additionally, pure MgB_2 has relatively poor flux pinning. Flux is predominantly pinned at the grain boundaries (2) and the high reaction temperatures required to synthesize the phase make it difficult to limit the grain size significantly below $1 \mu\text{m}$.

To overcome both of these potential drawbacks a solid understanding of the physics within this novel system needs to be developed. The primary focus of this work has been to study the ways in which different perturbations affect the upper critical field of MgB_2 with additional emphasis on understanding flux pinning within this material in hopes of finding a method to enhance in field critical current densities. MgB_2 is a phonon mediated (8; 9; 10) type II BCS superconductor. In typical, single gap, type II superconductors the upper critical field can be tuned by adding point defects (11). MgB_2 is, however, unconventional and has two superconducting gaps, associated with two different bands in the electronic structure (σ and π) (12). There are at least three scattering channels (9), within and between the two bands, which affect the superconducting properties of the material. In order to understand how different types of defects affect the various scattering channels and how these changes affect the evolution of $H_{c2}(T)$ we have performed systematic studies of the effects of carbon doping and neutron irradiation on the superconducting and normal state properties of MgB_2 .

Doping is the most straight forward mechanism for introducing point defects within a material but MgB_2 does not easily take point defects in solid solution. So far only two elements have shown concrete evidence for entering the structure: aluminum, which substitutes for magnesium, and carbon, which substitutes for boron (13). We have succeeded in increasing the upper critical field of polycrystalline MgB_2 wire segments from 16 T to near 36 T by the substitution of 5.2% carbon for boron. We present fabrication details and physical properties of $\text{Mg}(\text{B}_{1-x}\text{C}_x)_2$ for x up to 0.052. Carbon doping was achieved using a two step reaction technique which involved an initial carbon doping of boron wire segments using chemical vapor deposition (CVD) followed by exposure of the carbon doped boron segments to magnesium vapor. The carbon content was determined by the relative contraction of the a -lattice parameter of the MgB_2 phase. The superconducting transition temperature is suppressed by approximately 1 K/%C while $H_{c2}^{\parallel ab}(T=0)$ rises at a rate of nearly 4 T/%C. Carbon doping increases $H_{c2}^{\perp ab}$ at a faster rate than $H_{c2}^{\parallel ab}$, resulting in a decrease in the anisotropy ratio, $\gamma_H = \frac{H_{c2}^{\parallel ab}}{H_{c2}^{\perp ab}}$, approaching 1 near a doping level of $x=0.10$ (14). It should be noted that, whereas pure MgB_2 has a strongly temperature dependent anisotropy ratio with γ_H decreasing monotonically with

temperature (14; 15; 16; 47; 17), increasing the carbon content causes γ_H to become increasingly temperature independent. Whereas the suppression of T_c can be understood as a result of Fermi surface changes due carbon electron doping the system, the increase in H_{c2} and change in the temperature dependence of γ_H are a result of an increase in scattering, primarily within the π band (14).

Critical current densities in fully dense $\text{Mg}(\text{B}_{1-x}\text{C}_x)_2$ fibers drop off rapidly in field in spite of the enhancements in H_{c2} values. This is presumably due to poor flux pinning associated with the large grains which result from high reaction temperatures. Additionally, MgB_2 fibers produced by exposing boron filaments to Mg vapor are curly and extremely brittle and not particularly useful for practical applications. In order to take advantage of the high upper critical field values which result from carbon doping, we have investigated methods for enhancing critical current densities in $\text{Mg}(\text{B}_{1-x}\text{C}_x)_2$. We have also investigated different synthesis techniques for producing $\text{Mg}(\text{B}_{1-x}\text{C}_x)_2$ powders for use in powder-in-tube (PIT) applications.

Ti was added to $\text{Mg}(\text{B}_{1-x}\text{C}_x)_2$ filaments in order to explore the feasibility of creating TiB_x precipitates in carbon doped MgB_2 samples in order to enhance in-field critical current densities. Doped boron filaments were produced by chemical vapor deposition and conversion to MgB_2 was carried out by reacting these filaments in excess Mg vapor at temperatures up to 1200 °C. Ti formed TiB_2 precipitates and carbon entered the structure, enhancing H_{c2} . The high reaction temperatures necessary to convert the filaments resulted in coarsened precipitates and no enhancements in J_c were found.

Bulk $\text{Mg}(\text{B}_{1-x}\text{C}_x)_2$ samples were synthesized in sintered pellet form from mixtures of elemental Mg, B, and the binary compound B_4C . Carbon incorporation was dramatically improved by a two step reaction process at an elevated temperature of 1200 °C. This reaction process results in a solubility limit near $x \sim 0.07$. We found that impurities in the starting B cause an additive suppression of T_c . We combine these data with T_c and $H_{c2}(T=0)$ data from CVD wires as well as plasma spray synthesized powders and present a unifying H_{c2} and T_c versus x plot. Whereas these samples had similar improvements in H_{c2} associated with the carbon doping, the J_c values remain low. Once again the high reaction temperatures appeared

to lead to largish grain sizes.

In an attempt to combine the improved H_{c2} values from carbon doping with reduced grain sizes, nano-scale carbon doped boron particles were synthesized by a gas phase plasma synthesis method. Powders are approximately 50 nm in size and form lacy agglomerates that are of order 1-10 μm . Conversion to $\text{Mg}(\text{B}_{1-x}\text{C}_x)_2$ can be carried out in as little as 4 hours at 950 $^\circ\text{C}$. Pressed pellets exhibit improved critical current densities, carrying in excess of 10^5 A/cm^2 in a 5.5 T field at 5 K for sample containing 8.1% carbon. The fine grain nature makes these powders well suited for PIT applications.

Radiation using protons, heavy ions, neutrons, etc., is another route to systematically perturb the system. Of these possible routes, neutron irradiation offers the best avenue for uniformly damaging bulk MgB_2 . We have performed a systematic study of the evolution of the superconducting and normal state properties of neutron irradiated MgB_2 wire segments as a function of fluence and post exposure annealing temperature and time. There are two main sources of damage from neutron irradiation of MgB_2 . First, fast neutrons deposit energy through inelastic collisions with atoms, creating thermal and dislocation spikes (18). Second, ^{10}B , which has a natural abundance of 19.9%, has a large capture cross section for lower energy neutrons and readily absorbs these thermal neutrons, subsequently α decaying to ^7Li , with the energetic α particle leaving its own damage track. All fluences used suppressed the transition temperature, T_c , below 5 K and expanded the unit cell. For each annealing temperature T_c recovers with annealing time and the upper critical field, $H_{c2}(T=0)$, approximately scales with T_c . By judicious choice of fluence, annealing temperature and time, the T_c of damaged MgB_2 can be tuned to virtually any value between 5 and 39 K. The suppression of T_c results from both a decrease in the density of states at the Fermi surface and an increase in interband scattering.

Finally, we have studied the evolution of superconducting and normal state properties of neutron irradiated $\text{Mg}(\text{B}_{0.962}\text{C}_{0.038})_2$ wire segments as a function of post exposure annealing time and temperature. The initial fluence fully suppressed superconductivity and resulted in an anisotropic expansion of the unit cell. Superconductivity was restored by post-exposure

annealing. The upper critical field, $H_{c2}(T=0)$, approximately scales with T_c starting with an undamaged T_c near 37 K and $H_{c2}(T=0)$ near 32 T. Up to an annealing temperature of 400 °C the recovery of T_c tends to coincide with a decrease in the normal state resistivity and a systematic recovery of the lattice parameters. Above 400 °C a decrease in order along the c- direction coincides with an increase in resistivity, but no apparent change in the evolution of T_c and H_{c2} . To first order, it appears that carbon doping and neutron damaging affect the superconducting properties of MgB_2 independently.

This work is presented in the following order: A review of the relevant physics and discussion of theoretical predictions for a two gap superconducting compound is given in chapter 2. Chapter 3 provides a review of the basic properties of MgB_2 . Details of sample synthesis and characterization are given in chapter 4. Chapter 5 presents normal state and superconducting properties of $Mg(B_{1-x}C_x)_2$ wires. Attempts to increase critical current densities in filaments via titanium additions are discussed in chapter 6. In chapters 7 and 8 alternative methods for synthesizing doped MgB_2 powders are explored. In chapter 7 we synthesize $Mg(B_{1-x}C_x)_2$ up to $x=0.069$ using a mixture of Mg, B, and the binary compound B_4C . Chapter 8 explores an alternative method, plasma spray synthesis, to produce nanometer sized doped boron powders for powder-in-tube applications. The effects of neutron irradiation on pure MgB_2 wires is discussed in chapter 9. This is followed by a study of the effects of neutron irradiation on $Mg(B_{0.962}C_{0.038})_2$ wires, presented in chapter 10. I will summarize the results of all of these studies in chapter 11 and discuss future directions for research in understanding the physics behind this novel material as well as its development for practical applications.

CHAPTER 2. Physics Review

2.1 Properties of Superconductors

In 1957 Bardeen, Cooper, and Schrieffer (BCS) published a theory explaining superconductivity as a phonon mediated process among conduction electrons (19). The attractive potential created by lattice vibrations causes electrons with energy near the Fermi energy to participate in coherent scattering. These electrons form pairs, called Cooper pairs, consisting of electrons with equal and opposite momentum and opposite spin. By forming pairs through an attractive potential created by phonons the net energy of the system is lowered. In the condensed state, a superconducting energy gap opens about the Fermi surface and has magnitude

$$\Delta(0) = 2\hbar\omega_D \exp[-1/VN(E_F)] \quad (2.1)$$

where ω_D is the Debye frequency, which characterizes the lattice vibrations of the material, V is a measure of the strength of the electron phonon coupling, and $N(E_F)$ is the density of states at the Fermi surface. The size of the superconducting gap at zero Kelvin is related to the superconducting transition temperature, T_c :

$$k_B T_c = \frac{\Delta(0)}{1.764} = 1.13\hbar\omega_D \exp[-1/VN(E_F)] \quad (2.2)$$

This equation is valid in the weak coupling limit ($\lambda = VN(E_F) < 0.25$). For superconductors which exhibit strong electron phonon coupling, T_c is more accurately determined by the McMillan equation (20):

$$T_c = \frac{\theta_D}{1.45} \exp\left[-\frac{1.04(1 + \lambda)}{\lambda - \mu^*(1 + 0.62\lambda)}\right] \quad (2.3)$$

where μ^* is the coulomb pseudopotential and whose value is typically taken to be 0.1.

For any given material the critical temperature and thermodynamic critical magnetic field, H_c , define the phase space in which superconductivity is thermodynamically stable. The thermodynamic critical field is the point at which the field energy equals the condensation energy and is therefore related to the size of the superconducting gap:

$$\frac{1}{2}N(E_F)\Delta^2(0) = \frac{H_c^2}{8\pi} \quad (2.4)$$

Many materials can maintain superconductivity in fields much larger than H_c depending upon the ratio of two important length scales, the magnetic field penetration depth, λ , and the superconducting coherence length, ξ . In the presence of an externally applied field, screening currents within a superconductor expel magnetic flux from within the material (Meissner Effect). While the magnetic field within the bulk of superconductor is zero, Maxwell's equations dictate that B is continuous at any interface. Thus if a superconductor is immersed in an externally applied field, B decreases to zero within the superconductor over some length scale, which is referred to as the magnetic field or London penetration depth and is given by $\lambda_L = \sqrt{\frac{mc^2}{4\pi ne^2}}$. The length scale over which the density of superconducting electrons rises from zero to the bulk value is referred to as the superconducting coherence length.

The ratio of these two length scales gives rise to two different types of superconducting materials. In type I superconductors, $\kappa \equiv \frac{\lambda}{\xi} < \frac{1}{\sqrt{2}}$, interfaces between superconducting and normal regions contribute a positive amount of energy. The total energy of the system is minimized if there are as few of such interfaces as possible. As a result, for an infinite slab in a parallel field, the bulk excludes magnetic flux, exhibiting perfect diamagnetism, up until H_c (Figure 2.1a).

In a type II superconductor, $\kappa > \frac{1}{\sqrt{2}}$, there is a negative contribution to the total energy for each interface region. However, the formation of a vortex results in a reduction of the superconducting volume fraction. Therefore, the appearance of vortices within a superconductor occurs when the gain in energy associated with the decrease of the density of Cooper pairs is balanced by the decrease in magnetic and surface energy. Type II superconductors

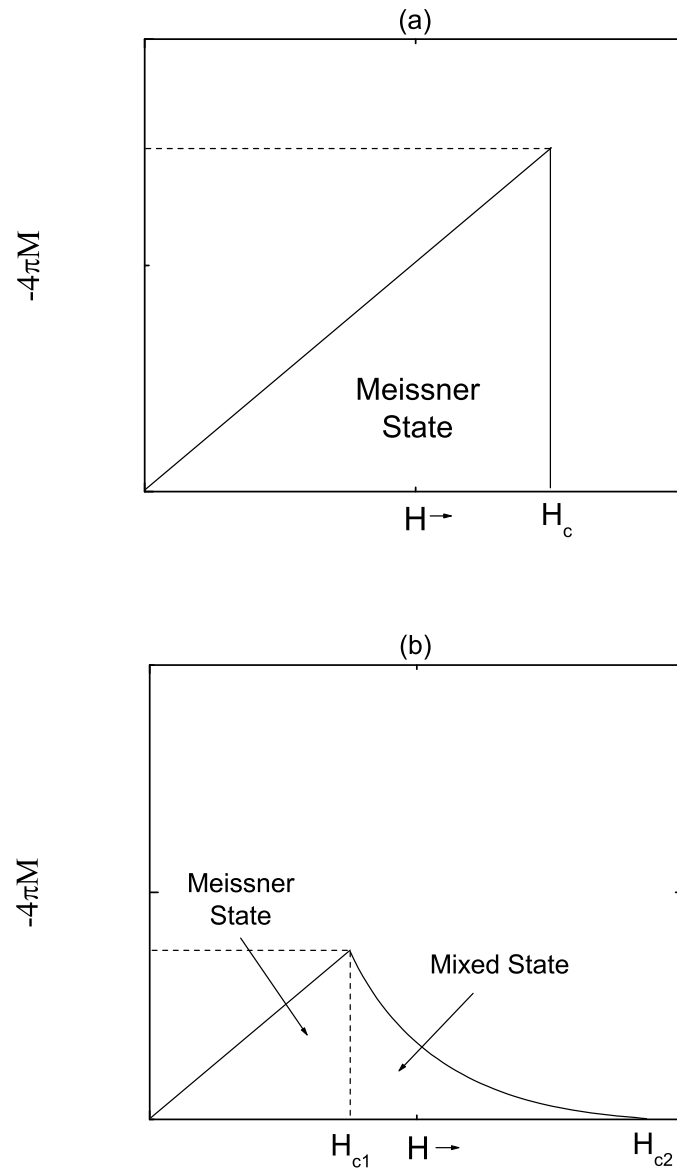


Figure 2.1 Schematic magnetization as a function of field for a (a) - type I and (b) - type II superconductors.

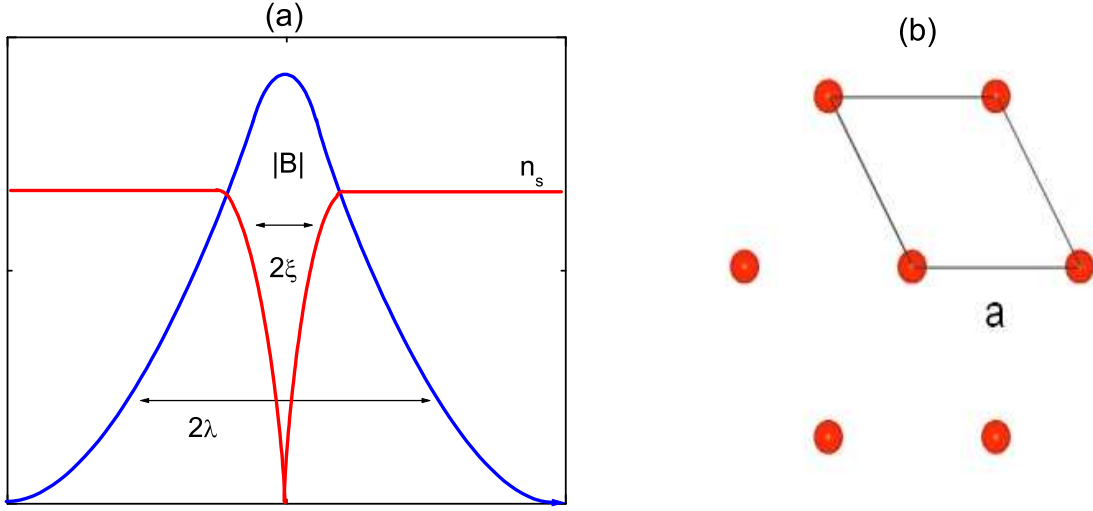


Figure 2.2 (a) Schematic of an individual vortex. Within the core of the vortex the density of superconducting electrons drops toward zero and the magnetic field strength rises to above that of the applied field value. (b) In the mixed state the vortices arrange themselves in a triangular lattice, with a field dependent vortex-vortex spacing.

exhibit perfect diamagnetism or Meissner screening up to a lower critical field, H_{c1} . Above H_{c1} magnetic flux penetrates the material in the form of quantized vortices (Figure 2.2a). One flux quantum, $\Phi_0 = \frac{hc}{2e}$, is determined by fundamental constants and has a magnitude of 2.07×10^{-7} G/cm². The radius of the core of a vortex is roughly the superconducting coherence length and near H_{c1} the magnetic field at the core of the vortex is roughly $2H_{c1}$ (21). The vortices within a superconductor usually arrange themselves in a triangular lattice with a field dependent spacing between vortices given by $a = 1.075 \left(\frac{\Phi_0}{B} \right)^{\frac{1}{2}}$ (Figure 2.2b). As the strength of the external field is further increased more vortices enter the superconductor and, since $\lambda > \xi$, fields from neighboring vortices begin to overlap. At the upper critical field, H_{c2} , the vortex cores overlap and superconductivity is destroyed. A schematic of the field dependence of the magnetization for a type II superconductor is given in figure 2.1b. As is clear from the preceding discussion, the values of κ , H_{c1} , and H_{c2} are all interrelated quantities and can be written in terms of the thermodynamic critical field, H_c :

$$H_c = \sqrt{H_{c1}H_{c2}} \quad (2.5)$$

$$H_c = \sqrt{2\kappa}H_{c1} \quad (2.6)$$

$$H_c = H_{c2}/\sqrt{2\kappa} \quad (2.7)$$

Upper critical field values in type II superconductors can be much larger than those attained in type I materials. It is not uncommon for type II superconductors to achieve H_{c2} values on the order of tens of Tesla, whereas type I superconductors typically have H_c values of order hundredths to tenths of a Tesla.

2.2 Ginzburg-Landau Theory

A thorough understanding of superconductivity requires the full machinery of the microscopic BCS theory of superconductivity. However, many of the thermodynamic properties of a superconductor can easily be understood within the phenomenological Ginzburg-Landau theory of superconductivity. The basic premise of the general Landau theory of phase transitions is that the thermodynamic properties of an ordered state can be determined by expanding the free energy in a Taylor series about an order parameter. In the Ginzburg-Landau theory of superconductivity (see reference (11) for an in-depth discussion) the order parameter, ψ , is related to the local density of superconducting electrons, n_s :

$$n_s = |\psi(x)|^2 \quad (2.8)$$

ψ is itself allowed to be a complex quantity and is generally expressed in the form:

$$\psi = |\psi| e^{i\varphi} \quad (2.9)$$

If the wave function varies slowly in space, then the series expansion of the free energy density is assumed to be:

$$f = f_{n0} + \alpha |\psi|^2 + \frac{\beta}{2} |\psi|^4 + \frac{1}{2m^*} \left| \left(\frac{\hbar}{i} \nabla - \frac{e^*}{c} \mathbf{A} \right) \psi \right|^2 + \frac{h^2}{8\pi} \quad (2.10)$$

f_{n0} is the free energy density of the normal state, α and β are temperature dependent parameters, m^* is the mass of the Cooper pair (twice the electron mass), e^* is the charge of the Cooper pair (twice the electron charge), \mathbf{A} is the magnetic vector potential, and h is the applied magnetic field density. Thermodynamic properties of the system can be extracted by minimizing the free energy with respect to the order parameter and vector potential solving the resultant differential equations with the appropriate boundary conditions for a given situation. Since the focus of much of this study has been on the understanding of the evolution of H_{c2} as different perturbations are made, what follows is an outline of the calculations and a discussion of the relevant parameters which influence the upper critical field.

The superconducting coherence length, which can be thought of as either length scale over which the bulk value of $|\psi|^2$ is achieved or the distance an electron travels before pairing with another electron, is defined as

$$\xi^2(T) \equiv \frac{\hbar}{2m^* |\alpha(T)|^2} = \frac{\Phi_0}{2\sqrt{2}\pi H_c(T)\lambda(T)} \quad (2.11)$$

where Φ_0 is the flux quantum, H_c is the thermodynamic critical field, and λ is the magnetic field penetration depth. If we then ignore higher order terms in ψ , a condition that is appropriate in the high field limit where the strength of the magnetic field has limited ψ , then the differential equation to be solved becomes:

$$\left(\frac{\hbar}{i} \nabla - \frac{e^*}{c} \mathbf{A} \right)^2 \psi = \frac{\psi}{\xi^2(T)} \quad (2.12)$$

By making an appropriate selection of the gauge ($A_y = Hx$) the energies of the system can be readily solved. The result allows for quantized field values of the form

$$H = \frac{\Phi_0}{2\pi(2n+1)} \left(\frac{1}{\xi^2} - k_z^2 \right) \quad (2.13)$$

where n is an integer and k_z is the z component of the wave vector. The highest allowed field value occurs at $n=k_z=0$ and defines the upper critical field, H_{c2} :

$$H_{c2} = \frac{\Phi_0}{2\pi\xi^2} \quad (2.14)$$

It should be noted that the length scale ξ is different than, but analogous too the Pippard coherence length, ξ_0 . The Pippard coherence length is a length scale estimated using the uncertainty principle. For a superconducting material with a superconducting gap $\Delta(0)$ and a spherically symmetric Fermi surface with Fermi velocity v_F :

$$\xi_0 \equiv \frac{\hbar v_F}{\pi\Delta(0)} \quad (2.15)$$

For our interests, we consider the functional relationship between the the electron mean free path, ℓ , and the superconducting coherence length. In general, ξ can be determined by numerical methods for an arbitrary ratio of ξ_0/ℓ (22). The superconducting coherence length decreases monotonically with decreasing mean free path, and approximate closed form expressions can be obtained in the clean and dirty limits:

$$\text{for } \ell \gg \xi, \quad \frac{1}{\xi} = \frac{1}{\xi_0} + \frac{1}{\ell}, \quad (2.16)$$

$$\text{for } \ell \ll \xi, \quad \xi = \sqrt{\xi_0 \ell}. \quad (2.17)$$

A plot of the coherence length as a function mean free path is given in figure 2.3. ξ_0 is taken to be 10 (arbitrary units) and equations 2.16 and 2.17 have been employed to calculate ℓ in the clean and dirty limits. The form of the curve in the intermediate region ($\ell/\xi_0 \sim 1$) can be determined by numerical methods, see references (22; 23).

The superconducting coherence length can be shortened by introducing point defects which decrease the mean free path whilst driving the material from the clean limit ($\ell \gg \xi$) into the dirty limit ($\ell \ll \xi$). As the mean free path decreases, the slope, $(dH_{c2}/dT)_{T=T_c}$, and magnitude H_{c2} increase (24). Qualitatively, decreasing the coherence length decreases the size of the vortex core and allows for a greater density of vortices within a superconductor, thereby increasing the upper critical field. Practically speaking, these results indicate the upper critical field of a single gap superconductor can be enhanced by introducing point defects which enhance

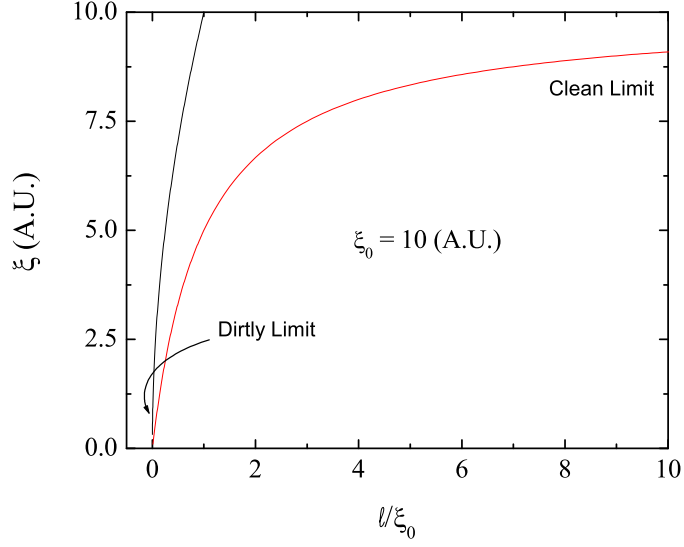


Figure 2.3 Superconducting coherence length as a function of mean free path. In the clean and dirty limits, ξ is determined by equations 2.16 and 2.17 respectively.

scattering and thereby decrease ℓ . The temperature dependence of the upper critical field for a single gap superconductor has been well described (?), with $H_{c2}(T=0)$ given by:

$$H_{c2}(T = 0) = 0.69T_c \frac{dH_{c2}}{dT} \Big|_{T_c} \quad (2.18)$$

For example, the upper critical field in Nb_3Sn has been shown to approach the paramagnetic limit, where superconductivity is destroyed due to the polarization of conduction electrons, with 20 atomic percent substitution of Ta for Nb (25) (Figure 2.4).

2.3 Two Gap Superconductivity

The situation is more complex for a two gap superconductor in which there are three scattering channels, corresponding to scattering within each of the bands in addition to scattering between the bands, which may influence the evolution of the upper critical field. A thorough theoretical treatment (in the dirty limit approximation) of the temperature dependence of the

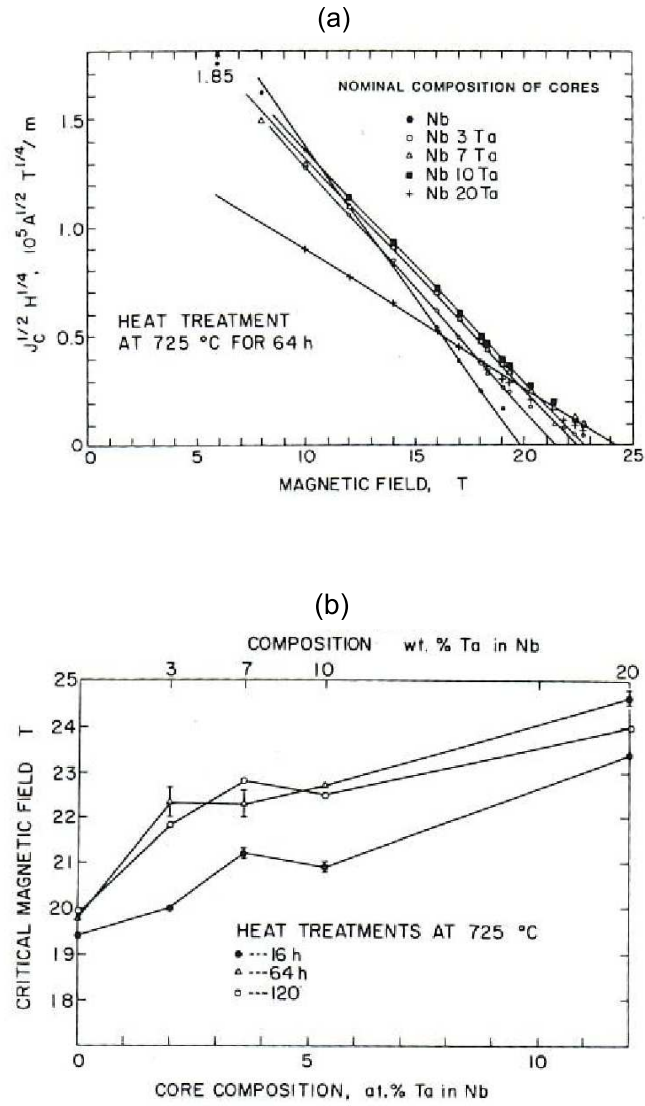


Figure 2.4 (a) Determination of $H_{c2}(T=0)$ values in Ta doped Nb by Kramer's formulation (25; 26). (b) $H_{c2}(T=0)$ values as a function of Ta content (25).

upper critical field as a function of the relative strength of the scattering within the three channels was done by A. Gurevich (27) and some of the results are summarized here. It should be noted that, whereas this theory can give some insight to how different scattering mechanisms can change H_{c2} values and ratios, it cannot be quantitative for lightly doped (or pure) MgB_2 since these compounds are near the clean limit.

In a two gap superconductor intraband scattering affects the anisotropy of the system but does not affect T_c (28) whereas interband scattering serves as a pair-breaking mechanism, which reduces T_c (29; 30). Gurevich's calculations reveal that the temperature dependence of the upper critical field depends greatly upon the relative strengths of the two intraband diffusivities. For $H_{c2}^{\parallel c}$ and near T_c Gurevich obtains the expression:

$$H_{c2}^{\parallel c} = \frac{8\Phi_0(T_c - T)}{\pi^2(a_1 D_\sigma + a_2 D_\pi)} \quad (2.19)$$

where a_1 and a_2 are terms which depend on the electron phonon coupling constants, whose values have been worked out using the results of *ab initio* calculations (31), and D_σ and D_π are the diffusivities of the σ and π bands respectively. This equation implies that near T_c H_{c2} is determined by the band which has the greater diffusivity (i.e. longer mean free path). At $T=0$ the interesting physics resides in the two extreme limits of different diffusivities. In these limits Gurevich finds:

$$H_{c2}(0) = \frac{\Phi_0 T_c}{2\gamma D_\pi} e^{\nu_1}, D_\pi \ll D_\sigma e^{\nu_2} \quad (2.20)$$

$$H_{c2}(0) = \frac{\Phi_0 T_c}{2\gamma D_\sigma} e^{\nu_3}, D_\sigma \ll D_\pi e^{\nu_4} \quad (2.21)$$

where γ is the Euler constant and ν_1 - ν_4 are all terms which depend upon electron phonon coupling constants. $H_{c2}(T=0)$ is determined by the band containing the minimum diffusivity. Dramatically different behavior for the evolution of $H_{c2}(T)$ is seen for these three differing cases (Figure 2.5a-c). For $D_\sigma = D_\pi$, the formulas reduce to the results for dirty single gap superconductors (32; 33). For strong intraband σ scattering, $D_\sigma \ll D_\pi$, $H_{c2}^{\parallel c}$ is predicted to

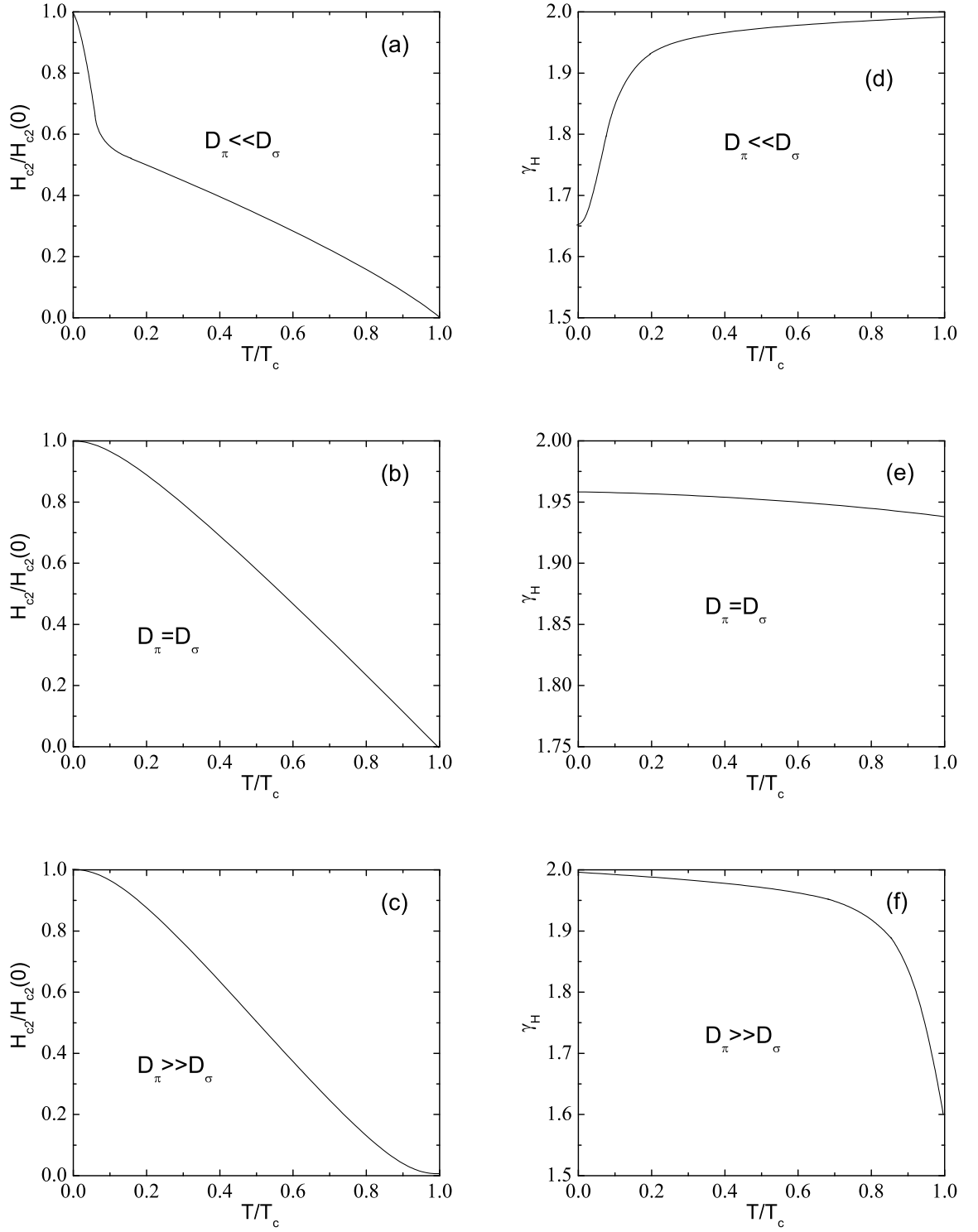


Figure 2.5 (a)-(c) Temperature dependence of the upper critical field, $H_{c2}^{\parallel c}$, within the three different scattering regimes. (d)-(f) Temperature dependence of the anisotropy ratio within the three different scattering regimes. Figures are recreated from reference (27).

exhibit positive curvature near T_c . In contrast for strong intraband π scattering, $D_\pi \ll D_\sigma$, H_{c2} approaches T_c linearly, but exhibits a dramatic upturn at low temperatures.

Pure MgB_2 has been shown to have an anisotropy ratio, $\gamma_H = \frac{H_{c2}^{\parallel ab}}{H_{c2}^{\perp ab}}$, near 6 at $T=0$, with γ_H decreasing monotonically as a function of temperature (14; 15; 16; 47; 17). If MgB_2 is driven into the dirty limit, then the three scattering regimes also lead to different angular dependencies of H_{c2} as can be seen most readily by comparing the temperature dependence of γ_H (Figure 2.5d-f). The evolution of the anisotropy ratio differs for the two extreme cases of scattering. If $D_\pi \ll D_\sigma$ then γ_H monotonically increases as a function of temperature. In the limit $D_\sigma \ll D_\pi$, γ_H decreases as a function of temperature. In the intermediate regime, $D_\sigma = D_\pi$, γ_H only moderately decreases as a function of temperature.

These calculations show that, in the dirty limit, the upper critical field and anisotropy ratio in MgB_2 can be tuned if the intraband diffusivity ratios can be selectively varied. It should be noted that, according to these calculations, in the dirty limit $\gamma_H < 2$, indicating that pure samples are far from the dirty limit. They also show that some subtleties in the temperature dependencies of H_{c2} and γ_H exist depending upon which specific scattering channel is most affected in driving MgB_2 into the dirty limit. In the case of increased π scattering, $D_\pi \ll D_\sigma$, H_{c2} shows a dramatic upturn at low temperatures coinciding with a decrease in the anisotropy ratio. Such a scenario would be advantageous for developing devices operating at low temperature and in high magnetic fields. In the other extreme, $D_\sigma \ll D_\pi$, the anisotropy is lower near T_c , which may be necessary for developing high current lower field devices which operate in the 20-30 K range as the anisotropic nature in pure MgB_2 severely limits in field critical current densities (6).

2.4 Critical Current Densities

Superconductors can carry current with zero resistance only up to a critical current density. The theoretical limit of the current density, referred to as the depairing current, corresponds to the point at which the increase in the kinetic energy of the electrons is greater than the superconducting energy gap, causing the Cooper pair to split. Said in another way, the addi-

tional momentum of the electrons shifts of the Fermi surface in k-space to such an extent that electrons near the Fermi surface can't find other electrons with equal and opposite momentum with which to pair. Within the framework of the Ginzburg-Landau theory, the depairing current density is given by (5)

$$J_{pair} = \frac{\Phi_0}{3\sqrt{3}\pi\lambda^2\xi} \quad (2.22)$$

For most type II superconductors, the theoretical limit of the critical current density is near 10^8 A/cm². In practice such a limit is never achieved because a voltage drop develops along the direction of the current flow resulting from the motion of vortices.

When a current flows through a type II superconductor in the mixed state the current exerts a force on the vortex. The superposition of the circulating currents about a vortex and the applied current results in a greater amount of current flowing on one side of the vortex (Figure 2.6a). Consequently, the magnitude of the $\mathbf{I} \times \mathbf{B}$ force is greater on one side, causing the the vortex to experience a force directed perpendicular to the direction of the current flow and having magnitude $F = J\Phi_0$ (Figure 2.6b). If there exists no mechanism to pin the vortex to a specific location, then the resultant motion creates a voltage in accordance with Faraday's law of induction ($\mathcal{E} = -\frac{d\Phi}{dt}$). The induced voltage drop is along the direction of current flow and hence this flux flow creates a resistance along the length of the superconductor (Figure 2.6c).

Critical current densities can be enhanced by introducing pinning centers. A pinning center can be any type of defect which is of order the size of the coherence length and locally suppresses the order parameter. The overall energy of the superconducting state is lowered by the condensation of electrons into cooper pairs. It costs energy to create a vortex and therefore, it is more energetically favorable for a vortex, whose core is in the normal state, to occupy a fixed region where superconductivity has been locally suppressed. Vortices can be pinned to a wide variety of defects. They can be pinned in grain boundaries in polycrystalline materials, in precipitates, which are non-superconducting secondary phases imbedded within the superconducting matrix, or at crystalline defects, which can be introduced, for example, by some type of irradiation. Thus J_c can be enhanced by minimizing grain size, including

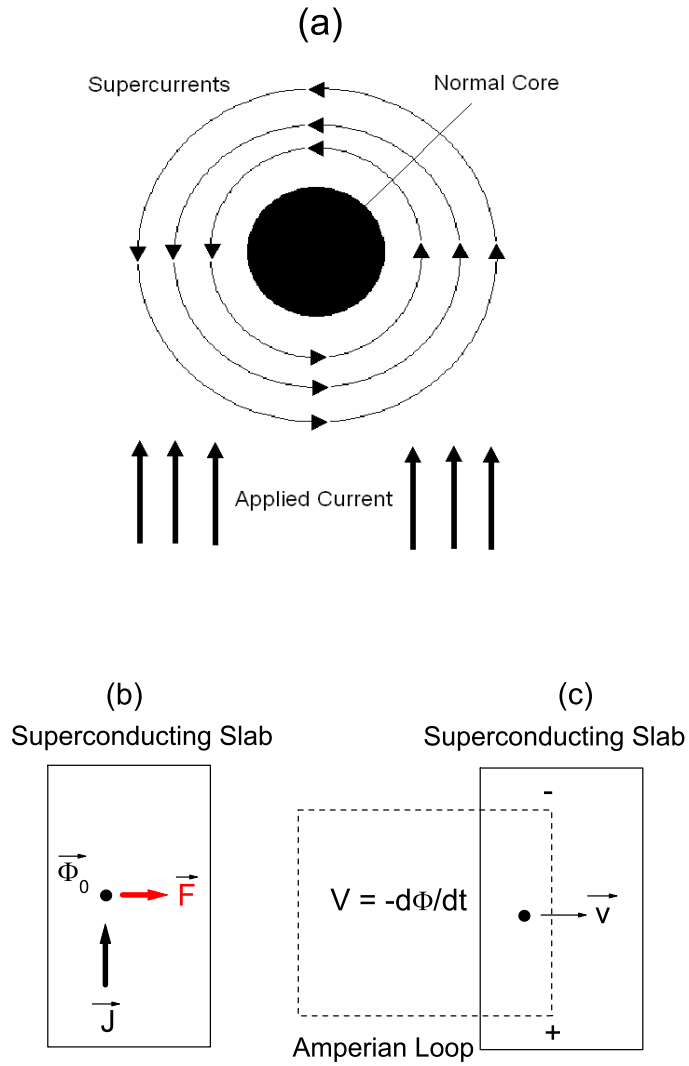


Figure 2.6 (a) Screening and applied currents in a type II superconductor in the mixed state. The sum of the currents creates a net difference on either side of the vortex. (b) The net current exerts a force on the vortex which causes it to move in a direction perpendicular to the current flow. (c) The motion of the vortex creates the voltage drop and hence a resistance.

precipitates, or controlled irradiation of superconducting materials.

2.5 Bean Critical State Model

Critical current densities should, formally, be determined by measuring the voltage along a sample as a function of applied current. For practical conductors, J_c is usually defined at the point at which an electric field of $0.1\mu\text{V}/\text{cm}$ develops along the direction of current propagation. In small research samples it is not practical to measure the critical current density using transport measurements, as sample heating at the current contacts can cause the sample to quench. In such cases the critical current density can be estimated from magnetization hysteresis loops using the Bean Critical State Model (34).

As an externally applied magnetic field is increased, vortices begin to enter the superconductor. Pinning forces prevent the flow of vortices into the center of the material, and a gradient of vortex density results (Figure 2.7a). Such a gradient induces the flow of current within the superconductor through the Maxwell equation

$$\nabla \times \mathbf{B} = \frac{4\pi}{c} \mathbf{J} \quad (2.23)$$

The underlying assumption of the Bean Critical State Model is that J_c is independent of H so that the gradient is constant and the resultant current equals the critical current. This allows for the determination of the critical current density for a sample of well defined geometry by measuring the width of the magnetization hysteresis loop. To illustrate this we present the calculation determining the critical current density for a superconducting annulus with outer radius r_o and inner radius r_{in} and containing a normal core. The hollowed out cylinder is assumed to be infinitely long with the magnetic field applied along the z -axis. This geometry reflects that of the filaments used in this study (see chapter 5).

Suppose we have performed an entire hysteresis loop in which we ramped the external field to a large value (several Tesla) in the positive z direction and then bring it back to zero. The flux pinning forces result in trapped flux with a profile sketched in Figure 2.7b. The magnetization along the z direction is given by

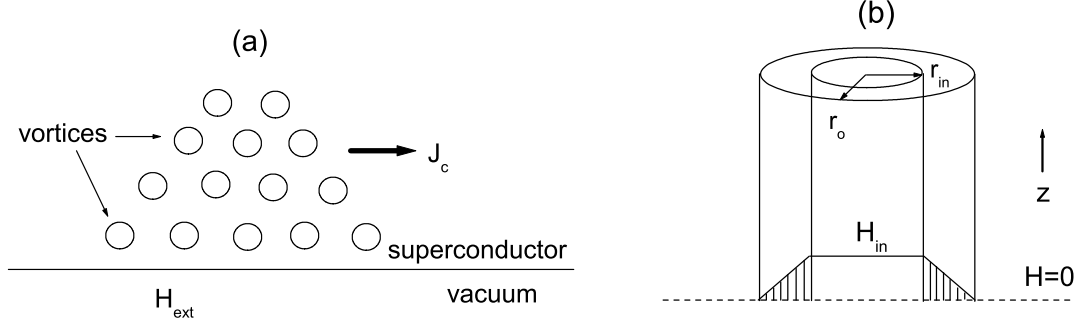


Figure 2.7 (a) Pinning forces within the superconductor create a gradient of vortex density which induces the flow of a current within the superconductor. The Bean Model assumes the gradient is constant and the induced current is the critical current. (b) Schematic of the trapped flux in an infinitely long superconducting wire with a hollowed out core following a hysteresis loop in which a large external field was initially applied in the $+z$ direction.

$$M_z = \frac{\mu_z}{V} \quad (2.24)$$

where the magnetic moment is

$$\mu_z = \frac{1}{2} \int \mathbf{r} \times \mathbf{j} dV \quad (2.25)$$

Under the assumption of a constant gradient of flux resulting in the flow of constant current J_c , $\mathbf{j} = J_c \hat{\phi}$. Expressing the integral in cylindrical coordinates ($dV = 2\pi l_z \rho^2 d\rho$) this becomes

$$\mu_z = \pi l_z J_c \int \rho^2 d\rho = l_z J_c \frac{\pi}{3} (r_o^3 - r_{in}^3) \quad (2.26)$$

The magnetization is therefore

$$M_z = \frac{J_c}{3} r_o \left(1 - \frac{r_{in}^3}{r_o^3} \right) \quad (2.27)$$

If we then perform the same loop only directing the field in the negative z direction, the magnetization of the sample has the same magnitude but but is in the opposite direction. If we subtract the two quantities we obtain

$$|\Delta M| = \frac{2}{3} J_c r_o \left(1 - \frac{r_{in}^3}{r_o^3}\right) \quad (2.28)$$

This equation can be rewritten to express J_c as a function of $|\Delta M|$;

$$J_c = \frac{3}{2} \frac{|\Delta M|}{r_o \left(1 - \frac{r_{in}^3}{r_o^3}\right)} \quad (2.29)$$

CHAPTER 3. Basic Properties of MgB₂

3.1 Crystal Structure and Bonding

MgB₂ forms a hexagonal crystal structure with hexagonal layers of Mg alternating with honeycomb layers of B (Figure 3.1a). MgB₂ is a fundamentally intermetallic compound, but with covalent boron with sp³ bonding. This can be seen most clearly in a plot of equi-electron density (Figure 3.1b). The in-plane bonding gives rise to quasi two dimensional tubes, called σ bands, in the Fermi surface (Figure 3.1c and 3.1d). The p_z orbitals form π bonds within the boron ring and overlap with neighboring layers, creating the 3-D tubular network, or π bands, of the Fermi surface. The bonding within the boron plane is similar to the bonding between carbon atoms in graphite. However, the presence of Mg²⁺ ions between the boron layers gives rise to charge transfer from the σ bands to the π bands. As a result the would be covalent bands within the boron plane become hole-like metallic bands (36).

3.2 Pairing Mechanism

Since the discovery of superconductivity by Onnes in 1911 (37) researchers have continually searched for materials with higher transition temperatures. Analysis of equation 2.2 shows there are three main parameters which influence T_c; the Debye frequency, the electron phonon coupling term, and the electron density of states at the Fermi surface. Since the electron phonon coupling term can not be predicted *a priori*, searches for materials with high transition temperatures involved compounds consisting of light elements (high ω_D) and transition metals (large N(E_F)).

Prior to the discovery of superconductivity in MgB₂, the highest known transition temperature for an intermetallic compound was 23 K in Nb₃Ge (38), matched decades later by

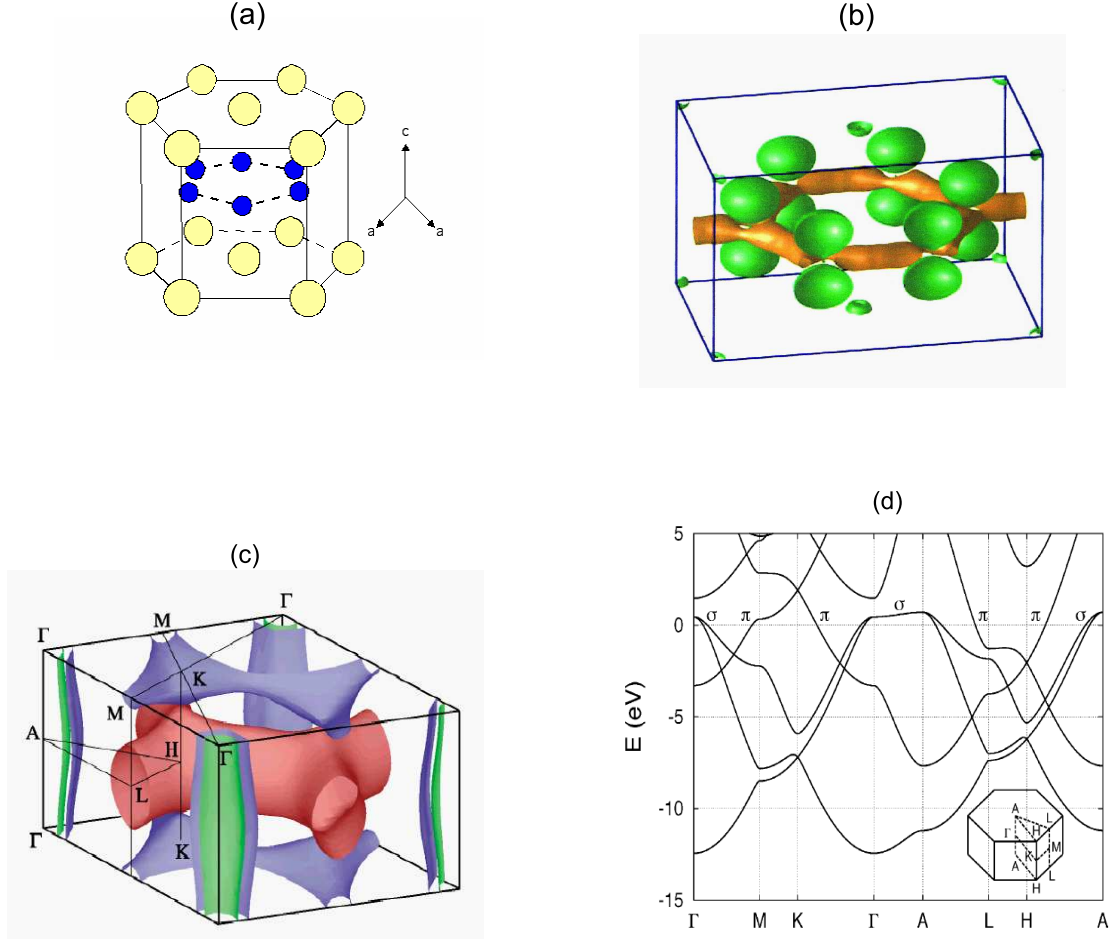


Figure 3.1 (a) Crystal structure (b) Equi-electron density plot (c) Fermi surface and (d) band structure of MgB₂. Two sigma bands are unfilled along the Γ -A line, which gives rise to the quasi 2-D tubes in the fermi surface. Crystal structure and electron density images courtesy of O. Jepsen, see reference (35). 3-d Fermi surface and band structure plots are from references (9; 10).

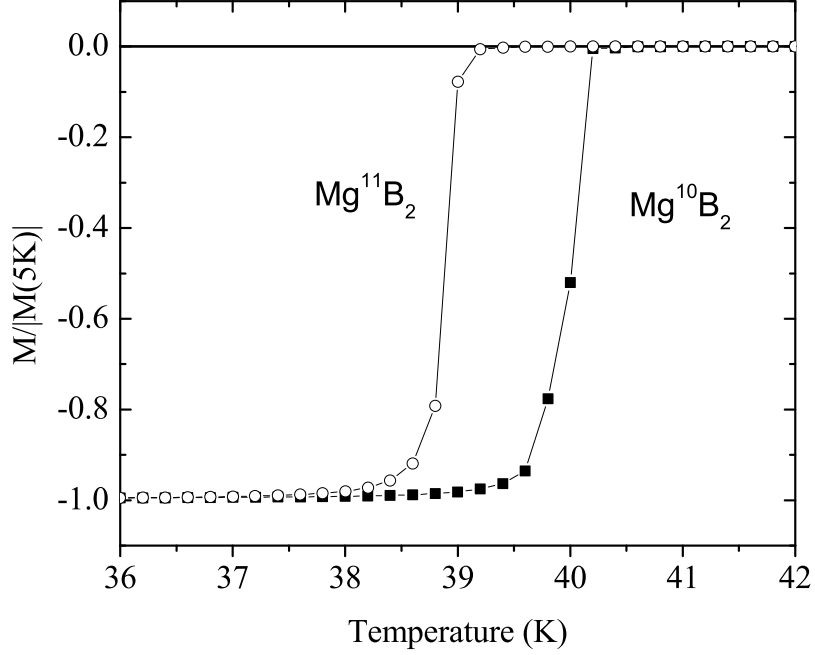


Figure 3.2 Normalized magnetization curves for Mg^{11}B_2 and Mg^{10}B_2 showing a near 1 K increase in T_c when ^{11}B is substituted with ^{10}B (41). This strong boron isotope effect is consistent with MgB_2 being a conventional phonon mediated BCS superconductor.

$\text{YPd}_2\text{B}_2\text{C}$ (39). High temperature superconducting oxides, a class of superconducting materials discovered in 1986 by Bednorz and Müller (40), pushed T_c values beyond 100 K, but these materials appear to have a different pairing mechanism than the "conventional" BCS superconductors. With the discovery of superconductivity near 40 K in MgB_2 (1), the first question to be addressed was what mechanism was responsible for the relatively high transition temperature. Was MgB_2 an extreme high T_c BCS superconductor or was some exotic new mechanism responsible for the electron pairing?

In the most simplistic model the Debye frequency is inversely proportional to the square root of the mass ($\omega_D \sim M^{-0.5}$). Therefore, the transition temperature for phonon mediated superconductors is related to the isotopic mass and BCS superconductors can be characterized

by an isotope coefficient, α , determined by $T_c \sim M^{-\alpha}$. MgB_2 shows a shift in T_c of approximately 1.0 K upon substituting ^{11}B with ^{10}B (Figure 3.2). Note that the simplest $1/\sqrt{M}$ calculation indicated a 0.87 K shift in T_c if the formula unit mass was used and a shift of 1.9 K if T_c was assumed to scale with the boron mass only (41). Therefore the observed 1.0 K also indicates that boron modes may be more important than Mg ones, something that was observed later when the Mg isotope effect was measured. The experimentally determined partial isotope exponents for Mg and B are $\alpha_B=0.26$ (41) and $\alpha_{Mg}=0.02$ (42). This strong isotope effect is consistent with MgB_2 being a phonon mediated BCS superconductor. In addition to the pairing being phonon mediated, MgB_2 exhibits the same pairing symmetry as traditional BCS superconductors. S-wave symmetry has been inferred for MgB_2 by NMR studies of the nuclear spin relaxation rate of ^{11}B (43).

That there exists a strong boron isotope effect and little or no magnesium isotope effect indicates that superconductivity is driven by vibrations within the boron plane. The high transition temperature is believed to result from strong coupling between the conduction electrons and the optical E_{2g} phonon, in which neighboring boron atoms move in opposite directions within the plane (44).

3.3 Thermodynamic Properties and Two Gap Nature

MgB_2 is a type II superconductor with a transition temperature near 39 K. Its type II nature has been verified by the temperature dependence of the equilibrium magnetization (45) as well as through direct visualization of the flux line lattice (46; 47). Defining the upper critical field using an onset criteria in resistivity versus temperature measurements on polycrystalline samples (Figure 3.3a), H_{c2} in pure MgB_2 approaches 16 T at $T=0$ (Figure 3.3b)(3). Transport measurements on polycrystalline materials determine the maximum upper critical field and conceal any anisotropies present. The anisotropic nature of H_{c2} can be inferred from magnetization measurements of polycrystalline samples (4). MgB_2 exhibits a highly anisotropic upper critical field with $H_{c2}^{max}(T=0) \approx 16$ T (3; 48) and $H_{c2}^{min}(T=0) \approx 2.5$ T (Figure 3.3b) (4; 48), which corresponds to an anisotropy ratio of $\gamma_H \sim 6-7$. The direction of the

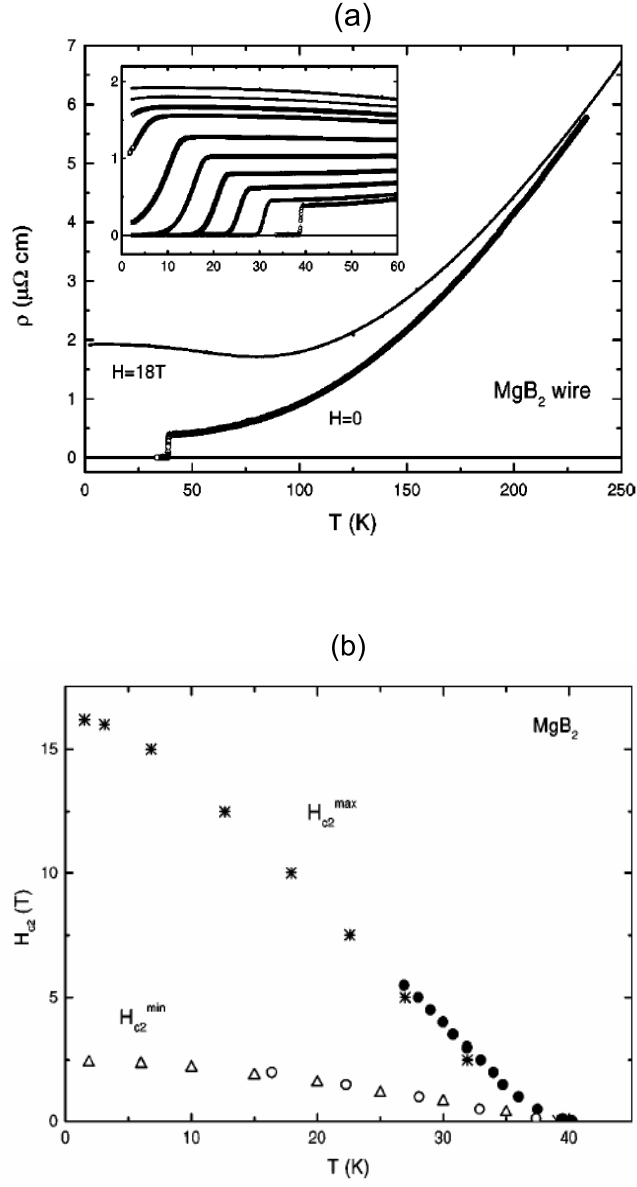


Figure 3.3 (a) Transport measurements on pure MgB_2 filaments taken in applied fields up to 18 T. This plot is taken from reference (3). (b) Upper critical field values for $H_{\parallel ab}$ and $H_{\perp ab}$ (16). $H_{\parallel ab}$ values were determined from an onset criteria in transport measurements and $H_{\perp ab}$ values were inferred from magnetization measurements, see references (3; 4).

maximum upper critical field ($H_{c2}^{max}=H_{c2}^{\parallel ab}$) was initially inferred from transport measurements on polycrystalline samples (49). This conclusion was supported by matching of the anisotropy in H_{c2} to the anisotropy of the Fermi velocities (see discussion below) (4). Subsequent transport and magnetization measurements on MgB_2 single crystals confirmed that the maximum upper critical field corresponds to $H_{\parallel ab}$ as well as the magnitude of H_{c2} in both directions (17).

One of the intriguing aspects of superconductivity in MgB_2 is that the E_{2g} phonon couples to both the σ and π bands, opening up two superconducting gaps. The existence of two gaps was first inferred from specific heat data (12) (Figure 3.4a) and later confirmed by tunnelling measurements (50) (Figure 3.4b). Two gap superconductivity was considered theoretically shortly after the publication of BCS theory (51; 52), but the field never fully matured due to a lack of actual compounds thought to manifest it. Although other materials have shown indications of a two gap nature (53; 54), MgB_2 is the clearest and, giving it high T_c , most compelling example to date of such a material.

One of the very early predictions made by Suhl and co-workers was that the two gaps should open at different temperatures unless there exists some interband scattering to partially mix the bands (51) (Figure 3.5) In the limit of weak interband scattering the smaller gap was predicted to have non-BCS like temperature dependence. In MgB_2 both gaps open at the same temperature, 39 K (50), indicating there exists some scattering between the two bands. Unlike the Suhl prediction, however, both gaps exhibit BCS like temperature dependencies.

The anisotropy of the upper critical field at low temperatures can be understood in terms of the anisotropy of the Fermi velocities in the σ band only (4). At $T=0$, the anisotropy ratio, $\gamma_H=H_{c2}^{max}/H_{c2}^{min}=H_{c2}^{\parallel ab}/H_{c2}^{\perp ab}$, is related to the average Fermi velocities by:

$$\gamma_H = \sqrt{\langle v_{ab}^2 \rangle / \langle v_c^2 \rangle} \quad (3.1)$$

Experimentally $\gamma_H \approx 6$. If the Fermi velocities are averaged over the entire Fermi surface, equation 3.1 yields a value slightly larger than 1. If only the Fermi velocities of the σ band are considered, then equation 3.1 gives a value close to 6. Thus, superconductivity at low temperatures is dominated by the quasi 2-D σ band and it can be inferred that the coupling

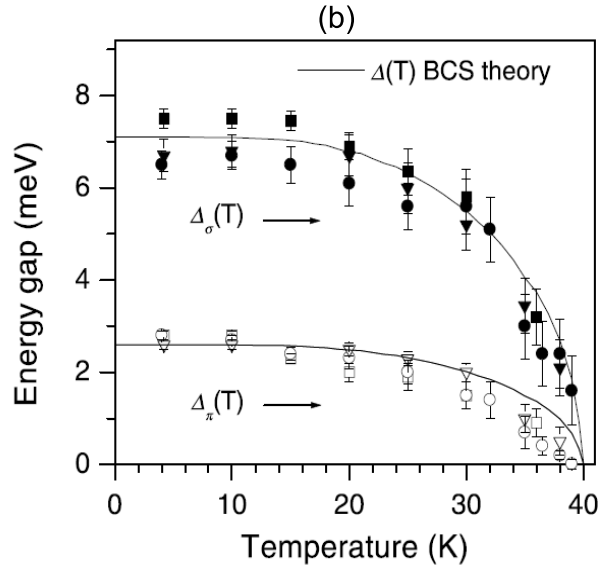
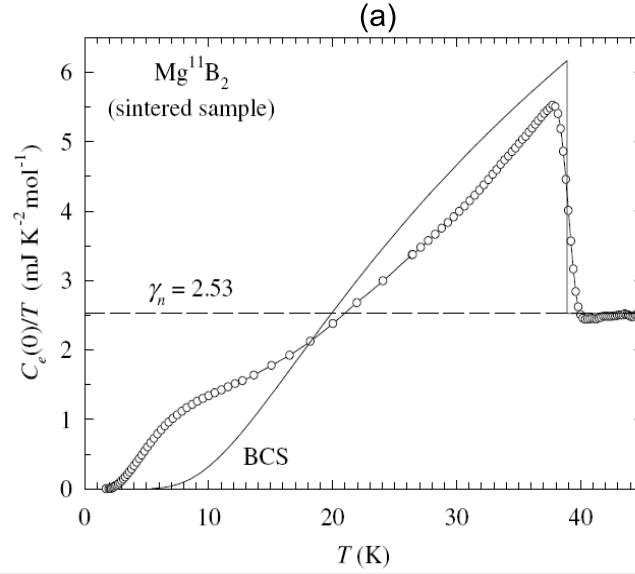


Figure 3.4 (a) Specific heat measurement on Mg¹¹B₂ showing a low temperature shoulder that deviates substantially from single gap BCS behavior (From reference (12)). (b) Temperature dependence of the two superconducting gaps as determined by point contact spectroscopy (From reference (50)).

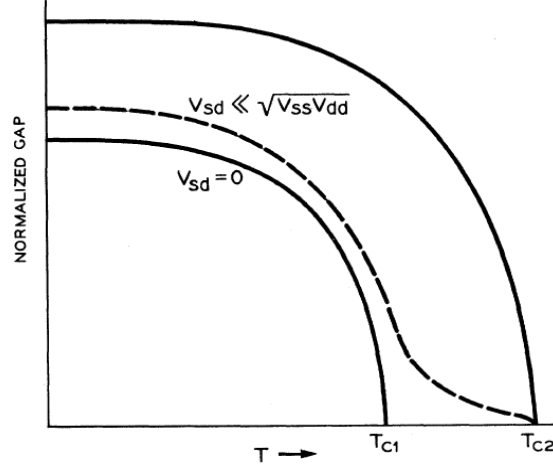


Figure 3.5 Theoretical temperature dependence of the superconducting gaps in a two gap material. If there is no interband scattering the gaps are expected to open at different T_c values. In the limit of weak interband scattering, they open at a single T_c , but the smaller gap exhibits non-BCS behavior. (From reference (51))

between the bands is relatively weak.

Experimentally probing the evolution of the magnitude and anisotropy of the upper critical field as impurities are introduced to the system is a question of importance for both fundamental and applied reasons. In a single gap type II superconductor, the evolution of the upper critical field can be understood in terms of the phenomenological Ginzburg-Landau theory (see Chapter 2). For pure MgB_2 , an estimate of a mean free path from the residual normal state resistivity, $\rho(40\text{K}) \sim 0.4 \mu\Omega \cdot \text{cm}$, yields $\ell \sim 60 \text{ nm}$ (55) and using equation 2.7 gives $\xi \sim 5 \text{ nm}$ (56). Such an estimate for the mean free path is a bit naive and perhaps a little misleading because MgB_2 has three scattering channels associated with the two bands ($\ell_{\sigma\sigma}, \ell_{\pi\pi}, \ell_{\sigma\pi}$). Extracting a single value for the mean free path hides the rich complexity underlying the unique superconducting properties of this novel material, but it does serve to indicate it is well within the

clean limit and foreshadows the ability to achieve substantially higher upper critical fields as MgB_2 is driven towards the dirty limit.

The low magnitude of $H_{c2}^{\perp ab}$ has a large influence on the critical current densities of MgB_2 . For randomly oriented polycrystalline samples the superconducting volume fraction will begin to decrease when the sample is in an external field equal to $H_{c2}^{\perp ab}$. In the case of wires produced by the powder-in-tube method or in fully dense MgB_2 filaments this causes a reduction of superconducting cross section, and hence critical current density in fields well below $H_{c2}^{\parallel ab}$ (6). This should be compared with Nb_3Sn , where J_c values in Nb_3Sn remain essentially constant out to H_{c2} (57). It is therefore desirable to decrease the anisotropy so as to extend the field range over which MgB_2 can carry large amounts of current (in excess of 10^4 A/cm^2).

With regards to the model proposed by Gurevich (27) (see chapter 2) the fundamental question that arises is “Can we selectively tune the scattering within each of the two bands?” The difficulty lies in the introduction of impurities which predominantly effect only one scattering channel. Conventional ”wisdom” holds that substitutions on the Mg site should affect π scattering, whereas substitutions on the B site could enhance either σ or π scattering. Intuitively one would expect that substitutions off of the ab plane should not significantly affect scattering in the quasi two dimensional σ band. It is therefore plausible that Mg site substitutions would predominantly effect π scattering. In the case of B site substitutions no such predictions can be made. Since the π bands are formed by bonding between p_z orbitals of the B atoms, and conduction along the c - direction is through the B plain, the possibility of increased π scattering can not be ruled out. Thus the effects of B site substitutions can not be accurately predicted *a priori*.

At the time that I began the work that is presented in this thesis, the community had already explored and developed a thorough understanding of the many unique physical properties in pure MgB_2 [see reference (58) and works therein for more discussion on the basic properties of MgB_2]. The theoretical work of A. Gurevich (27) suggested there was a wealth of interesting physics to explore if one could systematically control scattering rates within and between the bands.

Work done by Ribeiro and coworkers showed carbon could replace boron in the structure and the resultant scattering enhanced $H_{c2}^{\parallel ab}$ (59; 60; 61). For these experiments B_4C was used as the carbon source and there was no technique for systematically doping MgB_2 with low levels of carbon. I, along with my colleagues, have investigated various methods for synthesizing bulk $Mg(B_{1-x}C_x)_2$ in an attempt to develop a more thorough understanding of the properties and underlying physics in carbon doped MgB_2 . I present our results on samples made by carbon doping boron filaments using chemical vapor deposition (CVD) in chapter 5; mixing elemental Mg, B, and the binary compound B_4C in chapter 7; and carbon doping boron powders using CVD in chapter 8.

An additional route to introducing defects in through some type of radiation damage. Karkin et al. had previously reported the effects of a thermal neutron irradiation on MgB_2 containing natural boron (62). However, their study consisted of a single fluence level and performed an annealing study where only the temperature was varied. Through a collaboration with the Missouri University Research Reactor (MURR) we set out to develop a more complete understanding of the effects of this type of radiation damage on MgB_2 by using various fluence levels as well as studying the effects of annealing time and temperature. A systematic study of the effects of neutron irradiation on the superconducting and normal state properties of pure MgB_2 is presented in chapter 9. In chapter 10 we investigate the effects of neutron irradiation on carbon doped MgB_2 . This will allow us to add and subtract a different scattering mechanism in samples with already enhanced scattering.

In parallel with the study of the physics behind MgB_2 , the high transition temperature has led to a concerted effort to try and develop wire for practical applications. In each of the chapters I address how the synthesis and processing techniques employed effect critical current densities. Additionally, through our collaboration with Specialty Materials, we have been able, using CVD, to investigate various other particle additions to MgB_2 . Our attempts to include TiB_x precipitates to enhance J_c values in carbon doped MgB_2 are discussed in chapter 6.

CHAPTER 4. Sample Preparation and Characterization

4.1 Sample Preparation

4.1.1 Production of Boron Filaments

Fully dense wires of superconducting MgB_2 can be synthesized by exposing commercially available boron filaments to magnesium vapor (63; 64). Specialty Materials, Inc. uses Chemical Vapor Deposition (CVD) to deposit solid boron onto tungsten substrates, producing 0.99999 purity amorphous boron fibers with WB_x cores in kilometer length scales (Figure 4.1) (65). They manufacture filaments of 100 μm and 140 μm , which sell commercially for near \$1/meter and are used for structural reinforcement in applications where low weight is vital, such as in the aerospace and sporting goods industries.

For the production of kilometer length boron wire, 15 μm diameter tungsten filaments are continuously spooled through a ~ 10 meter long chamber. The tungsten is resistively heated to temperatures in the range 1100 $^\circ\text{C}$ -1300 $^\circ\text{C}$ via electrical contact through the water cooled liquid mercury seals at the top and bottom of the chamber. The temperature is not uniform through the entire length of the chamber, rather the fiber warms rapidly as it enters through the top seal and holds near the peak temperature for approximately 2/3 of the chamber before cooling slightly as it nears the bottom.

To produce pure boron filaments, process gasses of BCl_3 and H_2 are passed through the reaction chamber, with flow rates of 3000 cubic centimeters per minute (ccpm) and 5000 ccpm respectively. The high temperatures at the substrate cause the gasses to dissociate, depositing amorphous boron on the tungsten filament. Chlorine gas reacts with hydrogen to form gaseous HCl , which is swept out of the reaction chambers and through scrubbers. It should be noted

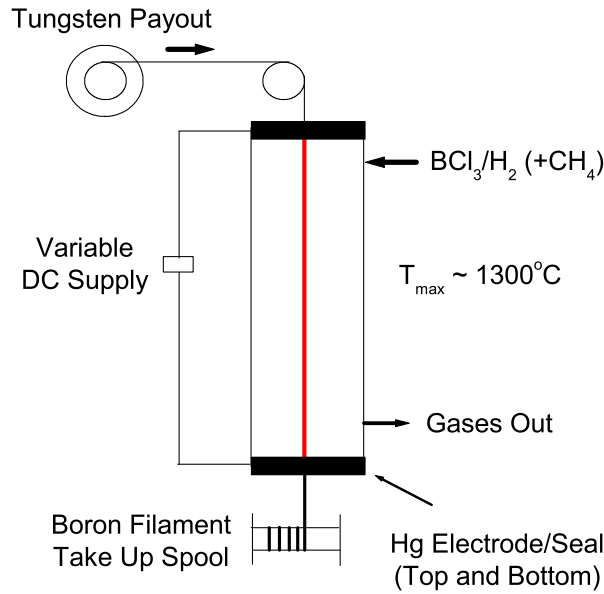


Figure 4.1 Schematic of the CVD reaction chamber used by Specialty Materials to synthesize kilometer length boron filaments.

that the tungsten core reacts with boron forming a host of tungsten borides, the dominant phase being W_2B_5 , swelling to a diameter of approximately $18\ \mu\text{m}$.

4.1.2 Conversion to MgB_2

The magnesium/boron binary phase diagram (Figure 4.2a) (66) shows there are three stable binary compounds; MgB_2 , MgB_4 , and MgB_7 . MgB_2 is a line compound which decomposes peritectically into Mg and MgB_4 . The lack of any liquid-solidous line prevents the growth single crystals by any means other than high temperature/high pressure techniques. High purity polycrystalline samples can be synthesized by exposing boron to magnesium vapor at elevated temperatures. A reaction between stoichiometric mixtures of fine boron powder (<100 mesh) and distilled magnesium pieces requires as little as 2 hours at $950\ ^\circ\text{C}$ to form phase pure MgB_2 powders (41).

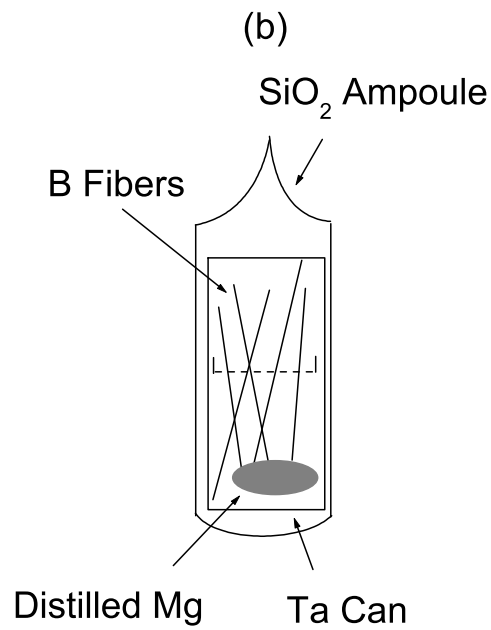
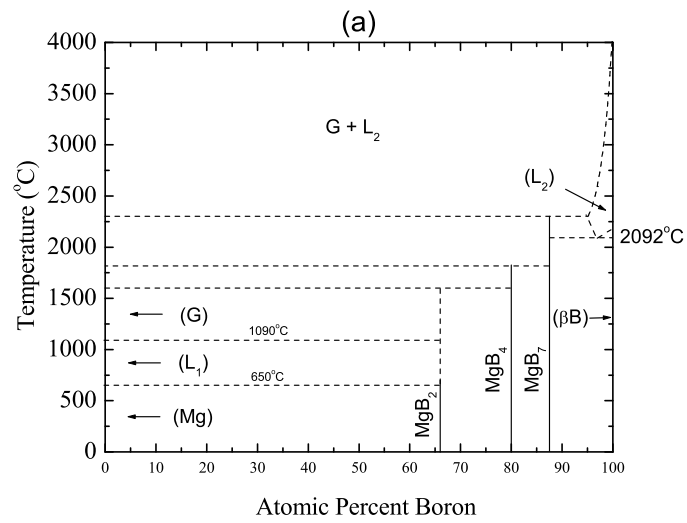


Figure 4.2 (a) Mg/B binary phase diagram recreated from "Desk Handbook - Phase Diagrams for Binary Alloys" (66). (b) Schematic of the reaction vessel used for converting boron filaments to MgB₂.

Boron filaments are converted to superconducting MgB_2 wires in a similar manner. Distilled elemental Mg and 4-5 cm long boron filaments, are held vertically within a sealed tantalum reaction vessel by a tantalum strainer. Since MgB_2 is the most Mg rich of the stable compounds, excess Mg can be used during the reaction, with the excess Mg ensuring an abundant supply of Mg vapor to drive the reaction to completion. Therefore, an approximate stoichiometric ratio of Mg:B 1:1 is used. The tantalum reaction vessel is then sealed under a partial Ar atmosphere in quartz ampoules (Figure 4.2b). The ampoules are placed in box furnaces for the desired time and temperature profiles. Upon removal from the furnace, one end of the ampoule was quenched in water, promoting condensation of the excess Mg on the colder, bottom of the Ta can, leaving relatively clean MgB_2 filaments. For pure boron fibers, with an initial boron fiber diameter of 100 μm , full conversion to MgB_2 can occur in as little as two hours at 950 $^\circ\text{C}$ (67). The reaction with Mg causes the wires to swell in diameter, become deformed, and brittle (64).

4.1.3 Carbon Doped MgB_2 Filaments

The process for synthesizing boron filaments can be modified to produce carbon doped boron filaments by simply adding small amounts of methane into the BCl_3 gas stream. Carbon doping was achieved by adding methane in flow rates of 15, 30, 60, and 100 ccpm. CH_4 molecules undergo a dissociation similar to BCl_3 in the 1100 $^\circ\text{C}$ -1300 $^\circ\text{C}$ temperature range. The level of carbon doping depends on the relative flow rates BCl_3 and CH_4 and presumably the substrate temperature as well.

Table 1 summarizes the deposition conditions for the pure and carbon doped boron filaments that will be discussed in various parts of this thesis. The substrate temperature for each fiber reached a maximum near 1190 $^\circ\text{C}$. As more carbon is incorporated in the boron filaments, they become increasingly brittle and more prone to fall apart under their own weight in the vertically oriented reaction chamber. The 100 ccpm wires fell apart within the CVD chamber and we were able to harvest only a small amount of material from the bottom of the chamber. SEM analysis of un-reacted fibers showed the presence of small droplets of mercury on the surface. No indication of the presence of mercury was found post reaction and we have no reason

Flow Rate BCl_3 (ccpm)	Flow Rate CH_4 (ccpm)	Inferred %C
3000	0	0
3000	15	0.4
3000	30	2.1
3000	60	3.8
3000	100	5.2

Table 4.1 Deposition conditions for carbon doping of boron filaments. The inferred carbon concentration was determined from the analysis of the shift in the a- and c- lattice parameters, as discussed in chapter 5 of the text.

to believe Hg entered the structure. More than likely, the Hg was removed by pre-reaction cleaning of the filaments, or it vaporized within the hot tantalum can and was condensed on the walls during the quench. The filaments were converted to $\text{Mg}(\text{B}_{1-x}\text{C}_x)_2$ in a similar manner to the case of pure B. Because carbon was found to decrease the reaction rate, various reaction profiles were explored. The reaction was optimized using the lowest three carbon doping levels and then applied to the 100 ccpm wires.

4.1.4 Neutron Irradiation

We synthesized fully dense, 140 micrometer diameter MgB_2 wire by reacting boron filaments with magnesium vapor at 950°C for 36 hours, as described previously. Once synthesized, three fibers, each approximately 1-2 cm in length, were sealed under a partial helium atmosphere in quartz ampoules with dimensions of 3 mm I.D., 4 mm O.D., and approximately 3 cm long. A partial atmosphere was necessary to provide thermal contact with the cooling water, preventing the filaments from overheating during the irradiation. Helium was used due to its low neutron capture cross section. A 2.5 cm diameter, 4.7 cm long water flooded aluminum can containing 25 ampoules was then exposed to reactor neutrons, consisting of 98% thermal neutrons ($E=25.3$ meV) and 2% epithermal neutrons (ranging in energy up to 10 keV), at the Missouri University Research Reactor (MURR) for time periods of 24, 48, 72, and 96 hours. The exposures corresponded to fluences of 4.75×10^{18} , 9.50×10^{18} , 1.43×10^{19} , and

Exposure Time (Hours)	Fluence (n/cm ²)	Atomic % Li
24	4.75*10 ¹⁸	0.37
48	9.50*10 ¹⁸	0.74
72	1.43*10 ¹⁹	1.11
96	1.90*10 ¹⁹	1.48

Table 4.2 Estimated fluences for each of the four exposure lengths and calculated atomic percentage of boron transmuted to lithium.

1.90*10¹⁹ neutrons/cm² respectively (Table 2). The fluences were estimated by measuring the activity level of a cobalt doped aluminum flux wire that was placed in the center of the water flooded can along with the MgB₂ ampoules. The density of Li atoms produced through the transmutation of boron can be estimated from the formula (68):

$$n_{Li} = n_B \sigma f \quad (4.1)$$

where n_{Li} is the density of Li atoms, n_B is the density of B atoms, σ is the absorption cross section, and f is the fluence level. The corresponding percentages of boron converted to lithium are included in table 2.

Normal state and superconducting properties were determined for a series of post exposure annealing profiles. In all cases the anneals were performed by placing samples, still sealed with their quartz ampoules, into a Lindberg model 55035 Mini-Mite tube furnace that was preheated to the desired annealing temperature. After the samples were annealed for the desired length of time, the ampoules were removed from the furnace and air quenched to room temperature.

The boron filaments used in this study contain a tungsten boride core. Fast neutrons colliding with ¹⁸²W atoms, which have a natural abundance of 26.3%, can be absorbed into the nucleus causing the emission of a proton and transforming the tungsten into ¹⁸²Ta. ¹⁸²Ta β decays back to ¹⁸²W, with a half life of 181 days. As a result the filaments were mildly radioactive and required appropriate safety measures in handling.

4.2 Sample Characterization

4.2.1 Powder X-ray diffraction (XRD)

Powder x-ray diffraction measurements were performed in order to determine the phase purity and lattice constants. The x-ray measurements were made at room temperature using $\text{CuK}\alpha$ ($\lambda=1.5406 \text{ \AA}$) radiation in a Rigaku Miniflex Diffractometer. The presence of a myriad of low level impurity phases introduced by the tungsten core prevented us from attaining accurate refinements using Rietveld analysis. As a result, we used a silicon standard to calibrate each pattern. Within each spectra, the peaks varied about some constant offset and this variation was used to estimate experimental uncertainty in the lattice parameters. Lattice parameters were determined from the position of the (002) and (110) peaks.

4.2.2 Magnetic Measurements

Magnetic measurements were performed in a Quantum Design Magnetic Properties Measurement System (MPMS) SQUID magnetometer. Zero field cooled (ZFC) magnetization versus temperature sweeps, typically between 5 K and 40 K and in a 50 Oe field, were used to determine the superconducting transition temperature. T_c was defined using either a 1% or 2% screening criteria. A typical measurement was done on sets of 8-10 wires, each approximately 5 mm in length and mounted to plastic drinking straws using GE 7031 varnish. In the case of neutron damaged samples, due to a limited number samples, measurements were performed on single filaments. The wires were oriented parallel to the applied field. In the vicinity of the transition, temperature steps were limited to no larger than 0.2 K.

Critical current densities at various temperatures and in applied fields up to 5.5 T were estimated using the Bean Critical State Model on magnetization hysteresis loops (see chapter 2). For a standard run, the field was initially set to $H=-5.5 \text{ T}$ then brought back to $H=0$. Data was taken in 0.02T increments up to 0.1 T, followed by 0.2 T increments to 1 T, and finally 0.5 T increments up to 5.5 T. Identical steps were used in the field down sweep to $H=0$. Most samples were measured at 5 K and 20 K, with extra data sets being taken for the study of $J_c(H,T)$ in neutron irradiated samples.

4.2.3 Transport Measurements

Transport measurements on polycrystalline wires were used to determine normal state resistivity and $H_{c2}^{\parallel ab}(T)$. We used a standard AC four probe technique, with platinum wires attached to the samples with Epotek H20E silver epoxy. The contacts were cured at 120 °C for 30 minutes in a Lindberg model 55035 Mini-Mite tube furnace and had a typical resistance near 1 *Omega*. Measurements were performed on samples which were typically 5-8 mm in length with 3-6 mm between voltage leads. Resistivity versus temperature in applied magnetic fields up to 14 T were carried out in a Quantum Design PPMS-14 system. Measurements were performed using a 1 mA/16 Hz a.c. test current and using a 1 second averaging time. Resistivity versus field was measured up to 32.5 T using a lock-in amplifier technique at the National High Magnetic Field Laboratory in Tallahassee, Florida. The sample stage for measurements at NHMFL was a "home built" platform designed by Scott Hannahs and is shown schematically in Figure 4.3. A set of two copper plates sandwiched a resistive heater. On one side of this sandwich was the thermometer and on the other the samples were imbedded in a thermally conductive grease (Apiezon N Grease). The entire assembly was wrapped with aluminized mylar to minimize thermal contact with the helium bath and attached to the end of a vacuum sealed probe. Data was taken at a rate of 40 points/T with the field sweeping at a rate of 2.5 T/minute.

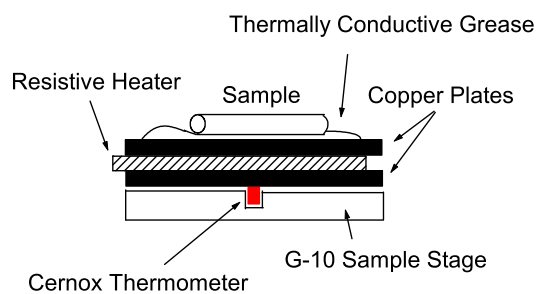


Figure 4.3 Schematic of the sample platform used for transport measurements performed at the National High Magnetic Field Lab in Tallahassee, Florida. Lead wires are not shown.

CHAPTER 5. Superconducting and Normal State Properties of $\text{Mg}(\text{B}_{1-x}\text{C}_x)_2$

Many early reports of carbon substitutions on the boron site via reacting mixtures of commercially available powders of C, B, and Mg are somewhat inconsistent (69; 70; 71; 72). Presumably this is due to an inability to mix the carbon and boron on an atomic scale, resulting in inhomogeneous and incomplete carbon incorporation. MgB_2 is thought to grow via Mg diffusion into the boron matrix, thus making intimate mixtures of boron and carbon prior to reaction a prerequisite for insuring uniform doping.

A novel technique for achieving pre-mixing at the atomic level was proposed by Michelson et al. (73) and successfully implemented by Ribeiro and co-workers (59). Ribeiro et al. reacted Mg and B_4C at elevated temperatures for 24 hours, finding a single superconducting phase with T_c near 22 K (59). Rietveld analysis of a neutron diffraction pattern taken on samples prepared with isotopically enriched $^{11}\text{B}_4\text{C}$ estimated relative abundances of MgB_2 and MgB_2C_2 consistent with the MgB_2 phase containing $10 \pm 2\%$ carbon (60). Whereas the T_c of this $\text{Mg}(\text{B}_{0.9}\text{C}_{0.1})_2$ sample was approximately 22 K, it still showed a clear two gap signature in its temperature dependent specific heat (59) and later tunneling studies clearly showed the continued existence of two gaps, even with this nearly 50% reduction in T_c (61). At the same time, transport measurements indicated $H_{c2}(T=0)$, defined by 90% of normal state resistance, is near 25 T, roughly 9 T higher than for pure MgB_2 (74).

These results indicated that the interesting region for practical applications is with $x < 0.1$, where T_c is greater than 22 K and $H_{c2}(T=0)$ is expected to be at least between 16 T and 25 T, or higher if $H_{c2}(x)$ is non-linear. Systematic studies using this technique appear intractable as B_4C is the most boron rich stable binary in the boron/carbon system (see figure 4.2a) (66).

Whereas B_4C has a relatively large width of formation, the lowest possible carbon level is just below 10%. Thus different techniques are needed for preparing homogeneously doped samples with under 10% carbon substitution.

In this chapter we present a detailed account of our optimization of reaction temperatures and times for the production of single phase $Mg(B_{1-x}C_x)_2$ filaments. As part of this optimization study we will also present a method for partial control over grain size in fully reacted samples. Finally we will present data for carbon doped samples for $0 < x < 0.052$ and show that carbon doping can indeed lead to $H_{c2}(T=0)$ values up to near 36 T, with indications that $H_{c2}(T=0)$ may reach as high as 40 T with judicious tuning of x .

5.1 Optimization of Reaction

The presence of carbon dramatically decreases the rate of conversion to MgB_2 . Previous studies showed full conversion of 100 μm diameter pure boron filaments to MgB_2 was achieved in as little as 2 hours at 950 $^{\circ}C$ (64). Under similar conditions, only a small fraction of the carbon doped fibers was converted. It was necessary to increase the reaction temperature to 1100 $^{\circ}C$ -1200 $^{\circ}C$ for full conversion of the wires. As a consequence, the size of the superconducting grains increased from micron or sub-micron to tens of microns.

Figure 5.1 presents optical images taken under polarized light and back scattered electron images (BSE) taken in a scanning electron microscope (SEM) for the 15 ccpm wire reacted for 4 hours at 950 $^{\circ}C$. EDS spectra (3c) indicate the co-existence of all three Mg-B phases within the wire: MgB_2 , MgB_4 , and MgB_7 . Fully reacted MgB_2 is confined to a small annulus, approximately 1 μm thick, on the surface of the wire, as well penetrating in veins towards the tungsten core. In addition to this inward growth from the outside surface, Mg vapor diffuses along the core due to cracks at the tungsten/boron interface, resulting in growth from the inside out (67). Further cracks within the boron filament allow for formation of these veins of Mg rich compounds. The MgB_4 phase can be found intermixed with the MgB_2 annulus as well as near the core. The majority of the fiber is MgB_7 . Extending the length of the reaction to 48 hours increases the thickness of the MgB_2 annulus to approximately 10 μm , but the bulk

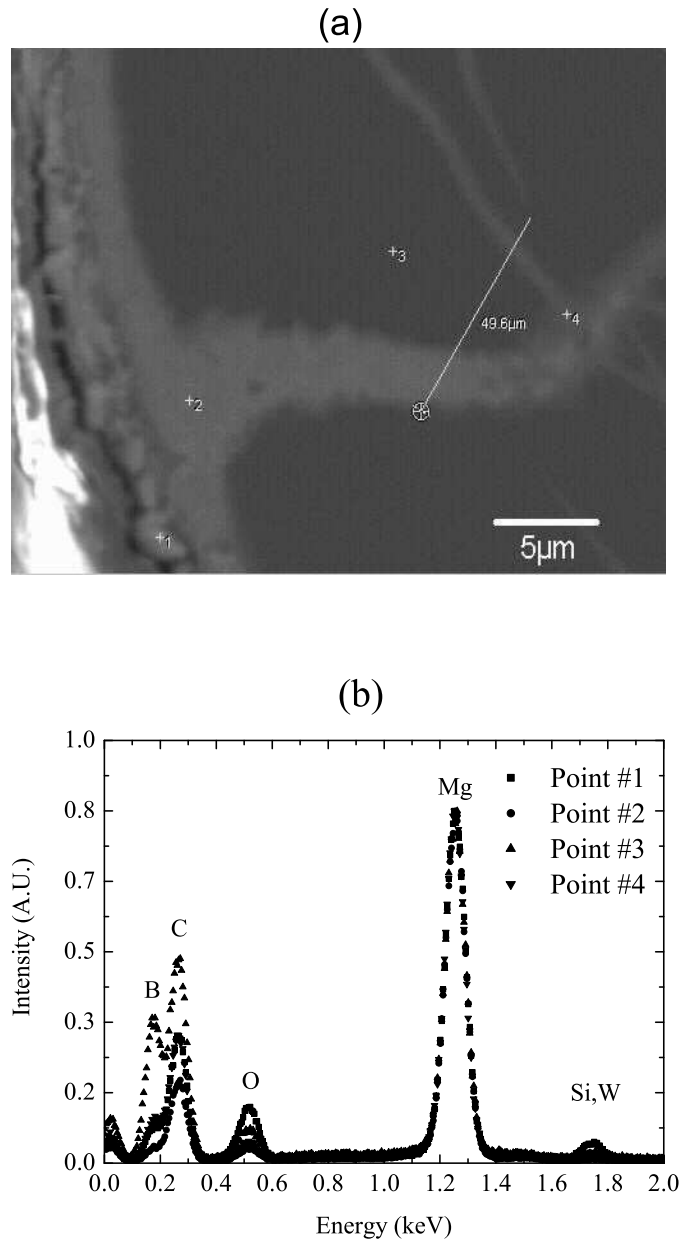


Figure 5.1 (a) SEM BSE image of a 15 ccpm fiber reacted for 4 hours at 950 °C. Only a portion of the wire has fully converted to MgB_2 . (b) A comparison of the EDS spectra for the points indicated in (a). The different Mg:B ratios indicate the co-existence of MgB_2 , MgB_4 , and MgB_7 phases in the wire.

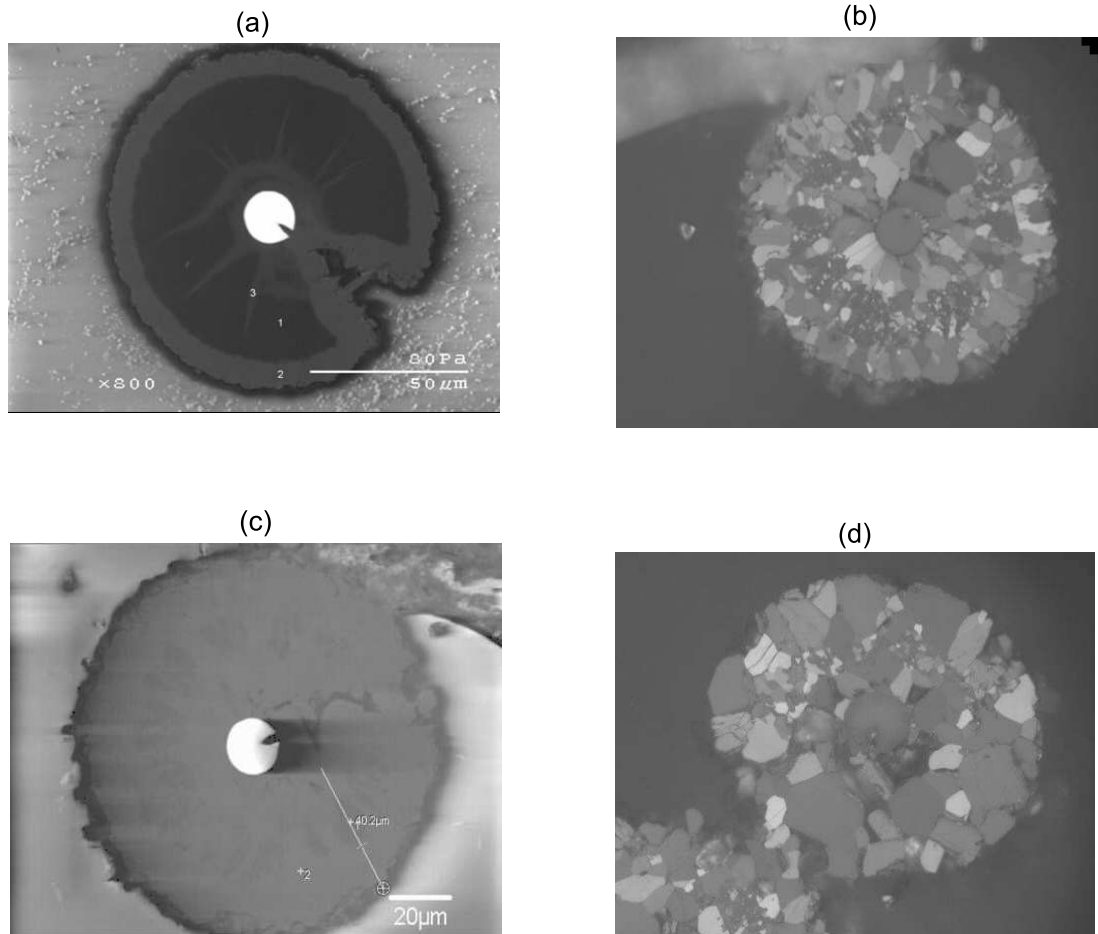


Figure 5.2 (a) BSE image taken in the SEM for a 15 ccpm carbon doped fiber reacted for 48 hours at 950 °C. Only the outer annulus is fully converted to MgB_2 . A small region near the core consists of MgB_4 , while the majority of the wire is MgB_7 . (b) and (c) Optical and BSE images of 15ccpm fiber reacted for 24 hours at 1100 °C. There is only a small ring of MgB_4 within the fiber. The W_2B_5 core is approximately $18\mu\text{m}$ in diameter and serves as an internal caliper for the optical images.

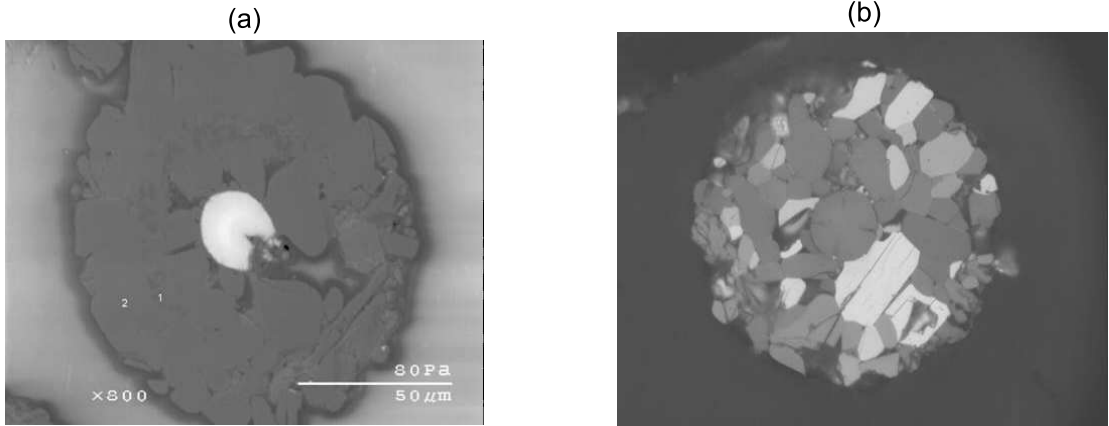


Figure 5.3 (a) 15 ccpm carbon doped filament reacted for 24 hours at 1200 °C. Small regions of MgB_4 are still present and can be most clearly seen in the BSE micrograph. (b) 60 ccpm fiber reacted at 1200 °C for 48 hours. The wire is fully converted to MgB_2 . The W_2B_5 core is approximately 18 μm in diameter and serves as an internal caliper for the optical images.

of the wire remains MgB_7 with isolated veins of MgB_4 growing from within the wire (Figure 5.2a).

Rather than further extending the reaction time, the reaction temperature was increased to shorten the time necessary for full conversion. Based on the success of Ribeiro et al. synthesizing a single superconducting phase with approximately 10% C incorporation by reacting at 1100 °C (59), we first reacted 15 ccpm segments with Mg vapor at 1100 °C for 24 hours. The 15 ccpm carbon doped sample was over 90% converted to MgB_2 . BSE images with Z contrast indicate the existence of two Mg-B phases (Figures 5.2b and 5.2c). EDS spectra showed a decrease in the Mg:B ratio consistent with the non-superconducting grains being MgB_4 . Raising the temperature to 1200 °C reduces the amount of MgB_4 present to roughly 5% of the sample (Figures 5.2d and 5.3a). Finally extending the reaction time at 1200 °C to 48 hours yields a fully converted fiber, even for the higher 60 ccpm carbon doping level (Figure 5.3b). The optical photographs show a steady increase in the MgB_2 grain size as a function of the reaction temperature. In increasing the reaction temperature from 1100 °C to 1200 °C the

average grain size approximately doubles.

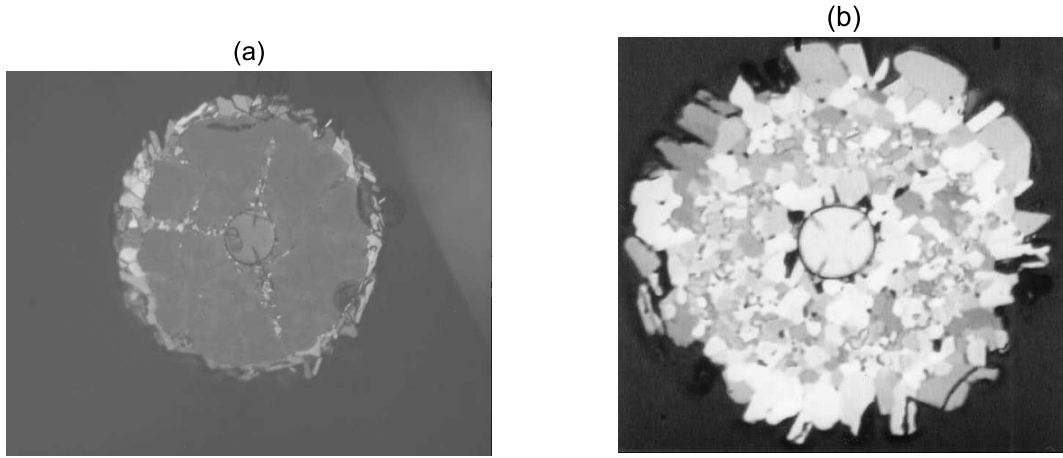


Figure 5.4 Optical photographs taken under polarized light of 60 ccpm carbon doped fibers reacted using a ramped temperature profile. (a) Ramping 650 °C - 1100 °C over 96 hours. (b) Ramping 650 °C - 1200 °C over 96 hours. Having the temperature above 1100 °C appears vital to insuring full reaction of the fiber. Even at these high temperatures, many of the grains are limited to a few microns in size. The W_2B_5 core is approximately 18 μm in diameter and serves as an internal caliper.

Reaction at low temperatures yielded small grains but did not fully convert the fibers. In contrast, high temperatures led to fully converted wires, which had larger grains. This prompted us to experiment with different reaction conditions in an attempt to fully react the sample in a reasonable period of time while limiting the size of the grains as much as possible. We discovered that ramping the temperature, rather than holding it steady, created a distribution of grain sizes ranging from a micron to tens of microns. Figure 5.4 shows optical images taken under polarized light of the 60 ccpm carbon doped samples reacted by steadily ramping the temperature from 650 °C to 1100 °C (a) and 650 °C to 1200 °C (b) over 96 hours. When the maximum temperature was limited to 1100 °C, only a small fraction of the sample was fully converted to MgB_2 . Reacting at temperatures above 1100 °C appears crucial for fully converting the fibers, consistent with the isothermally grown samples mentioned previously. Comparison of samples ramped from 650 °C to 1200 °C and samples grown isothermally at

1200 °C (Figure 5.2f) shows that the ramped sample is fully reacted and has a distribution of grain sizes, many of which are less than 10 μm in contrast to the isothermally grown sample which has grains that are consistently above 20 μm in size. Applying this ramping profile to the 15 and 30 ccpm carbon levels resulted in fully converted fibers with similar grain size distributions to the 60 ccpm wire. It should be noted that pure MgB_2 filaments prepared using the 650 °C to 1200 °C ramping profile had large grains similar to those grown isothermally at 1200 °C. Further studies using various ramping profiles in the hopes of minimizing the time necessary to achieve fully reacted, small grain samples are presently underway.

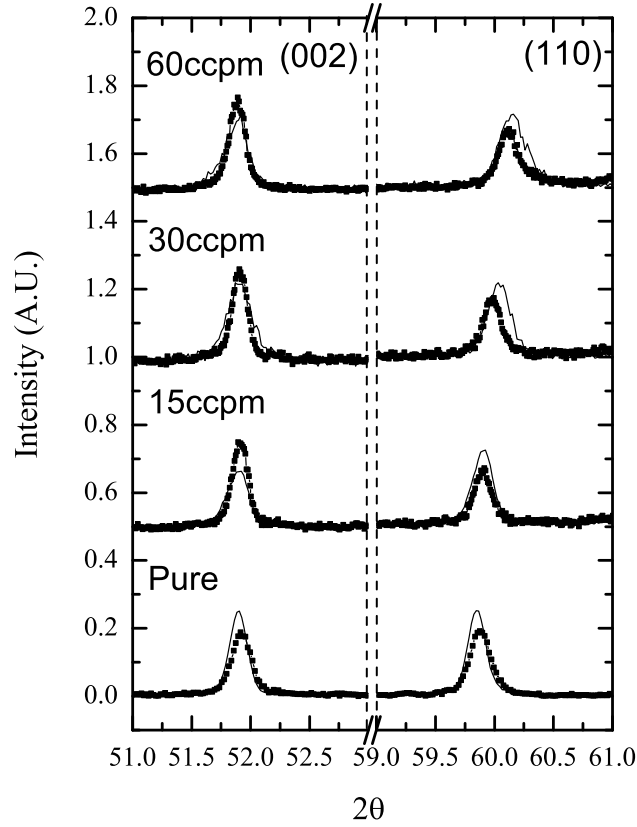


Figure 5.5 X-ray comparison of ramped (line) and isothermally grown samples (solid symbols). Ramped samples show similar (002) peaks, but slightly broader (110) peaks.

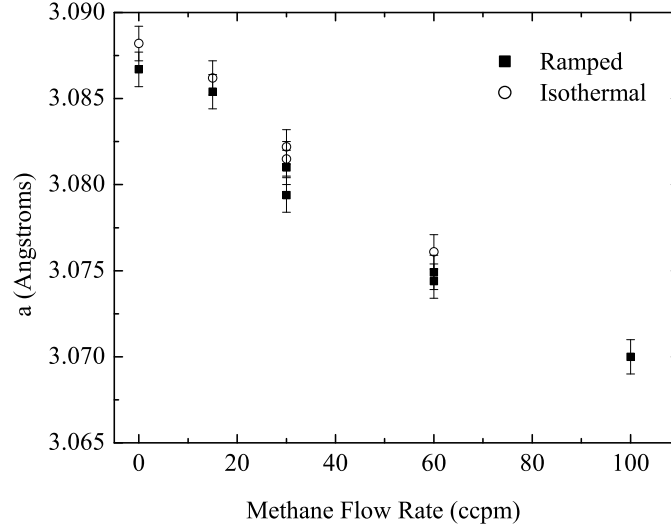


Figure 5.6 Comparison of the a-lattice parameter for ramped and isothermally grown samples as determined by the position of the MgB_2 (110) peak

In order to estimate the carbon content in these samples, x-ray powder diffraction measurements were made to determine the lattice parameters. Carbon has been shown to contract the a-lattice parameter whereas only slightly expanding the c-lattice parameter (60; 75). Avdeev et al. (60) showed a contraction of $|\Delta a| = 0.032 \text{ \AA}$ for $x=0.10 \pm 0.02$ in $\text{Mg}(\text{B}_{1-x}\text{C}_x)_2$. Assuming a linear contraction of the a-lattice parameter as a function of carbon content, the level of carbon incorporation can be estimated by comparing the relative positions of the (110) peaks (75). Figure 5.5 shows comparisons of the spectra obtained for the two sample preparation techniques on the pure as well as each of the three lowest carbon doping levels. The (002) peak, which probes changes in the c-lattice parameter, remains virtually unchanged for each doping level and is independent of the preparation technique. The (110) peaks are slightly broader and have a centroid occurring at a higher 2θ value for the ramped samples. The differences in peak positions are relatively minor as can be seen by comparing a-lattice values for the various methane flow rates (Figure 5.6). Using Δa , calculated from reference samples of pure MgB_2

Ramped Samples			
Flow Rate CH ₄ (ccpm)	a (± 0.001)	Δa (± 0.001)	Calculated x (± 0.3)
0	3.0867	-	0
15	3.0854	0.0013	0.4
30	3.0810	0.0057	1.8
30	3.0794	0.0073	2.3
60	3.0749	0.0118	3.7
60	3.0744	0.0123	3.8
100	3.0700	0.0167	5.2
Isothermal Samples			
Flow Rate CH ₄ (ccpm)	a (± 0.001)	Δa (± 0.001)	Calculated x (± 0.3)
0	3.0882	-	0
15	3.0862	0.0020	0.6
30	3.0822	0.0060	1.9
30	3.0815	0.0067	2.1
60	3.0768	0.0124	3.9

Table 5.1 x in Mg(B_{1-x}C_x)₂ calculated from the shift in the a-lattice parameter as determined by the MgB₂ (110) peak position. Dual entrants represent different batches prepared under the same reaction conditions.

synthesized in the same manner, to determine the carbon content yields similar average values, though both techniques do show some spread in the data (Table 5.1). The broader (110) peaks suggests the main difference in the two preparation techniques is a slight distribution in carbon incorporation in the ramped samples. The bulk material incorporates the same level of carbon, regardless of heat treatment, as can be seen by the similarities in Δa , which fall within the experimental error bars.

The (002) and (110) x-ray peaks for the entire series of the 650 °C - 1200 °C ramped samples, including the 100 ccpm carbon doping level, are given in figure 5.7. At higher carbon levels, the (002) peak is shifted to slightly lower 2θ relative to the pure, indicating a minor increase in the c-axis lattice parameter. This is consistent with the result found by Avdeev on in the case 10% carbon doping (60). As for the (110) peak, it systematically shifts to higher 2θ , showing we've incorporated an even higher level of carbon for the 100 ccpm carbon doped filament. Determining Δa relative to a pure sample given the same ramping heat treatment,

we estimate the level of carbon in this sample to be approximately $x=0.052$. Hence forth we will refer to the carbon content in terms of the average values inferred from the shift in the (110) peak for each of the methane flow rates; namely $x=0.004$, .021, 0.038, and 0.052.

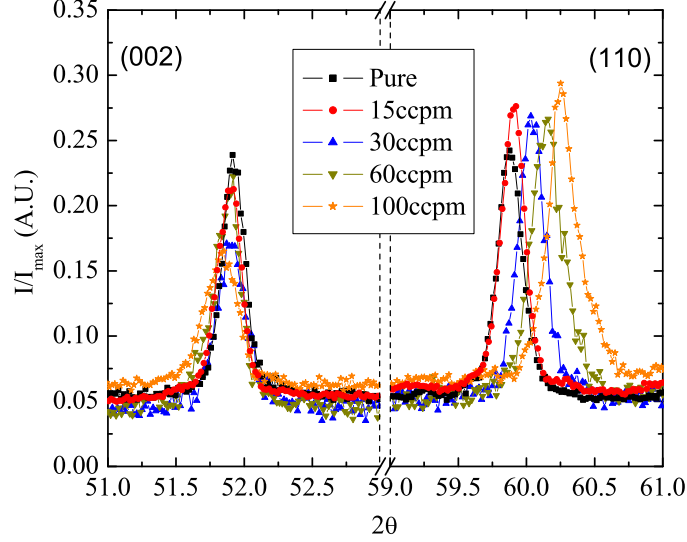


Figure 5.7 (002) and (110) x-ray peaks for pure, 15, 30, 60, and 100 ccpm carbon doped samples prepared by ramping the temperature from 650 °C - 1200 °C over 96 hours. The shift of the a- lattice parameter relative to the pure sample yields calculated carbon concentrations of approximately 0.4, 2.1, 3.8, and 5.2%.

5.2 Thermodynamic and Transport Properties

Magnetization and transport measurements were performed to further compare the superconducting properties of the two reaction profiles. Zero field cooled magnetization measurements were performed in an externally applied 50 gauss field. For both types of reaction conditions, $-4\pi M$ values exceeded 50 gauss and ranged from 60-100 gauss, indicating the slight curvature in the wires resulted in non-zero demagnetization factors. Normalized magnetization and zero field resistance curves for $x=0.004$, 0.021, and 0.038 carbon doped wires are given in

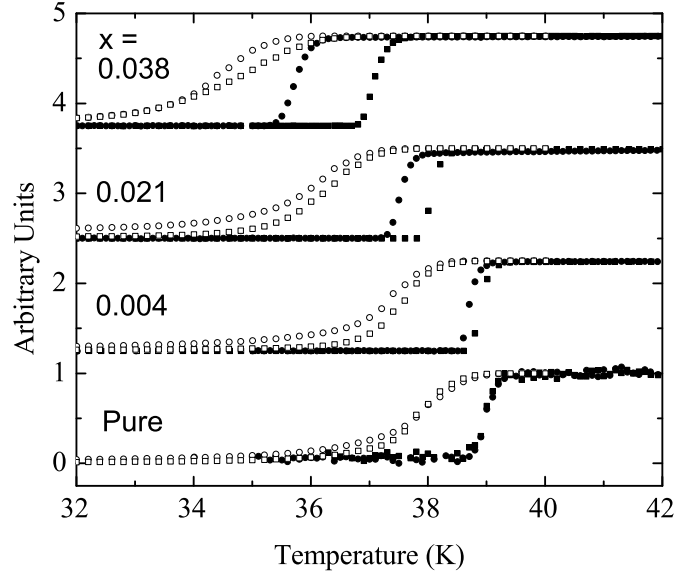


Figure 5.8 Comparison of normalized magnetization (open symbols) and transport (closed symbols) measurements on isothermally (circles) and ramped (squares) growths of pure, $x=0.004$, 0.021 , and 0.038 in $\text{Mg}(\text{B}_{1-x}\text{C}_x)_2$ wires.

figure 5.8. Defining the transition temperature using 2% screening from magnetization curves and using the onset criteria for resistive measurements, all three doping levels show a higher T_c for the ramped samples than for the isothermally grown samples. For the lower two doping levels there is a slight difference in T_c from magnetization but the spread for $x=0.038$ is nearly 1 K. The difference in T_c from transport measurements increases with carbon doping level. All of these differences are consistent with the ramped samples having regions of lower carbon incorporation. Carbon incorporation results in a suppression of the superconducting transition temperatures so regions which have incorporated slightly less carbon will become superconducting at slightly higher temperatures. The increase in the difference in transition temperatures with increased carbon content thus reflects the larger range of carbon incorporation present. Transport measurements yield superconducting transitions not indicative of the bulk, rather zero resistance occurs when approximately 25% of the material is supercon-

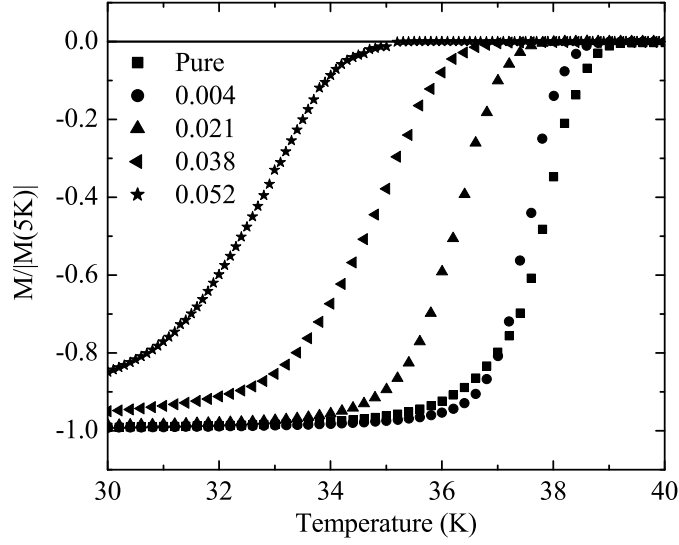


Figure 5.9 Normalized magnetization curves for pure, $x=0.004$, 0.021 , 0.038 , and 0.052 in $\text{Mg}(\text{B}_{1-x}\text{C}_x)_2$ wires grown with the 650°C - 1200°C over 96 hours ramping profile.

ducting, when a continuous superconducting path is established (76). Magnetization shows less discrepancy in T_c than resistive measurements, but differences in homogeneity within the sample still manifest themselves. The magnetic transitions of the entire 650°C - 1200°C ramped series are presented in figure 5.9. This highest carbon doping level continues the trend of T_c being suppressed at a rate near $1\text{ K}/\%\text{C}$ (see figure 5.17 below).

Figure 5.10 plots the resistivity versus temperature and applied magnetic field measurements for pure as well as the $x=0.038$ carbon doped sample. Defining the upper critical field using the onset criteria, H_{c2} values are comparable for all temperatures in the undoped case. In addition, for both $x=0.038$ carbon doped samples, H_{c2} values converge at lower temperatures for the two synthesis techniques. The difference in onset of superconductivity for $x=0.038$ at 14 T is a mere 0.2 K (see figure 5.12 below). The major difference lies in the width of the transitions. The ramped sample completes its transition in an externally applied 14 T field near 10 K , whereas the isothermally grown sample has a broader tail and doesn't reach zero

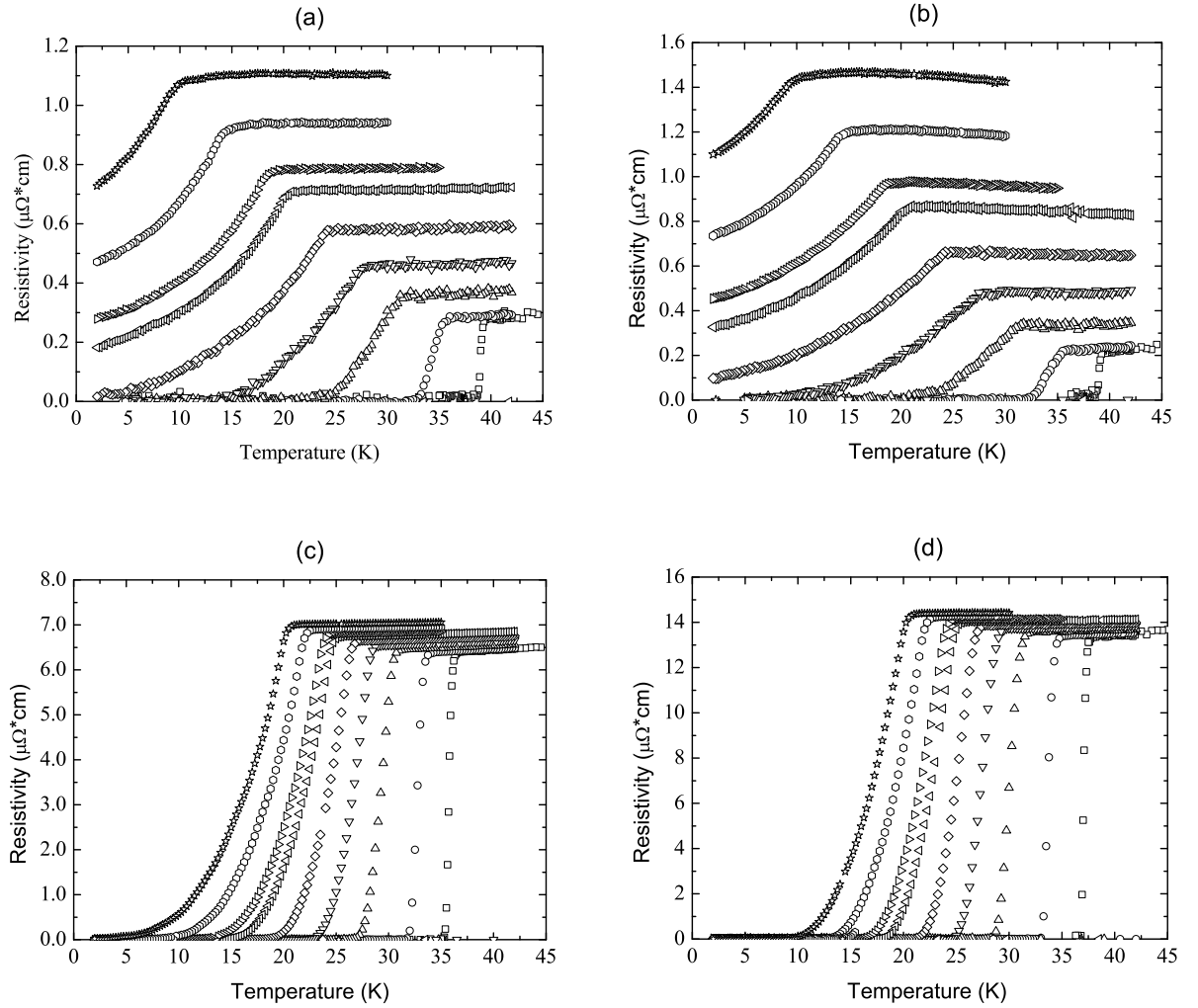


Figure 5.10 Comparison of in-field resistive transitions for the two types of reaction profiles. Shown are isothermal and ramped pure samples ((a) and (b)) and isothermal and ramped $x=0.038$ samples ((c) and (d)). The applied magnetic field values are 0,1,3,5,7,9,10,12, and 14 T.

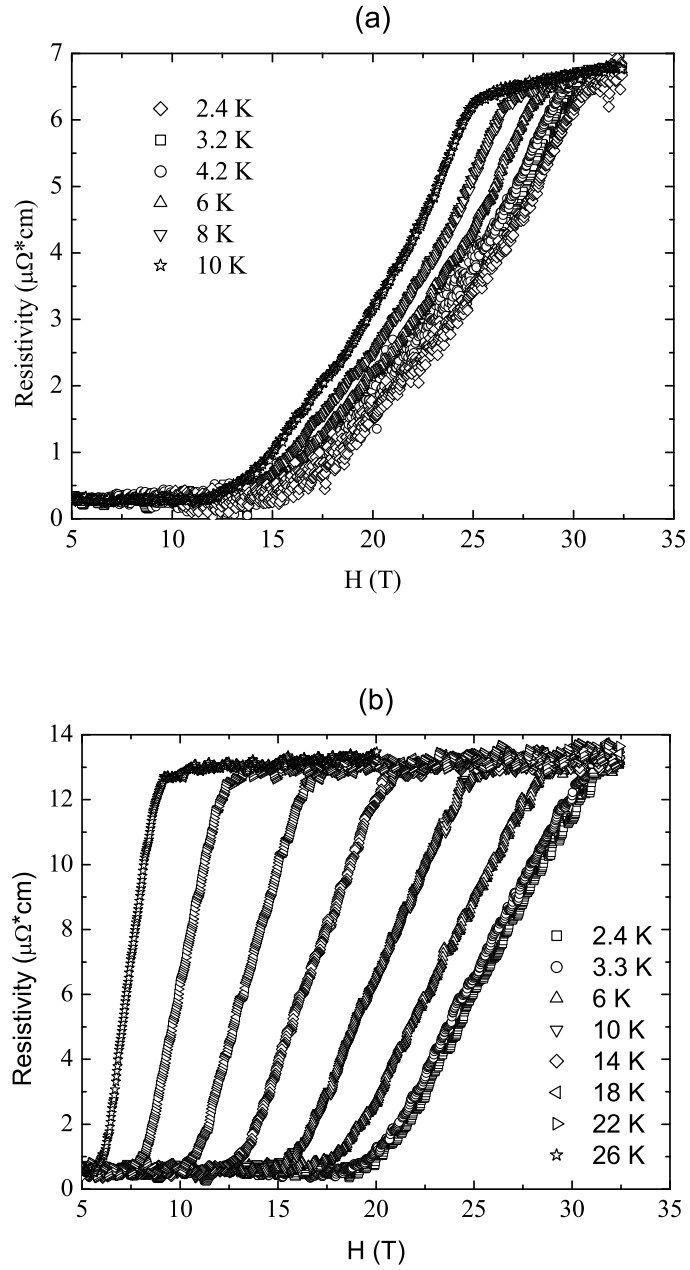


Figure 5.11 Resistivity versus field curves for $\text{Mg}(\text{B}_{.962}\text{C}_{.038})_2$ measured at NHMFL. (a) 48 hours at 1200 °C (b) Ramped 650 °C - 1200 °C over 96 hours. Note - resistivity values are scaled to be consistent with figure 10.

resistance until below 5 K. The $x=0.004$ and $x=0.021$ carbon levels showed similar increases in the in field transition widths of the isothermally grown samples relative to ramped samples. We also see a substantial broadening of the in-field transitions in the pure wires reacted at 1200 °C relative to ones reacted at 950 °C reported in reference (67). For the carbon doped samples, the main difference between the ramped and isothermal reactions, is the increased grain size in the isothermally grown samples associated with the increased time at 1200 °C. We therefore conclude that the sharpness of the in-field resistive transitions is a function of the critical current densities determined primarily by the size of the superconducting grains. By minimizing the grain size using the ramped temperature profile we've increased the sharpness of the in field transitions in the carbon doped samples.

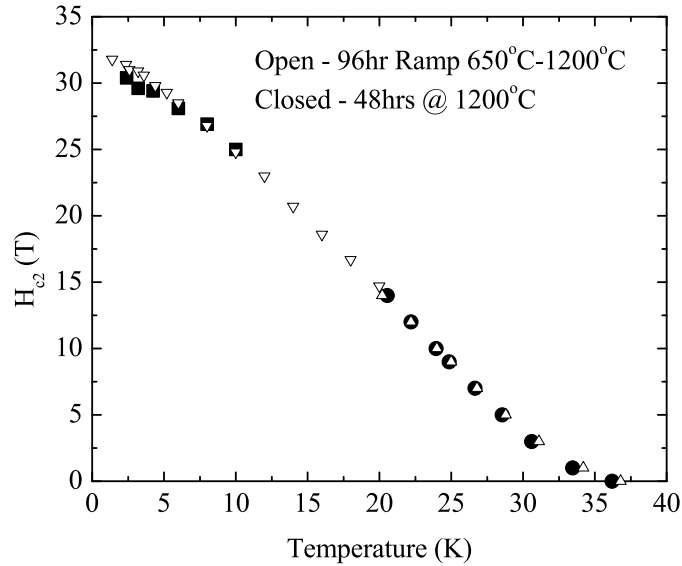


Figure 5.12 Upper critical field comparison for ramped and isothermally grown $\text{Mg}(\text{B}_{.962}\text{C}_{.038})_2$ samples. Using the onset criteria, the two synthesis techniques yield comparable results.

Upper critical field values at low temperatures were determined by the onset criteria in resistivity versus field measurements taken at the National High Magnetic Field Lab in Tallahassee, FL. Figure 5.11 shows a comparison of ρ vs. H curves for $x=0.038$ samples grown

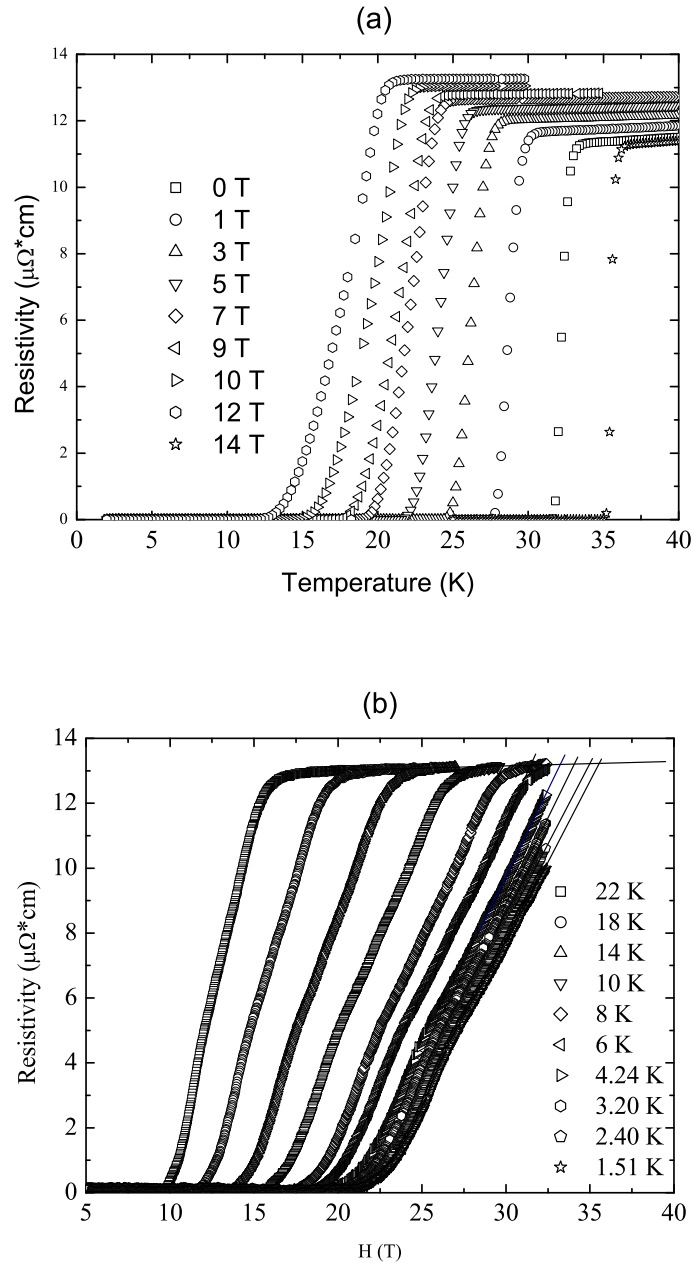


Figure 5.13 Resistivity versus temperature in externally applied magnetic fields (a) and resistivity versus field for various temperature (b) for $\text{Mg}(\text{B}_{0.948}\text{C}_{0.052})_2$.

isothermally and with the 96 hour 650 °C - 1200 °C ramping profile. Here again the larger grained, isothermally grown sample shows broader transitions. In contrast, the transitions for the ramped sample are sharper, and show a linear increase in ρ as a function of field. The superconductive onsets for $x=0.038$ compare favorably over the full temperature range, as shown in Figure 5.12.

Resistivity versus temperature and applied magnetic field data for the $x=0.052$ sample are shown in figure 5.13a. T_c is suppressed a further 1.5K relative to the $x=0.038$ sample, but the $x=0.052$ sample has a greater slope, dH_{c2}/dT (See figure 15 below). Resistivity versus applied magnetic field and temperature data for $x=0.052$ are plotted in figure 14b. At low temperatures, H_{c2} exceeded the 32.5 T achievable in the resistive magnet used at NHMFL. Therefore, H_{c2} values above this level were estimated by the intercept of the extrapolation of the normal state resistance from higher temperature measurements with the linear extrapolation of the transitions (Figure 5.13b). $Mg(B_{.948}C_{.052})_2$ has an upper critical field increased to near 36 T. The full $H_{c2}(T)$ curves for all four carbon doping levels prepared using the ramping profile is presented in figure 5.14.

It should be noted that linear regions in resistivity versus field measurements were observed for the $x=0.021$, 0.038 and 0.052 samples (see e.g. Figure 5.13). Such behavior is believed to be the result of flux flow resistivity, where resistivity develops as the result of vortex motion. During the transition the resistivity is given by (57):

$$\rho_{ff} = \rho_n \frac{H}{H_{c2}} \quad (5.1)$$

where ρ_{ff} is the magnitude of the flux flow resistivity, ρ_n is the normal state resistivity, H is the applied field and H_{c2} is the upper critical field. In the case of these carbon doped samples, ρ_n is approximately temperature independent and therefore the slope, $k \equiv \frac{d\rho_{ff}}{dH}$, is a linear function of $1/H_{c2}(T)$ (Figure 5.15). It should be noted that the slope of k vs. $1/H_{c2}(T)$ yields estimates of the normal state resistivity which are a factor of 2-3 higher than the experimentally determined values. Whereas the flux flow model assumes an isotropic upper critical, MgB_2 exhibits a highly anisotropic upper critical field. How anisotropies affect the development

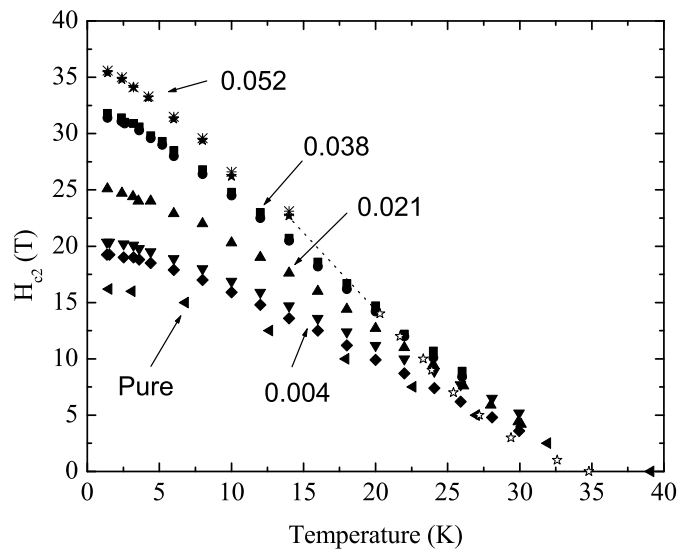


Figure 5.14 Upper critical field curves, determined using the onset criteria, for $\text{Mg}(\text{B}_{1-x}\text{C}_x)_2$ up to $x=0.052$ synthesized using the 650 °C - 1200 °C over 96 hours ramping profile. Two data sets are shown for the $x=0.004$, 0.038, and 0.052 levels.

of resistivity within the flux flow regime, and whether they are responsible for the observed difference in inferred and measured normal state resistivity values, is not fully understood.

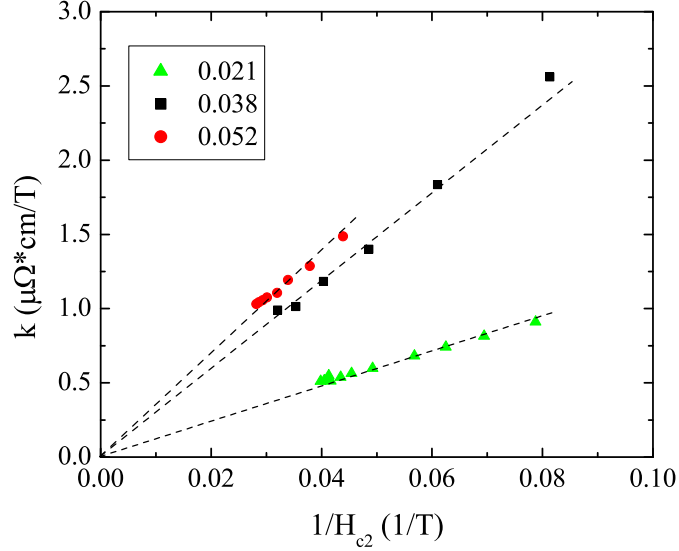


Figure 5.15 Experimentally determined slopes from resistivity versus field measurements as a function of the inverse upper critical field. Dashed lines show extrapolations to 0,0. The linear dependencies and extrapolations through the origin support the notion that the development of resistivity during the transitions are a result of flux flow resistivity (57).

Critical current densities were estimated from magnetization hysteresis loops using the Bean Critical State Model (34). A comparison between J_c values at 5 K and 20 K for the ramped and isothermally grown pure and $x=0.038$ samples is presented in figures 16a and 16b respectively. In the case of the pure sample, the critical current densities are virtually identical. This is consistent with the fact that using the ramping profile on the un-doped sample had no apparent effect on either the grain size or the resistive transition widths. For the carbon doped sample however, there is roughly a five fold increase in J_c values at all applied field values. This correlates with the decrease in the average grain size in the ramped carbon doped samples and the sharpening of the resistive transitions, seen in figure 11. Despite this increase, J_c values

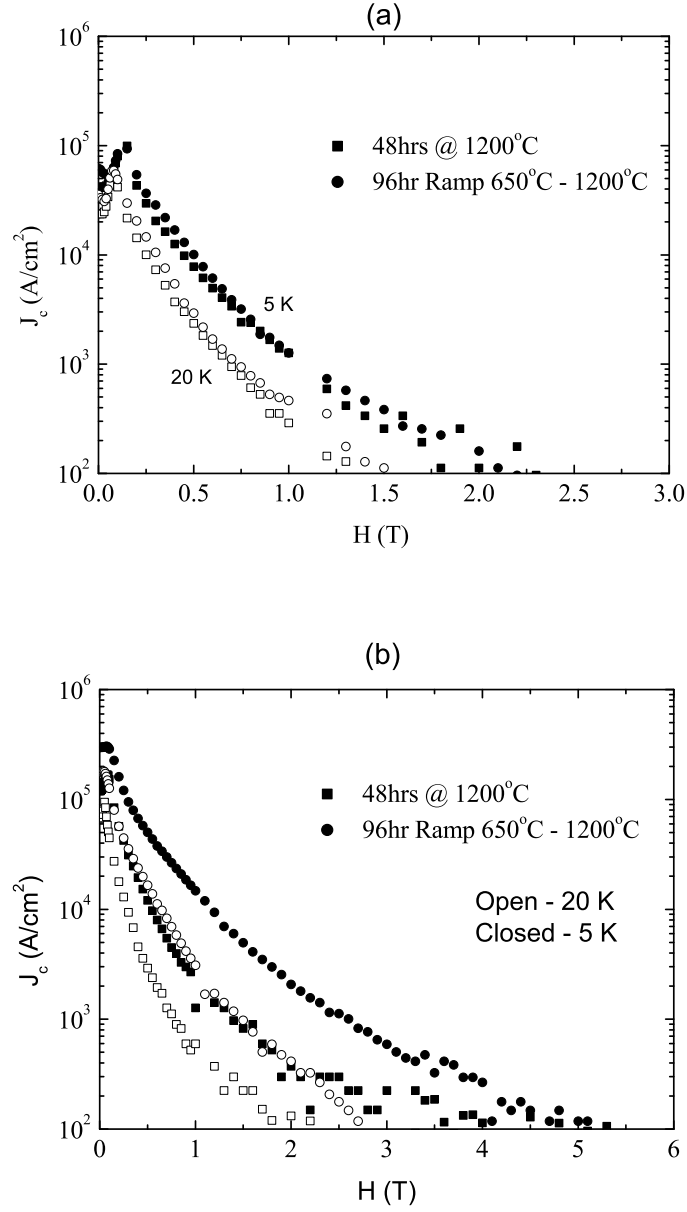


Figure 5.16 Comparison of critical current densities in (a) pure MgB₂ (b) and Mg(B_{0.968}C_{0.032})₂ for the two different heat treatments discussed in the text. Using the 650 °C - 1200 °C over 96 hours ramping profile has no real effect on grain size or J_c in undoped wires, but it does decrease the grain size in the carbon doped wires, improving J_c at all fields.

remain low, dropping below 10^4 A/cm² at 5 K in less than a 2 T externally applied field for our $x=0.038$ carbon doped fiber, despite having an upper critical field of order 25 T. Similar critical current densities have been achieved in fully dense wires of pure MgB₂ by reacting at 950 °C (64).

5.3 Discussion

One goal on the trail to producing practical MgB₂ superconducting wire is to increase the upper critical field. This can be done without dramatically suppressing T_c by doping with carbon. By intimately mixing boron and carbon at an atomic scale using CVD, we have a route to consistently produce wire segments with controlled levels of carbon. As the carbon level is increased from $x=0$ to $x=0.052$ in $\text{Mg}(\text{B}_{1-x}\text{C}_x)_2$, $H_{c2}(T=0)$ monotonically increases from 16 T to 36 T. Figure 5.17 summarizes the superconducting properties of carbon substituted MgB₂ wires as a function of the relative change in the a-lattice parameter and inferred carbon doping level. Data presented is for both isothermally grown and ramped samples. The scatter in T_c is more pronounced at larger x -values and is thought to be due to the inhomogeneities in carbon incorporation for the ramped samples. The true T_c for a given carbon content, and hence a -value, presumably lies closer to the manifold associated with the isothermally grown samples. In contrast, there exists little spread in $H_{c2}(0)$, as both synthesis routes have comparable bulk carbon incorporation. The 10% carbon doped sample of Ribeiro had an upper critical field at zero kelvin near 25 T (74). Our data suggest we have not reached the maximum $H_{c2}(0)$ achievable by carbon doping. Reports on carbon doped single crystals have indicated that the maximum lies near 35 T (77). We have achieved a value near 36 T and it appears probable that the maximum attainable H_{c2} through carbon doping of bulk MgB₂ lies in the vicinity of 40 T. Unfortunately, due to the fragile nature of carbon doped boron filaments, another technique must be employed to synthesize polycrystalline samples with carbon levels above $x=0.052$.

Pure MgB₂ has a highly anisotropic upper critical field, with $H_{c2}^{\parallel ab}(T=0) \sim 16$ T and $H_{c2}^{\perp ab}(T=0) \sim 2.5$ T (3; 4). The lower H_{c2} value limits the field range in which MgB₂ can carry large amounts of current (6). The transport measurements and resultant H_{c2} values presented

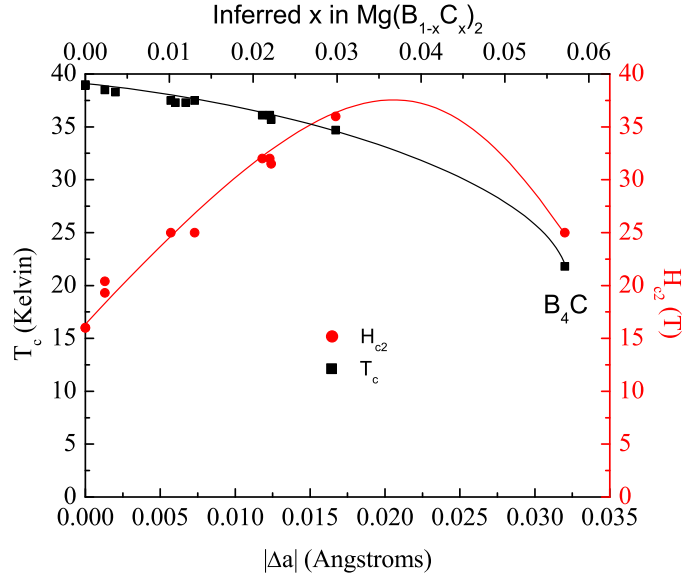


Figure 5.17 Summary of T_c and $H_{c2}(0)$ as a function of $|\Delta a|$. Up to a doping level of $x=0.052$ in $\text{Mg}(\text{B}_{1-x}\text{C}_x)_2$ there exists a strong trend of both a nearly linear decrease in transition temperatures and linear increase in upper critical field values as a function of carbon content. Data shown are for both reaction profiles discussed in the text. Data for sample made from B_4C is from references (60; 61).

here represent the higher, $H_{c2}^{\parallel ab}$ value. Measurements of $H_{c2}^{\perp ab}$ on the $x=0.038$ sample synthesized with the ramping temperature profile indicate carbon incorporation only moderately decreases the anisotropy. The anisotropy ratio, γ_H , drops from near 6 to approximately 5.4, but does so by increasing $H_{c2}^{\perp ab}$ more rapidly than $H_{c2}^{\parallel ab}$ (14). By substituting 3.8% carbon for boron, $H_{c2}^{\perp ab}(T=0)$ is increased from 2.5 T in the pure to approximately 6 T. Such an increase would allow for extension of the applicability of MgB_2 to higher magnetic fields.

A second goal in the materials engineering of MgB_2 is to improve the flux pinning so as to increase the current carrying capacity. Even though the presence of carbon within the MgB_2 structure dramatically increases the upper critical field, no enhancement in J_c is seen. Presumably, carbon acts as a point defect rather than a precipitate, and does not contribute

to the pinning of vortices. In these samples, the flux pinning is thought to be dominated by grain boundary pinning. Therefore to optimize the critical current density, the size of the superconducting grains must be minimized. Using fully dense 100 μm diameter carbon doped boron fibers as the starting material requires reaction at elevated temperatures of 1100 $^{\circ}\text{C}$ to 1200 $^{\circ}\text{C}$ for time periods in excess of a day to fully convert to MgB_2 . Doing so promotes the growth of large grains, and the resultant wires have poor current carrying capabilities. The grain size can be somewhat limited by using a ramped temperature profile, rather than reacting at a single temperature. The corresponding enhancement in J_c is still insufficient for fabricating wire for high current applications in this manner.

Either additional impurities, which form 1-20 nm precipitates and can act as pinning sites, must be included or the size of the superconducting grains needs to be further reduced. A wide range of impurities have been shown to enhance J_c to near 10^6 A/cm^2 in self fields at temperatures up to 10 K: Ti (78; 79), SiO_2 (80), Y_2O_3 (81), and SiC (82). For Y_2O_3 additions, the authors report the formation of YB_4 precipitates (81). In the case of SiC doping, it is believed that the carbon enters the MgB_2 structure while the silicon precipitates out as Mg_2Si . The combination of enhanced upper critical field and the addition of pinning centers results in enhancements of in-field J_c values, remaining above 10^4 A/cm^2 in a 5 T externally applied field at 20 K (82). Similarly, simultaneous deposition of Ti and C, in the process outlined above, resulted in MgB_2 wires containing TiB_2 precipitates and H_{c2} values consistent with doping with carbon alone (83). The critical current densities were enhanced relative to carbon doped wires presented here, achieving 10^4 A/cm^2 in a 2 T external field and at 5 K, values well below those achieved by Dou et al. (82). The requirement of high reaction temperatures and long reaction times resulted in a coarsening of the TiB_2 precipitates to typical sizes of 20-100 nm, decreasing their effectiveness as pinning centers (84). In order to overcome these slow reaction rates and promote the growth of fine grains, sub-micron sized doped boron powders, in which the grain size is limited by the initial boron particle size, should be used as the starting material. Initial reports on nanometer sized carbon doped powders, formed using plasma spray synthesis, show promising results for achieving high current densities (84).

CHAPTER 6. Enhancing Critical Current Densities in $\text{Mg}(\text{B}_{1-x}\text{C}_x)_2$

Carbon doping is an effective way to enhance the upper critical field in MgB_2 . However, wire segments with 5.2% carbon incorporation are only able to carry a little in excess of 10^4 A/cm² at 5 K in fields up to only 3 T, in spite of the fact that $H_{c2}(T=0)$ is near 36 T. It is believed that, since flux is pinned predominantly at the grain boundaries, the poor flux pinning is the result of the large grains associated with the high reaction temperatures necessary to synthesize carbon doped MgB_2 . In order to fully take advantage of the enhanced H_{c2} values resulting from carbon doping it is necessary to improve the flux pinning. This can be done either by adding impurities, which are approximately the size of the superconducting coherence length, or by reducing the grain size. In this chapter we investigate the possibility of adding Ti using CVD processing, in hopes of introducing nanometer sized TiB or TiB_2 precipitates. In the following two chapters we pursue alternative approaches, in an attempt to synthesize doped boron powders for PIT applications.

6.1 Titanium Additions to MgB_2

Various chemical additions have been shown to enhance the critical current densities in MgB_2 . Of those reported in the literature, Ti can most readily introduced into boron fibers synthesized by Specialty Materials' CVD process by simply adding TiCl_4 into the gas stream. At room temperature TiCl_4 is a liquid and therefore gas phase introduction is done by bubbling H_2 gas through liquid TiCl_4 . The 1100 °C - 1300 °C temperature of the filament causes gaseous TiCl_4 to dissociate, leading to the growth of Ti doped boron filaments. The level of Ti additions is controlled by the flow rate of H_2 through the bubble chamber to that of and presumably the substrate temperature as well.

Anderson et al. previously showed that Ti additions to pure MgB_2 result in a substantial increasing in J_c values at low fields (79). They reacted thin, 4-10 μm thick, annuli of Ti doped B, deposited on a carbon passivated SiC fiber, in as little as 1 hour at 950 $^\circ\text{C}$. J_c values exceeded $5 \cdot 10^6 \text{ A/cm}^2$ in self fields at 5 K. The titanium additions also extended the field range over which the wires could carry large amounts of current. For these thin annuli titanium pushed the field at which J_c exceeded 10^4 A/cm^2 from near 3 T to approximately 5 T at 5 K. Although these results demonstrated the viability of using Ti to enhance J_c values in pure MgB_2 wires, the architecture of these filaments could not be used to study the feasibility of adding Ti to carbon doped filaments. The carbon passivation layer atop the SiC core allows for an unknown level of carbon to diffuse into the MgB_2 . In the case of the Anderson et al. experiments, it is believed that little carbon was able to diffuse off of the core during the low temperature and short time reactions (79). Since carbon dramatically suppresses the growth rate, we anticipate that, even for thin annuli of carbon doped boron, the reaction times and temperature necessary to form $\text{Mg}(\text{B}_{1-x}\text{C}_x)_2$ would need to be increased sufficiently so as to question the validity of such an assumption. We therefore used a tungsten core architecture, similar to the carbon doped filaments discussed in chapter 5, to study the effects of titanium additions to carbon doped MgB_2 wires.

Since the wire architecture was changed, we performed a systematic study of the superconducting properties of MgB_2 with Ti additions only. Standard H_2 and BCl_3 flow rates of 5000 ccpm and 3000 ccpm were used. To this gas stream we added TiCl_4 in flow rates of 0.42 ccpm, 1.26 ccpm, and 2.6 ccpm. The resultant Ti doped boron filaments were 80 μm in diameter. Following exposure to Mg vapor at elevated temperatures, the Ti content was determined by energy dispersive spectroscopy in the scanning electron microscope. Multiple point scans and large area scans indicate that the Ti/Mg ratio is consistent with 0.3, 0.5, and 1.6% Ti additions to the MgB_2 (Figure 6.1). These levels are approximately an order of magnitude lower than was used by Anderson et al. Their Ti doped annulus contained near 9% Ti near the surfaces and approximately 5% over the majority of the sheath (79).

The presence of Ti suppressed the rate of reaction in the filaments. For a sample containing

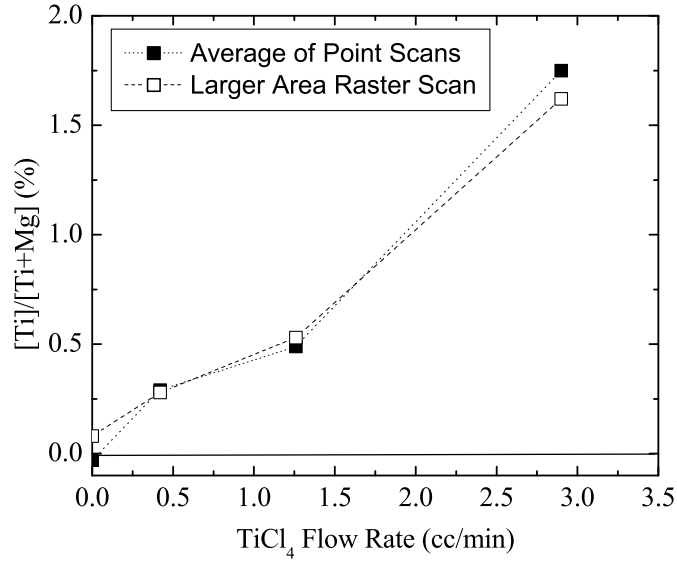


Figure 6.1 Ti/Mg ratio as a function of TiCl_4 flow rate determined by EDS analysis.

approximately 0.5% Ti, at a reaction temperature of 1000 °C, it took 72 hours to convert over 95% of the fiber to MgB_2 . As the reaction temperature is increased, the necessary time to complete the reaction decreases: 48 hours at 1100 °C and 24 hours at 1200 °C. Presumably, Anderson et al. (79) were able to synthesize MgB_2 with Ti additions in short times at lower reaction temperatures because the annuli were significantly thinner. MgB_2 is thought to grow via vapor diffusion of Mg into solid B. Therefore, in the case of Ti doped B annuli, by limiting the thickness of the boron layer, the necessary diffusion length is decreased and the reaction can presumably be carried out at lower temperatures. In the case of the Ti doped B on tungsten filaments, since the fibers are 80 μm in diameter, the diffusion length is increased by an order of magnitude, and hence, the reaction times at a given temperature are also increased by roughly an order of magnitude.

The superconducting transition temperature was found to depend upon both the reaction temperature and the Ti content (Figure 6.2). As the reaction temperature increases, the

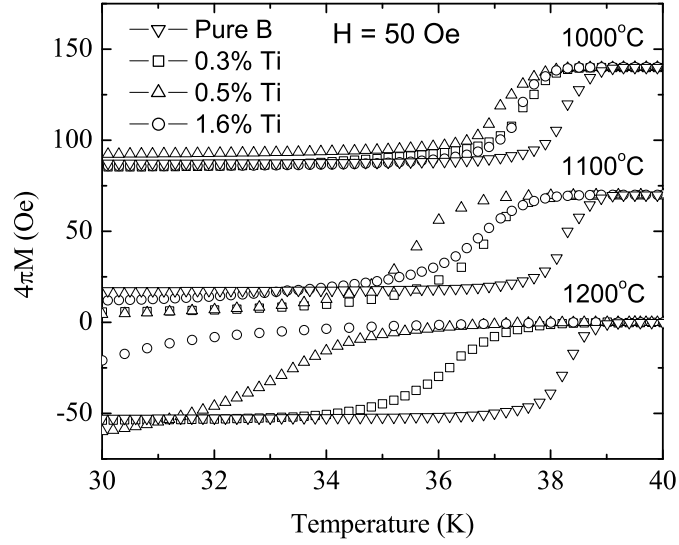


Figure 6.2 Zero field cooled magnetization curves for the set of MgB_2 wire with Ti additions reacted at various temperatures.

transitions broaden and the superconducting onset decreases. (Note: for comparison the T_c of pure MgB_2 , made from pure B filaments, does not shift with increasing reaction temperature.) For the reactions at 1000 °C and 1100 °C, T_c did not vary monotonically with Ti content. At 1200 °C there appears to be a monotonic decrease in T_c with Ti content.

Powder diffraction x-ray measurements were used to determine the lattice parameters (Figure 6.3). The a- lattice parameter tends to decrease with Ti content up to the 0.6% level, at which point it saturates at a value near 3.084 \AA , 0.004 \AA less than that of a pure sample. For the c- lattice parameter, there appears to be no systematic change with either reaction temperature or Ti content. The values seem to fluctuate about that of undoped samples. The contraction in the a- lattice parameter may indicate some partial substitution of Ti, presumably for Mg, into the structure, but more work must be done to definitively determine whether or not this is the case. For the 0.5% Ti additions the a- lattice parameters are comparable for all reaction temperatures whereas the superconducting transition temperatures vary by several K. It is therefore likely that the variation of T_c is due to a different, as yet unknown,

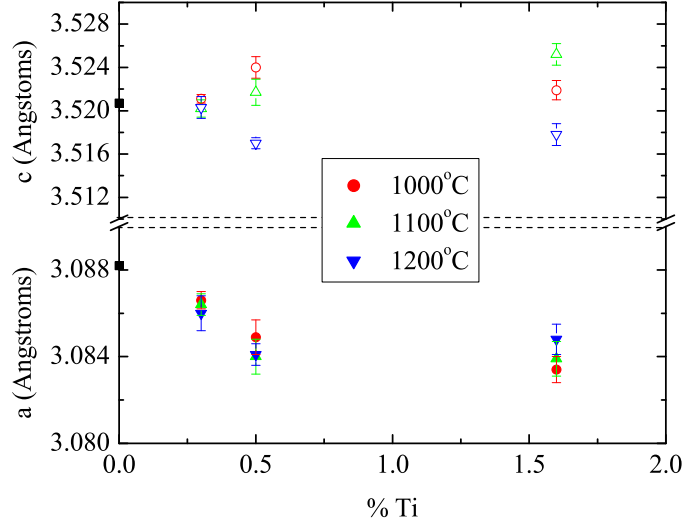


Figure 6.3 Summary of the a- and c- lattice parameters as a function of reaction temperature and Ti content for MgB_2 samples with Ti additions.

mechanism.

Transport measurements were carried out on samples reacted at 1100 °C to determine the impact of Ti on the upper critical field. Figure 6.4a plots resistivity as a function of temperature in various applied fields up to 9 T for a sample containing 0.5% Ti additions. The in-field transitions are quite broad and show considerable rounding near T_c . Such rounding was not observed in pure MgB_2 samples (e.g. see chapter 5 or reference (86)). In order to determine H_{c2} values using the onset criteria for the Ti doped samples, we used an extrapolation of the linear portion of the transition. A plot comparing H_{c2} values for all three Ti addition levels reacted at 1100 °C and a pure sample (3) is plotted in figure 6.4b. All of the samples containing Ti show slightly depressed H_{c2} values relative to the pure sample. However, there appears to be no systematic evolution of H_{c2} as a function of Ti content.

Critical current densities at 5 K and 20 K inferred from magnetization hysteresis loops for the entire set of samples with Ti additions reacted at 1100 °C are compared to a pure wire

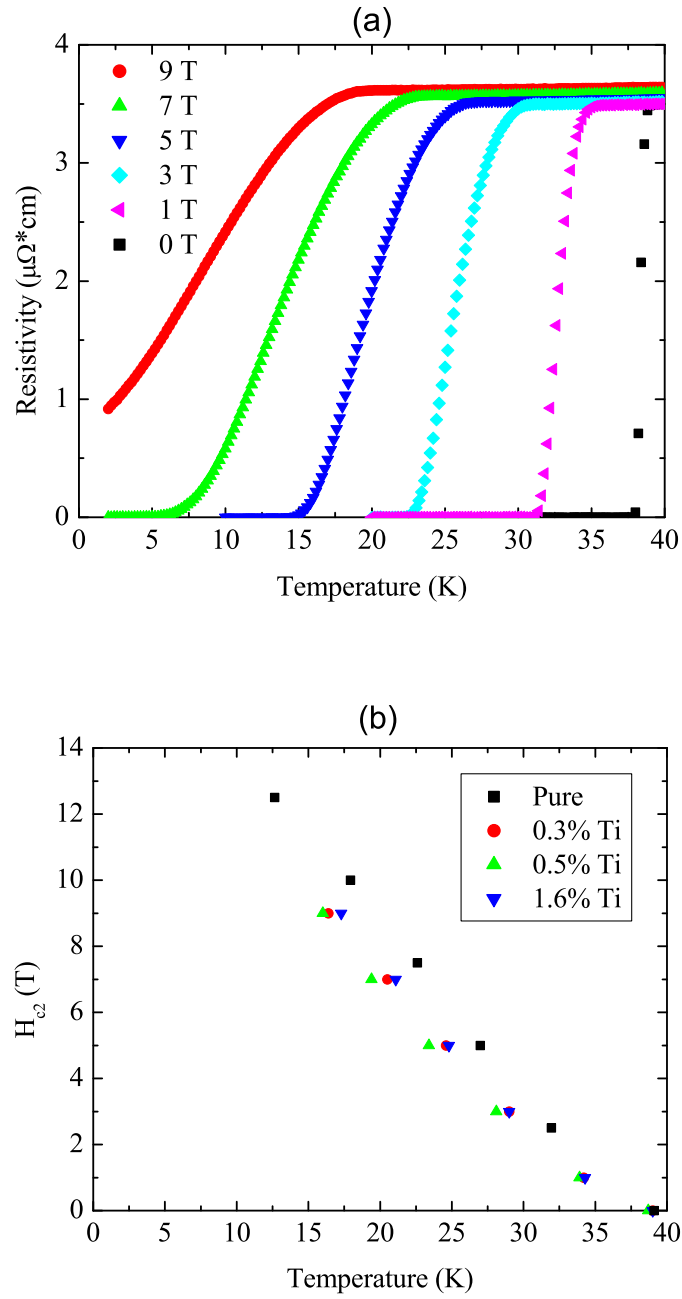


Figure 6.4 (a) Resistivity versus field up to 9 T for a sample containing 0.5% Ti additions and reacted at 1100 °C. (b) H_{c2} versus temperature for the entire set of Ti doped samples reacted at 1100 °C and a pure reference sample.

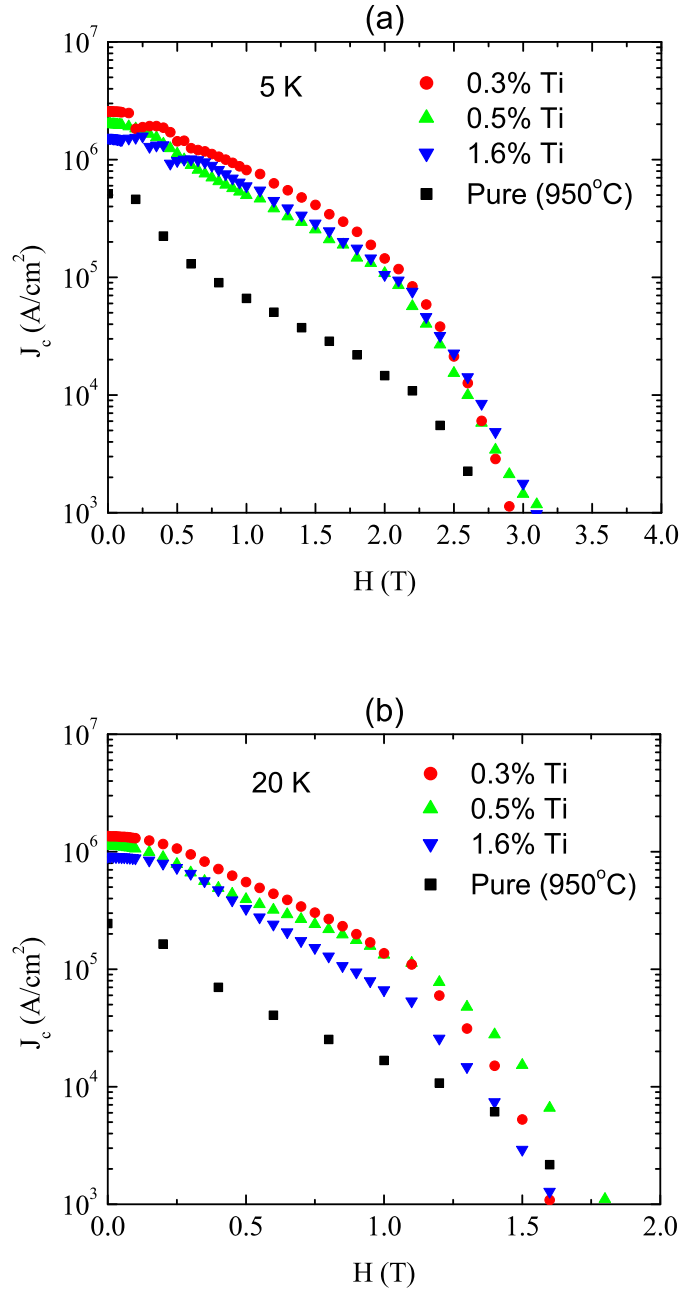


Figure 6.5 Critical current densities at 5 K and 20 K for the entire series of Ti doped samples reacted at 1100 °C. Data are compared to a pure MgB₂ filament reacted at 950 °C (64)

reacted at 950 °C in figure 6.5. All three samples containing Ti additions show comparable $J_c(H)$ values at both temperatures and, at low fields, are enhanced relative to the pure sample by approximately an order of magnitude. In intermediate fields, J_c values for the samples containing Ti additions are comparable to those of the pure sample, and all samples shown drop below 10^3 A/cm², at both 5 K and 20 K, in approximately the same field. That is, the Ti additions appear to enhance low field J_c values, but, relative to an undoped sample, J_c falls off more rapidly as the strength of the field is increased and, as a result, Ti additions do not extend the field range in which appreciable amounts of current can be carried. For the samples with Ti additions, J_c is virtually independent of Ti level, in spite of the fact that the grain size clearly decreases as a function of Ti level (Figure 6.6). It should be noted that the highest Ti level is not fully reacted and this may result in an estimate of J_c that is artificially low.

In the case of the Ti additions to MgB₂ on SiC substrates, the Ti formed 1-20 nm TiB precipitates which were imbedded within the MgB₂ matrix (83). For these lower level Ti samples, TEM micrographs reveal that the precipitates, which index to TiB₂ (83), are all 20 nm or larger (Figure 6.7). It should be noted that the forming of intragranular precipitates was not found by Zhao et al. when they mixed powders of Mg, B, and Ti together (85). They found TiB₂ precipitates on the grain boundaries and attributed enhancements in J_c to Ti limiting the size of the MgB₂ grains to near 10 nm. For the set of samples reacted at 1100 °C, increasing the Ti level in the samples appears to result in a higher density of precipitates, but does not dramatically alter the precipitate size. The 20-50 nm sized precipitates obtained by reacting the filaments at 1100 °C are too large to be effective in pinning vortices.

The very complex nature of pinning in these samples is not fully understood, but it appears that the largest enhancements in J_c result from limiting the size of the precipitates to near 10 nm. Short time reactions at temperatures of 950 °C or lower are necessary to prevent the precipitates from coarsening. For fully dense, 80 μ m diameter fibers, the slow growth rate of MgB₂ with Ti additions forces us to increase the reaction time and temperature, preventing us from achieving the enhancements attained by Anderson et al. (79).

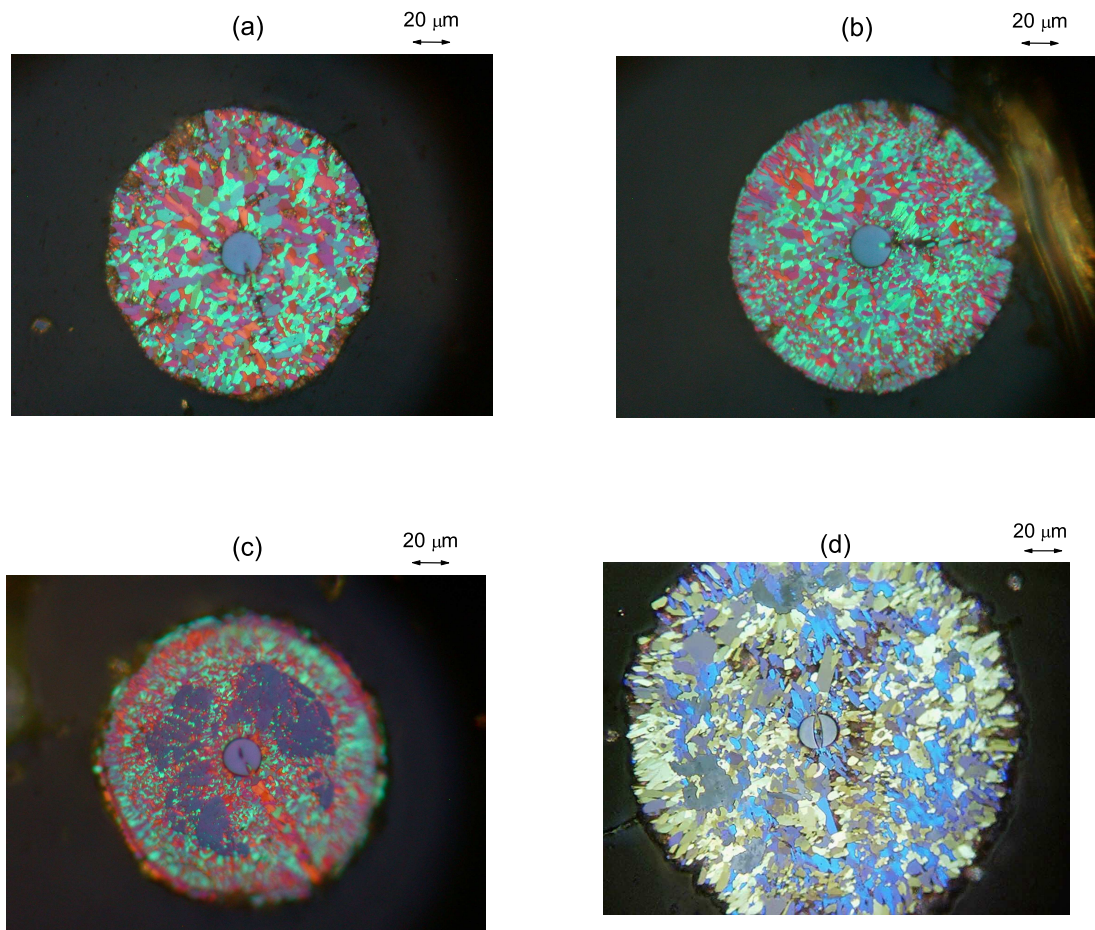


Figure 6.6 Optical images of an MgB_2 wire containing (a) 0.3%, (b) 0.5%, and (c) 1.6% Ti and reacted at 1100 °C for 48 hours. (d) Pure fiber reacted at 950 °C for 4 hours.

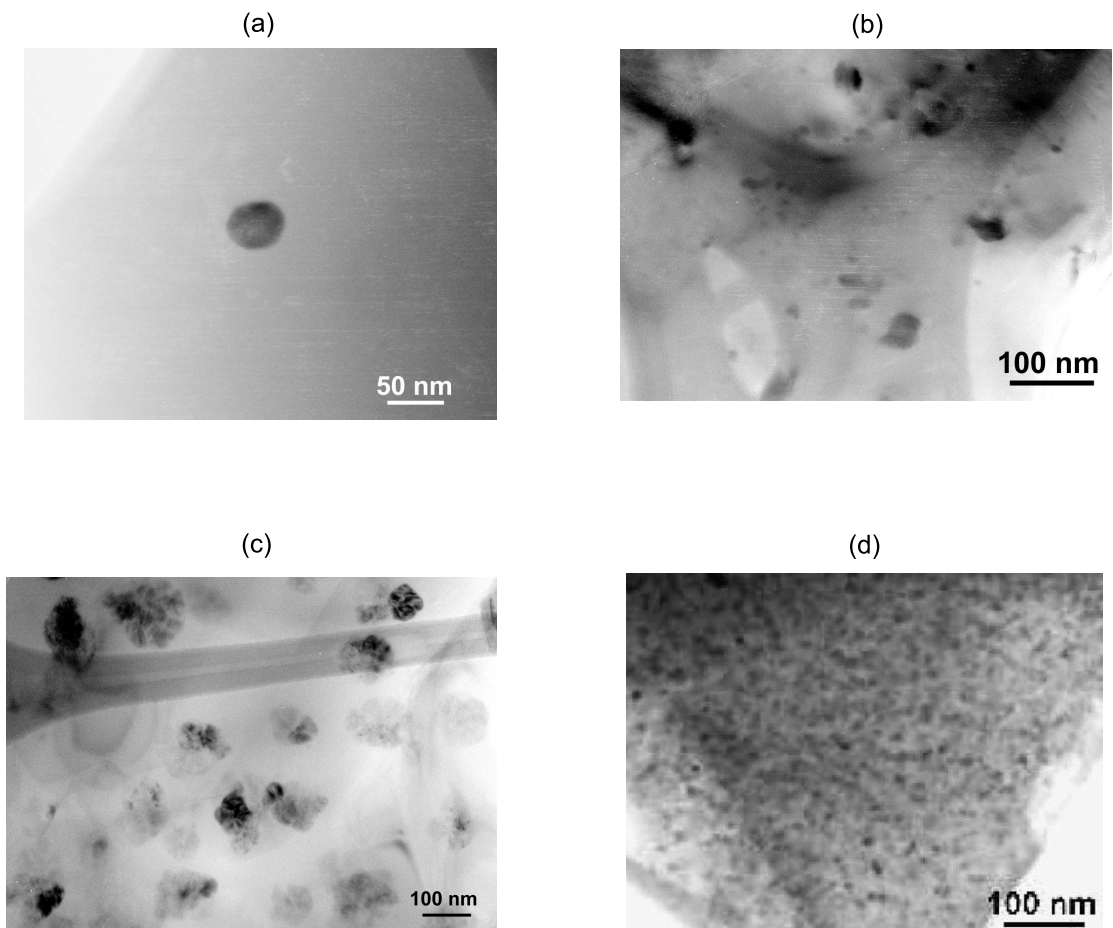


Figure 6.7 TEM micrographs for samples containing (a) 0.3%, (b) 0.5%, and (c) 1.6% Ti and reacted at 1100 °C for 48 hours. (d) Micrograph of 5% Ti additions to a 10 μm thick B sheath on an SiC substrate reacted for 1 hour at 950 °C.

6.2 Titanium Additions to Carbon Doped MgB_2

In spite of the fact that we were unable to obtain 1-10 nm TiB_x precipitates in the MgB_2 filaments on W substrates, we pursued the feasibility of adding Ti to carbon doped MgB_2 wires using this same synthesis technique and wire geometry. Although it is known *a priori* that the necessary reaction times and temperatures will prevent us from attaining significant enhancements in in-field J_c values, there are several key questions we can address. First, will we form TiB_x precipitates in carbon doped MgB_2 or will we precipitate out TiC? Second, if we do successfully add TiB_x precipitates to carbon doped MgB_2 , will these precipitates affect the scattering and alter the temperature dependence of H_{c2} ?

Samples were prepared by introducing BCl_3 , TiCl_4 , CH_4 and H_2 into the gas stream of the CVD chamber. The standard flow rates of 3000 ccpm of BCl_3 and 5000 ccpm H_2 were used. The TiCl_4 flow rate was set to 1.26 ccpm, which yields a Ti/Mg ratio consistent with 0.5% Ti additions. Since carbon content is estimated by the contraction of the a- lattice parameter, which would be difficult to track in these doubly "doped" samples, flow rates corresponding to known carbon concentrations were used from reference (86). We therefore used CH_4 flow rates of 15 ccpm and 30 ccpm, which, for the isothermal reactions discussed below, were shown to yield $x=0.006$ and $x=0.021$ in $\text{Mg}(\text{B}_{1-x}\text{C}_x)_2$ (86). To ensure fully reacted fibers, the samples were reacted with excess Mg vapor for 48 hours at 1200 °C.

Figure 6.8 presents the x-ray (002) and (110) peaks, for pure sample, a 2.1% carbon doped sample, a sample with 0.5% Ti additions, and a sample with both 2.1% carbon and 0.5% Ti. The shift towards higher 2θ for the samples with Ti or C only additions reflects the contraction of the a- lattice parameter which results from the addition of each of these dopants, as was discussed in the previous section and in chapter 5. When both Ti and C are added, the (110) peak shifts to even higher 2θ , suggesting the contraction of the a- lattice parameter is additive in the case of Ti additions to carbon doped MgB_2 .

Although the contraction in the a- lattice parameter appears to be additive, the suppression in T_c appears to be dominated by the suppression associated with the Ti additions (Figure 6.9). The samples containing 0.5% Ti all exhibit similar T_c values, nearly independent of the

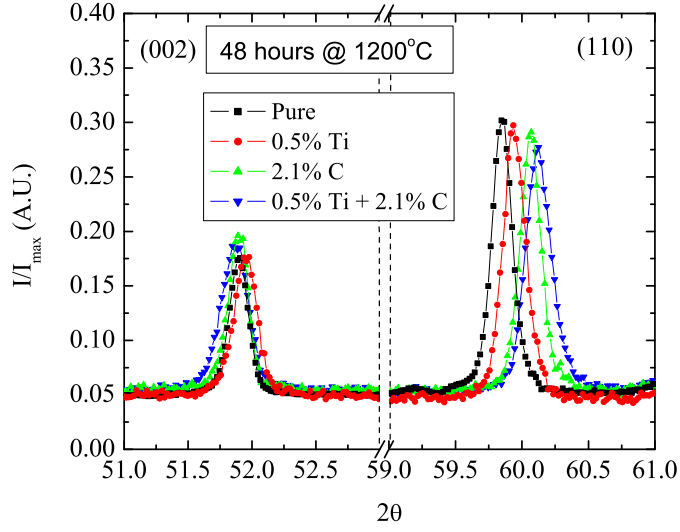


Figure 6.8 X-ray (002) and (110) peaks for samples with various levels of Ti and C additions.

carbon content, and well below the T_c values of the carbon only doped samples.

If the Ti additions are not dramatically altering the scattering, the upper critical field values of samples containing both Ti and C should closely resemble those of the carbon doped filaments. As with the carbon only doped filaments, the low temperature upper critical field values were determined by an onset criteria in resistance versus field curves in fields up to 32.5 T. For samples with both Ti and C the transitions were considerably rounded (Figure 6.10a) making it difficult to uniquely define H_{c2} . In order to compare the temperature dependence of H_{c2} for carbon doped and carbon doped with Ti additions, we used two different extrapolations in the latter samples to determine the onset. One extrapolation was from the beginning of the transition and the other was from near the end of the transitions. $H_{c2}(T)$ curves for the carbon doped and carbon doped with Ti additions are plotted in figure 6.10b. The two criteria used to determine H_{c2} for the samples containing Ti and C yield considerable spread in the data. However, for both the 0.6% and 2.1% carbon doped samples with 0.5% Ti additions, the spread envelops the H_{c2} values associated with 0.6% and 2.1% carbon doping only. Thus, in

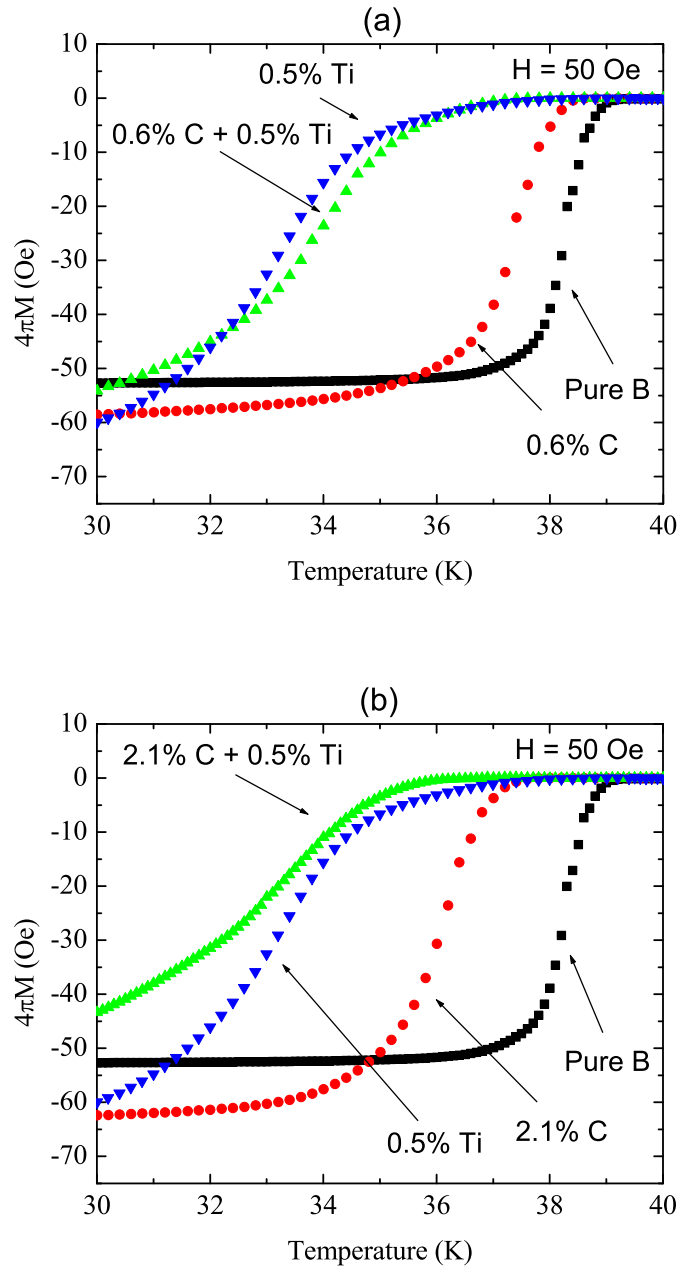


Figure 6.9 Magnetization curves for samples containing various levels of Ti and C.

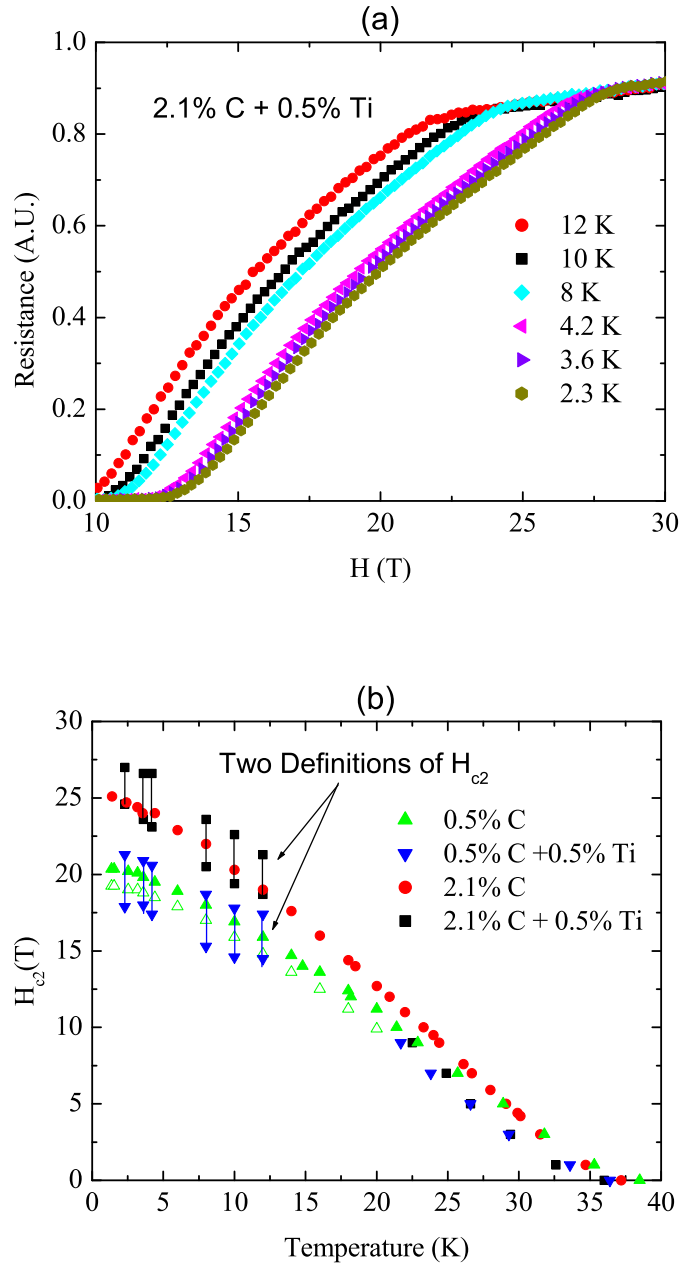


Figure 6.10 (a) Resistance versus field curves used to determine $H_{c2}(T)$ for a 2.1% carbon doped MgB_2 sample containing 0.5% Ti additions. (b) Comparison of $H_{c2}(T)$ for carbon doped samples with and without Ti additions.

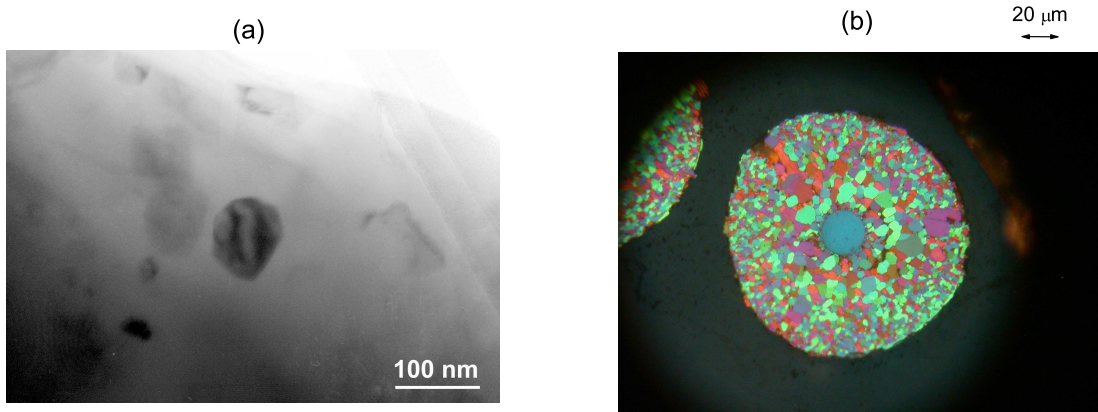


Figure 6.11 (a) TEM micrograph showing a TiB₂ precipitate in a 2.1% carbon doped MgB₂ sample containing 0.5% Ti additions. (b) Optical photo taken under polarized light of the same filament.

spite of the fact that the samples with 0.5% Ti and differing carbon levels all exhibited similar T_c values, the low temperature upper critical field values are consistent with the Ti and C additions acting independently, indicating that the Ti is not affecting the intraband scattering responsible for the enhancements in H_{c2} .

TEM analysis of a sample containing 0.5% Ti and 2.1% C shows the presence of precipitates as large as 40-50 nm (Figure 6.11a). It should be noted that selected area diffraction patterns (not shown) are consistent with the precipitates being TiB₂. Presumably, the high reaction temperature has resulting in a coarsening of the precipitates, making them too large to be effective at pinning vortices. While the presence of Ti was able to limit the size of the grains to approximately 1-5 μm (Figure 6.11b), the critical current densities in these carbon doped samples with Ti additions show no enhancement relative at 5 K to a pure sample reacted for 4 hours at 950 °C (64), in spite of the enhancements in H_{c2} (Figure 6.12).

All of these data support the notion that Ti can be added to carbon doped MgB₂ without harming the beneficial effects carbon doping has on the superconducting properties. For the case of 1200 °C reactions, the carbon appears to still enter the structure enhancing H_{c2} to comparable levels, while the Ti precipitates out as TiB₂. Once again the high reaction

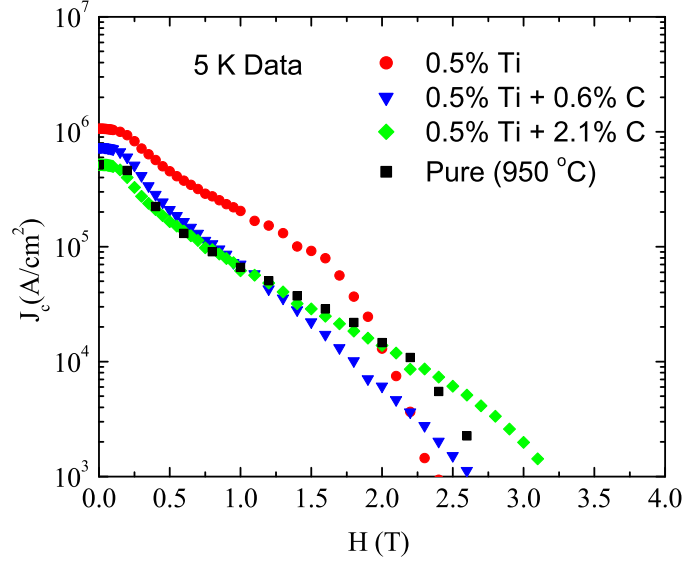


Figure 6.12 Critical current densities at 5 K for the set of 0.5% Ti additions and varying carbon levels. Data are compared to a pure sample which was reacted for 4 hours at 950 °C (64).

temperatures resulted in a coarsening of the precipitates which contributed to low J_c values. While these data suggest a combination of Ti and C additions to MgB_2 may yield dramatic improvements in J_c values, alternative synthesis techniques need to be employed to realize any potential improvements.

CHAPTER 7. Synthesis of $\text{Mg}(\text{B}_{1-x}\text{C}_x)_2$ Powders

The enhancement of H_{c2} achieved by carbon doping MgB_2 motivates a desire to synthesize bulk $\text{Mg}(\text{B}_{1-x}\text{C}_x)_2$ in a form that is more suitable for practical applications than the filaments discussed in chapter 5. Using doped boron filaments made with CVD processing required high reaction temperatures which lead to large grain sizes and poor J_c values (86). Reports of successful fabrication of superconducting wire using powder-in-tube processing (87; 88), coupled with the fact that J_c values in powder samples can readily be increased by the addition of various particles (80; 81; 89; 90) suggest single phase carbon doped MgB_2 powder would be a more suitable route towards developing superconducting wire. Carbon doped bulk polycrystalline MgB_2 with approximately 10% carbon incorporation has previously been synthesized by mixing elemental Mg and the binary B_4C (59; 60). In the next two chapters we explore possible ways of preparing $\text{Mg}(\text{B}_{1-x}\text{C}_x)_2$ with $x < 0.10$. First we attempt to introduce stoichiometric amounts of carbon using a mixture of B and B_4C . In chapter 8 we attempt to use doped boron powders synthesized by a plasma spray process.

7.1 Sample Synthesis

Powder samples of $\text{Mg}(\text{B}_{1-x}\text{C}_x)_2$ were prepared in a two step process. First, stoichiometric mixtures of distilled Mg, elemental B, and the binary compound B_4C were reacted for 48 hours at 1200 °C. The resultant sample was then reground in acetone, pressed into a pellet, and re-sintered for an additional 48 hours at 1200 °C. Two different batches were made. The first with 0.995 purity B (metals basis) from Alpha Aesar, and the second with 0.9997 purity isotopically enriched ^{11}B from Eagle Picher. The three main impurities in the 0.995 purity B are C, Si, and Fe, which have relative atomic abundances of 0.25% and 0.20%, and 0.10% respectively.

The isotopically enriched ^{11}B contained 0.02% Ta, 0.001% Cu, and 0.001% Fe. Samples made with isotopically enriched ^{11}B were shown to have a higher residual resistivity ratio (RRR) than samples made with nominal 0.9999 purity B, indicating the isotopic enrichment process yields perhaps the purest boron available (91). B_4C from Alpha Aesar was used as the carbon source in both runs. The B_4C had a nominal purity of 0.994 metals basis with the two primary impurities being Si and Fe, which occur in relative abundances of 0.37% and 0.074% respectively, values similar to those in the 0.995 purity B. Since impurities in the boron have been shown to suppress T_c (91), two differing boron purities were used to examine the effects of the starting boron purity on the T_c and $H_{c2}(T=0)$ values in carbon doped MgB_2 . We found it necessary to use multiple reaction steps to incorporate the carbon as uniformly as possible. To avoid confusion regarding the meaning of x in $\text{Mg}(\text{B}_{1-x}\text{C}_x)_2$, we will henceforth refer to the nominal carbon content as x_n and the inferred carbon content after the m -th reaction step as x_{im} .

7.2 Results and Discussion

Using the lower purity boron, we reacted a sample with nominal carbon content of $x_n=0.05$ for 48 hours at 1200 °C. The carbon content can be estimated by the shift of the x-ray (110) peak position relative to that of a nominally pure MgB_2 sample made under the same conditions (60; 75). Although the B_4C is a different B source than that used for the reference sample, the 0.994 purity B_4C and 0.995 purity B contain similar concentrations of impurity phases, and we cautiously proceed with estimates of the carbon content ignoring minor differences between boron sources. Indexing of the (110) peak for the pure sample and that containing a nominal carbon content of $x_n=0.05$ yielded an inferred carbon level after this first reaction step of approximately $x_{i1}=0.031$. In order to ensure the carbon was fully incorporated and uniformly distributed within this sample, it was reground in acetone, pressed into a pellet, and sintered for an addition 48 hours at 1200 °C. The subsequent sample showed a further increase in the (110) peak position (Figure 7.1) which yielded an inferred carbon content of $x_{i2}=0.069$. This sample also showed decrease in T_c (Figure 7.2), which is consistent with more carbon being

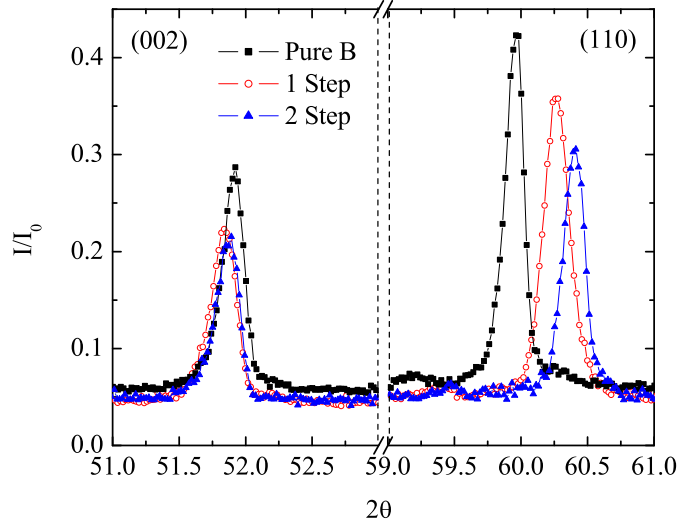


Figure 7.1 Powder x-ray diffraction (002) and (110) peaks for pure and nominal $\text{Mg}(\text{B}_{.95}\text{C}_{.05})_2$ samples made using the 0.995 purity boron as the starting material. The pure sample was reacted using two steps. For the carbon doped sample, the second sintering step shifts the (110) peak position to higher 2θ indicating the incorporation of a higher carbon concentration.

incorporated in the structure. In addition to shifting to higher 2θ , the (110) peak became sharper. The full-width-at-half-maximum (FWHM) decreased from 0.221° to 0.157° after the second sintering step. Therefore the second sintering step not only incorporated more carbon but it appears to have resulted in a more uniform carbon distribution. It should be noted that after the two sintering steps the FWHM values of the MgB_2 peaks were comparable to those of the Si standard, indicating we have achieved a fairly high level of homogeneity. It is also worth noting that whereas the (110) peak shifts and sharpens as a result of a second reaction step, the (002) peak does neither, having FWHM values comparable to, but slightly larger than, the neighboring Si (311) peak after both reaction steps. This indicates that the c-axis spacing and periodicity are particularly insensitive to this degree of carbon doping and/or disorder.

Whereas the x_{i2} value exceeds the nominal value of $x_n=0.05$ in the starting material,

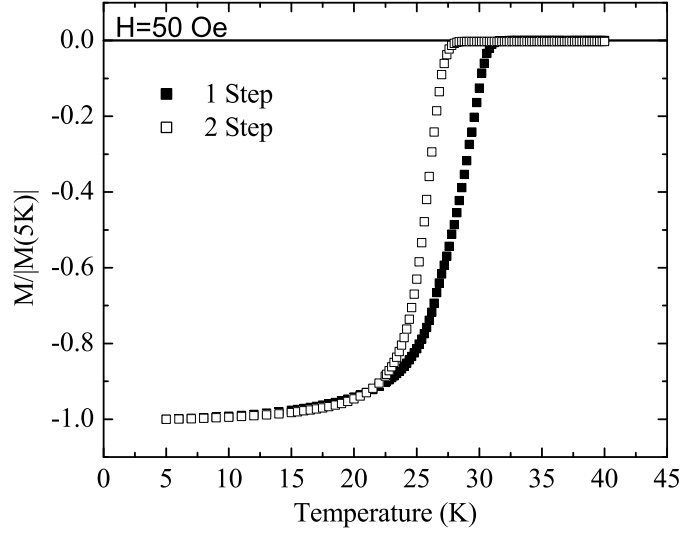


Figure 7.2 Normalized magnetization curves for nominal $\text{Mg}(\text{B}_{0.95}\text{C}_{0.05})_2$ samples. The second sintering step lowers T_c , consistent with the incorporation of a higher carbon concentration.

the presence of MgB_4 , as evidenced by strong peaks in the x-ray spectrum (Figure 7.3) may account for the discrepancy if we assume no carbon enters the MgB_4 structure. Comparison of the x-ray spectra for the single and two step reactions shows an increase in the intensity of the MgB_4 peaks after the second reaction step. This step was done without the addition of any extra Mg to compensate for potential Mg loss. It is possible that while sintering at 1200 °C, some Mg is driven out of the MgB_2 structure and this loss results in conversion of MgB_2 to MgB_4 , with the excess Mg forming MgO and possibly condensing on the walls of the tantalum reaction vessel during the quench. To determine whether or not Mg loss is responsible for the apparent increase in the carbon content, the second sintering step for a sample with nominal concentration $x_n=0.05$ was carried out in an atmosphere of excess Mg vapor. This sample exhibited a T_c of 29.8 K and a shift in the (110) x-ray peak yielding an inferred carbon concentration of $x_{i2}=0.050$ (Figure 7.4), consistent with the nominal concentration. Thus the apparent difference in carbon content for samples which undergo a second sintering

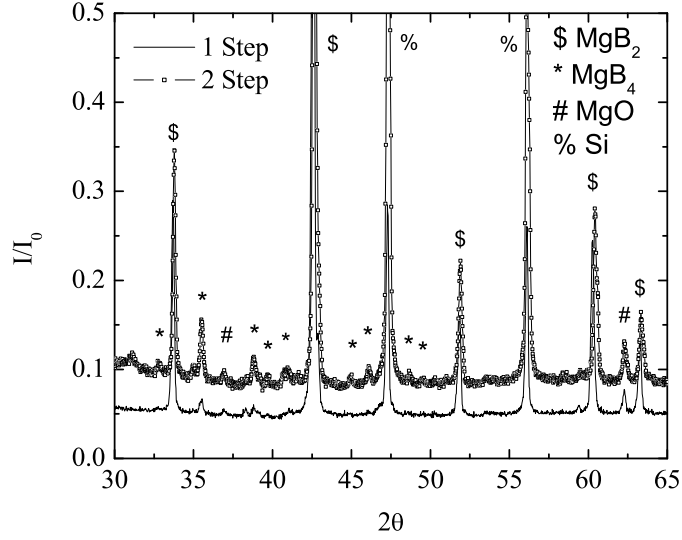


Figure 7.3 Normalized powder x-ray pattern for a sample with $x_n=0.05$ synthesized using a one step and a two step reaction. The two step sample clearly contains enhanced amounts of MgB_4 .

step without the presence of excess Mg to compensate for Mg loss relative to those which undergo the second sintering step with excess Mg is presumably the result of a fixed amount of carbon being incorporated into a decreased amount of MgB_2 . To avoid the potential creation of percolation networks of Mg within the samples we chose to perform the second sintering step without any additional Mg.

Using 0.995 purity boron and 0.994 purity B_4C , an entire series with nominal carbon levels of $x_n=0, 0.0125, 0.025, 0.035, 0.05, \text{ and } 0.075$ was prepared using the two step reaction profile. The (002) and (110) x-ray peak positions for the entire series are plotted in figure 7.5. The (002) peak position is roughly constant for all carbon levels, consistent with the results found by Avdeev et al. and (60) Wilke et al. (75), which showed only a slight expansion along the c-axis for carbon doping levels up to $10\pm 2\%$. The (110) peak position shifts towards higher 2θ values as x is increased up to $x_n=0.05$, at which point it appears to be saturated. Using the (110) peak position for the nominally pure sample as our standard, the inferred carbon

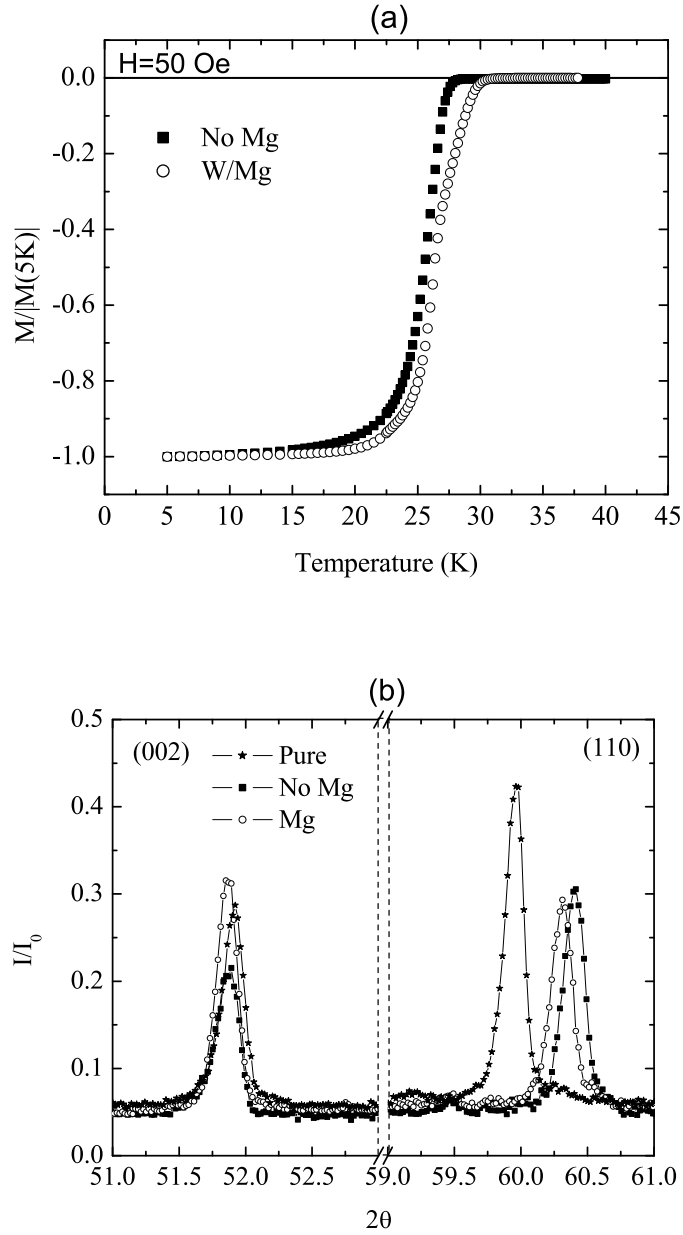


Figure 7.4 (a) Normalized magnetization curves and (b) x-ray (002) and (110) peaks for a sample of $x_n=0.05$ reacted using a two step process. If the second sintering step is performed without any excess Mg to compensate for potential losses, the resultant carbon content within the MgB_2 phase is increased.

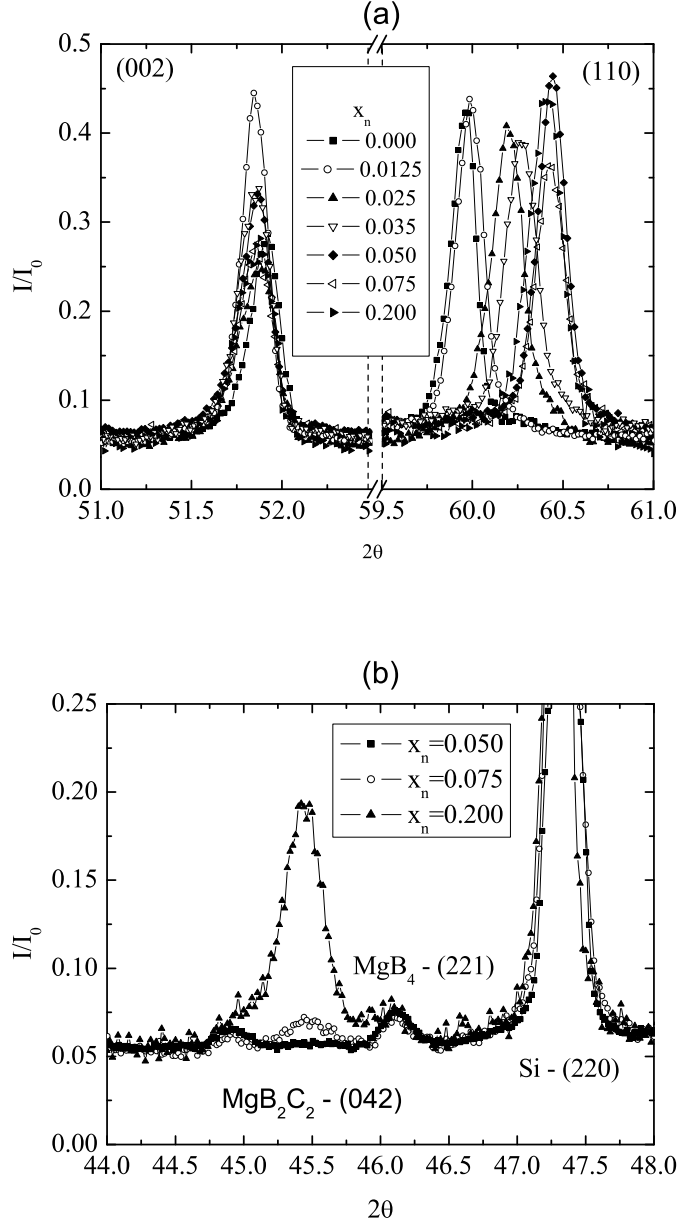


Figure 7.5 (a) Evolution of the (002) and (110) x-ray peaks for $\text{Mg}(\text{B}_{1-x}\text{C}_x)_2$ samples with nominal $x_n = 0, 0.0125, 0.025, 0.035, 0.05, 0.075$, and 0.20 synthesized using a two step reaction. The shift of the (110) peak relative to that of the un-doped yields inferred carbon concentrations of $x_{i2} = 0.01, 0.034, 0.044, 0.069, 0.067, 0.065$. (b) For samples saturating near $x_{i2} = 0.07$ the excess carbon precipitates out in the form of MgB_2C_2 as can be seen by the emergence of the MgB_2C_2 (042) peak as a function of nominal carbon content.

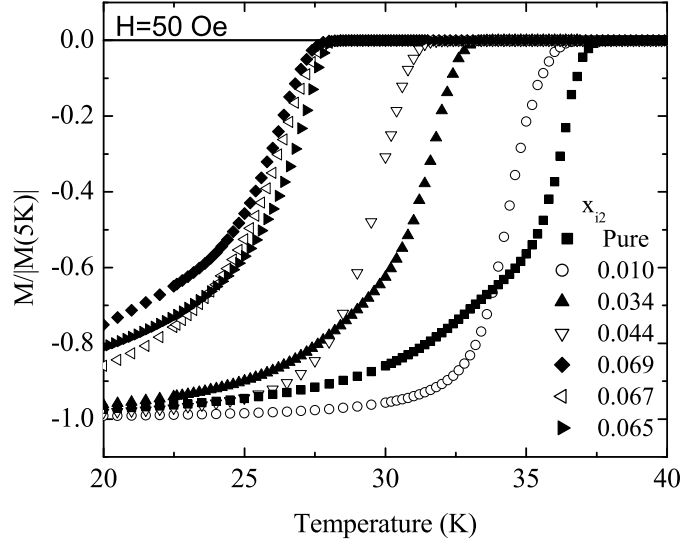


Figure 7.6 Normalized magnetic transitions for the series of $\text{Mg}(\text{B}_{1-x}\text{C}_x)_2$ with $x_{i2}=0.01, 0.034, 0.044, 0.069, 0.067, 0.065$, synthesized with 0.995 purity B and reacted using a two step process.

concentrations for the entire series are $x_{i2}=0, 0.01, 0.034, 0.044, 0.069$, and 0.067 . The samples with carbon concentrations saturating near $x_{i2}\sim 0.07$ show an increase in the MgB_2C_2 phase as a function of the nominal carbon content (Figure 7.5b). Thus the excess carbon is precipitating out as MgB_2C_2 .

Normalized magnetization measurements (Figure 7.6) confirm the highest two doping levels have incorporated roughly the same amount of carbon. Their transition temperatures all lie slightly below 28 K. Defining T_c using a 2% screening criteria the $x_{i2}=0.069$ and 0.067 levels have T_c values of 27.5 K and 27.8 K respectively. For these higher doping levels, the nominal concentrations did not yield systematic increases in carbon level, but the change in the a-lattice parameter and T_c are consistent with one another; i.e. samples which apparently incorporated more carbon had smaller a-lattice parameters and lower T_c values.

This saturation near $x_{i2}\sim 0.07$ is not entirely unexpected given the results of $10\pm 2\%$ carbon incorporation using B_4C reported by Ribeiro et al. (59) and Avdeev et al. (60). In optimizing

the reaction, Ribeiro found that under certain conditions, T_c values below the near 22 K reported for the optimal 24 hours at 1100 °C reaction could be attained, suggesting higher carbon content phases may be metastable. To test whether the saturation we observed was an effect due to the use of a two step reaction, as opposed to the single step employed by Ribeiro et al., we repeated their work, making a sample of nominal concentration $\text{Mg}(\text{B}_{0.8}\text{C}_{0.2})_2$ using only Mg plus B_4C . This sample underwent an initial 48 hour reaction at 1200 °C to form the superconducting phase and a second sintering for 48 hours at 1200 °C. After the first 48 hours at 1200 °C we find a superconducting phase with T_c near 22 K, and a lattice parameter shift which yielded inferred values of $x_{i1}=0.092$ slightly less than the $x_i=0.10$ obtained by Ribeiro and coworkers using isotopically enriched $^{11}\text{B}_4\text{C}$ as the carbon source (60). After the second sintering step, T_c rises to 27.9 K. The (110) x-ray peaks shifted to lower 2θ , yielding an inferred $x_{i2}=0.065$ (Figure 7.7). Although two reaction steps were used, no change in the FWHM of the (110) peak was observed. As in the case of the $x_n=0.075$ sample, the decrease in carbon content could be due to carbon precipitating out in the form of MgB_2C_2 . The relative intensity of the most prominent MgB_2C_2 peak to that of MgB_2 approximately doubles going from the single step reaction to the two step reaction. In order to check if more carbon would be precipitated out in the form of MgB_2C_2 by simply adding more sintering steps to the growth process an additional sample underwent a three step reaction: an initial 48 hours at 1200 °C to form the superconducting phase followed by two additional sintering steps of 48 hours at 1200 °C. After this third reaction step, the sample exhibited a T_c of 27.9 K and the (110) peak position yielded an inferred carbon content of $x_{i3}=0.064$ (Figure 7.7). These values are comparable to our previous results with only two sintering steps. Thus the carbon content appears to saturate in the vicinity of an inferred carbon content of $x_i=0.065$. The fact that saturation near $x_{i2}=0.065$ occurred for samples which had x_{i1} both above and below this level indicates that in equilibrium the solubility limit for 1200 °C reactions near 1 atm is in the range $0.065 < x_i < 0.07$.

Transport measurements were made in order to determine the upper critical field. An onset criteria was used in both resistance versus temperature and resistance versus field. Figure 7.8a

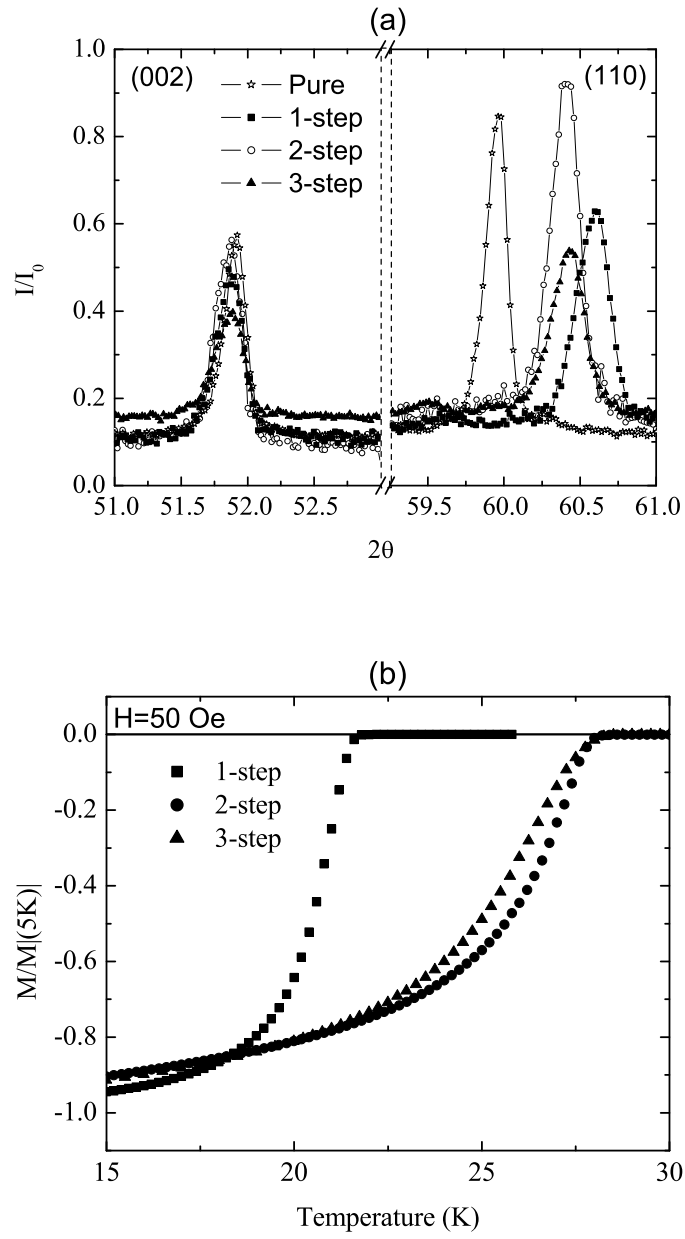


Figure 7.7 (a) (002) and (110) x-ray peaks for nominal $\text{Mg}(\text{B}_{0.8}\text{C}_{0.2})_2$ using B_4C as the boron and carbon source and reacted using 1, 2, and 3 step reaction processes. (b) Normalized magnetic transitions for these samples.

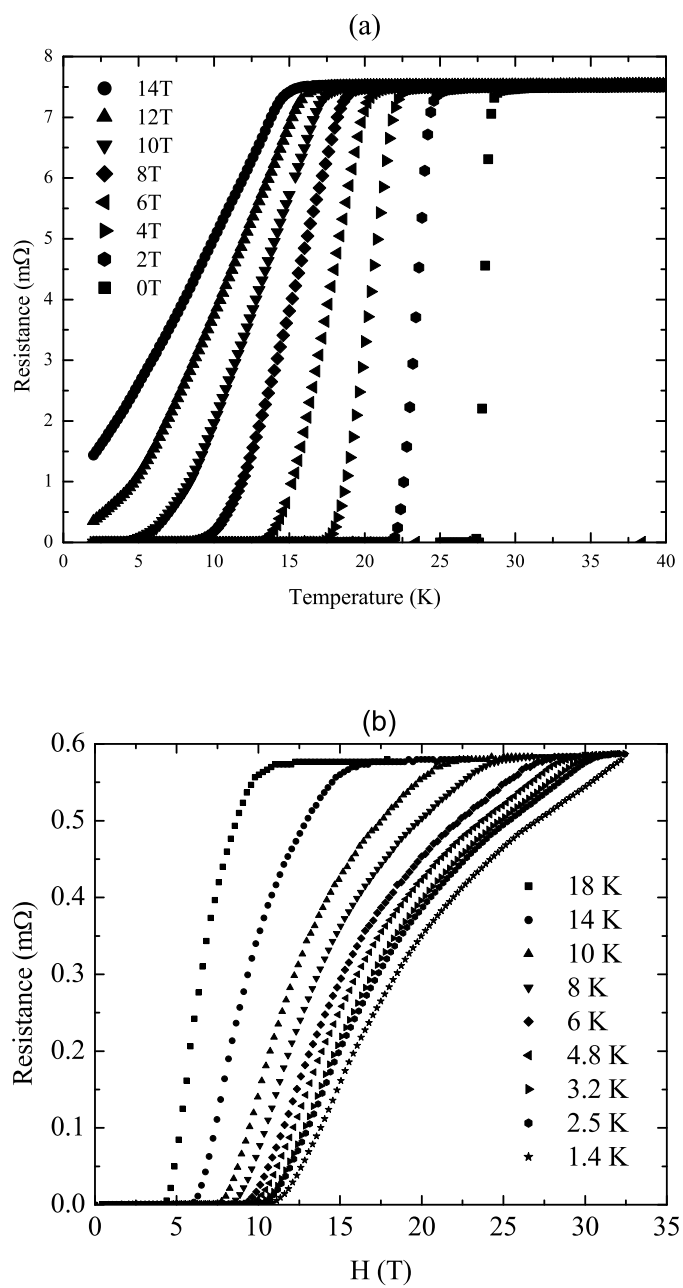


Figure 7.8 (a) - Resistance versus temperature and (b) - resistance versus field for a sample with $x_{i2}=0.069$.

plots resistance versus temperature in applied fields up to 14 T and figure 7.8b plots resistance versus field at temperatures down to 1.4 K for the sample with a carbon level of $x_{i2}=0.069$ ($x_n=0.05$). The zero field resistive transition has a width of less than 1 K, but this significantly broadens as the strength of the applied field increases. The R vs. H measurements show a related broadening. For example, the width of the transition at 1.4 K is nearly 20 T wide. This should be compared to the 10 T wide, approximately linear transitions reported for 5.2% carbon doped filaments (86). Optical images taken under polarized light show the superconducting grains in the powder sample are 5-10 μm in size. In the case of the wire sample a majority of the grains are in the 1-5 μm range (86). We therefore ascribe the increased width of this transition to a combination of poor flux pinning due to the large grain size associated with the high reaction temperature as well as to possible remaining inhomogeneities in carbon incorporation within the sample.

H_{c2} curves for $x_{i2}=0.034$ and $x_{i2}=0.069$ along with a pure wire (3) and a carbon doped wire with an inferred carbon content of $x_i=0.052$ (86) are plotted in figure 7.9. The powder sample with $x_{i2}=0.034$ has a T_c slightly less than that of the carbon doped wire with $x_i=0.052$ and an $H_{c2}(T=0)$ more than 5 T lower. This marked difference shows that for carbon doped samples made with differing nominal boron purities, T_c alone is not a good caliper of $H_{c2}(T=0)$. The sample with inferred carbon content of $x_{i2}=0.069$ has a T_c nearly 7 K below the aforementioned wire and an $H_{c2}(T=0)$ just above 30 T. Comparing the two powder samples to one another, we see an increase in the slope of H_{c2} near T_c for the higher doping level, which results in a higher $H_{c2}(T=0)$, consistent with our earlier findings (75; 86).

Carbon has been shown to suppress T_c at a rate of roughly 1 K/%C for up to 5% carbon substitution (86). The magnetization and transport measurements indicate T_c of the powder samples made with the 0.995 purity Alpha Aesar boron is also being suppressed at a rate of roughly 1 K/%C, but relative to the suppressed, near 37 K, transition of the nominally pure sample. The suppressed transition temperature of the nominally pure MgB_2 sample lies approximately 2 K below results obtained using high purity natural boron wires (64). MgB_2 made from lower purity boron has been shown to have lower transition temperatures (91).

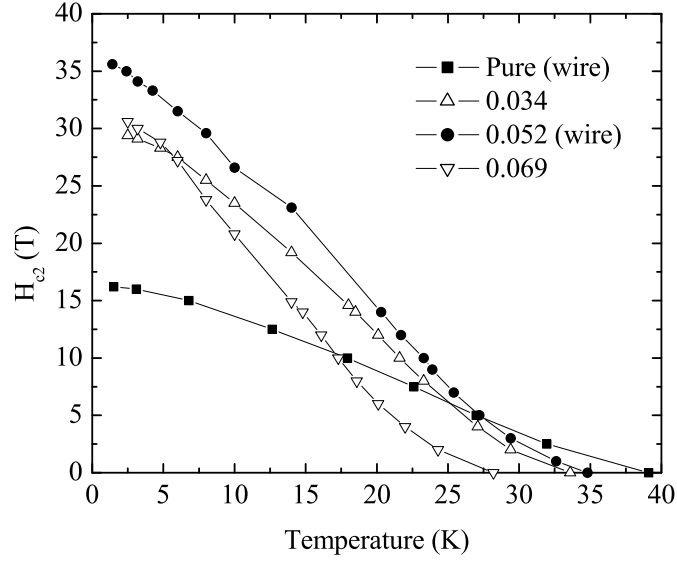


Figure 7.9 Comparison of upper critical field curves for pellets with carbon doping levels of $x_{i2}=0.034$ and 0.069 with wires containing $x_i=0$ and 0.052 . The $x_i=0$ and 0.052 samples were made by reacting Mg vapor with boron filaments, see reference (75).

In figure 7.10, a comparison of T_c versus $|\Delta a|$ for carbon doped samples prepared with lower purity boron to carbon doped wires made with high purity boron shows the manifold associated with the impure boron powder is shifted downward by approximately 2 K for all carbon levels. To confirm that this difference is a result of the purity of the starting boron, a second set of two step process samples made with isotopically enriched ^{11}B were measured. The results are included in figure 10. Also included is a set of carbon doped powders made by a plasma spray process (84) (see next chapter). The agreement between the CVD wires, plasma spray powders, and ^{11}B samples shows that high purity boron in a variety of forms responds to carbon doping in a similar manner. These data also seem to indicate that there is some additional impurity in the 0.995 pure Alpha Aesar boron that is systematically suppressing T_c .

Figure 7.11 plots a comparison of the (002) and (110) x-ray peaks of pure MgB_2 using the three different purity levels of boron. The sample made with the nominal 0.995 purity boron

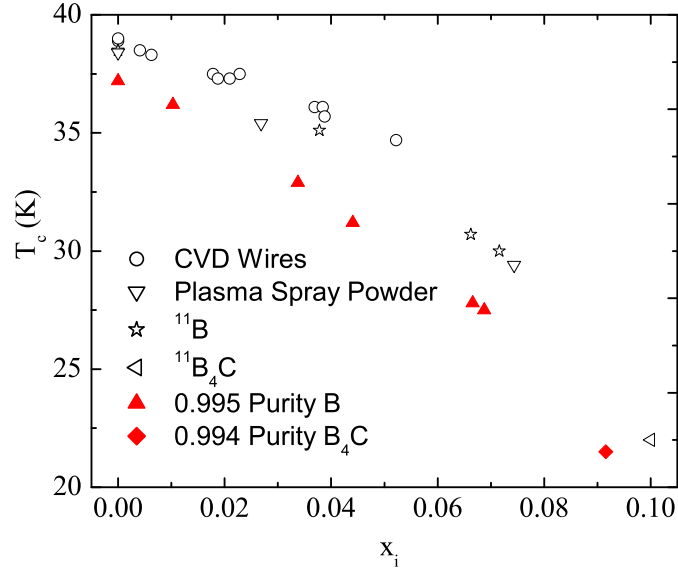


Figure 7.10 Evolution of T_c as a function of x_i . CVD wires and powders are from references (86) and (84) respectively. Data on the sample prepared with isotopically enriched $^{11}\text{B}_4\text{C}$ is from reference (60).

shows a shift of the (110) peak to higher 2θ by 0.09° , which, if it were to be associated with carbon doping, would be consistent with carbon doping of approximately 1.8%. This level far exceeds the stated carbon impurity level of 0.25% in the 0.995 purity B as claimed in the certificate of analysis provided by Alpha Aesar. To check whether by using lower purity boron we have inadvertently doped with carbon to such a high level, we measured the resistive onset of superconductivity in an externally applied 14 T field for the nominal pure MgB_2 using the 0.995 purity boron and compared the temperature with those attained for carbon doped fibers reported in reference (40). MgB_2 fibers reacted at 1200 °C for 48 hours showed an onset of superconductivity in an externally applied magnetic field of 14 T at 10.2 K, 14.8 K, and 18.5 K for pure, 0.6%, and 2.1% carbon doping (86). If the shift of the (110) peak in the nominally pure MgB_2 made from 0.995 purity boron were a result of inadvertent carbon doping, we would expect an onset of superconductivity in an applied 14 T field at a temperature between 15 K

and 18 K. However, such a measurement yielded an onset near 13 K indicating if carbon is present as an impurity, it is less than 0.6%, which consistent with the estimate provided by Alpha Aesar. Therefore the manifold of T_c versus $|\Delta a|$ for the lower purity boron is shifted downward by some as of yet unidentified impurity associated with the Alpha Aesar boron.

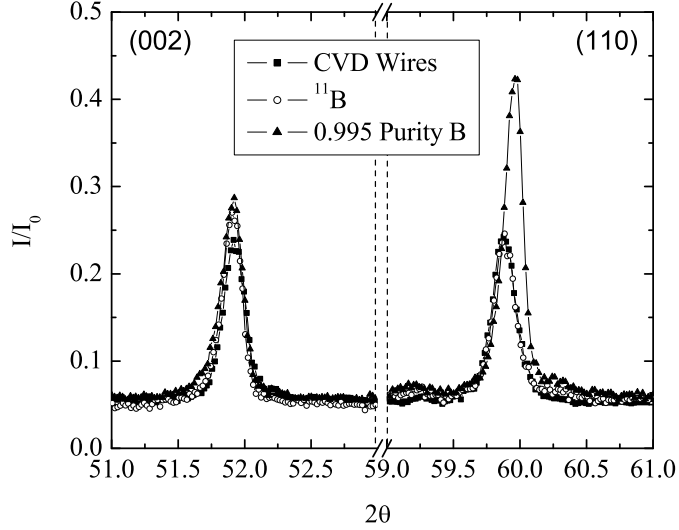


Figure 7.11 Comparison of (002) and (110) x-ray diffraction peaks for pure MgB_2 made using different purity boron as the starting material. The 0.995 purity shows a shift in the (110) peak which presumably is not a result of inadvertent carbon doping.

H_{c2} values were determined using an onset criteria in resistivity versus temperature and resistance versus field measurements. Pellets made using the isotopically enriched ^{11}B lacked structural integrity and were unsuitable for transport measurements. Therefore we could only attain $H_{c2}(T=0)$ values only for samples made from the CVD wires, plasma spray powders, and the 0.995 purity boron (Figure 7.12). For the dirtier, 0.995 purity powder, at a doping level of $x_{i2}=0.034$ the upper critical field agrees with the results of a carbon doped wire with an inferred carbon content of $x_i=0.038$ from reference (75). At doping levels near $x_{i2}=0.065$, H_{c2} values fall several Tesla below the manifold for "clean" carbon doped samples. In carbon doped

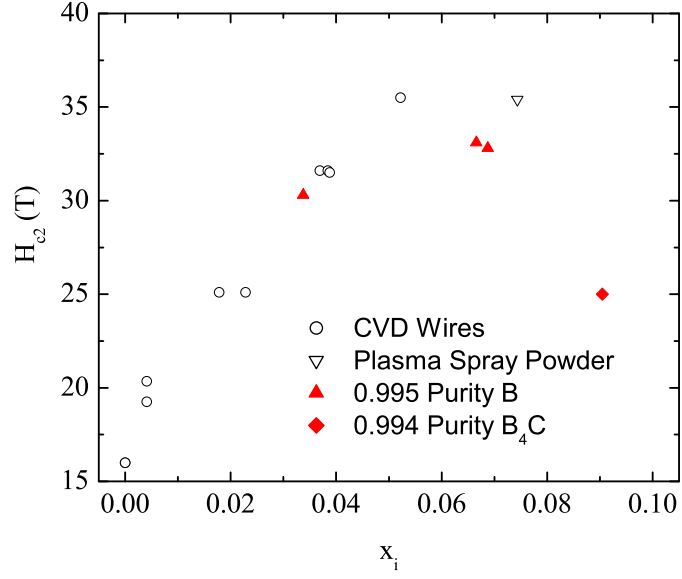


Figure 7.12 $H_{c2}(T=0)$ curves for the samples with different purity in the starting boron. CVD wires and plasma spray powders are from references (86) and (84) respectively. H_{c2} data on the highest doping level is from reference (74).

MgB_2 , enhancement of H_{c2} due to scattering effects (14; 27) competes with the suppression of T_c caused by electron doping (14). By further suppressing T_c by introducing additional impurities in the system, we may have limited the maximum H_{c2} attainable through carbon doping.

CHAPTER 8. Plasma Spray Synthesized Doped Boron Powders

Critical current densities in fully dense carbon doped MgB_2 wires were found to depend upon the size of the superconducting grains (see chapter 5); as the grain size decreases, in-field J_c values increase. Therefore, an additional route to improving critical current densities in MgB_2 is to develop methods for synthesizing carbon doped MgB_2 with smaller grains. In the case of the dense carbon doped filaments, the slow growth rate of $\text{Mg}(\text{B}_{1-x}\text{C}_x)_2$ required reaction temperatures in excess of 1100 °C for time periods longer than 24 hours, resulting in large (1-20 μm) grains. A possible solution to decreasing the grain size is to use fine doped powders as the starting material. The size of the superconducting grains will be partially limited by the particle size. Additionally, the Mg diffusion length for conversion to $\text{Mg}(\text{B}_{1-x}\text{C}_x)_2$ is decreased, and should, therefore, allow us to react at lower temperatures for shorter periods of time. In this chapter we attempt to synthesize $\text{Mg}(\text{B}_{1-x}\text{C}_x)_2$ using carbon doped boron powders made via a plasma spray process.

8.1 Powder Synthesis

Fine carbon doped boron powders can be prepared in an analogous manner to the wire production discussed in chapter 5. The same process gases (H_2 , BCl_3 , CH_4) are injected into an inductively coupled Ar plasma, rather than being passed over a resistively heated filament. Within the plasma the dissociated process gasses form an aerosol of fine carbon doped boron particles. A series of powders were synthesized at SUNY-Stoneybrook using a Tekna PL-50 torch with both swirl and radial Ar flow (Figure 8.1). The ratio of the flow rates of the process gases was set to yield samples with nominal carbon concentrations, hereafter designated as x_n , of $x_n = 0, 0.01$ and 0.02 . Table 8.1 gives, as an example, the flow rates for the synthesis of

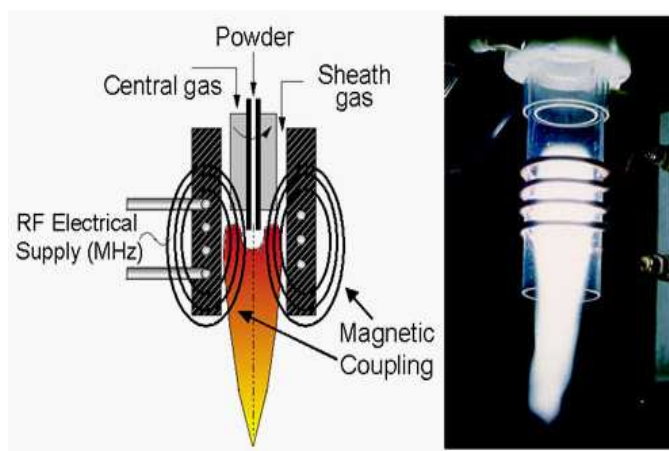


Figure 8.1 Schematic diagram and photograph of the Tekna PL-50 RF Induction Plasma Torch used to synthesize doped boron powders.

nominally 2% carbon doped boron powder. The system was set to an operating pressure of ~ 300 Torr and an input power of ~ 45 kW was used to maintain plasma. The doped powders were deposited on a stainless steel screen. Samples were scraped off the screen, sealed under Ar, and shipped to Iowa State University.

Figure 8.2 shows SEM images of the as-synthesized powders. The grains are approximately 50 nm in size and tend to collect in lacy agglomerates, which can be as large as $10\ \mu\text{m}$. X-ray scans, using copper K_α radiation ($\lambda=1.5406\ \text{\AA}$), showed no peaks over the range $20\text{-}90^\circ\ 2\theta$

Process Gas	Flow Rate (ccpm)
Ar (radial)	70000
Ar (swirl)	30000
H ₂	12000
BCl ₃	5000
CH ₄	100

Table 8.1 Gas flow rates for the synthesis of nominally 2% carbon doped boron powder.

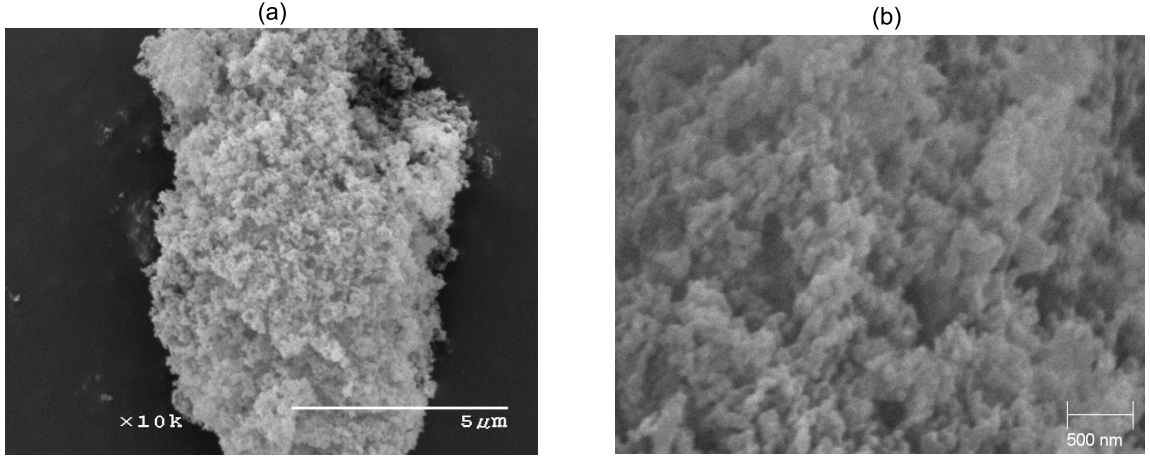


Figure 8.2 (a) Low magnification SEM BSE image of as synthesized $x_n=0$ powder. (b) High magnification image showing the particles are of order 50 nm in size. The powders tend to clump together forming lacy agglomerates with typical dimensions of order 10 μm .

indicating the powders are either in an amorphous state or have a structural coherence length less than the wavelength of the incident x-rays.

8.1.1 Superconducting and Normal State Properties

As with the case of the wires, the nominal concentrations differ greatly from the actual carbon content of the powders. In order to estimate the actual carbon content, powders were reacted with Mg for 48 hours at 1200 °C and the relative contraction of the a -lattice parameter in the carbon doped samples relative to the pure sample was used to determine x in $\text{Mg}(\text{B}_{1-x}\text{C}_x)_2$ (60; 75). A high temperature and long time reaction profile was used in order to ensure the samples were fully reacted and to promote carbon incorporation that was as homogeneous as possible. The x-ray (002) and (110) peaks for $x_n=0$, 0.01, and 0.02 samples prepared in this manner are plotted in figure 8.3. To distinguish from nominal carbon content, the inferred carbon content for this set of high temperature reactions will be designated as x_{ih} . Indexing of the peaks in figure 8.3 yields $x_{ih}=0.027$ and $x_{ih}=0.074$ for the $x_n=0.01$ and

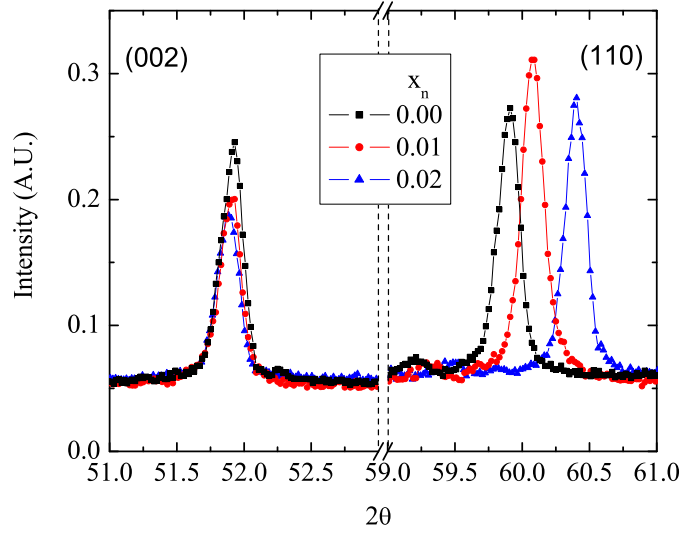


Figure 8.3 X-ray (002) and (110) peaks for pure, nominal 1%, and nominal 2% sample reacted for 48 hours at 1200 °C. Estimates of the carbon content, based on the contraction of the a - lattice parameter in the carbon doped samples relative to that of the pure (60; 75), yields $x_{ih}=0.027$ and $x_{ih}=0.074$ in $\text{Mg}(\text{B}_{1-x}\text{C}_x)_2$ for the $x_n=0.01$ and $x_n=0.02$ samples, respectively.

$x_n=0.02$ samples respectively.

The superconducting transition temperatures for these doped powders were determined using a 2% screening criteria in zero-field-cooled magnetization measurements. The normalized magnetization versus temperature curves are plotted in figure 8.4. The transitions are quite broad, presumably due to a combination of factors; poor connectivity between the loose powder, the existence of a wide range of demagnetization factors within the powder, and possible sample inhomogeneities. It should be noted that T_c drops of rapidly as a function of x for samples with $x>0.05$ (see Figure 8.5 below). Therefore, in heavily doped samples, inhomogeneous carbon incorporation should result in a distribution of T_c values, which span a larger temperature range than would inhomogeneities in samples with $x<0.05$. The extremely broad transition for the $x_{ih}=0.074$ sample may, therefore, be the result of inhomogeneous carbon incorporation. The

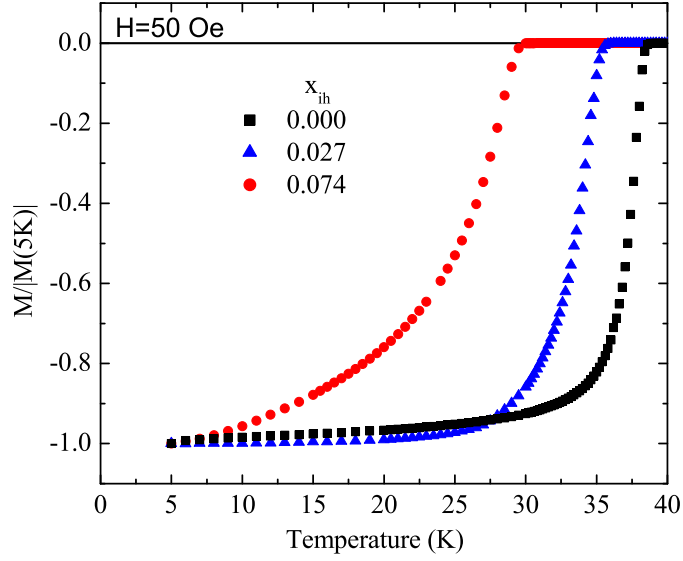


Figure 8.4 Normalized magnetization measurements for the set of $Mg(B_{1-x}C_x)_2$ powders synthesized at 1200 °C for 48 hours.

inferred carbon contents and resultant transitions temperatures for the carbon doped powders are consistent with those of the carbon doped filaments discussed in chapter 5. Plotting T_c as a function of $|\Delta a|$ for both sets shows that the manifold associated with the plasma spray powders is shifted downward by approximately 0.5 K (Figure 8.5). As discussed in the previous chapter, such a shift is presumably the result of unknown impurities in the starting boron causing a suppression of T_c which is additive to that of carbon doping.

A second set of samples was made by exposing pressed pellets of unreacted boron to excess Mg vapor at 950 °C for 4 hours. We used reaction vessels similar to those used for converting B fibers to MgB_2 (see chapter 3). Here the pressed pellet rested upon the strainer and was therefore separated from any liquid Mg on the bottom of the Ta can. An Mg:B stoichiometric ratio of 1:1 was used to promote complete reaction. As with the case of the wires, the excess Mg vapor condenses on the bottom of the can during the quench in water.

In the case of carbon doped wires, it was shown that long reaction times and high reaction

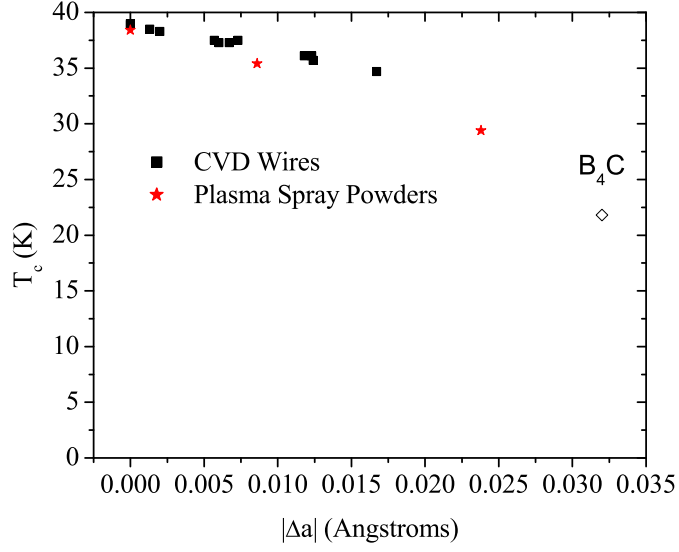


Figure 8.5 T_c as a function of the $|\Delta a|$ in carbon doped CVD wires and plasma spray powders. Wire data is from reference (86) (see chapter 5). The $|\Delta a|=0.032$ Å sample is from reference (60)

temperatures were necessary to fully convert 80 μm diameter fibers to $\text{Mg}(\text{B}_{1-x}\text{C}_x)_2$ (86). In the case of these fine grained powders, nearly all of the material has been converted to the superconducting phase in only 4 hours at 950 °C. The powder x-ray diffraction pattern for the sample with $x_n=0.02$ shows that in addition to the Si standard, the primary phases present are MgB_2 and MgO (Figure 8.6). Several MgB_4 peaks are just beginning to emerge from the background, indicating the reaction has not gone fully to completion, but the intensity of these peaks is approximately 1% that of the most prominent MgB_2 peaks.

The lower temperature reaction resulted in a substantial broadening of the MgB_2 x-ray peaks. In the pure sample, the (110) and (002) peaks had FWHM values of 0.297° and 0.256° respectively. These values are considerably larger than in the case of the 48 hour at 1200 °C reaction, where the (002) and (110) peaks had FWHM of 0.170° and 0.169° . For the $x_n=0.01$ sample, the FWHM of the (002) and (110) peaks for the 950 °C reaction were 0.295° and 0.260° , while for the 1200 °C reaction they were 0.172° and 0.174° . Similarly the $x_n=0.02$ sample had

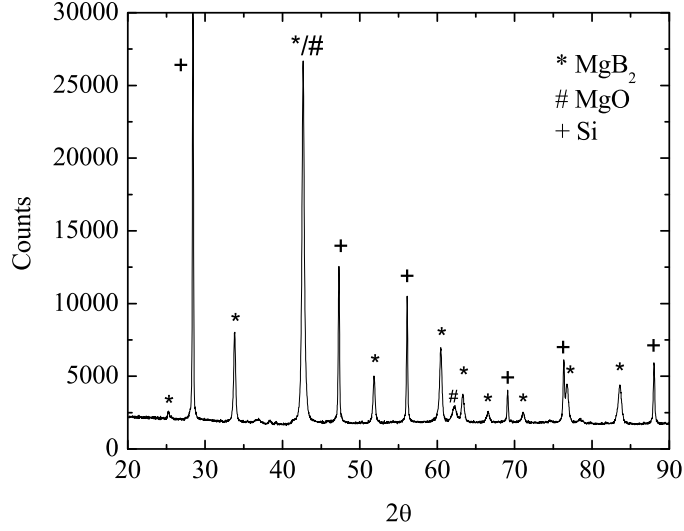


Figure 8.6 Powder X-ray diffraction pattern for a sample with $x_n=0.02$ reacted for 4 hours at 950 °C. In addition to the Si standard, the only prominent impurity peaks are consistent with MgO.

FWHM values of 0.299° and 0.363° for the 950 °C reaction and 0.179° and 0.175° for the 1200 °C reaction. The width of the (002) peak remains consistent for a given reaction temperature, and the broadened peaks associated with the lower reaction temperature presumably indicate a greater degree of disorder within these samples. All of the (110) peak widths remain consistent for a given reaction temperature except for the $x_n=0.02$ sample reacted at 950 °C. Here the peak width increases substantially, even relative to the already broad peaks associated with the lower reaction temperature. This indicates that at high carbon levels, the carbon incorporation is highly inhomogeneous for the low reaction temperature. It should be noted that indexing of the peaks also results in slightly different inferred carbon contents in the samples reacted at 950 °C. The inferred carbon contents for these low temperature reactions, designating as x_{il} , are $x_{il}=0.029$ and $x_{il}=0.081$ for the $x_n=0.01$ and $x_n=0.02$ samples, respectively.

Magnetization measurements show that the pellets reacted at 950 °C have superconducting onsets consistent with the 48 hour at 1200 °C reactions (Figure 8.7). The highest carbon level

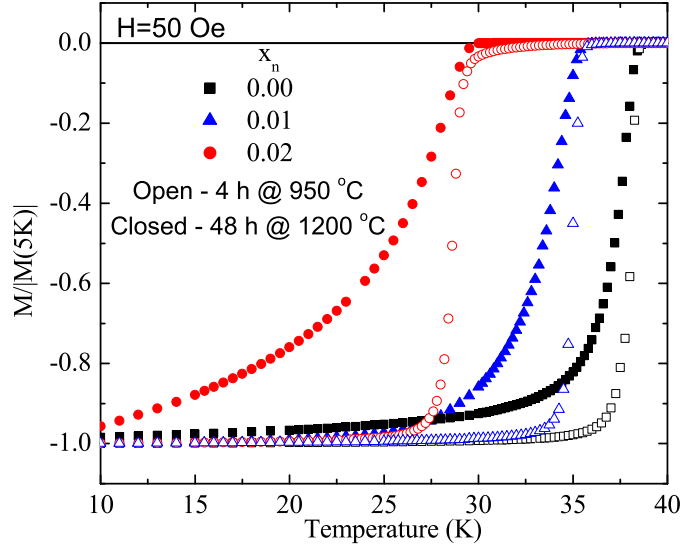


Figure 8.7 Normalized magnetization measurements for carbon doped powders reacted at either 1200°C for 48 hours or 950°C for 4 hours.

sample has a rounded transition, which is consistent with the notion that this sample contains a distribution of T_c values resulting from inhomogeneities in carbon incorporation. In both the pure and $x_n=0.01$ samples, the onset temperatures are comparable for both reaction profiles.

Rectangular rods were cut from the pellets in order to estimate critical current densities using magnetization hysteresis loops at 5 K and 20 K. The data are plotted along with results for a pure boron filament reacted for 4 hours at 950°C (67) and a sample with 10 weight percent SiC added to MgB_2 (82) in figure 8.8. All plasma spray powders show an enhancement in J_c at both 5 K and 20 K relative to the pure fiber. We attribute this increase to a decrease in grain size. Optical images taken under polarized light show that the plasma spray powders lead to superconducting grain sizes that are approximately $1 \mu\text{m}$, whereas the grain size for a fully reacted boron filament is approximately $5 \mu\text{m}$ (Figure 8.9). For the series of plasma spray powders, J_c at 5 K is higher in field for samples with higher carbon levels, with the $x_{il}=0.081$ sample showing J_c values comparable to one of the best reports in literature (82).

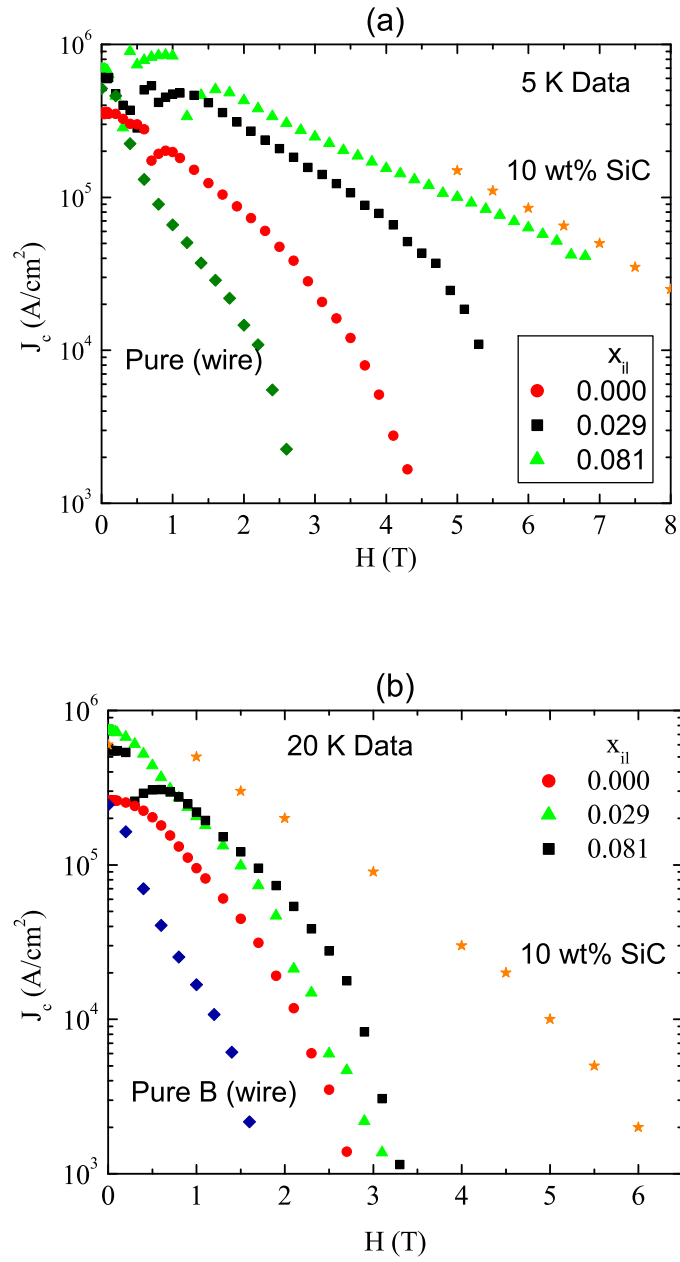


Figure 8.8 J_c values for pressed pellets of carbon doped MgB₂ inferred from magnetization hysteresis loops. Data are compared to a fully dense wire of pure MgB₂ (64) and a pressed pellet containing 10 weight% SiC additions (82).

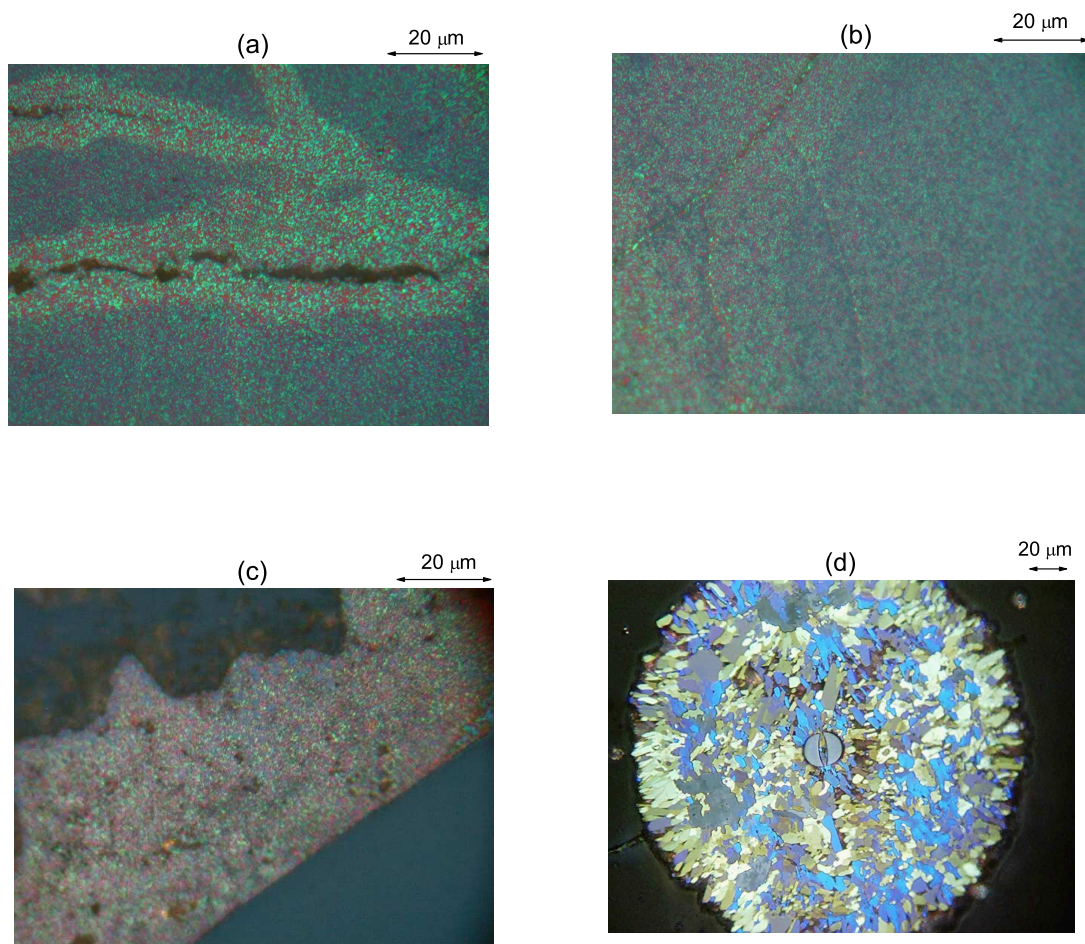


Figure 8.9 Optical images taken under polarized light of carbon doped MgB₂ samples. (a) Pure, (b) $x_{il}=0.029$ and (c) $x_{il}=0.081$ carbon doped powders made by plasma spray processing. (d) Pure fiber made using CVD. All samples were reacted for 4 hours at 950 °C.

The near 1 μm grain size in each of the powder samples is near the resolution limit in an optical microscope and thus we are unable to observe differences in grain sizes between the differing carbon levels. It is therefore uncertain whether the increases in in-field performance are due to grain size effects, enhancements in H_{c2} , or some combination of the two.

At 20 K the in-field performance is non-monotonic in carbon content and all of the data fall well below that of the 10 weight percent SiC addition to MgB_2 of Dou et al. (82). However, the J_c values for the $x_{il}=0.081$ sample, which showed comparable J_c values to the sample with SiC additions at 5 K, are presumably suppressed due to the reduced temperature (T/T_c) of the measurement. Whereas the sample of Dou et al. had a T_c near 37 K, the $x_{il}=0.081$ sample had a T_c near 30 K. It should also be noted that the SiC samples have been shown to have nanometer sized Mg_2Si and other precipitates imbedded within the MgB_2 matrix (92). It is possible that these Mg_2Si precipitates lead to stronger flux pinning than in the case of the plasma spray powders, where flux pinning is believed to be dominated by grain boundary pinning. Even without extra precipitates, the grain boundary pinning in the plasma spray powders is comparable to the pinning in the sample containing SiC additions of Dou et al., as can be seen by the similar J_c values at 5 K of Dou's sample and those obtained for the $x_{il}=0.081$ sample. It would therefore be desirable to synthesize a sample with an inferred carbon content near $x_i=0.05$, where reduced temperature effects won't limit J_c values at 20 K as much as for the $x_{il}=0.081$ case discussed above.

8.2 Powder In Tube Fabrication

Commercial superconducting wire consists of a set of superconducting strands imbedded within a normal metal matrix. The normal metal serves to provide thermal contact to a cold bath, provide a low resistance path to dump excess current in the event of a quench, and add structural stability in the case of brittle superconducting materials, such as MgB_2 . There are many important considerations when designing practical wires, but the vital first step is to develop techniques for fabricating long length jacketed wire. The fine grain nature and low reaction temperatures required to form $\text{Mg}(\text{B}_{1-x}\text{C}_x)_2$ make the plasma spray synthesized pow-

ders ideally suited for powder-in-tube (PIT) fabrication. In this section, we, in collaboration with our industrial partners, Hyper Tech Research, Inc., fabricate and characterize an initial prototype Fe jacketed wire.

8.2.1 Sample Synthesis

Unreacted powder of nominal carbon concentrations $x_n=0$ and $x_n=0.02$ were sent to Hypertech Inc., where they made jacketed PIT wire using their Continuous Tube Forming Folding (CTFF) process (Figure 8.10a). (For a detailed discussion of the CTFF process see reference (93)). The boron powders were mixed with Mg powder in a stoichiometric ratio of Mg:B 1:2 and wrapped into a cylindrical geometry within an iron jacket. They were then placed in seamless $\text{Cu}_{0.7}\text{Ni}_{0.3}$ tubes and drawn down. A set of samples was reacted at 700 °C, 800 °C, and 900 °C for 30 minutes. These reactions were performed by placing samples into preheated furnaces for the desired time and then removing them and allowing them to cool in air. The final wire consisted of an approximately 500 μm diameter MgB_2 core, 800 μm outer diameter Fe jacket, and 1 mm outer diameter $\text{Cu}_{0.7}\text{Ni}_{0.3}$ sheath (Figure 8.10b). Two additional samples were made using a Hot Isostatic Press (HIP). These wires were reacted at 900 °C for 30 minutes under a pressure of 30 ksi. In order to perform magnetization measurements on all of these Fe jacketed samples, we stripped the Fe by mechanical polishing, forming parallelepipeds of approximate dimensions 5 mm x 0.3 mm x 0.4 mm. Magnetization measurements were performed with the long axis of the parallelepipeds aligned with the applied field.

8.2.2 Results and Discussion

Figure 8.11a plots a comparison of the x-ray (002) and (110) peaks for a pure B PIT wire reacted at 900 °C for 30 minutes and the sample of pure B powder reacted for 48 hours at 1200 °C. The PIT processed wire has broader peaks, whose positions differ slightly from those of the 48 hours at 1200 °C reaction, suggesting that the CTFF process is either introducing some strain or some unknown impurity into the system which is effecting the lattice parameters. Additionally the increased width of the peaks suggests the CTFF processed PIT wires are

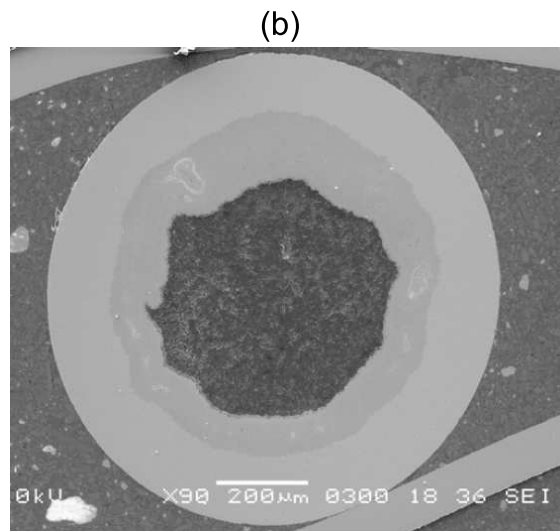
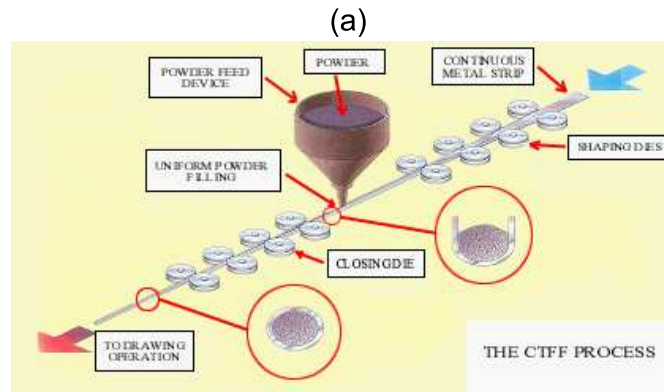


Figure 8.10 (a) Schematic of the CTFF process used by Hyper Tech Research, Inc. for the production of long length PIT MgB_2 wires (93). (b) SEM image of an MgB_2 wire produced by the CTFF process.

more disordered than the powder reacted for 48 hours at 1200 °C.

A comparison of the set of nominal 2% carbon doped PIT wires made by the CTFF process and reacted at various temperatures and powder reacted for 48 hours at 1200 °C is given in figure 8.11b. The 700 °C reaction has poorly defined, broad, weak peaks, suggesting poor reaction. Indexing of the peaks for the entire set reveals a slight decrease in the *a*- lattice parameter as a function of the reaction temperature. Using the *a*- lattice parameter from the pure boron PIT wire reacted at 900 °C for 30 minutes as a standard, the carbon content of the three samples is estimated to be $x=0.048$, 0.051 , and 0.058 for the 700 °C, 800 °C, and 900 °C reactions respectively. These values are considerably lower than those attained on the same powder reacted either for 48 hours at 1200 °C or for 4 hours at 950 °C, where inferred carbon contents were $x=0.074$ and 0.081 , respectively. This suggests that for the case of the PIT wires, the carbon incorporation, which appears to be temperature dependent, is incomplete, even for the 900 °C reaction. It should be noted that it is possible that some of the carbon is being lost to the sheath and the carbon level obtained for the 900 °C reaction represents "full" carbon incorporation. It would be necessary to measure samples reacted at higher temperatures (up to 1200 °C) to test such a hypothesis.

X-ray powder diffraction measurements taken on both pure and carbon doped samples reacted for 30 minutes at 900 °C showed significant amounts of MgB_4 , MgO , and Mg present within the sample (Figure 8.12). Since the samples were prepared in air, rather than under an argon atmosphere within a glove box, there exists some oxygen contamination, which accounts for the presence of MgO . A $\text{Mg}:\text{B}$ molar ratio of 1:2 was used for synthesizing the MgB_2 wires and, therefore, the presence of MgO insures the presence of MgB_4 . That Mg peaks are also present indicates that neither of the reactions were fully driven to completion. Despite the fine grain nature of the starting powders, to ensure full conversion, either the reaction temperature needs to be increased above 900 °C, or the reaction time needs to be extended beyond 30 minutes, or both. Given the temperature dependence of the carbon incorporation, presumably the reaction temperature needs to be increased to at least 950 °C, where full, albeit inhomogeneous, carbon incorporation was observed in the case of pressed pellets.

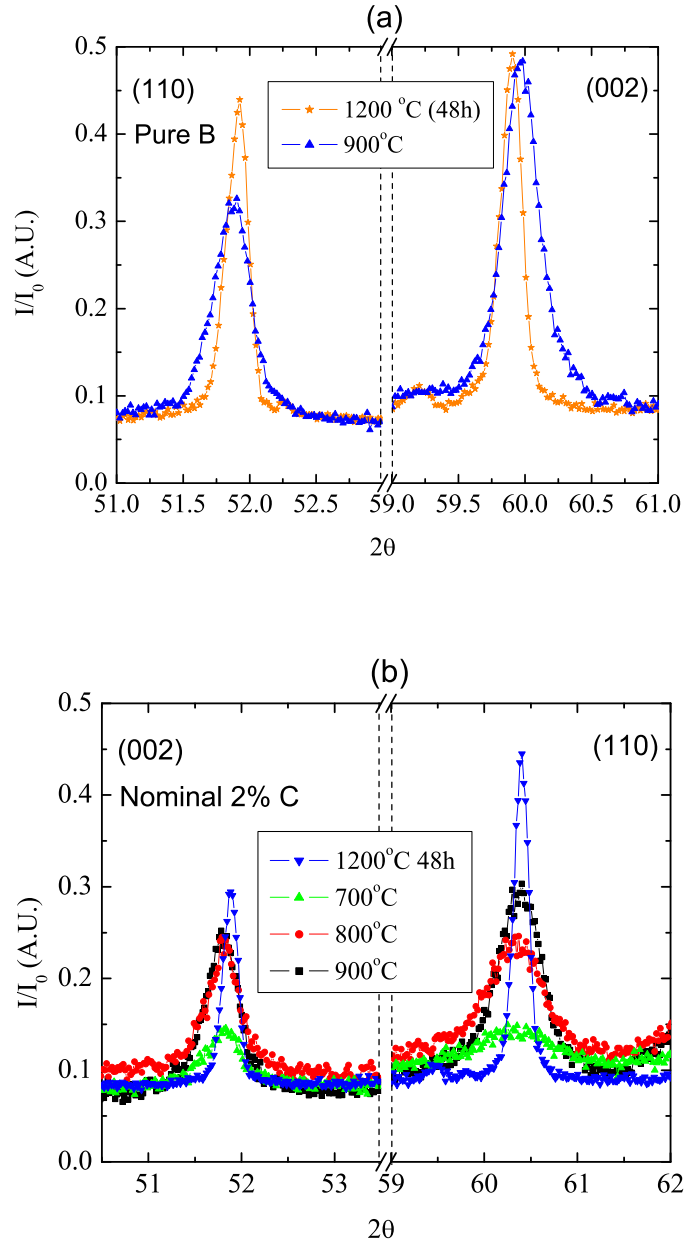


Figure 8.11 (a) Comparison of the x-ray (002) and (110) peaks for PIT wires made from pure B and a sample of the same B reacted for 48 hours at 1200 °C. (b) Comparison of the x-ray (002) and (110) peaks for PIT wires made from nominally 2% carbon doped B and a sample of the same B reacted for 48 hours at 1200 °C.

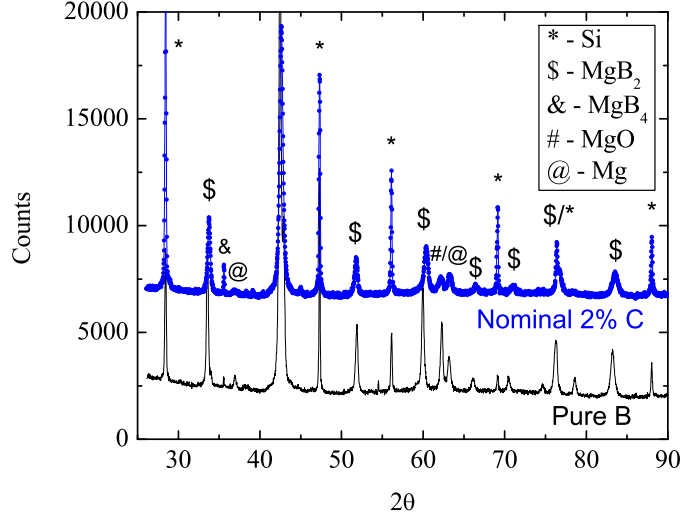


Figure 8.12 Powder x-ray scans for pure and nominal 2% carbon doped PIT wires made using the CTFF process and reacted at 900 °C for 30 minutes.

Magnetization measurements for pure samples reacted for 30 minutes at different temperatures are compared to the 48 hour at 1200 °C reaction in figure 8.13a. All three PIT samples show T_c values near 37 K, more than 1 K below that of the 48 hour at 1200 °C reaction. In addition, both the 700 °C and 800 °C reactions don't show full Meissner screening, indicating incomplete reactions at these temperatures. For the Hyper Tech processed wires, only the 900 °C reaction yields a calculated $4\pi M$ which is consistent with full flux expulsion. Such a calculation does not guarantee full reaction within the sample, as the sample may contain unaccounted for demagnetization factors which lead to artificially high $4\pi M$ values. For example, the measurement on the 48 hour at 1200 °C growth was done on loose powder, which contains a variety of differently shaped samples with differing demagnetization factors, and yielded a $4\pi M$ value far in excess of the applied field.

The reaction temperature independent T_c of the Hyper Tech processed samples suggests that it is additional impurities, which suppress T_c , that are being introduced by the CTFF

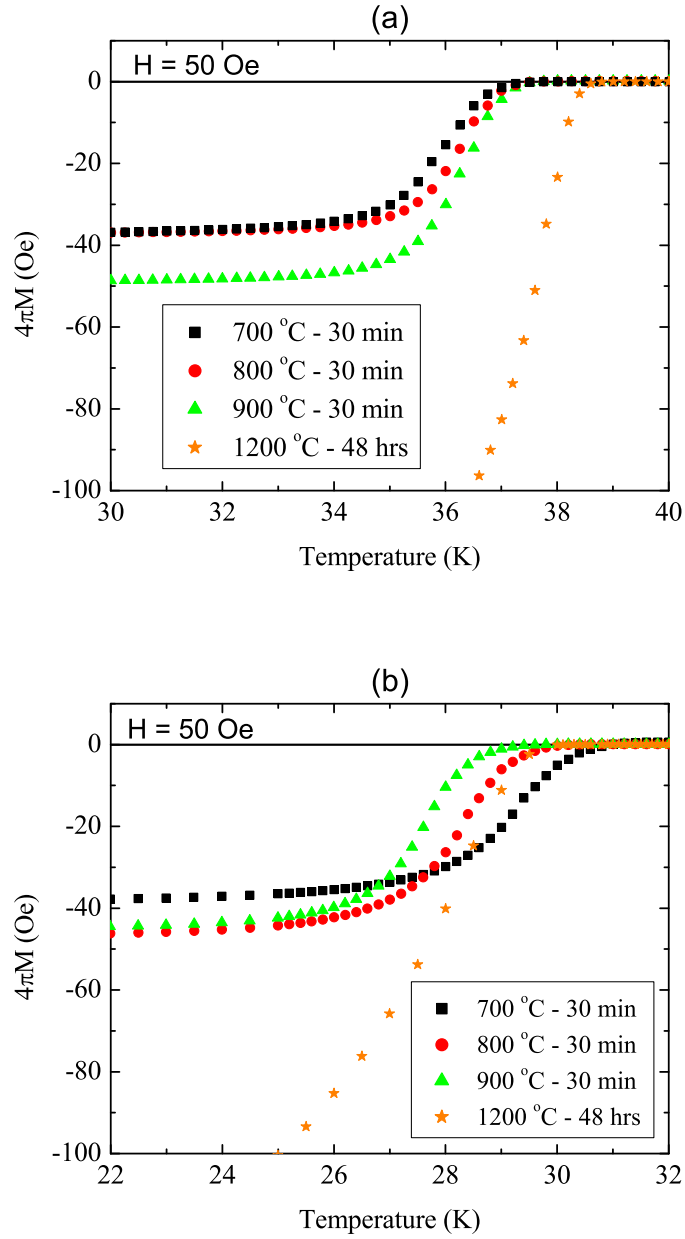


Figure 8.13 (a) Comparison of normalized ZFC magnetic transitions on PIT wires containing pure B and reacted at 700 °C, 800 °C, and 900 °C, with a sample of the same B reacted for 48 hours at 1200 °C. (b) - Similar comparison for samples made with nominally 2% carbon doped B as the starting material.

process. Had the suppression been the result of some type of strain induced by the wire drawing process, increased reaction temperatures should have relieved more of the strain, resulting in a systematic increase in T_c as a function of the reaction temperature. No such behavior was observed.

For the series of wires made with nominally 2% carbon doped powders, the transition temperature depends upon the reaction temperature (Figure 8.13b). T_c monotonically decreases as the reaction temperature is increased from 700 °C to 900 °C. Such behavior supports the notion that the amount of carbon incorporated within the structure depends upon the reaction temperature. That T_c for the 900 °C, 30 minute reaction is below that of the 48 hour at 1200 °C reaction, is presumably a result of the additional, as of yet unknown, impurities introduced during the CTFF process. Impurities which lower T_c in pure MgB_2 have been shown to suppress T_c in carbon doped samples as well (94). Additionally, none of these samples exhibit full flux expulsion. The x-ray data, superconducting transition temperatures, and calculated $4\pi M$ values all indicate that the samples are not fully reacted and have incomplete carbon incorporation. Plotting T_c as a function of Δa shows how the manifold associated with the carbon doped PIT wires is dramatically suppressed relative to the high purity fibers discussed in chapter 5 (Figure 8.14).

A Back Scatter Electron (BSE) image of the nominal 2% carbon doped PIT wire reacted for 30 minutes at 900 °C shows alternating regions of light and dark (Figure 8.15a). Typically in BSE images, such contrast is a result of changes in atomic densities, i.e. z-contrast, which would indicate alternating regions of MgB_2 and MgB_4 . Although the x-ray spectra indicate that MgB_4 is present (Figure 8.12), an Energy Dispersive Spectroscopy (EDS) X-ray line scan shows simultaneous dips in the boron and Mg counts (Figure 8.15b). It is therefore likely that the contrast observed in the BSE image is partially a result in changes in density, indicating a high level of porosity within the sample.

To improve the density of the PIT wires, a pure and a nominally 2% carbon doped PIT wire were reacted in a hot isostatic press. In order to react the filaments, unreacted Fe/CuNi jacketed wires, approximately 5 cm in length, were welded under an argon atmosphere into a

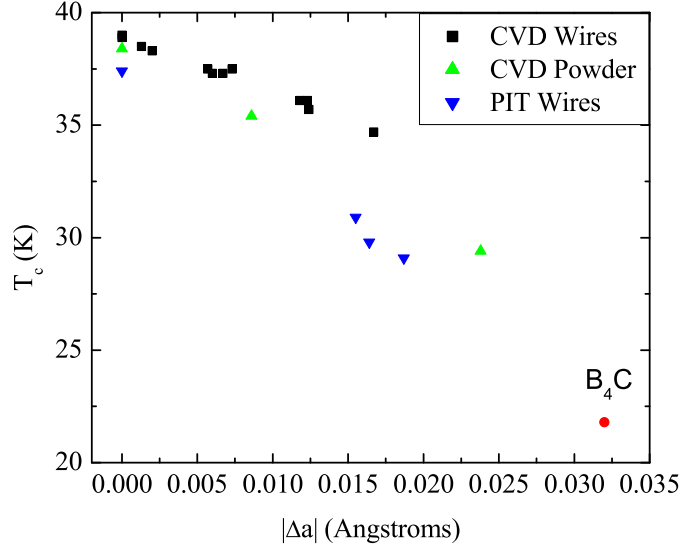
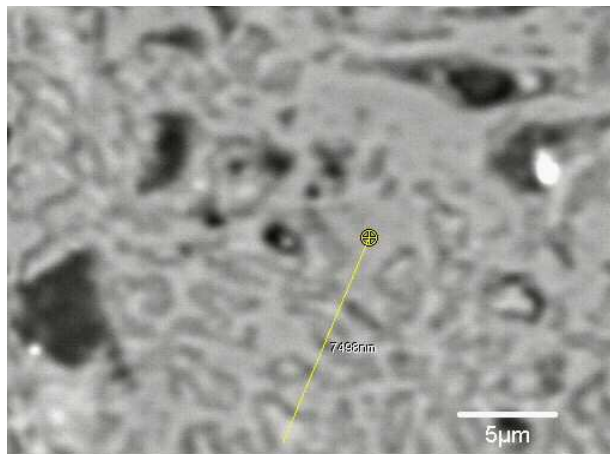


Figure 8.14 T_c versus $|\Delta a|$ for high purity CVD wires (86), plasma spray powders (84), and PIT wires. Data for the sample made from B_4C is from reference (60). The downward shift of the manifold associated with the PIT wires indicates the CTFF process is introducing impurities which are causing an additive suppression to T_c .

copper tube with inner diameter 1.2 mm, and outer diameter 3.0 mm. Figure 8.16 shows the temperature and pressure profiles for the reaction. It should be noted that, while the reaction is nominally 900 °C for 30 minutes, since MgB_2 is believed to form above the melting point of Mg, 650 °C, the ramp up and cool down times for the furnace will have some effect on the growth characteristics of the samples.

Magnetization measurements on the HIP samples again show incomplete Meissner screening, indicating the reactions are presumably incomplete (Figure 8.17). Included in figure 8.17 are the curves for the same starting materials reacted for 30 minutes at 900 °C. The two pure samples exhibit virtually identical superconducting onset temperatures. In the case of the nominally 2% carbon doped PIT wires, the HIP sample has a T_c which is approximately 0.5 K less than the isothermally reacted sample. That there was no difference in T_c for the pure

(a)



(b)

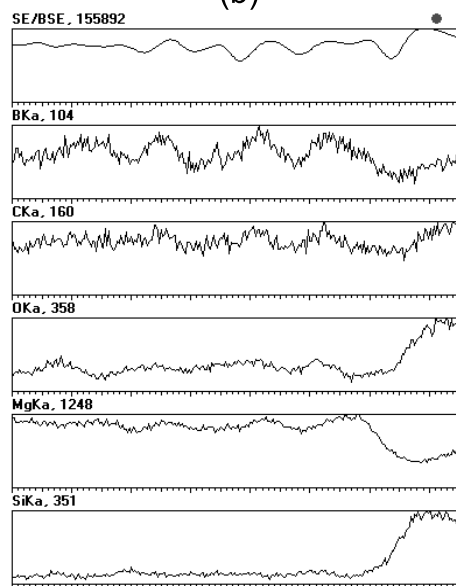


Figure 8.15 (a) BSE image of a nominal 2% carbon doped PIT wire reacted for 30 minutes at 900 °C. (b) EDS line scan from image in (a).

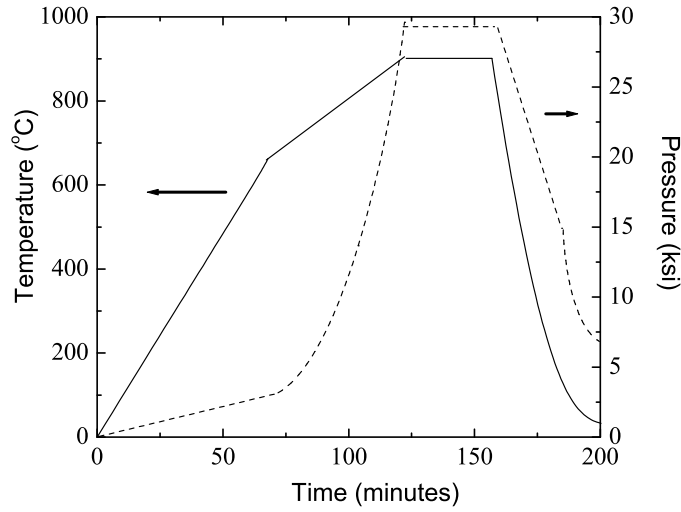


Figure 8.16 Temperature and pressure profiles for reaction pure and nominally 2% carbon doped powder-in-tube wires in a hot isostatic press.

sample and a decrease for the carbon doped sample suggests that more of the carbon has been incorporated into the structure by the HIP reaction profile.

Critical current densities inferred from magnetization measurements for MgB_2 pellets, PIT wires, and HIPed PIT wires made from the plasma spray powders are plotted in figure 8.18. Figure 8.18a shows 5 K and 20 K data for samples made using the pure B plasma spray powders, and figure 8.18b contains the 5 K data for samples made with the nominally 2% carbon doped boron.

In the case of the pure MgB_2 samples, all of the PIT processed wires exhibited improved in-field critical current densities, at both 5 K and 20 K, relative to a pressed pellet reacted for 4 hours at 950 °C. Within the set of PIT wires, the samples reacted at 800 °C and 900 °C, which had comparable $J_c(H)$ values, were approximately a factor of two higher at all fields than the sample reacted at 700 °C. Using the HIP treatment extended the field range at which J_c was in excess of 10^5 A/cm^2 at 5 K from near 4 T in the case of the 900 °C reaction to approximately 5 T. Similar enhancements in the in-field performance was also seen for 20 K

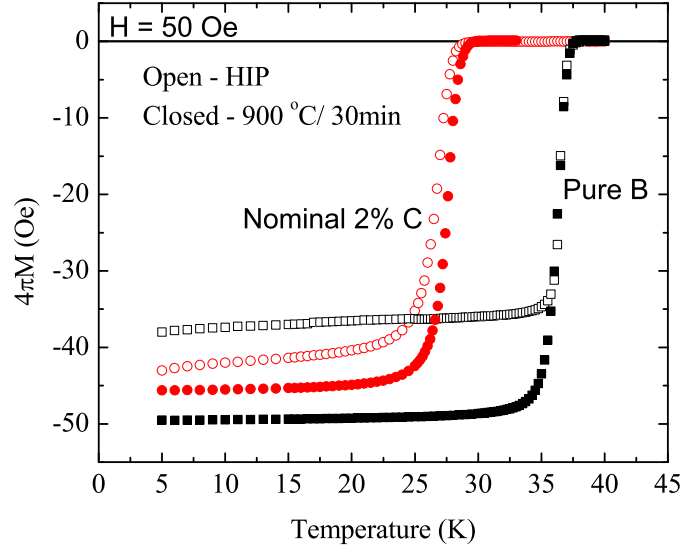


Figure 8.17 Zero field magnetization curves for PIT wires reacted either isothermally or in a hot isostatic press.

data. In-field increases in critical current densities for HIPed samples have been attributed to increases in flux pinning resulting from the introduction of a high density of structural defects caused by high temperature deformation during the HIP process (95).

J_c data for the nominally 2% carbon doped samples was only taken at 5 K, as differences in T_c for the various samples will manifest themselves as differences in J_c values at 20 K due to reduced temperature (T/T_c) effects. For these samples, the pressed pellet reacted for 4 hours at 950 °C shows the best performance in all fields. Amongst the PIT wires, there is a monotonic increase in in-field J_c values with reaction temperature. Once again the HIP sample shows an improvement in high field J_c values, relative to other PIT samples.

Thus for pure MgB_2 samples, PIT wires manufactured using the CTFF process yielded the highest J_c values, whereas for the nominally 2% carbon doped samples, J_c values for PIT wires all fell at least a factor of 5 below those of a pressed pellet. That the carbon doped PIT wires under performed relative to the pressed pellet is perhaps not surprising. All of the data on the carbon doped PIT wires suggest incomplete reactions, which would lead to

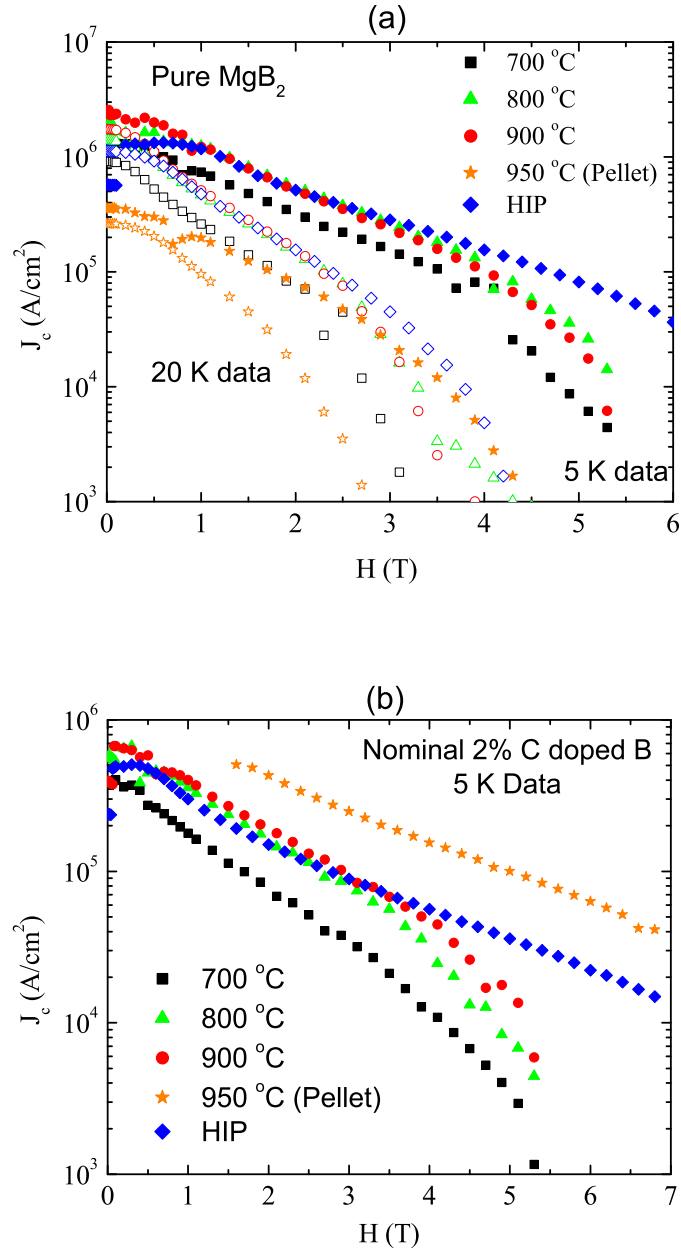


Figure 8.18 Critical current densities for the PIT wires, HIPed PIT wires, and pressed pellets.

decreases in effective cross sections and diminish current carrying capability. More surprising, though, is that the pure MgB_2 PIT wires, which also showed evidence of not being fully reacted, outperformed the pressed pellet. It is possible that in the case of the pure MgB_2 samples, whose grain sizes are highly sensitive to reaction temperature, the higher reaction temperature of the pressed pellet lead to larger grain sizes and was thus responsible for the lower J_c values. As stated previously however, the grain sizes in these powders are below the resolution limit in an optical microscope and other, more sophisticated techniques, would be necessary to definitively determine if such a relationship between reaction temperature and grain size exists in these samples. Such an explanation would also require that there exists some interplay between grain size and connectivity which conspired to yield nearly identical J_c values for the 800 °C and 900 °C reacted PIT wires. More work is necessary to understand these interconnected issues so as to optimize critical current densities in PIT wires.

It is worth noting that for the two HIPed wires, whereas the pure MgB_2 wire carried in excess of 10^5 A/cm² in fields up to near 5 T at 5 K, the nominally 2% carbon doped wire could maintain such a level only in fields up to 3 T. Thus, in spite of the fact that fully reacted samples made from the carbon doped powder have significantly enhanced upper critical field values, with $H_{c2}(T=0)$ in excess of 35T (84), the in-field performance of the PIT carbon doped wires is significantly worse than pure MgB_2 wires manufactured in the same manner.

In the case of the carbon doped MgB_2 wires, alternative approaches to the PIT wire fabrication need to be explored. First and foremost, the carbon level needs to be reduced, such the T_c is near 35 K, which would allow operation near 20 K. Secondly, to ensure complete reaction for carbon doped samples, it may be necessary to use ex-situ processing. To enhance flux pinning in these samples it may be necessary to introduce additional impurities, such as Ti. Additionally, the cause of the 1 K suppression resulting from the CTFF processing needs to be determined and eliminated, as such a suppression in T_c may profoundly impact J_c values at 20 K.

CHAPTER 9. Superconducting and Normal State Properties of Neutron Irradiated MgB₂

In addition to chemically doping a compound, damaging or disordering of the sample using protons, heavy ions, neutrons, etc., is another route to systematically changing the system. Of these possible routes, neutron irradiation offers the best avenue for uniformly damaging bulk MgB₂. There are two main sources of damage from neutron irradiation of MgB₂. First, fast neutrons deposit energy through inelastic collisions with atoms, creating thermal and dislocation spikes (96). Second, ¹⁰B has a large capture cross section for thermal neutrons ($3.87 \times 10^{-21} \text{ cm}^2$) and readily absorbs these thermal neutrons, subsequently α decaying to ⁷Li. Early neutron damage studies focused on irradiation of powders or pressed pellets of MgB₂ containing natural boron (62; 97; 98; 99).

The absorption of slow neutrons by ¹⁰B leads to self shielding and prevents uniform damage in bulk MgB₂ samples significantly larger than the penetration depth. Under the assumption of linear absorption, the intensity of the incident beam decreases exponentially within the sample, and is given by (68):

$$I(t) = I_0 \exp(-t\sigma N) \quad (9.1)$$

where I_0 is the initial intensity, t is the sample depth, σ is the absorption cross section, and N is the number density of atoms. Here, N corresponds to the number of ¹⁰B atoms per cm³. A calculation of the half depth in MgB₂ synthesized from natural boron, which consists of 19.9% ¹⁰B, yields a depth of approximately 130 μm . Samples with dimensions significantly larger than 130 μm will contain substantial gradients of damage associated with slow neutron absorption. Therefore several different approaches have been employed to minimize neutron

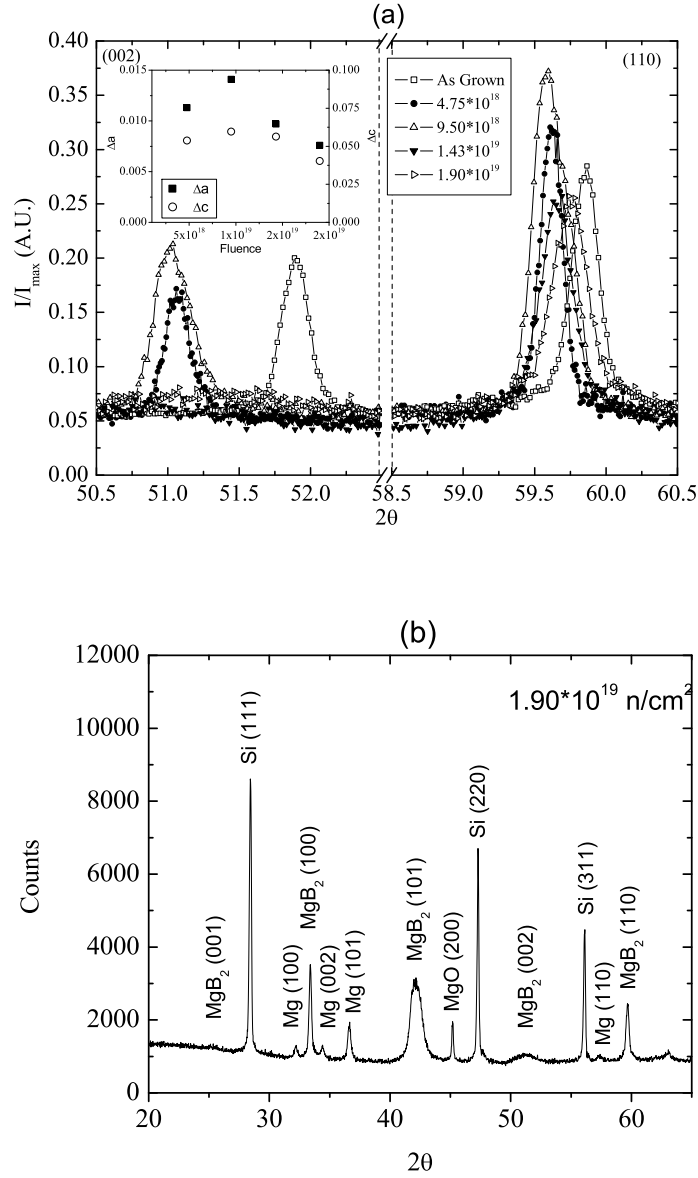


Figure 9.1 (a) (002) and (110) X-ray peaks for un-damaged, 4.75×10^{18} , 9.50×10^{18} , 1.43×10^{19} , and 1.90×10^{19} n/cm² fluence as-damaged samples. The highest two fluence levels show a broadened (002) peak indicating a decrease in order along the c-axis. The inset shows the relative shift of the a- and c- lattice parameters as a function of fluence level. (b) The fuller diffraction pattern of the as-damaged 1.90×10^{19} n/cm² fluence level sample. On this fuller range the broadened (002) peak is clearly visible.

capture, ensuring homogeneous damage throughout bulk samples. Thermal neutrons have been blocked by a cadmium shield (97; 100; 101) or the natural boron has been replaced with isotopically enriched ^{11}B (102; 103).

An alternate approach is to damage MgB_2 objects with characteristic dimensions comparable to or smaller than $130\text{ }\mu\text{m}$. In this case natural boron can be used and relatively homogeneous absorption of slow neutrons can be assumed. In this paper we report on the isotropic irradiation of fully dense, $140\text{ }\mu\text{m}$ diameter, MgB_2 wires with both thermal and fast neutrons. Although these fibers contain natural boron, they were exposed to an isotropic fluence and had sample dimensions comparable to the penetration length, implying the defect structure should be fairly uniform throughout the samples. Table 4.2 in the experimental methods section (chapter 4) gives the fluence levels and estimated percentages of ^{10}B transmuted to ^7Li for the four different exposure times used in this study.

9.1 Fluence and Annealing Studies

Normal state and superconducting properties were found to be a function of fluence, annealing time, and annealing temperature. We present the data in the following order: (a) structural studies on as-damaged wires, (b) 24 hour anneals at varying temperatures for a fluence of $4.75 \times 10^{18}\text{ n/cm}^2$, (c) Variable time anneals for a fluence of $4.75 \times 10^{18}\text{ n/cm}^2$, (d) 24 hour anneals for all measured fluence levels, and (e) 1000 hour anneals on all four fluence levels.

9.1.1 Structural Studies of As Damaged Samples

The x-ray (002) and (110) peaks for an un-damaged wire and the entire set of as-damaged samples are plotted in Figure 9.1a. The lowest exposure level, $4.75 \times 10^{18}\text{ n/cm}^2$, shows an anisotropic expansion of the unit cell. The a- lattice parameter increases from $3.0876(5)\text{ }\text{\AA}$ in the un-damaged sample to $3.0989(2)\text{ }\text{\AA}$, an increase of $0.0113(7)\text{ }\text{\AA}$ or 0.37%. The c- lattice parameter increases from $3.5209(7)\text{ }\text{\AA}$ to $3.5747(2)\text{ }\text{\AA}$, an increase of $0.0538(9)\text{ }\text{\AA}$ or 1.02%. Similar anisotropic expansion of the unit cell was seen by Karkin et. al. (62). The authors

report lattice parameter increases of $\Delta a = 0.0075 \text{ \AA}$ or 0.24% and $\Delta c = 0.0317 \text{ \AA}$ or 0.9% for a fluence of $1 \times 10^{19} \text{ n/cm}^2$ thermal neutrons and $5 \times 10^{18} \text{ n/cm}^2$ fast neutrons. For irradiation of isotopically enriched Mg^{11}B_2 , little change was seen in the a- lattice parameter up to a fluence level of 10^{17} n/cm^2 (102). For this fluence level the authors report a 0.008 \AA or 0.23% increase in the c- lattice parameter relative to an undamaged sample. Due to the large differences in Δa and Δc reported for different irradiation conditions, we performed systematic study of the lattice parameters as a function of fluence level, annealing temperature, and annealing time for samples all prepared in the same manner.

Relative to the $4.75 \times 10^{18} \text{ n/cm}^2$ fluence level, filaments exposed to a fluence of $9.50 \times 10^{18} \text{ n/cm}^2$ show a further expansion of the unit cell, with the a- and c-lattice parameters reaching $3.1017(7) \text{ \AA}$ and $3.5805(10) \text{ \AA}$, respectively. The response to further increases in exposure qualitatively changes. For an exposure level of $1.43 \times 10^{19} \text{ n/cm}^2$ the (002) peak broadens substantially and the a- and c- lattice parameters contract relative to the samples exposed to the $9.50 \times 10^{18} \text{ n/cm}^2$ fluence level. Increasing the fluence further to $1.90 \times 10^{19} \text{ n/cm}^2$ results in a further contraction of both the a- and c- lattice parameters with the (002) remaining broad. The x-ray scan for the as-damaged, $1.90 \times 10^{19} \text{ n/cm}^2$ fluence level sample, from $2\theta = 20\text{--}65^\circ$ is plotted in figure 9.1b. The peak widths for the MgB_2 (hk0) peaks are within a factor of two of the widths for neighboring Si peaks, whereas the MgB_2 (001) peak is not resolvable and the (002) peak is more than five times as broad as the Si peaks. It should be noted that in pure, undamaged MgB_2 all x-ray peaks have full width at half maximum (FWHM) values comparable to those of the Si standard. For example, the peaks used to determine the lattice parameters in the undamaged wires used in this study, the (002) and (110), had FWHM values of 0.216° and 0.221° respectively. The neighboring Si peak, the (311) peak which occurs at $56.110^\circ 2\theta$, had a FWHM of 0.190° .

In the case of a fluence level of $1.90 \times 10^{19} \text{ n/cm}^2$, the MgB_2 (100) peak, occurring at $2\theta = 33.397^\circ$ has a full FWHM of 0.216° , in comparison to the FWHM of 0.180° for the Si (111) peak at $2\theta = 28.422^\circ$. Similarly the MgB_2 (110) and Si (311), which occur at 59.686° and $56.110^\circ 2\theta$, had FWHM values of 0.291° and 0.163° respectively. In contrast, the MgB_2 (002)

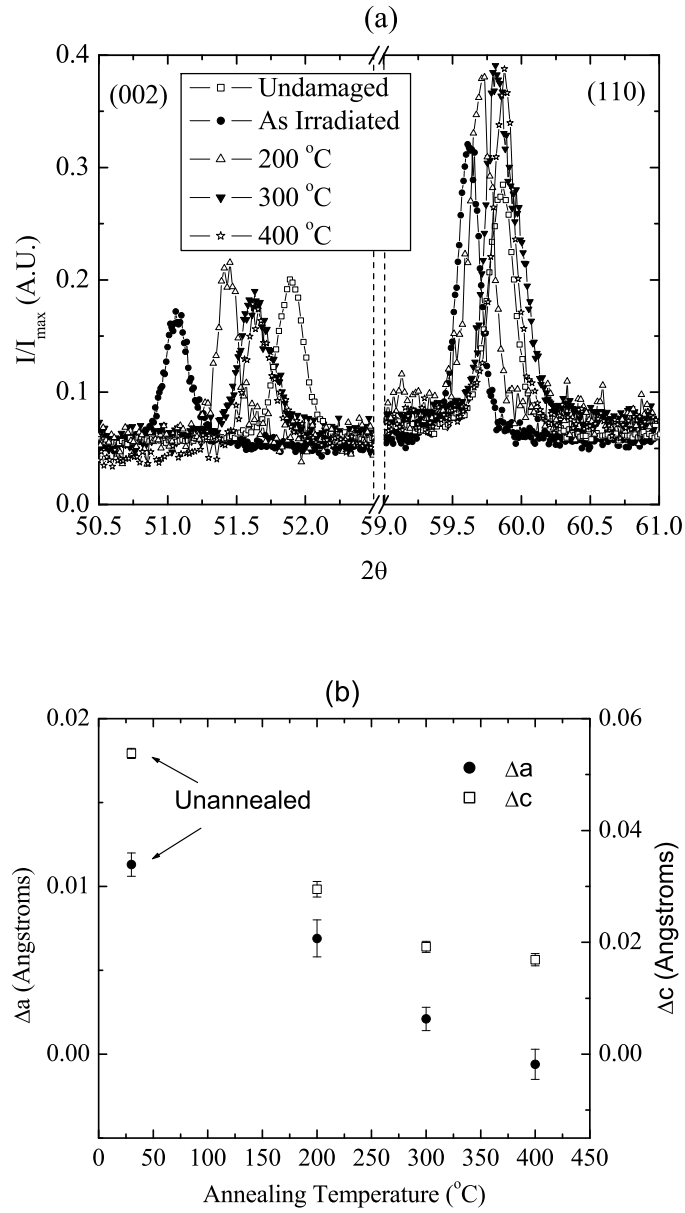


Figure 9.2 (a) (002) and (110) x-ray peaks used to determine the a- and c-lattice parameters for the set of 24 hour anneals on samples exposed to a fluence of 4.75×10^{18} n/cm². (b) The evolution of the lattice parameters as a function of annealing temperature. Closed symbols represent Δa , and open symbols are Δc .

peak has a FWHM of 1.335° . The resultant correlation lengths, given by $\Delta 2\theta = \lambda/d \cdot \cos(\theta)$, are approximately 4000 Å in the plane and 700 Å along the c-direction. The mixed (101) peak has a FWHM of 1.045° and a correlation length near 1000 Å, values intermediate between the two extrema. The two highest fluence levels have resulted in an anisotropic change in the correlation length, with a decrease in long range order between the boron planes. Since the (002) peak has substantially broadened for higher fluence levels, tracking the trend in Δc becomes harder due to the inherent decrease in accurately defining peak position.

9.1.2 24 Hour Anneals of Samples Exposed to a Fluence of $4.75 \cdot 10^{18}$ n/cm²

As-damaged samples showed a suppression of T_c to below 5 K. This is a much larger suppression than seen upon irradiating Mg^{11}B_2 (102): the authors report a T_c of 12.2 K for a fluence of $3.9 \cdot 10^{19}$ n/cm². Irradiation of MgB_2 , i.e. with natural boron, using a fast neutron fluence of $2 \cdot 10^{18}$ n/cm² gave a T_c of 30.2 K (98). Thus damage induced via neutron capture and subsequent alpha decay appears to play a significant role in suppressing superconductivity. To further investigate the effects of uniform irradiation on samples containing natural boron we have performed a systematic study of the normal state and superconducting properties as a function of annealing temperature for samples annealed for 24 hours.

We annealed a set of wires, exposed to a fluence of $4.75 \cdot 10^{18}$ n/cm², for 24 hours at 100 °C, 150 °C, 200 °C, 300 °C, 400 °C, and 500 °C. X-ray measurements indicate the initial expansion of the unit cell could be systematically reversed by subsequent annealing (Figure 9.2), with the Δa and Δc values decreasing with increasing annealing temperature (Figure 9.2b). The a-lattice parameters is completely restored after annealing at 400 °C whereas the c- lattice parameter appears to be saturating at a value near 0.6% larger than that of the undamaged sample.

The superconducting transition temperatures were determined using a 1% screening criteria in zero field cooled DC magnetization measurements (Figure 9.3a) and an onset criteria in resistivity versus temperature measurements (Figure 9.3b). The magnetic transitions for the entire set are fairly sharp, typically achieving 95% of the saturated value 2.5 K below the 1%

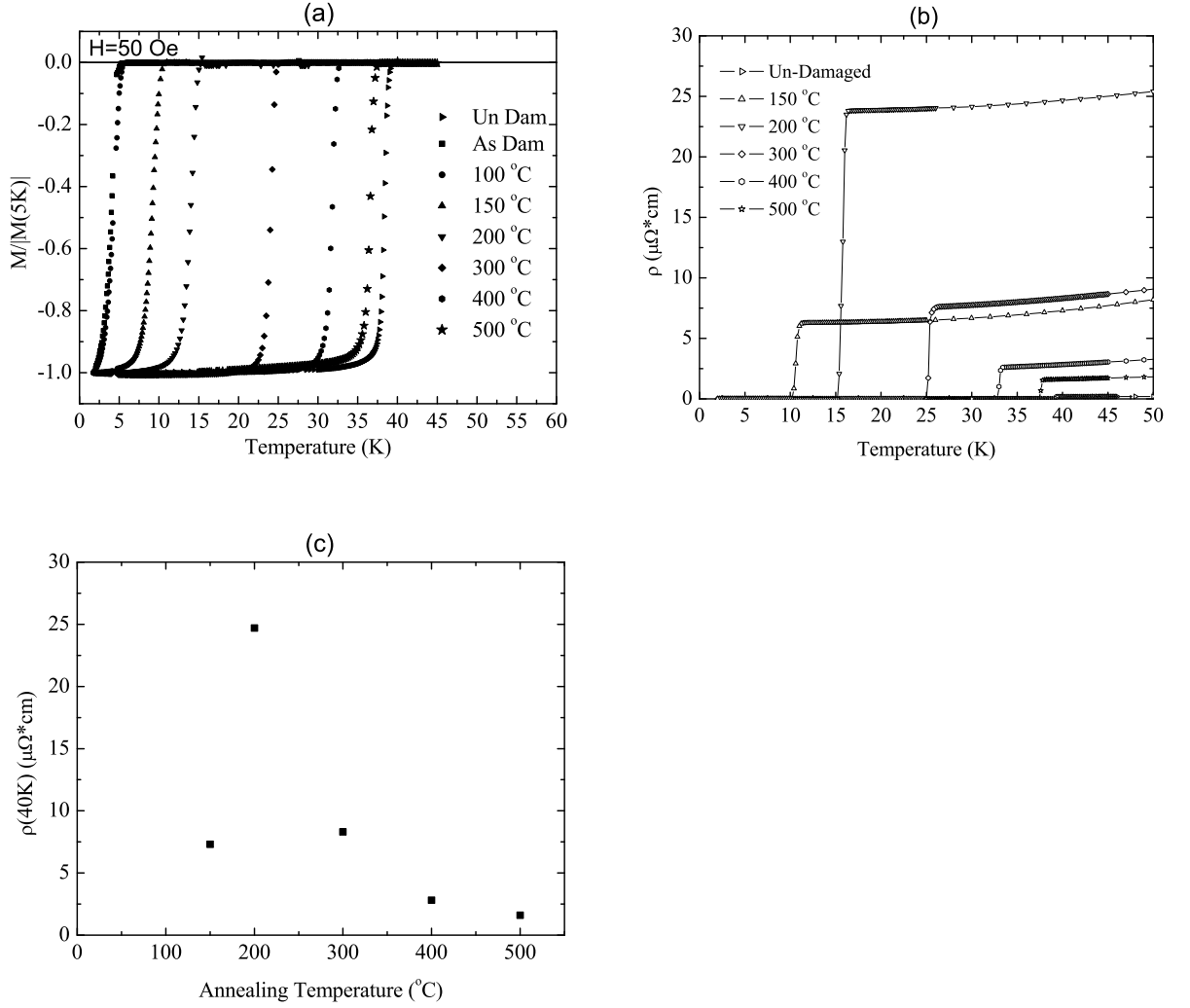


Figure 9.3 (a) Normalized magnetization and (b) resistivity curves for the set of 24 hour anneals on samples exposed to a fluence of $4.75 \times 10^{18} \text{ n/cm}^2$. (c) The normal state resistivity at 40 K. The resistivity shows a sharp increase at an annealing temperature of 200 °C, then decreases approximately exponentially as a function of annealing temperature.

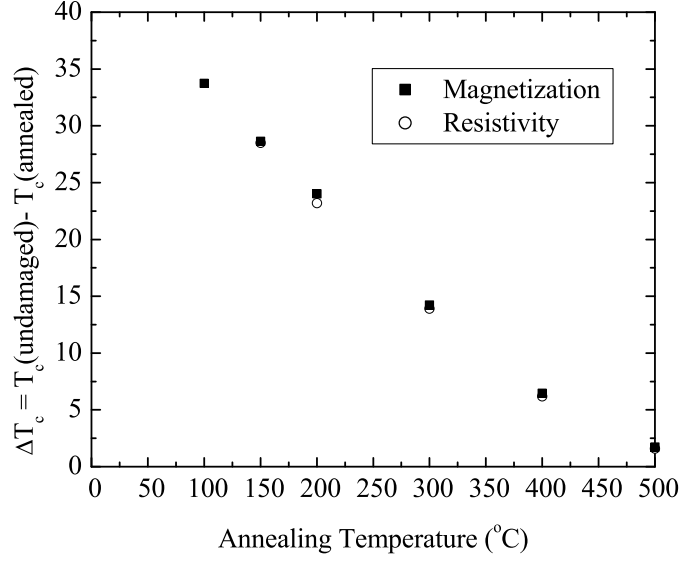


Figure 9.4 Restoration of superconductivity by post exposure annealing for samples exposed to a fluence of 4.75×10^{18} n/cm² and subsequently annealed for 24 hours at various temperatures. Transition temperatures were determined using a 1% screening criteria in magnetization and an onset criteria in resistivity. Annealing at 500 °C yields a T_c near 37.5 K, less than 2 K below that of the undamaged sample.

criteria used for T_c . This suggests a relatively homogeneous damaging of the sample. We were unable to obtain reliable transport measurements on as damaged as well as the 100 °C annealed samples due to the 120 °C temperature required to cure the silver epoxy contacts. The 30 minute 120 °C cure of the epoxy, as well as the possible exotherm associated with the epoxy curing, placed the sample into a poorly defined annealed state. As shown in figures 9.3a and 9.3b, superconductivity is restored by the annealing process. ΔT_c , defined as the difference between the undamaged T_c and that of the annealed sample, monotonically approaches zero as the annealing temperature is increased (Figure 9.4).

The zero field temperature dependent resistivity data are plotted in figure 9.3b. The sample annealed at 150 °C has a low temperature normal state resistivity slightly above $6 \mu\Omega \cdot \text{cm}$,

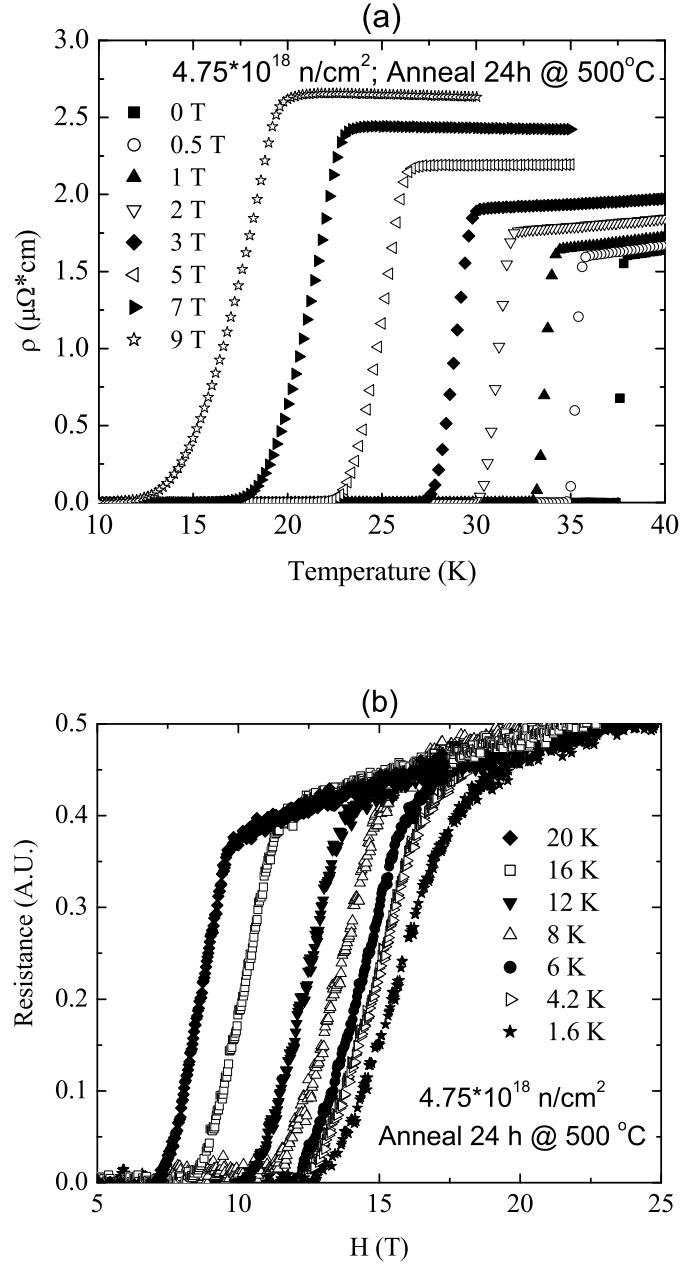


Figure 9.5 Transport measurements on a sample exposed to a fluence $4.75 \times 10^{18} \text{ n/cm}^2$ and annealed at 500°C for 24 hours. H_{c2} values were determined using an onset criteria in both (a) resistivity versus temperature and (b) resistance versus field.

which is an order of magnitude larger than the undamaged value of $0.2 \mu\Omega\cdot\text{cm}$. After annealing at a temperature of 200°C , ρ increases by another four fold. Further increases in the annealing temperature result in a monotonic decrease of the normal state resistivity, to $1.6 \mu\Omega\cdot\text{cm}$ at an annealing temperature of 500°C . This increase in ρ at 200°C is thought to be a real effect, as it also manifests itself in normalized $\rho/\rho(300\text{ K})$ plots, indicating it is not associated with a pathologic geometric problem such as cracks. The initial annealing may result in a change in the defect structure. For example, vacancies don't necessarily immediately recombine with interstitials to eliminate defects. Vacancies can initially cluster together to form higher order defects, which can be relatively stable (96). Thus the initial increase in resistivity may result from a reorganization of defects into higher order clusters which may enhance scattering. It is worth noting though, that whereas there is a very non-monotonic evolution of ρ_0 with annealing temperature, ΔT_c varies smoothly from $\Delta T_{\text{anneal}}=100^\circ\text{C}$ to $T_{\text{anneal}}=500^\circ\text{C}$ (Figure 9.4).

The upper critical field was determined using an onset criteria in resistivity versus temperature in applied fields up to 14 T (a representative set is shown in figure 9.5a) and, in the case of the 500°C anneal, resistance versus field sweeps up to 32.5 T (Figure 9.5b). The upper critical field curves form a sort of Russian doll pattern with $H_{c2}(T=0)$ approximately scaling with T_c (Figure 9.6). The curves for samples annealed at temperatures up to 200°C do not show any positive curvature near T_c and are qualitatively similar to single gap superconductors with Werthamer, Helfand, and Hohenberg (WHH) (33) like behavior. Experimentally determined $H_{c2}(T=0)$ values for the 150°C , 200°C , and 300°C anneals are 2.9 T, 4.7 T, and 7.3 T respectively. Using the formula $H_{c2}(T=0)=0.69T_c dH_{c2}/dT$ we obtain estimates of 2.9 T, 4.3 T and 5.9 T. Thus whereas only in the cases of the 150°C and 200°C anneals can we fit $H_{c2}(T)$ with WHH behavior, the deviations increase with the annealing temperature, suggesting that the bands may become fully mixed only when T_c is suppressed to near 10 K. The 300°C , 400°C , and 500°C anneals exhibit positive curvature near T_c that is similar to what is found in pure MgB_2 . The 500°C anneal data show that either the undamaged $H_{c2}(T)$ is restored or that there is a slight increase in $H_{c2}(T=0)$, rising from approximately 16 T in the undamaged case to near 18 T.

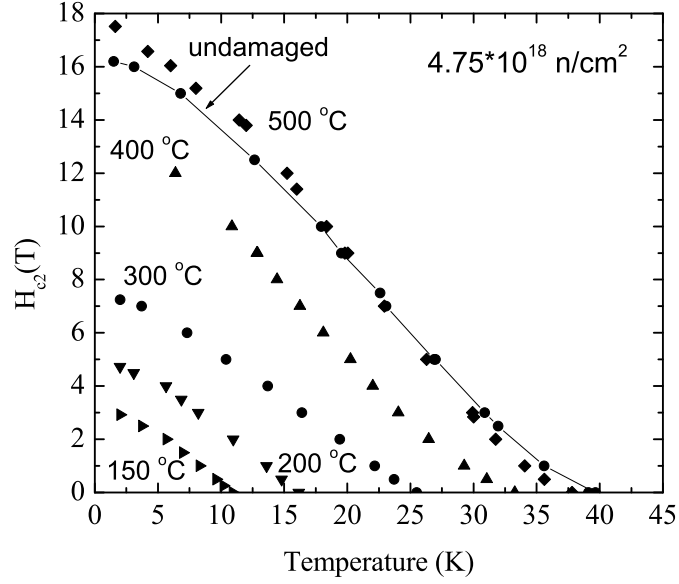


Figure 9.6 Upper critical field curves for undamaged as well as for samples exposed to a fluence of $4.75 \times 10^{18} \text{ n/cm}^2$ and annealed at 150, 200, 300, 400, and 500°C for 24 hours.

This behavior in H_{c2} differs from other types of neutron damaging studies. For the case of irradiating isotopically enriched Mg^{11}B_2 , Putti et. al found a fairly substantial increase in H_{c2} values when T_c was in the 36-38 K range (100). For a sample with $T_c = 36.1 \text{ K}$, they report $H_{c2}(T=12\text{K})$ of 20.3 T. For unshielded irradiation of MgB_2 containing natural boron, Eisterer et. al reported that, relative to an undamaged sample with a T_c just below 38 K, a sample with a suppressed T_c of approximately 36 K had a near doubling of the slope dH_{c2}/dT in the linear regime above 2 T (97). In both of these cases the fluences used were an order of magnitude lower than in our experiment and no post exposure annealing was performed.

Figure 9.7 presents the critical current densities for the series of 24 hour anneals at 5 K and 20 K as determined by the Bean critical state model (34) from magnetic hysteresis loops. At both 5 K and 20 K, J_c is suppressed for samples annealed at 300°C and below, presumably due to the larger reduced temperature (T/T_c) of the measurements. In field J_c values become

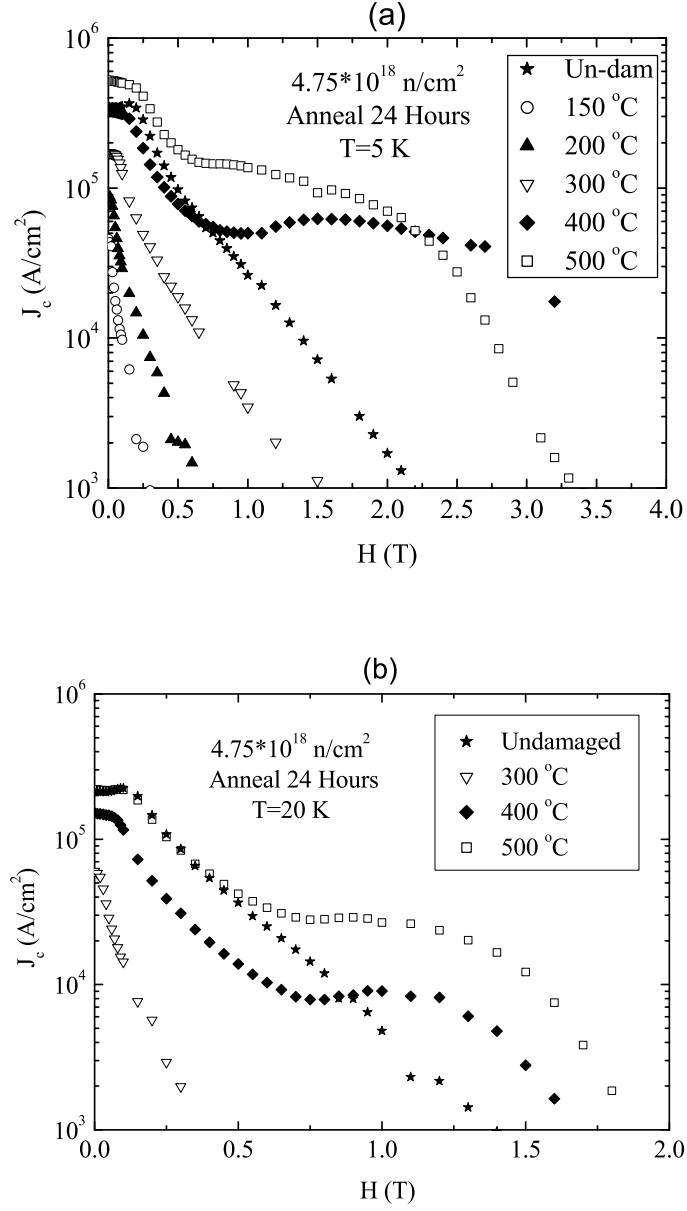


Figure 9.7 Critical current densities as a function of field at (a) 5 K and (b) 20 K for samples irradiated with a fluence of 4.75×10^{18} n/cm² and subsequently annealed for 24 hours at various temperatures.

enhanced at both 5 K and 20 K for the 400 °C and 500 °C anneals, and show a slight fish-tail or second peak behavior. The fish tail effect has been seen in fast neutron irradiation of MgB₂ single crystals (99). The authors report a second peak in the magnetization hysteresis loops for H_⊥ab, which became more pronounced with increasing fluence up to 4*10¹⁹ n/cm². No such behavior was observed for H_{||}ab. Low level thermal neutron fluence, of order 10¹⁴-10¹⁵ n/cm², of polycrystalline MgB₂ showed an enhancement in flux pinning, but no second peak or fishtail behavior (98). The infield enhancement of J_c for the sample annealed at 500 °C pushes the point at which J_c crosses 10⁴ A/cm² at 20 K out to near 1.5 T. This increase in field roughly doubles the crossing point of the undamaged wire, but falls well below best reports in literature of 10⁴ A/cm² at near 5 T reported for 10 weight percent addition of SiC to MgB₂ (82).

9.1.3 Variable Time Anneals on Samples Exposed to a Fluence of 4.75*10¹⁸ n/cm²

The annealing time for the set of 4.75*10¹⁸ n/cm² fluence samples was varied to further probe the characteristics of damage induced by neutron irradiation. An extensive set of anneals was carried out at 300 °C, consisting of 0.33, 1, 3, 6, 24, 96, and 1000 hours. For annealing temperatures of 200 °C and 400 °C, measurements were done on 1, 24, and 96 hour anneals. Two anneals were performed at 500 °C, one for 24 hours and the other for 1000 hours.

The magnetic transitions for the entire set of samples annealed at 300 °C are shown in figure 9.8. Annealing at this temperature for only 0.33 hours raised T_c from below 5 K to slightly above 19 K. Therefore, the defects causing the suppression of superconductivity must have a fairly low activation energy. For defects which can be annealed by a single activated process with a constant activation energy, the rate of change of the defect concentration is given by (96):

$$dn/dt = -F(n)K_0e^{-E_a/k_BT} \quad (9.2)$$

where n is the defect concentration, F(n) is some continuous function of n, K₀ is a constant, E_a is the activation energy, k_B is Boltzman's constant, and T is the temperature. If we assume

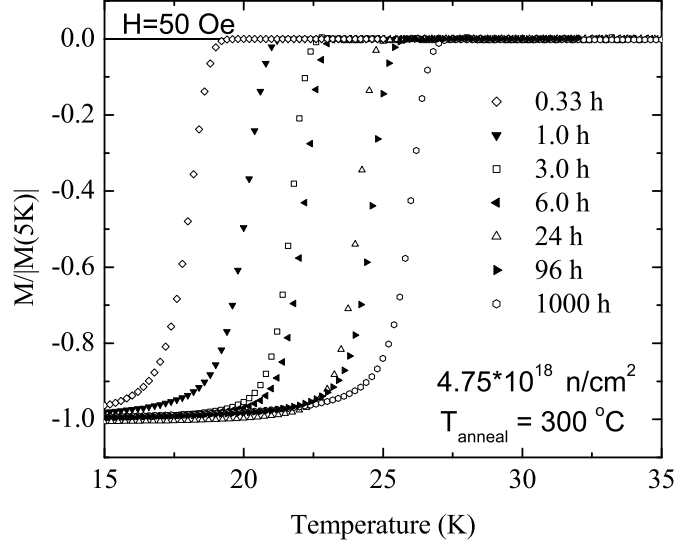


Figure 9.8 Normalized magnetization curves for fluence level of 4.75×10^{18} n/cm^2 annealed at 300°C for 1/3, 1, 3, 6, 24, 96, and 1000 hours.

random diffusion, then $F(n)=n$, and the defect concentration decreases exponentially with time:

$$n = n_0 e^{-\lambda t} \quad (9.3)$$

where n_0 is the initial defect concentration, $\lambda = K_0 e^{E_a/k_B T}$ is a rate constant, and t is time. Taking ΔT_c as a measure of the defect concentration, we see this exponential behavior in samples annealed at 200°C , 300°C and 400°C (Figure 9.9). Since we only have two samples annealed at 500°C , which are longer time anneals and thus presumably would fall further out on an exponential tail, we can not extract a meaningful value from an exponential fit of these data. For samples which do show an exponential behavior in the decrease of ΔT_c (and by presumption) the defect density as a function of annealing time the activation energy, assuming a single activation process, can be determined by the so-called cross-cut procedure (96). This involves comparing the annealing time for which different temperature anneals reached the

same defect density, i.e. ΔT_c . If a ΔT_c is reached by annealing at a temperature T_1 for a time t_1 and by annealing at a temperature T_2 for a time t_2 , then the activation energy is related to these quantities by:

$$\ln \frac{t_1}{t_2} = \frac{E_a}{k_B} \left(\frac{1}{T_1} - \frac{1}{T_2} \right). \quad (9.4)$$

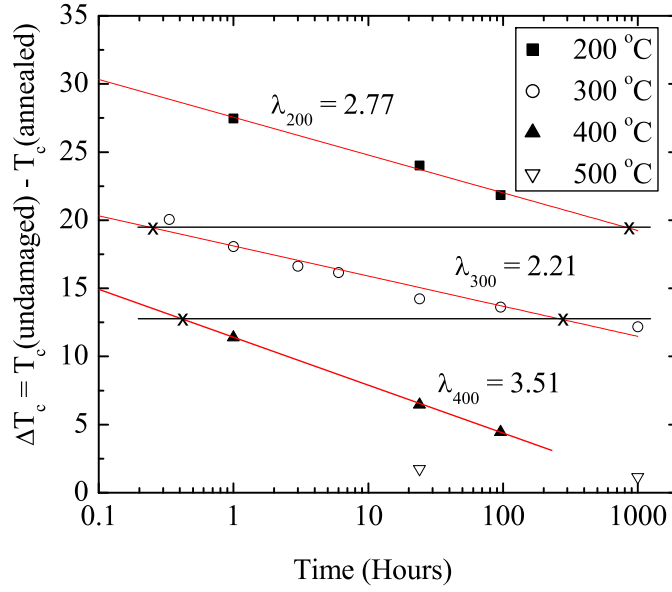


Figure 9.9 Semi-log plot of the suppression of the superconducting transition temperature as a function of annealing time at various annealing temperatures. All samples shown were exposed to a fluence level of 4.75×10^{18} n/cm². Using a linear fit over up to three decades yields non-systematic values in the rate constants for the 200 °C, 300 °C, and 400 °C annealing temperatures. The activation energy is estimated using the cross cut procedure on extrapolations of these fits to the data (comparison points are given by the x symbols). By comparing points with identical ΔT_c values we obtain estimates of $E=1.90$ eV and 2.15 eV. (see equation 7.4)

Unfortunately, no overlap region in T_c exists for our set of data. To achieve an overlap region in the experimental data we'd need to shorten the annealing times below 0.33 hours

or extend them to well beyond 1000 hours. Short time anneals, less than 0.33 hours, are not feasible as we'd be unable to ensure thermal equilibrium of the samples within the furnace for such a short time. Extending the annealing an additional order of magnitude, to 10^4 hours, is simply not practical. We can still estimate the activation energy by extrapolating the ΔT_c curves at each temperature to shorter and longer times so as to create overlap regions (Figure 9.9). Calculating E_a from the overlap between the 200 °C and 300 °C curves and between the 300 °C and 400 °C curves yields values of 1.90 eV and 2.15 eV respectively.

An alternative approach to determining the activation energy is to use the ratio of slopes method (104). Experimentally a set of samples is annealed isothermally for different times at a temperature T_1 and an identical set of samples is annealed at a different temperature T_2 . The differing temperatures result in different time evolution of ΔT_c , and hence, different slopes, $d\Delta T_c/dt$. The ratio of the slopes for the two different temperatures at the point where both annealing temperatures have yielded the same ΔT_c , is related to the activation energy by:

$$\frac{d\Delta T_{c1}}{dt_1} / \frac{d\Delta T_{c2}}{dt_2} = \exp\left(\frac{E_a}{k_B} \left(\frac{1}{T_1} - \frac{1}{T_2}\right)\right) \quad (9.5)$$

where the subscripts 1 and 2 refer to temperatures T_1 and T_2 . By comparing the slopes from the 200 °C and 300 °C anneals and those from the 300 °C and 400 °C anneals, we obtain estimates of 1.07 eV and 1.63 eV, respectively. It should be noted that, while these estimates were made using real data, rather than extrapolations as in the previous calculation, there is inherent inaccuracy in such a calculation due to the lack of a true overlap in ΔT_c . Additionally, the low density of data points limits our ability to accurately determine the linear slope from the ΔT_c versus time curves where ΔT_c tends to decay exponentially.

Depending on the calculation method and data set used, we obtain activation energies ranging from 1.07 eV to 2.15 eV. It is likely that some of the variation is real, as, in these heavily damaged samples, there exist both point defects and defect complexes. The annealing of point defects is expected to have a lower activation energy than the dissolving of the defect complexes. While we can not assign definitive values for the activation energies of these two processes, merely stating a single activation energy hides some of the rich complexity underlying

the annealing process in these heavily damaged samples. It should be noted that the activation energies in these neutron irradiated MgB₂ samples are the same order of magnitude as those for annealing quenched in defects out of gold (104). That our samples yielded a relatively small spread in activation energies and were comparable in magnitude to values associated with the annealing of simple defects in other metals suggests the defects within the neutron irradiated MgB₂ samples are being annealed by single activation processes.

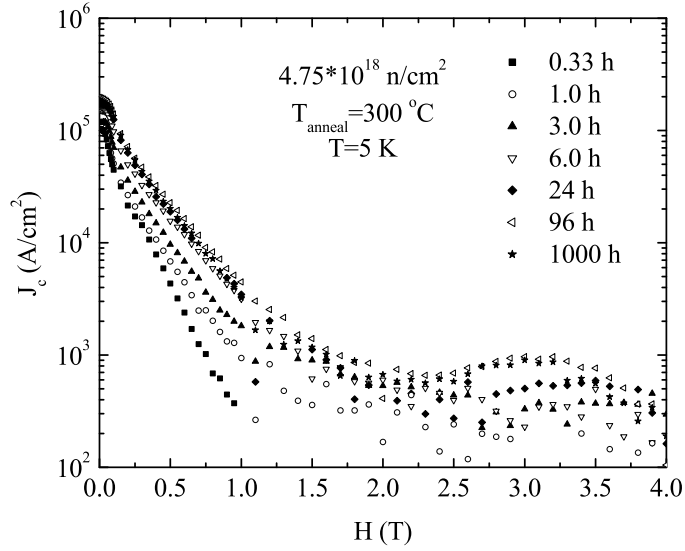


Figure 9.10 J_c curves (inferred from magnetization data) for the set of $4.75 \times 10^{18} \text{ n/cm}^2$ fluence samples annealed at 300°C for various times. In-field J_c values increase as a function of annealing time due to increases in T_c .

For the set of wires annealed at 300°C , critical current densities at $T=5 \text{ K}$ and low fields approximately scale with annealing time and hence T_c (Figure 9.10). The field at which J_c drops below 10^4 A/cm^2 steadily rises from near 0.5 T to approximately 1 T when increasing the annealing time from 20 minutes to a 1000 hours. For annealing times of 6 hours and shorter, J_c monotonically decreases as a function of applied field. After a 24 hour anneal, J_c begins to flatten above 3 T at a value of approximately 500 A/cm^2 . Extending the annealing time to

96 and 1000 hours results in the emergence of a clear second peak at an applied field slightly above 3 T. The curves for the 96 and 1000 hour anneal are virtually identical and reflect the small 1.5 K or 6% increase in T_c resulting from the order of magnitude longer annealing time.

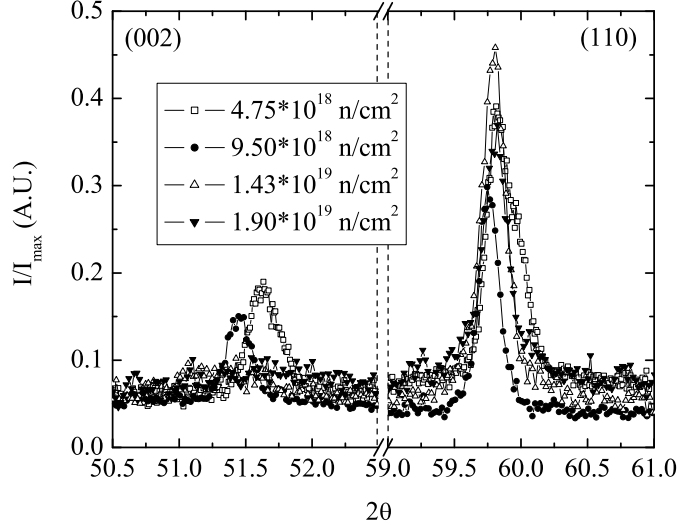


Figure 9.11 (002) and (110) X-ray peaks for all four exposure levels annealed at 300 °C for 24 hours. The highest two levels continue to show a substantially broadened (002) peaks indicating a degradation of long range order along the c-direction.

9.1.4 Variable Fluence Levels, 24 Hour Anneal

We annealed samples from each of the damaged levels for 24 hours at 200 °C, 300 °C, 400 °C, and 500 °C. The (002) and (110) x-ray peaks for samples of all four damage levels annealed at 300 °C for 24 hours are given in figure 9.11. Annealing at 300 °C for 24 hours did not restore long range order along the c-axis in the samples exposed to the two highest fluence levels of $1.43 \times 10^{19} \text{ n/cm}^2$ and $1.90 \times 10^{19} \text{ n/cm}^2$. For these 24 hour anneals, up to an annealing temperature of 400 °C the (002) peak maintains a FWHM above 1° , which corresponds to a structural coherence length of approximately 1000 Å (Figure 9.12). MgB_2 has a superconducting coherence length near 50 Å (56), so that while there is shorter range structural

order along the c - direction, it is still an order of magnitude larger than the superconducting coherence length. It is therefore not unexpected that superconductivity exists in samples with degraded long range order. Only after the temperature reaches 500 °C does the correlation length along the c - direction exceed 1000 Å (Figure 9.11). The relative shift of the a - and c - lattice parameters for the various heat treatments is plotted in Figure 9.13.

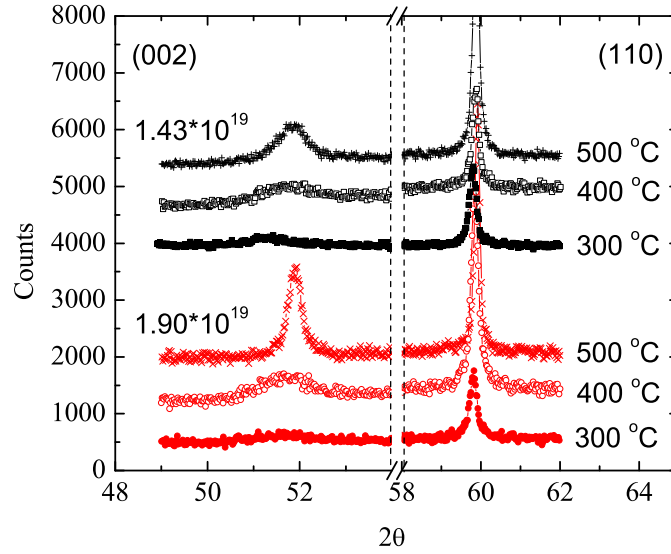


Figure 9.12 Evolution of the (002) and (110) X-ray peaks for the 1.43×10^{19} and 1.90×10^{19} n/cm² exposure levels annealed for 24 hours with the annealing temperature increasing from 300 °C to 500 °C. In both cases, the (002) attains a FWHM less than $1^\circ 2\theta$ only after the annealing temperature reaches 500 °C.

Magnetization measurements were performed on all of the annealed samples (Figure 9.14a). A summary of the resultant transition temperatures, given in terms of ΔT_c , is plotted in figure 9.14b. In general terms, the higher fluence levels lead to lower superconducting transition temperatures for a given temperature post-exposure anneal. For a given fluence level, higher annealing temperatures yield higher T_c values. That is, the samples exposed to higher fluence levels behave in a qualitatively similar manner to lowest level, but the added exposure leads to

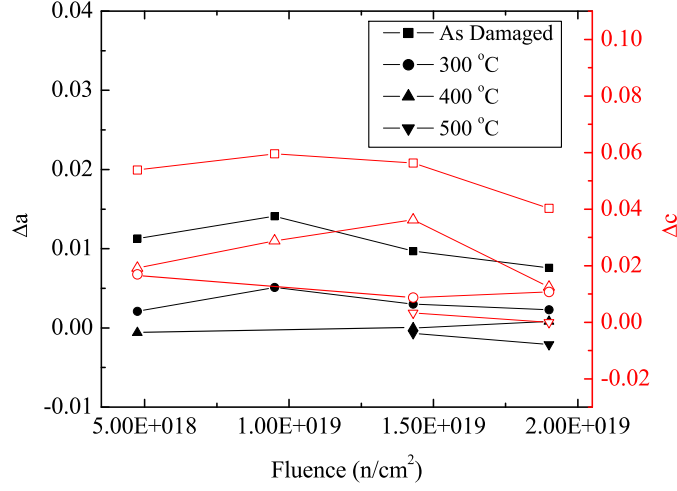


Figure 9.13 Calculated lattice parameter shifts for all four damage levels annealed at temperatures up to 500°C. Closed symbols represent Δa , and open symbols are Δc . Lines serve as guides to the eye.

increased defect densities which manifest themselves in terms of lower transition temperatures for a given annealing profile.

9.1.5 Long Time Annealing Studies

The conversion of ^{10}B to ^7Li through neutron absorption and subsequent alpha decay introduces the possibility of observing the effects of lithium doping MgB_2 . In order to distinguish the effects of Li doping from those associated with structural defects introduced through inelastic collisions between neutrons and the underlying lattice it is necessary to minimize the density of these defects. As shown, by annealing for long times at high temperatures the number of structural defects can be systematically reduced. Since Li can't be annealed away, the resultant superconducting and normal state properties should increasingly reflect the effects of Li doping. The density of Li atoms produced through the transmutation of boron can be estimated from the formula (68):

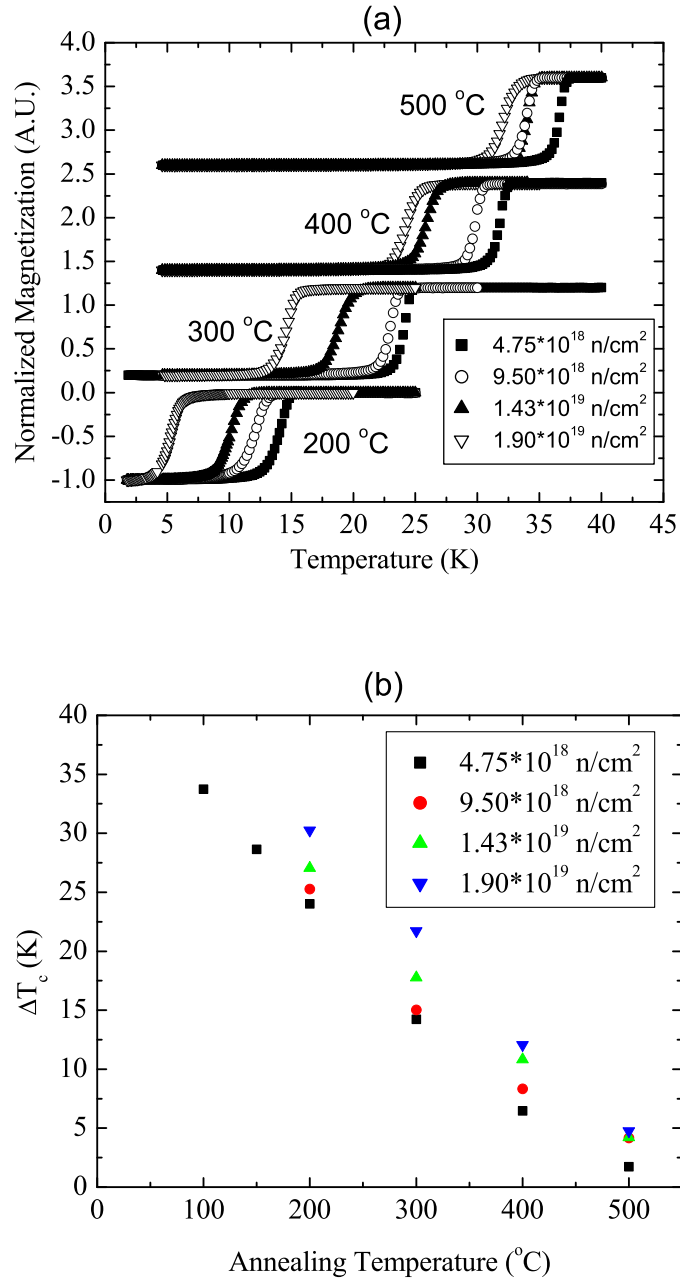


Figure 9.14 (a) Normalized magnetic transitions as a function of annealing temperature and fluence level for all four damage levels. The time for each anneal was 24 hours. (b) T_c values, as determined by a 1% screening criteria, as a function of annealing temperature and fluence level.

$$n_{Li} = n_B \sigma f \quad (9.6)$$

where n_{Li} is the density of Li atoms, n_B is the density of B atoms, σ is the absorption cross section, and f is the fluence level. Computing the corresponding atomic percentages yields an increase from 0.37% to 1.48% as the fluence is increased from 4.75×10^{18} n/cm² to 1.90×10^{19} n/cm² (see chapter 4).

We therefore annealed all four of the damage levels for 1000 hours at 500 °C. Normalized magnetization curves for this series are plotted in figure 9.15a. In each case the transition temperatures have increased relative to samples annealed at 500 °C for 24 hours as can be seen by plotting ΔT_c versus time (Figure 9.15b). Using a linear fit on the semi-log plot, the resultant slopes are much lower than was seen for the 4.75×10^{18} n/cm² fluence level samples annealed for various times at 200 °C, 300 °C, and 400 °C (Figure 9.9), indicating ΔT_c is beginning to saturate above 24 hours. Since we don't have any intermediate time points, we can't determine if we've achieved fully saturated ΔT_c values at 1000 hours, but we can take the 1000 hour anneals at 500 °C as an upper limit on the effects of lithium doping.

Transport measurements were performed in order to determine the normal state resistivity and temperature dependence of H_{c2} for these samples. We were unable to contact the samples exposed to the two highest dose levels. The normal state resistivity ($T=40$ K) for the sample exposed to a fluence of 4.75×10^{18} n/cm² and annealed for 1000 hours was approximately $5.3 \mu\Omega \cdot \text{cm}$, which is more than three times the $1.6 \mu\Omega \cdot \text{cm}$ measured on the sample annealed for 24 hours. The 1000 hour anneal sample also had a lower residual resistivity ratio (RRR), 3.3 versus 5.9, indicating the increase in ρ_0 isn't merely an artifact associated with possible geometric effects (cracks within the sample). The 9.50×10^{18} n/cm² fluence level sample, which was annealed for 1000 hours, had a normal state resistivity of $6.6 \mu\Omega \cdot \text{cm}$ and RRR=5.0. Karkin et al. saw increases in ρ for annealing temperatures above 300 °C, which they attributed to changes in inter-grain transport (62). It is possible that by annealing at an elevated temperature for 1000 hours we have degraded the inter-grain connectivity in some fashion, leading to the observed increases in resistivity.

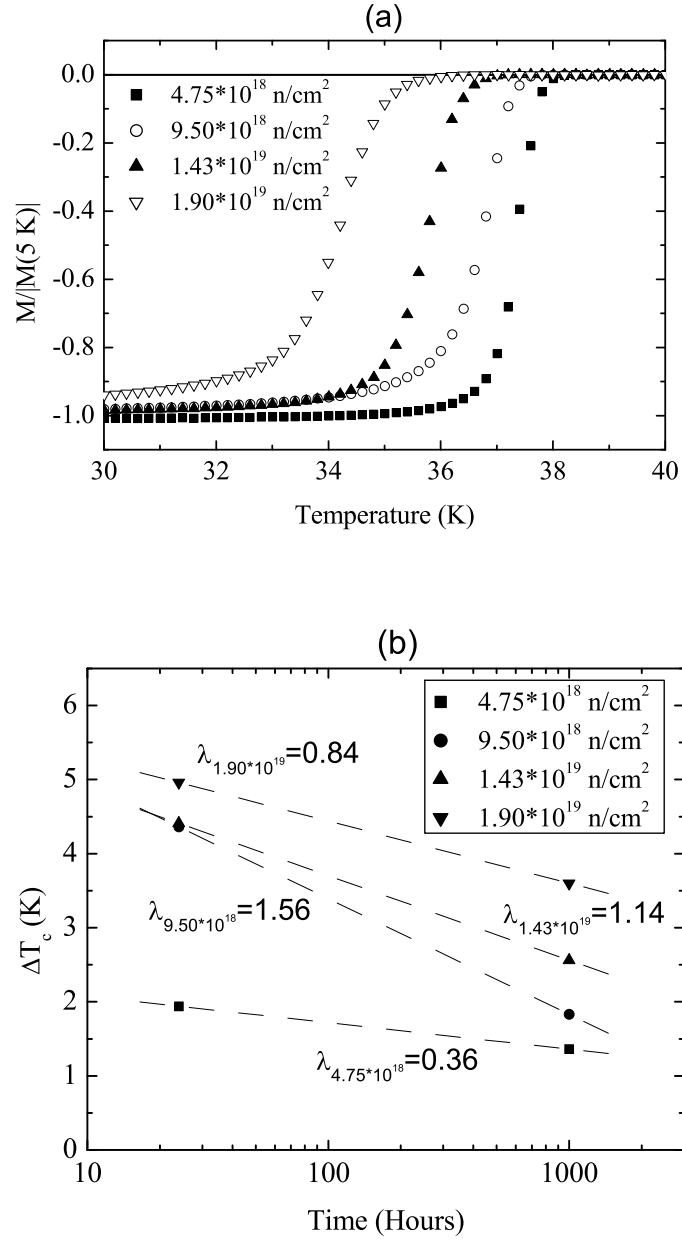


Figure 9.15 (a) Normalized magnetic transitions for all four fluence levels annealed at 500 °C for 1000 hours. (b) ΔT_c for samples annealed at 500 °C for 24 and 1000 hours. For each of the four fluence levels, extending the annealing time results in a further recovery of T_c towards that of the undamaged sample.

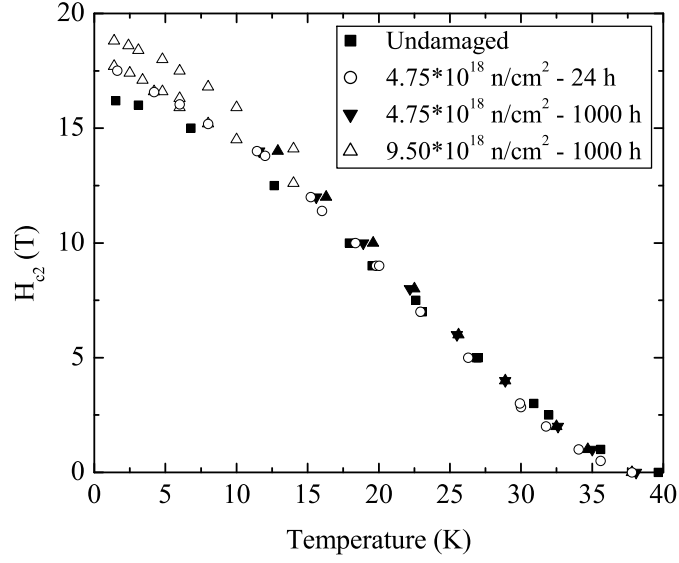


Figure 9.16 H_{c2} curves for the 4.75×10^{18} n/cm² and 9.50×10^{18} n/cm² fluence levels annealed for 1000 hours at 500 °C. Both damage levels show a possible enhancement relative to the undamaged sample, but there is some spread in the data as illustrated by the two 9.50×10^{18} n/cm² fluence level samples shown.

The temperature dependance of H_{c2} is plotted in figure 9.16. It was found that for the 4.75×10^{18} n/cm² fluence level $H_{c2}(T)$ data for a 1000 hour anneal sample was comparable to that of the 24 hour anneal sample, both showing possible, slight enhancement relative to the pure sample. In the case of the 1000 hour anneal on the 9.50×10^{18} n/cm² fluence level, H_{c2} had some spread in the data, but extrapolated to 18-19 T at zero Kelvin. The upper critical fields of the two lowest fluence levels annealed at 500 °C for 1000 hours appear to be similar, with slight differences arising due to inherent sample to sample variation.

9.2 Discussion

The initial irradiation of MgB₂ wire segments results in an increase in the size of the unit cell and suppression of the superconducting transition temperature. Post exposure annealing

tends to return both the lattice parameters and T_c towards their undamaged values. If the superconducting properties of the neutron irradiated samples were purely a result of changes in the unit cell dimensions, correlations should exist between the superconducting properties of neutron irradiated MgB_2 and pure MgB_2 placed under external pressure. Since an expansion is qualitatively analogous to an effective negative pressure one would anticipate the changes in T_c to be an extension to negative pressure of the results attained for the application of positive pressure. Application of external pressure has been shown to compress the unit cell and suppress T_c (105). Thin films grown epitaxially on (0001) sapphire substrates exhibited an enhanced T_c above 41 K which was attributed to tensile strain (106). In the case of neutron irradiated MgB_2 , the expansion of the lattice parameters coincides with a decrease in T_c and the evolution of T_c as a function of Δa , Δc , and V/V_0 behaves differently than MgB_2 under pressure (Figure 9.17). In the case of externally applied pressure, it is believed that the changes in the frequency of the E_{2g} phonon mode are responsible for the suppression of T_c (105; 107). With such dramatically different behavior between the neutron irradiation and pressure results, it is clear that the changes in T_c can not simply be linked to changes in the unit cell volume.

In addition to the structural changes, neutron irradiation also introduces a chemical impurity into the system through the ^{10}B neutron capture and subsequent alpha decay to ^7Li . The amount of lithium produced in this manner is, however, quite small and for all but the 1000 hour anneals at 500 °C, we can not sort the possible effects of such from the effects of the structural perturbations. The atomic percentage of B converted to Li through nuclear processes for all four exposure levels is estimated to be on the order of 1% (Table 1). Therefore, for lower temperature and/or shorter time anneals the effects of Li production are presumably insignificant next to the changes resulting from structural damage caused by inelastic collisions between the fast neutrons, emitted alpha particles, and recoiled ^7Li atoms and the underlying lattice. It is worth noting, though, that whereas low level Li substitution for Mg was proposed as a possible route to increasing T_c (108), our data show suppressed T_c values for our 1000 hour annealed samples. This does not preclude the possibility that Li substitution could, under other circumstances, raise T_c , but it certainly does not support it. It should be noted though

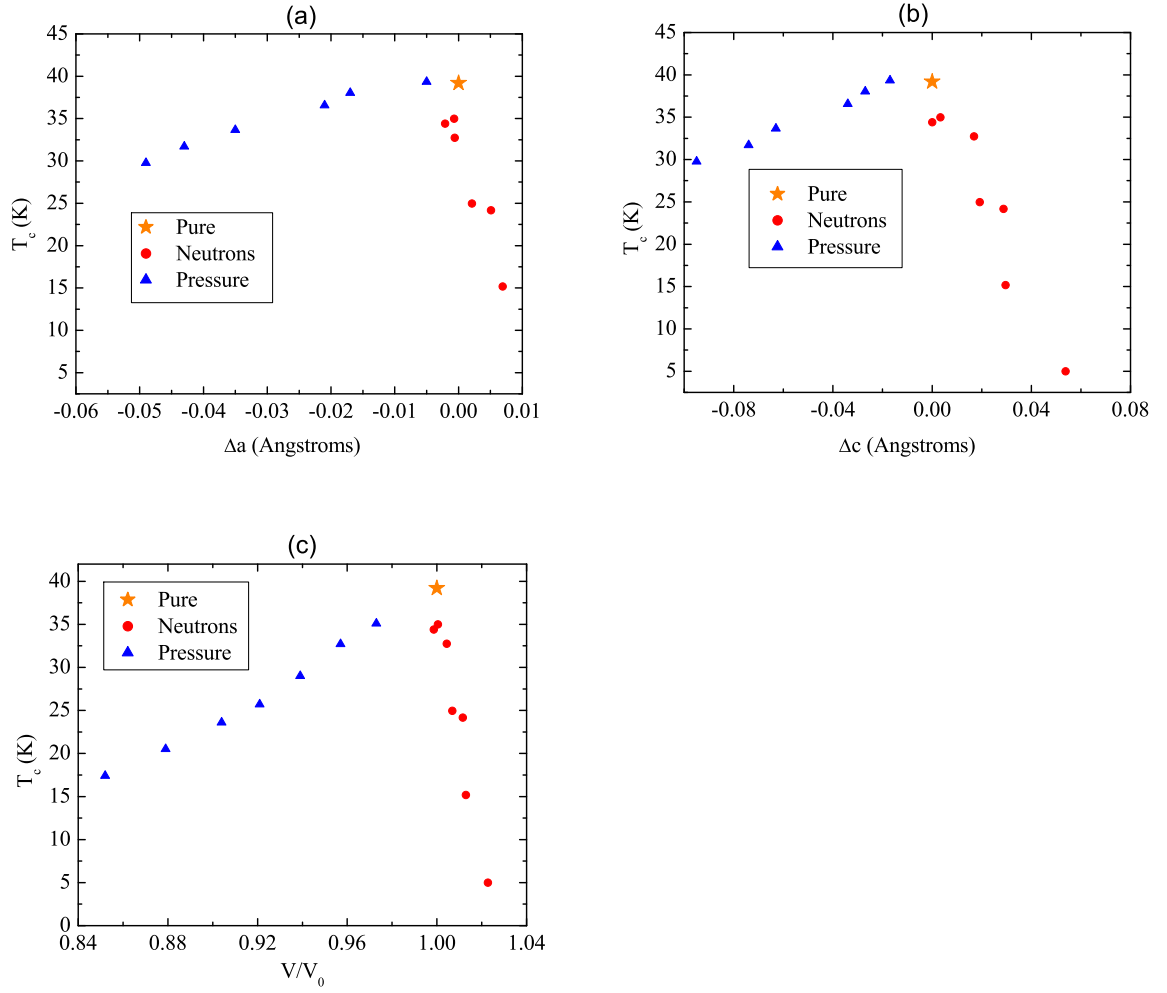


Figure 9.17 Comparison of the different development of T_c with (a) Δa , (b) Δc , and (c) unit cell volume for neutron irradiated MgB_2 and MgB_2 under external pressure. Pressure data are recreated from reference (105).

that this form of lithium doping is far from the ideal one. In the case of transmutation of ^{10}B the resulting sample is $\text{MgLi}_x\text{B}_{2-x}$ with boron vacancies and no clear site for the lithium. The more desirable form of lithium doping is $\text{Mg}_{1-x}\text{Li}_x\text{B}_2$ with the lithium substituting for the magnesium and no disruption of the boron sublattice.

The samples annealed at 500 °C for 1000 hours suggest that at low levels, Li doping has little or no effect on H_{c2} . The 9.50×10^{18} n/cm² fluence sample has twice the amount of Li of the 4.75×10^{18} n/cm² fluence sample, yet their $H_{c2}(T=0)$ values are approximately equal and only slightly differ from the un-damaged case. If the 18 T H_{c2} value seen for the 4.75×10^{18} n/cm² fluence level is truly a 2 T enhancement relative to the un-damaged sample and is the result of Li doping, then we would expect the 9.50×10^{18} n/cm² fluence level to exhibit a $H_{c2}(T=0)$ near 20 T, which we did not observe. Since we can not insure that we have fully annealed out all of defects, it is possible that this slight increase in $H_{c2}(T=0)$ is a result of scattering associated with structural defects. In this case $H_{c2}(T=0)$ should be determined more by T_c than by the particular fluence level or post exposure annealing profile. The T_c values for the 4.75×10^{18} n/cm² fluence level annealed at 500 °C for 24 and 1000 hours and that of the 9.50×10^{18} n/cm² fluence level annealed at 500 °C for 1000 hours are all within half a degree of one another. This suggests that $H_{c2}(T=0)$ is controlled more by scattering associated with residual defects rather than any inadvertent Li doping. Since these low levels of Li do not appear to have any major impact on the superconducting properties, we can limit the discussion to possible influences of disorder, scattering, and possible changes in the Fermi surface.

The evolution of the superconducting transition temperature as a function of the unit cell dimensions (Δa , Δc , and V/V_0) shows definite trends and is in good agreement with the results of other neutron irradiation studies (62; 102) (Figure 9.18). Although there is considerable spread in the data, all three reports show that T_c tends to decrease with both Δa and Δc and hence V/V_0 . These data show that, for neutron damaged samples, there is some correlation between the unit cell dimensions and the superconducting properties. They do not, however, uniquely determine if the changes are a result of changes in the Fermi surface, perhaps due to a repositioning of the atoms, or if they are due to an introduction of additional scattering

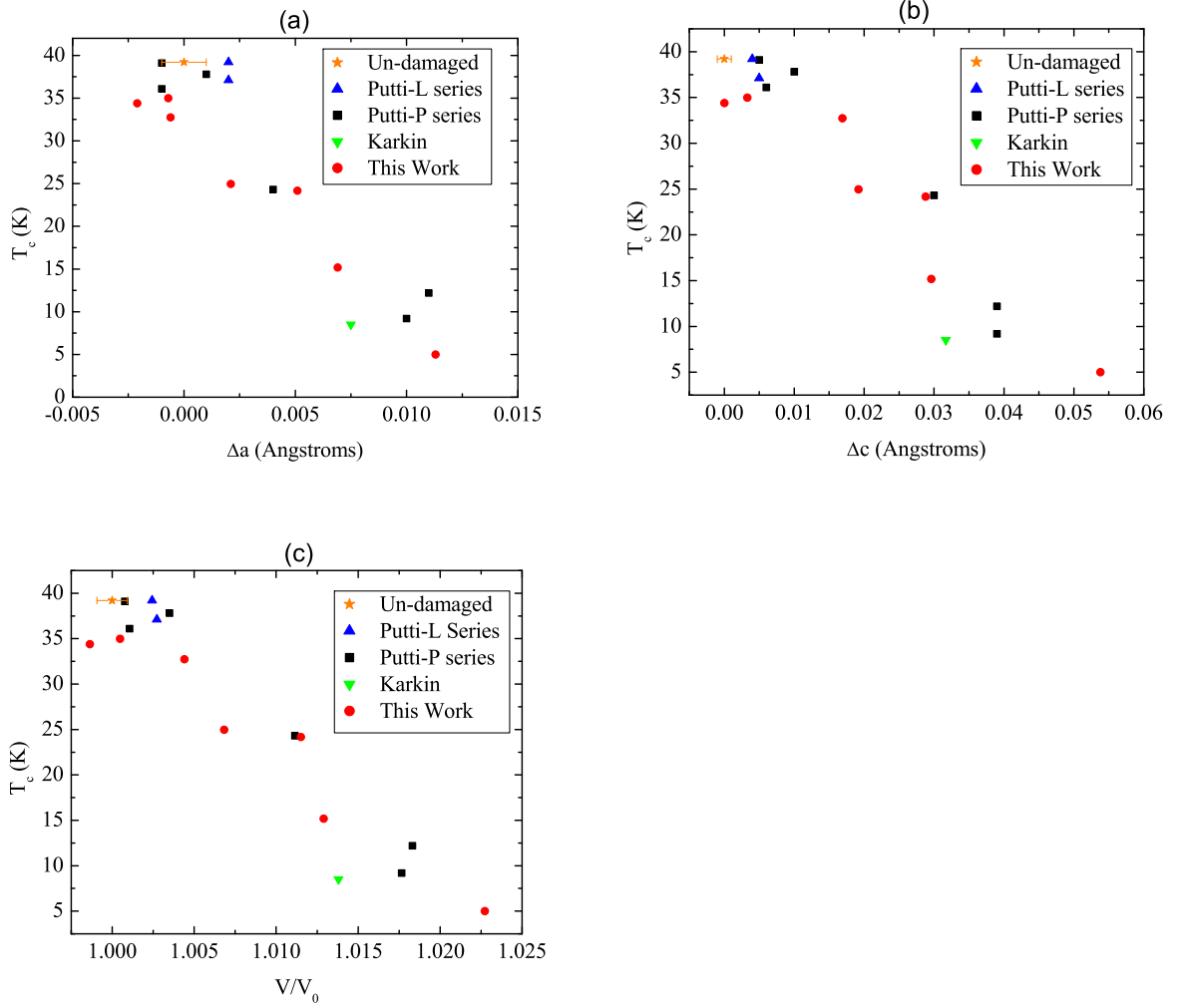


Figure 9.18 Comparison of the different development of T_c with (a) Δa , (b) Δc , and (c) unit cell volume for neutron irradiation from different groups. Data includes results from references (62; 102). In parts (a) and (b) the error bars on the pure sample represent typical experimental error in determining lattice parameters. In the part (c), the error bars represent the propagation of the error in the lattice parameters to the calculated V/V_0 value. All of our data in these plots should be considered to have comparable uncertainty.

centers. In the case of substantial neutron irradiation induced damage, where T_c is below 10 K, NMR measurements indicate the suppression of superconductivity is the result of a decrease in the density of states of the boron $p_{x,y}$ orbitals (109). This technique has been successful in experimentally determining a decrease in the density of states in $Mg_{1-x}Al_xB_2$ and AlB_2 (110; 111). It should be noted however, that measurements of the nuclear spin relaxation rate, T_1^{-1} , on ^{11}B yielded comparable T_1T values, which are directly related to the density of states at the Fermi surface, for both a neutron irradiated sample which had a T_c near 7 K (109) and a sample with 30% aluminum substituted for magnesium which had a T_c near 25 K (110). That the neutron damaged sample exhibits a dramatically lower T_c despite having virtually the same density of states at the Fermi surface suggests additional mechanisms act to suppress superconductivity in neutron irradiated MgB_2 . This notion is supported by the fact that for the 24 hour anneals at 300 °C, 400 °C, and 500 °C, the relative changes in the lattice parameters are fairly small. This should only contribute to minor changes in the Fermi surface, yet T_c is suppressed to near 25 K in the case of the 300 °C anneal.

Although there exist correlations between our data and literature reports on the evolution of T_c and the lattice parameters, the evolution of $H_{c2}(T=0)$ varies depending upon the irradiation conditions. This present work on heavily irradiated MgB_2 containing natural boron followed by post exposure annealing led to little or no enhancement of the upper critical field. In contrast others have reported enhancements of H_{c2} for low fluence levels on MgB_2 containing either natural boron or isotopically enriched ^{11}B (97; 100). Since enhancements have been seen for both natural and isotopically enriched samples, the defects responsible for increasing H_{c2} are presumably caused by collisions between neutrons and the underlying lattice, rather than by the transmutation of ^{10}B to 7Li . When a neutron capture and subsequent alpha decay event occurs, the resultant damage is a large cluster of dislocations. Primary knock-on events cause a cascade of displacements which can be spread over a distance as large as a hundred atomic distances (96). As mentioned previously, T_c suppression in as damaged samples containing natural boron is much more rapid than those with either isotopically enriched ^{11}B or those which have been shielded from low energy neutrons. Therefore it is presumably the clusters

associated with the neutron capture event which are primarily responsible for the suppression of T_c . These clusters presumably have low activation energy and can be largely repaired by the annealing process, which explains why we saw such a rapid increase in T_c for short time and low temperature anneals. In order to see an enhancement in H_{c2} we need to anneal for a sufficient time and temperature so as to increase T_c to a level where we aren't being limited by a low transition temperature. Since the defect clusters from the alpha decay of ^{11}B to ^7Li are large, and we are relying on random diffusion to recombine vacancies and interstitials, higher reaction temperatures are necessary to restore T_c . By going to higher annealing temperatures we begin to repair defects with higher activation energies. Therefore, regardless of the actual energy associated with repairing the defects caused by primary knock-on events, we are most likely annealing many of them away while restoring T_c . If it is these defects which are responsible for H_{c2} enhancement then it is the annealing process which causes the different development of H_{c2} we observe. Based on this analysis it seems likely that a study of wire samples that have been exposed to much smaller fluences of neutrons (e.g. an exposure level that yields as damaged samples with a transition temperature in the range $30 < T_c < 37$) should yield different, and higher, $H_{c2}(T)$ data.

Damage induced by neutron irradiation is fundamentally different from doping with aluminum or carbon. Both carbon and aluminum enter the structure and are believed to act as point defects in addition to electron doping the system. Both carbon and aluminum doping are believed to increase scattering within the π band relative to the σ band, but the effect is much more pronounced in the case of carbon doping (14). The development of H_{c2} is dominated by scattering effects for carbon substitutions and by Fermi surface effects for aluminum substitution. For neutron irradiated samples, as discussed above, the effects of the introduction of Li through nuclear processes are negligible and the changes in the superconducting properties are due to an increase in interband scattering and a decrease in the density of states. Insights can be made into the effects of neutron irradiated samples by comparison to carbon and aluminum doping.

The different development of interdependencies of $H_{c2}^{\parallel ab}$, T_c , and ρ_0 in carbon doped (86;

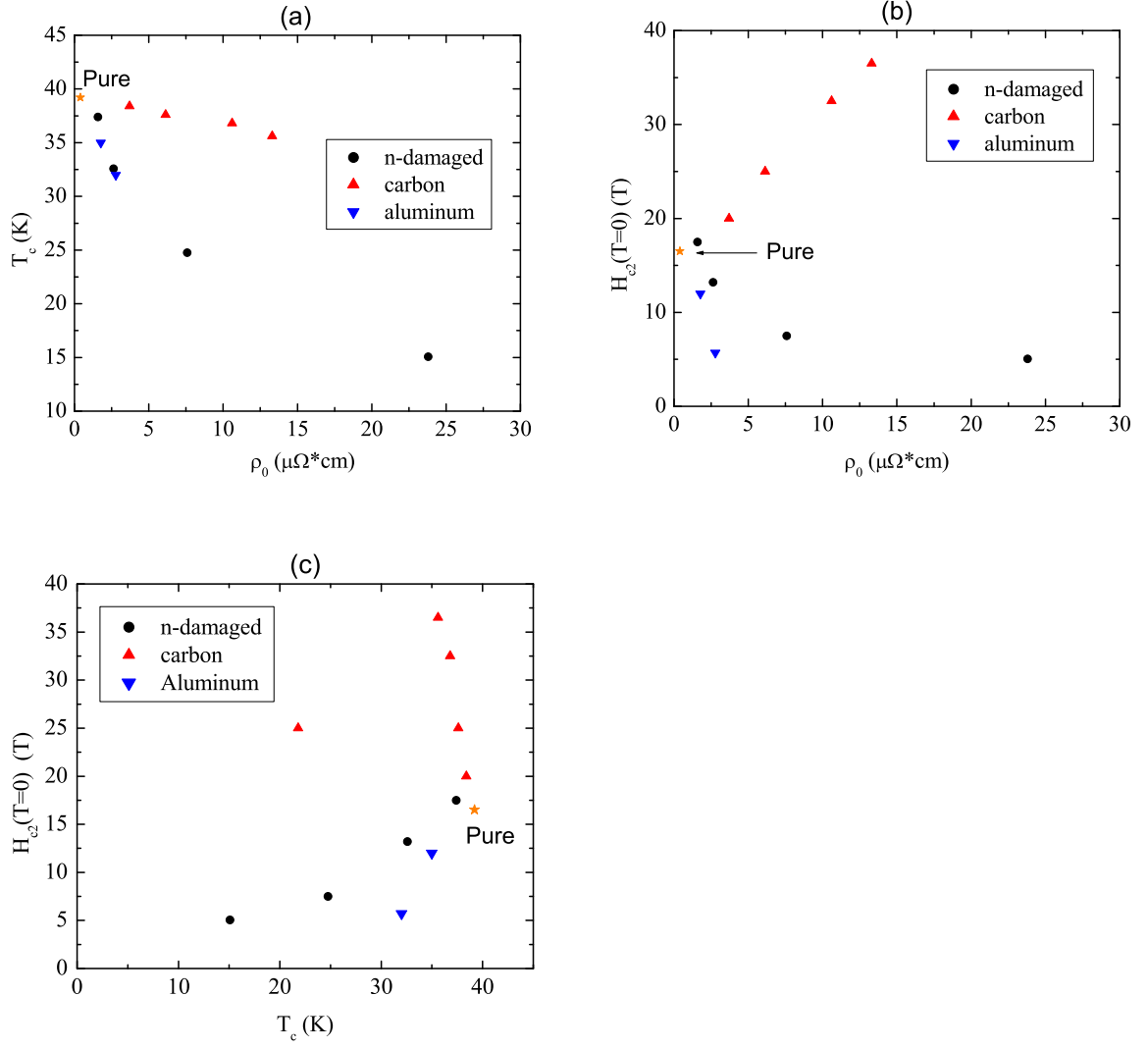


Figure 9.19 Interdependencies of T_c , $H_{c2}(T=0)$, and ρ_0 for carbon doped (86; 112), aluminum doped single crystals (113), and neutron irradiated samples. (a) T_c vs. ρ_0 , (b) $H_{c2}(T=0)$ vs. ρ_0 , and (c) $H_{c2}(T=0)$ vs. T_c .

112), aluminum doped single crystals (113), and neutron irradiated samples, those exposed to a fluence of 4.75×10^{18} n/cm² and annealed for 24 hours, are plotted in figure 9.19. Figure 9.19a shows the evolution of the transition temperature as a function of residual resistivity for these three types of perturbations. The suppression of T_c with ρ_0 for low resistivity values is quite similar for the neutron damaged and aluminum doped samples; T_c drops rapidly with increased scattering. In contrast, the suppression of T_c as a function of resistivity in carbon doped samples is quite gradual. This is consistent with both aluminum doping and neutron damaged samples having more interband scattering than carbon doped compounds.

Figure 9.19b plots $H_{c2}(T=0)$ as a function of ρ_0 . Here all three perturbations behave uniquely. The aluminum and neutron damage samples show a decrease in H_{c2} , whereas the carbon doped samples show a dramatic increases. The decrease in H_{c2} is more rapid in the aluminum doped samples than in neutron damaged samples. This can also be seen by plotting H_{c2} as a function of T_c (Figure 9.19c).

Direct comparison between the evolution of T_c and $H_{c2}(T=0)$ for carbon doping and neutron irradiation shows the scattering associated with each type of perturbation is different. Within the model proposed by Gurevich (27), enhancements in H_{c2} result from differences in the relative strength of scattering within each band, whereas the suppression of T_c is a function of scattering between the bands. The neutron irradiated samples on these plots with a T_c greater than 25 K are samples which were annealed at 300 °C, 400 °C, and 500 °C. In each of these samples, annealing has reduced the a-lattice parameter to nearly the undamaged value (Figure 9.2b). With the defect structure lying between nearly undamaged boron planes, one would not expect the scattering within the σ band to be substantially affected. If the scattering was confined primarily to the 3-D π band, the resultant differences in intraband diffusivity values should manifest themselves in terms of enhanced H_{c2} , analogous to carbon doping. Since no significant enhancement is seen, we believe the scattering is primarily interband scattering and contributes to the suppression of T_c . The range in T_c for $V/V_0 \sim 1$ in post exposure annealed samples (Figure 9.18c) supports the notion that neutron irradiation increases interband scattering.

The suppression in T_c in neutron irradiated samples is the result of a combination of a decrease in the density of states at the Fermi surface and an increase in inter-band scattering. In the case of aluminum doping, the suppression of T_c is believed to be primarily a result of a changes in the Fermi surface (14). Samples of neutron damaged MgB_2 exhibit higher H_{c2} values than aluminum doped MgB_2 samples with similar T_c values (Figure 9.19c). This suggests that changes in the density of states suppress H_{c2} to a greater degree than inter-band scattering.

CHAPTER 10. Effects of Neutron Irradiation on Carbon Doped MgB_2 Wire Segments

Carbon doping appears to weakly decrease T_c and increase H_{c2} by preferentially increasing scattering within the π band, whereas neutron damaging appears to decrease T_c and H_{c2} by increasing the inter-band scattering. The focus of this chapter is to examine the effects of combining these two scattering mechanisms by inducing and removing the effects of neutron damage in carbon doped MgB_2 samples. This will allow us to add and subtract inter-band scattering in samples with already enhanced intra- π -band scattering.

Carbon doped, $\text{Mg}(\text{B}_{0.962}\text{C}_{0.038})_2$, was prepared in a two step reaction process as described in detail previously (86). Carbon doped boron filaments, produced by Specialty Materials, Inc., were exposed to excess Mg vapor while the temperature was ramped from 650 °C to 1200 °C over 96 hours. Three filaments, each approximately 5 mm in length, were sealed in quartz ampoules under a He atmosphere and irradiated with an isotropic fluence of 7.13×10^{18} n/cm² reactor neutrons at the Missouri University Research Reactor (MURR), as described in the preceding chapter and in reference (114). The $\text{Mg}(\text{B}_{0.962}\text{C}_{0.038})_2$ filaments had a diameter of 110 μm , indicating the isotropic irradiation should result in essentially uniform damage.

10.1 Structural Properties

Figure 10.1 presents the (002) and (110) x-ray peaks for the entire set of 24 hour anneals. In the as-damaged samples both peaks are shifted to lower 2θ , indicating the irradiation resulted in an expansion of the unit cell. The calculated a- and c- lattice parameters yield relative increases with respect to the undamaged sample of $\Delta a = 0.0168(7)$ Å and $\Delta c = 0.0650(10)$ Å. In the case of neutron irradiation on pure MgB_2 , samples exposed to a fluence of 4.75×10^{18}

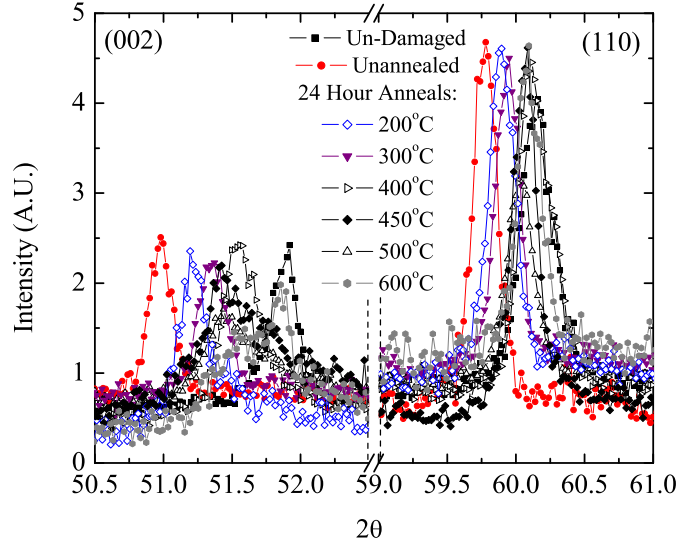


Figure 10.1 (002) and (110) x-ray peaks for the series of neutron irradiated $\text{Mg}(\text{B}_{0.962}\text{C}_{0.038})_2$ samples annealed for 24 hours at various temperatures.

n/cm^2 showed an increase in the a- and c- lattice parameters of $0.0113(7) \text{ \AA}$ and $0.0538(9) \text{ \AA}$. At a higher fluence of $9.50 \times 10^{18} \text{ n}/\text{cm}^2$ a greater expansion of the lattice parameters was observed, with a- and c- increasing by $0.0141(9) \text{ \AA}$ and $0.0596(12) \text{ \AA}$, respectively (15). Thus the magnitude of the increase in the lattice parameters is greater in the case of the carbon doped MgB_2 samples than was observed in pure MgB_2 samples even when they are exposed to a higher fluence level.

As the annealing temperature is increased up to a temperature of 400°C we see a systematic shift of both the (002) and (110) peaks to higher 2θ , indicating a contraction of both the a- and c- lattice parameters. At 400°C the a-lattice parameter appears to reach a minimum, measuring $3.0769(11) \text{ \AA}$, which is $0.0020(13) \text{ \AA}$ or 0.065% larger than the undamaged sample. The c-lattice parameter decreases monotonically as a function of temperature up to 400°C , where it has a value of $3.5466(12) \text{ \AA}$, which is $0.0314(14) \text{ \AA}$ or 0.89% larger than the undamaged value. For anneals at 450°C and above, a qualitative change in the evolution of the x-ray peaks

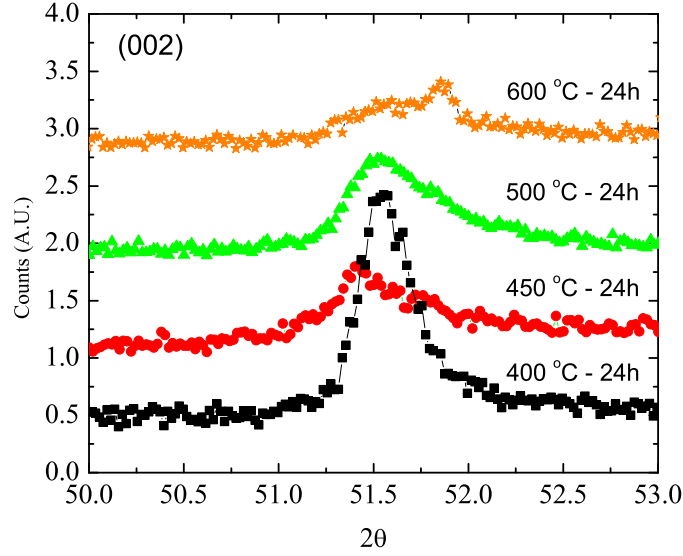


Figure 10.2 Evolution of the x-ray (002) peak as a function of annealing temperature for 24 hour anneals.

occurs. The (002) peaks begin to broaden substantially (Figure 10.2). For the 450 °C and 500 °C anneals, the stable peak refinements for the (002) peak were unattainable, preventing us from attaining estimates of the c - lattice parameter. The corresponding (110) peaks shifts to lower 2θ , indicating that the a - lattice parameter may be expanding slightly. After annealing at 600 °C for 24 hours, the (002) peak appears to bifurcate, and indexing as two different peaks yields one Δc value which is comparable to that attained for an annealing at 400 °C and another which is considerably lower (Figure 10.3). The (110) peak position, and hence calculated Δa , is comparable to that of the 400 °C anneal. The full set of calculated changes in lattice parameters relative to the undamaged samples for the series of 24 hour anneals is plotted in figure 10.3. Included in figure 10.3 is the evolution of the relative change in the lattice parameters as a function of annealing temperature for a pure MgB_2 sample exposed to a fluence of $4.75 \times 10^{18} \text{ n/cm}^2$ from reference (15).

The (002) and (110) x-ray peaks for a series of samples annealed at 500 °C for times up to

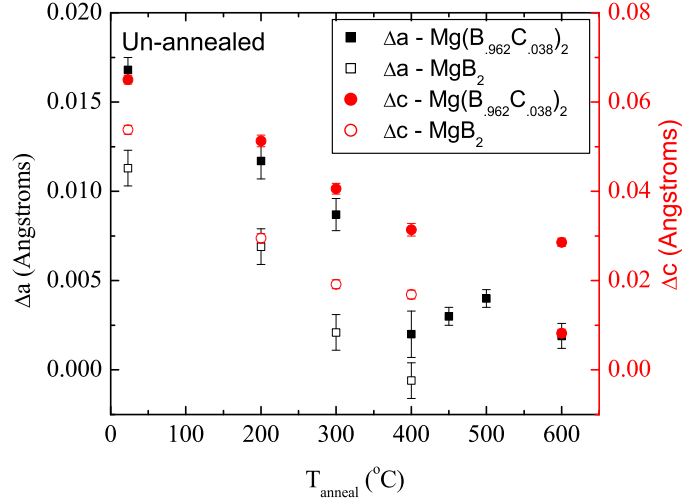


Figure 10.3 Lattice parameters as a function of annealing temperature for 24 hour anneals, as calculated from the positions of the (002) and (110) x-ray peaks. Included are data on a pure MgB₂ sample exposed to a fluence of 4.75×10^{18} n/cm² from reference (11).

1000 hours are shown in figure 10.4a. The (002) peaks continue to broaden as the annealing time at 500°C is increased. Stable peak refinements for the (002) peaks were unattainable due to their distorted shape. The (110) peaks monotonically shift to higher 2θ as a function of annealing time up to 96 hours, at which point the a- lattice parameter is within experimental error of the undamaged value (Figure 10.4b). While the a- lattice parameter is larger for the case of the 24 hour anneal at 500 °C relative to the 24 hour anneal at 400 °C, increasing the annealing time to 96 hours at 500 °C results in a continued contraction of a. Extending the annealing time an additional order of magnitude results in a negligible change in a. It appears that continued annealing at 500 °C causes the structure to become more disordered in the c- direction while the a- lattice parameter is returned to near the undamaged value.

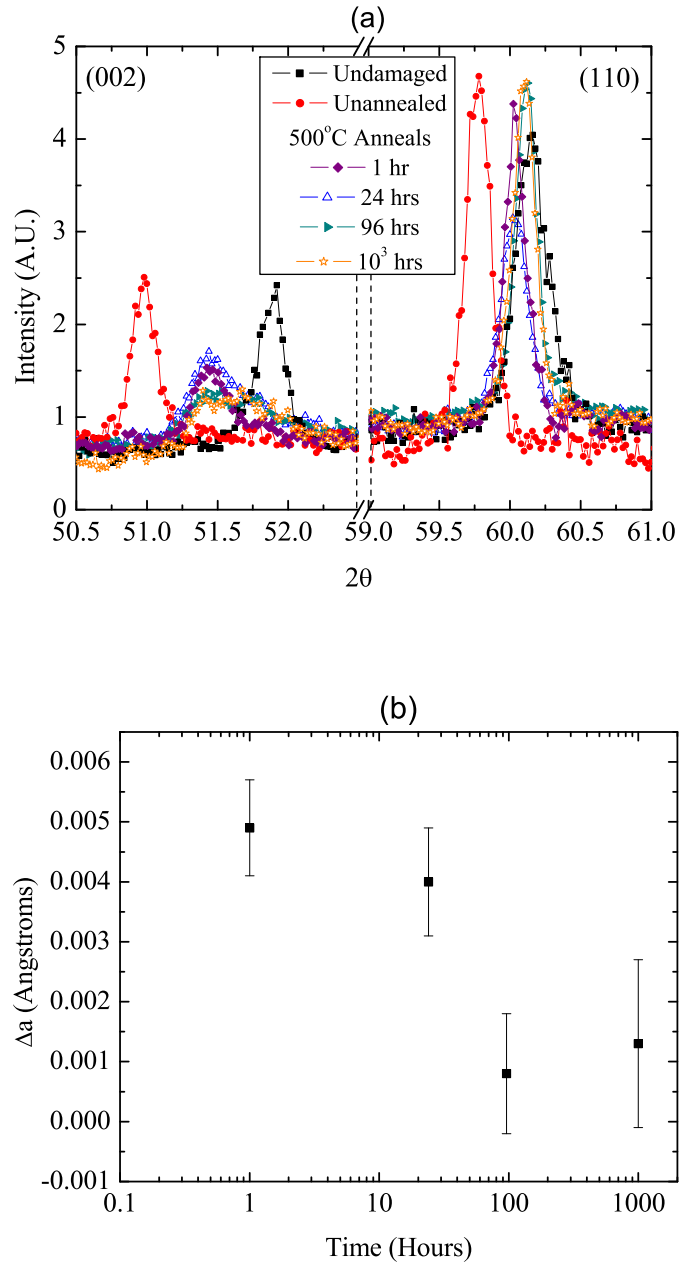


Figure 10.4 (a) Evolution of the (002) and (110) x-ray peaks as a function of annealing time at 500 °C. (b) Calculated shift of the a-lattice parameter from the undamaged sample.

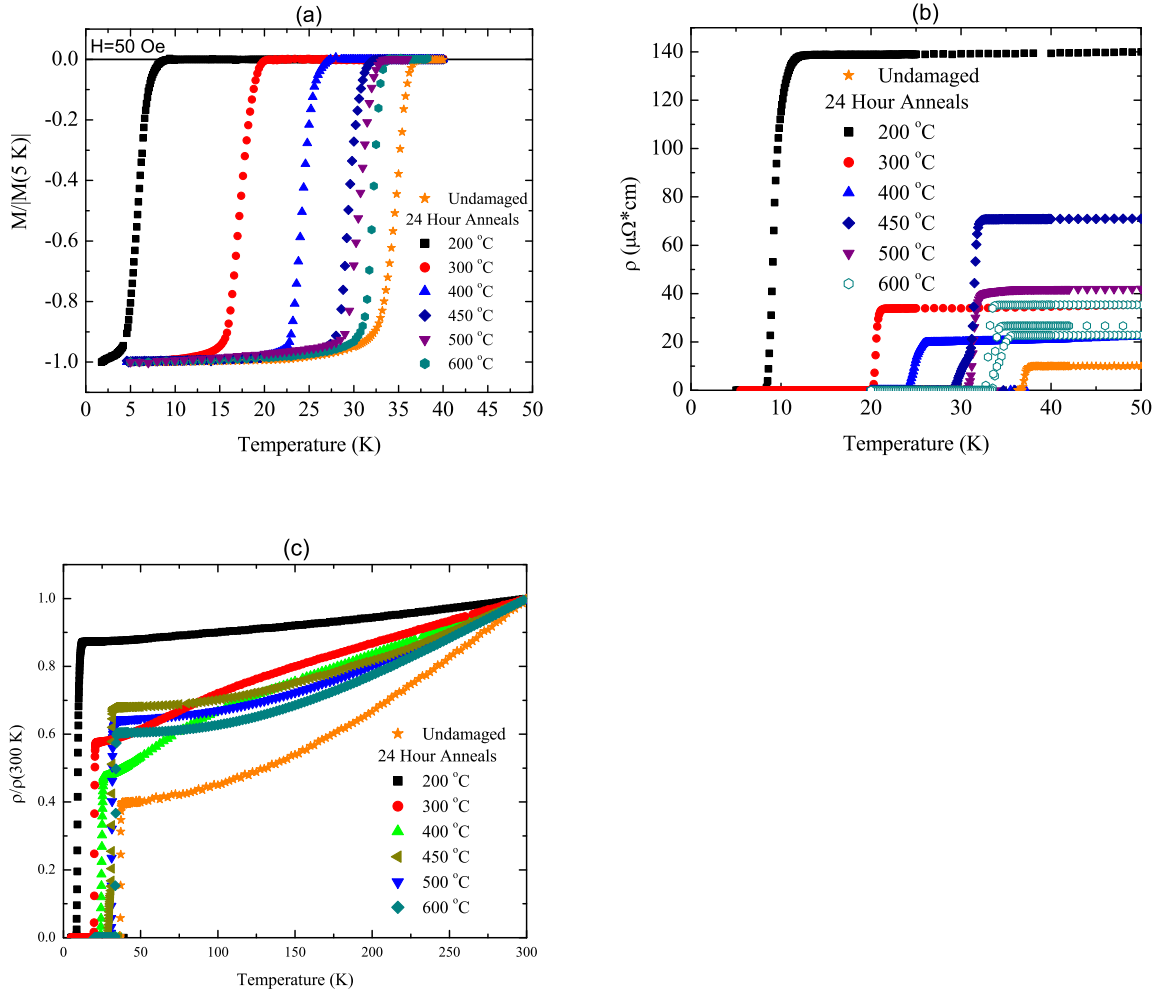


Figure 10.5 Normalized magnetization (a) and zero field resistivity curves (b) for samples annealed at various temperatures for 24 hours. (c) Normalized resistivity curves for neutron irradiated $\text{Mg}(\text{B}_{0.962}\text{C}_{0.038})_2$ samples annealed for 24 hour at various temperatures.

10.2 Thermodynamic and Transport Measurements

Magnetization and transport measurements were performed to determine the evolution of T_c , H_{c2} , and normal state resistivity as a function of annealing time and temperature. T_c was determined using an onset criteria in resistivity measurements and a 1% screening criteria in magnetization. Figure 10.5a presents normalized magnetization curves for the entire set of one day annealed samples. As the annealing temperature is increased, the transition temperature monotonically approaches the undamaged value of 36.8 K. It is worth noting that all of the $M(T)$ curves show sharp transitions.

Resistivity versus temperature data is plotted in figure 10.5b. Normal state resistivity values decrease monotonically as a function of annealing temperature up until $T_{anneal}=450$ °C, at which point ρ_0 increases approximately by a factor of four. The exact cause of this jump in ρ_0 is unknown, but it coincides with the broadening of the (002) x-ray peak. Subsequent increases in the annealing temperature result in decrease in ρ_0 relative to the $T_{anneal}=450$ °C sample. (It has to be mentioned that an alternative way of describing these data is to note that the residual resistivities of samples annealed at 200 °C, 450 °C, 500 °C, and 600 °C are monotonic as a function of the annealing temperature, raising the question as to whether it is the resistivities of the 300 °C and 400 °C annealed samples that are in fact anomalous.) Multiple measurements of samples annealed at 600 °C for 24 hours are included in figure 10.5b and illustrate the spread in the data. It should be noted that all three of these filaments are from the same quartz ampoule. All three samples show a decrease in resistivity relative to that of the 500 °C annealed sample, but are still above the minimum attained by annealing at 400 °C.

A plot of the normalized, $\rho/\rho(300\text{ K})$, resistivity shows that there are two interesting features in the evolution of the normal state resistivity as a function of annealing temperature (Figure 10.5c). For the samples annealed at 300 °C and 400 °C, the temperature dependence, $\rho(T)$, has an odd hump in the 100 K to 150 K range. Such a hump was not been observed in pure MgB_2 wires (55) but has been reported for for neutron damaged pure MgB_2 annealed up to a temperature of 400 °C for 24 hours (15). The trends seen in the calculated normal

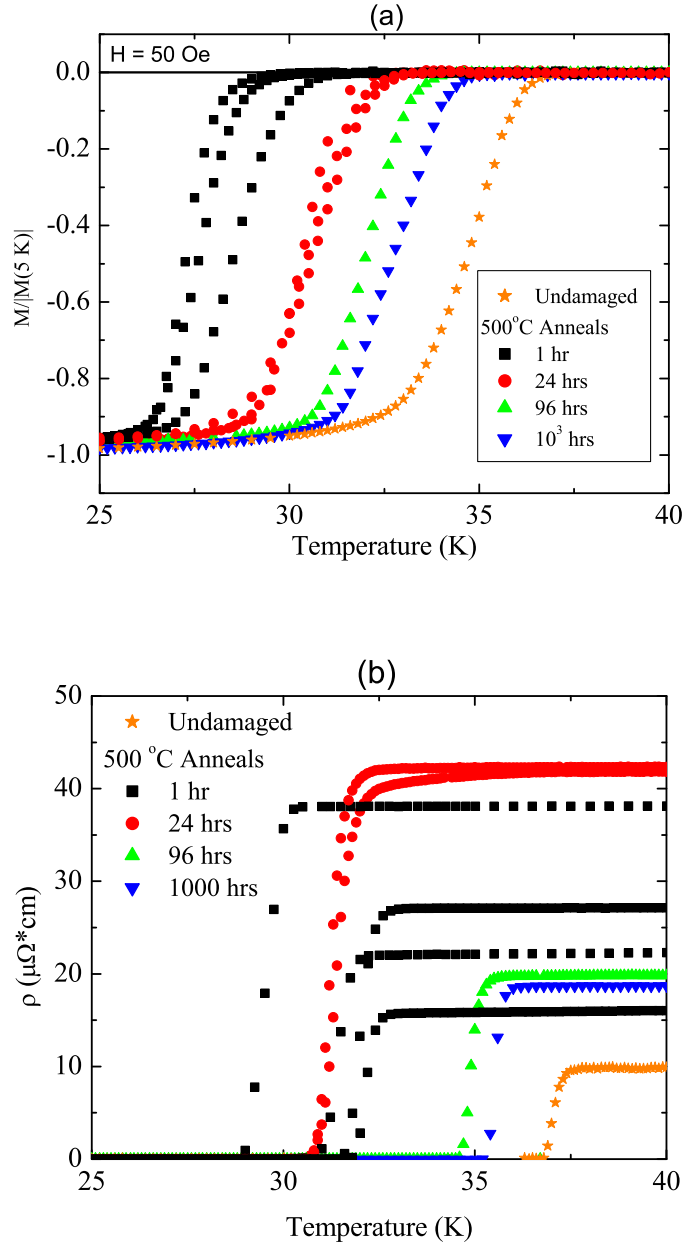


Figure 10.6 Normalized magnetization (a) and zero field resistivity curves (b) for samples annealed at various times at 500 °C.

state resistivity values are also seen in normalized resistivity (Figure 10.5c), indicating the apparent increase in resistivity occurring at 450 °C is a real effect and not the result of some type of geometrical effect, such as cracking. It should be noted that whereas the transport measurements show changes in the evolution of both ρ_0 and $\rho(T)$ as a function of annealing temperature for samples annealed from 300 °C to 450 °C, the magnetization data showed smooth, sharp transitions with monotonic increases in T_c throughout this range of annealing temperatures.

Magnetization and transport curves for the series of samples annealed at 500 °C for various times are plotted in figure 10.6. Multiple measurements of samples annealed for 1 hour and 24 hours were performed. The 1 hour anneal transport data consists of sets of two wires from two different ampoules. One set was then used for magnetization measurements and is included along with a filament from a third ampoule. The 24 hour data consists of 2 wires from a single ampoule and an additional filament from a second ampoule. The normalized magnetization transitions for the 1 hour anneals all fall below those of the 24 hour anneals (Figure 10.6a). However, for the transport data, the range of T_c values is broader and several of the transitions occur at temperatures greater than is seen for the 24 hour anneals (Figure 10.6b). It should be noted that for the samples annealed at 500 °C for 1 hour for which both magnetization and transport measurements were performed, in both cases the transport data showed a T_c that were approximately 0.5 K to 1 K higher than was observed in the magnetization measurements. Such a spread was also observed in the case of neutron irradiation on pure MgB₂ (15), suggesting the spread in the data is a reflection of sample to sample variation.

The multiple transport measurements on samples annealed at 500 °C for one hour also exhibit considerable spread in the the normal state resistivity values, and no systematic evolution of ρ_0 as a function of annealing time is observed. But residual resistivity ratios of these samples indicate that the observed spread in resistivity values represents true sample to sample variation in ρ_0 .

In the case of samples annealed at 500 °C for various times, generally speaking, extending the annealing time tends to decrease ΔT_c , although there is considerable spread in the data

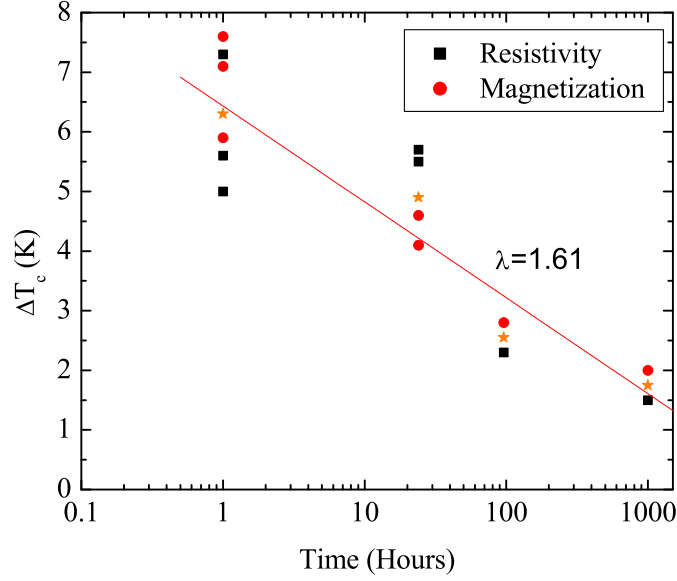


Figure 10.7 ΔT_c as a function of time for 500 °C anneals. The stars represent the midpoint of spread for a given time and the rate constant, λ , is determined by a linear fit of these data.

(Figure 10.7). For neutron irradiated pure MgB₂ wires, ΔT_c , which was taken as a measure of the defect concentration, was found to decrease exponentially with time (15), indicating defects are being annealed out by a singly activated process with random diffusion (96). For such samples, the defect concentration, n , obeys the relation

$$n = n_o e^{\lambda t} \quad (10.1)$$

where n_o is the initial defect concentration, λ is a rate constant, and t is the time. λ is a function of the activation energy, E_a , and diffusion coefficients. For samples which do show an exponential behavior in the decrease of ΔT_c (and by presumption) the defect density as a function of annealing time the activation energy can be determined by the so-called cross-cut procedure (96). This involves comparing the annealing time for which different temperature anneals reached the same defect density, i.e. ΔT_c . If a ΔT_c is reached by annealing at a

temperature T_1 for a time t_1 and by annealing at a temperature T_2 for a time t_2 , then the activation energy is related to these quantities by:

$$\ln \frac{t_1}{t_2} = \frac{E}{k} \left(\frac{1}{T_1} - \frac{1}{T_2} \right). \quad (10.2)$$

Unfortunately, we did not have a sufficient number of samples to perform studies of the temperature dependence of ΔT_c as a function of annealing time at any temperatures other than 500 °C. However, if we assume that the primary difference between neutron irradiation of pure and carbon doped MgB_2 is in the activation energies, then we can gain some insight by comparing λ values attained from the two sets of samples. For the case of the carbon doped samples, since the spread in T_c for a given annealing time is so large, we can obtain only a rough estimate, based on a fitting of the midpoint of the T_c values. Such a calculation yields a rate constant of $\lambda = 1.61 \text{ s}^{-1}$. For irradiation on pure MgB_2 anneals at 200 °C, 300 °C, and 400 °C yielded rate constants of 2.77 s^{-1} , 2.21 s^{-1} , and 3.51 s^{-1} respectively (15). Although there is considerable spread in the rate constants for the pure MgB_2 case, and considerable uncertainty in the rate constant associated with the carbon doped MgB_2 samples (estimates of λ from raw data range from 1.00 s^{-1} to 2.03 s^{-1}), analysis of equation 2 show that the since carbon doped sample has a lower rate constant than pure MgB_2 samples the activation energy is higher for carbon doped samples. It should be noted that higher reaction temperatures were required to synthesize carbon doped MgB_2 than pure MgB_2 (86), suggesting that there are different energy scales associated with carbon doping.

Upper critical field values were determined using the onset criteria in both resistivity versus temperature in applied fields up to 14 T and resistivity versus field in field sweeps up to 32.5 T (Figure 10.8). The complete $H_{c2}(T)$ curves for the entire set of annealing profiles is given in figure 10.9. The set forms a sort of "Russian doll pattern," with $H_{c2}(T=0)$ approximately scaling with T_c . Such behavior was also observed for neutron irradiation and post-exposure anneals on pure MgB_2 filaments (15).

Critical currents densities were estimated from magnetization hysteresis loops using the Bean Critical State Model (18) for cylindrical geometry. Figure 10.10a shows the field depen-

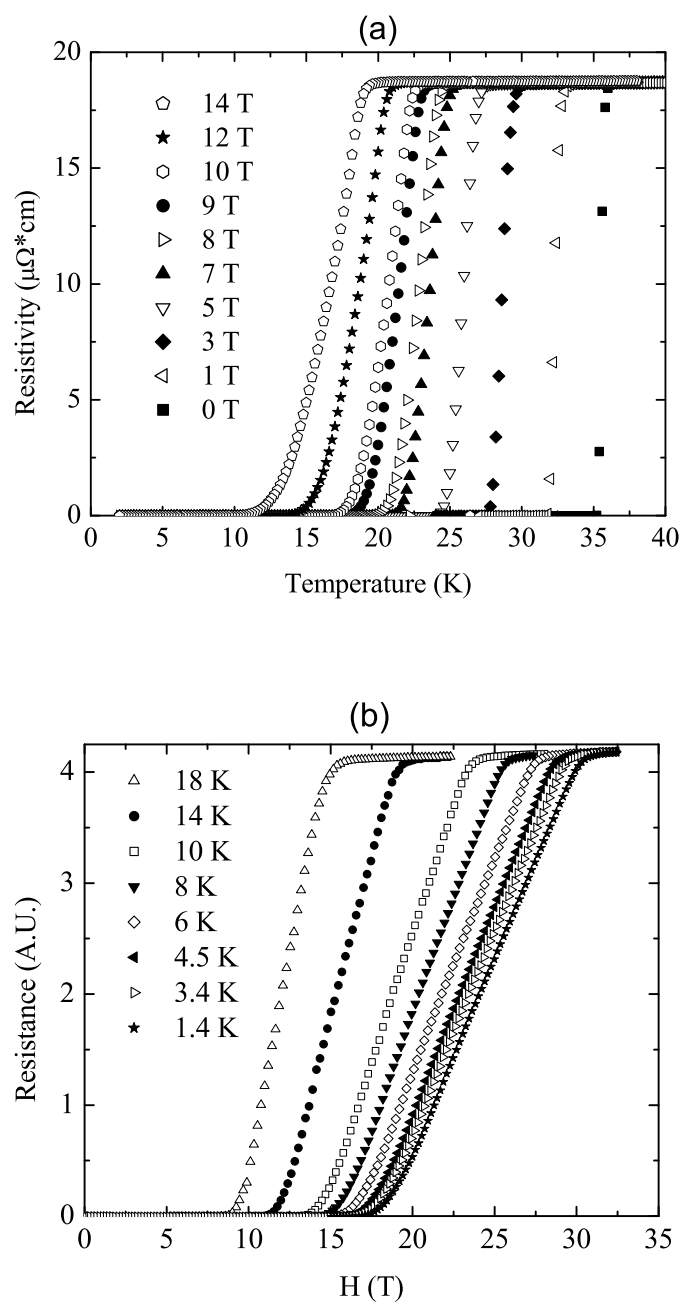


Figure 10.8 Resistivity versus temperature (a) and resistivity versus field (b) for a sample annealed at 500 °C for 1000 hours.

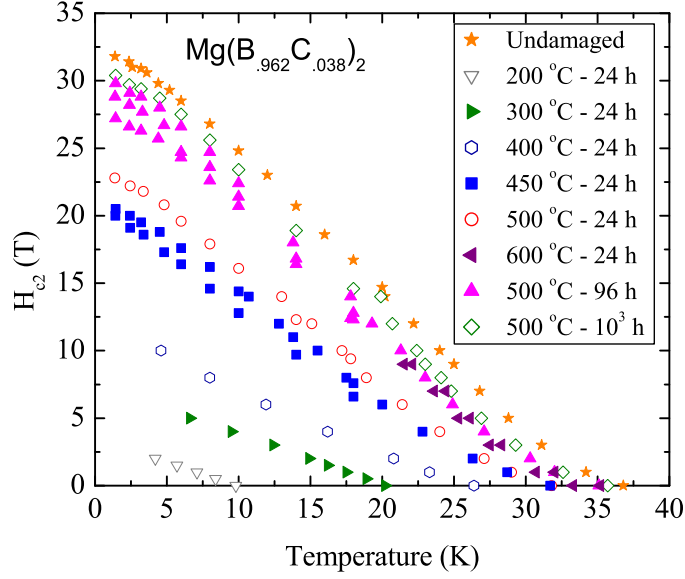


Figure 10.9 Upper critical field curves for samples annealed for 24 hours at various temperatures and samples annealed for various times at 500 °C. Multiple data sets exist for the 450 °C/24 hour and 500 °C/96 hour anneals. $H_{c2}(T=0)$ approximately scales with T_c .

dence of J_c at $T=5$ K for the entire set of 24 hour anneals at various annealing temperatures. For the set of one day anneals, the in field performance improves with annealing temperature, up to 500 °C. Presumably the increase transition temperature and hence decreased reduced temperature (T/T_c) of the measurement, is the primary cause of the enhancement. However, there exists a much greater increase in in-field J_c values between the sample annealed at 400 °C and the sample annealed at 450 °C than between the sample annealed at 300 °C and the sample annealed at 400 °C. Whereas increasing the annealing temperature from 300 °C to 400 °C results in a near 7 K or 36% increase in T_c but only a factor of two improvement in J_c at all fields, increasing the annealing temperature from 400 °C to 450 °C results in only an additional 5 K increase or 17% increase in T_c , but nearly an order of magnitude increase in in-field J_c values. This suggests the increase in disorder between the hexagonal planes, which coincided

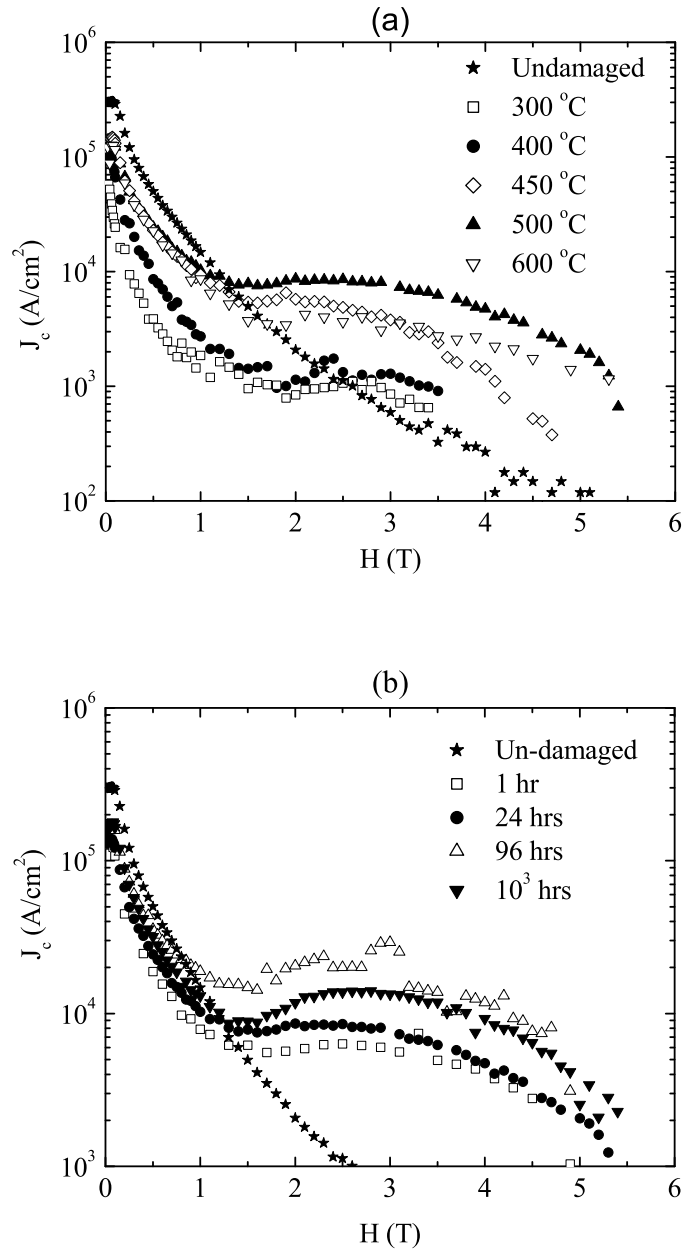


Figure 10.10 Critical current densities at 5 K inferred from magnetization hysteresis loops. (a) Samples annealed at various temperatures for 24 hours. (b) Samples annealed at 500 °C for various times.

with an increase in resistivity, may also play a role in enhancing the flux pinning. The sample annealed at 600 °C shows slightly reduced $J_c(H)$ values relative to the 500 °C anneal. Thus, at 600 °C, either the increased order along c is diminishing J_c , or we are beginning to anneal out some of the defects which are effective at pinning vortices, or some combination thereof.

Extending the annealing time from 1 hour to 96 hours at 500 °C results in relatively minor increases in in-field J_c values (Figure 10.10b). The data for the 500 °C and 96 hour anneal is particularly noisy and may not truly be enhanced relative to the 500 °C/10³ hour anneal. All of these 500 °C anneals show J_c remaining fairly constant over the field range of 1-4 Tesla.

At 5 K, the best in field performance, which results from the 96 and 1000 hour anneals at 500 °C, yield J_c values which maintain 10^4 A/cm² in an applied field of 4 T. In comparison, the best in field performance at 5 K for a sample of neutron irradiated pure MgB₂ dropped below 10^4 A/cm² in an applied field of approximately 1.5 T (15) and an undamaged carbon doped filament dropped below this level near 1 T (86).

10.3 Discussion

Up to an annealing temperature of 400 °C, the behavior of irradiated carbon doped samples is quite similar to that of irradiation of pure MgB₂ filaments. As-damaged samples have expanded unit cells and suppressed superconducting transition temperatures. Post exposure annealing tends to return the lattice parameters and T_c towards the undamaged values. In both cases, the upper critical field values, $H_{c2}(T=0)$ tend to scale with T_c .

The intriguing aspect of neutron damage in the carbon doped samples is the temperature induced decrease in structural order in the c - direction which occurs near $T_{anneal}=450$ °C. No such effect was seen in the case of neutron irradiation in pure MgB₂ filaments. The feature doesn't appear to be a phase segregation as no double transition is seen in magnetization. Furthermore, samples annealed at 500 °C showed sharp, single transitions in both magnetization and resistivity, while the having broad (002) peaks. The sample annealed for 24 hours at 600 °C showed evidence of having two distinct phases with different c - lattice parameters but the same a - lattice parameter. Here again, both the magnetization and transport data showed

only single transitions. Thus the transition temperature appears to be insensitive to the c-lattice parameter. The a-lattice parameter is presumably not the sole determining factor for T_c , as samples annealed for 24 hours at 450 °C and 500 °C showed increases in Δa relative to the sample annealed for 24 hours 400 °C, while also having increased T_c values. It should be noted that although measurements on single filaments showed sharp, single transitions, there was significant spread in the T_c values between different samples.

The broadening of the (002) peak coincides with a near 4 fold increase in the normal state resistivity and approximate order of magnitude increase in in-field J_c values. Increases in normal state resistivity for annealing temperatures above 400 °C have been observed in neutron irradiation of pure MgB_2 (62). In this case, the authors report a continued increase in ρ_0 as a function of annealing temperature above 400 °C and attribute it to a loss of intergrain connectivity. In contrast our data show a decrease in ρ_0 for 24 hour anneals at 500 °C and 600 °C, which supports the notion that a different mechanism is responsible for the anomalous behavior in the normal state resistivity of neutron irradiated carbon doped samples.

Despite the decrease in structural order along the c-axis and large increase in resistivity at $T_{\text{anneal}}=450$ °C, no qualitative changes to the evolution of T_c and H_{c2} as a function of annealing temperature were observed. The transition temperature tends to approach that of the undamaged sample and H_{c2} continues to roughly scale with T_c . Even the 500 °C, 1000 hour anneal shows a suppressed $H_{c2}(T=0)$ value relative to the undamaged sample. This is in contrast to the results obtained with irradiation of pure MgB_2 filaments (11). For fluence levels of 4.75×10^{18} n/cm² and 9.50×10^{18} n/cm², two values which envelop the 7.13×10^{18} n/cm² fluence level used in this study, $H_{c2}(T=0)$ was enhanced by approximately 2 T and 3 T respectively.

Both pure and carbon doped samples show increases in normal state resistivity after annealing (Figure 10.11). Pure MgB_2 wires irradiated with a fluence of 4.75×10^{18} n/cm² and subsequently annealed for 24 hours at various temperatures showed an increase in ρ_0 at an annealing temperature of 200 °C. In contrast, for $\text{Mg}(\text{B}_{0.962}\text{C}_{0.038})_2$ filaments exposed to a fluence of 7.13×10^{18} n/cm² and subsequently annealed for 24 hours at various temperatures, the apparent anomalous increase occurs for an annealing temperature of 450 °C. For both sets of

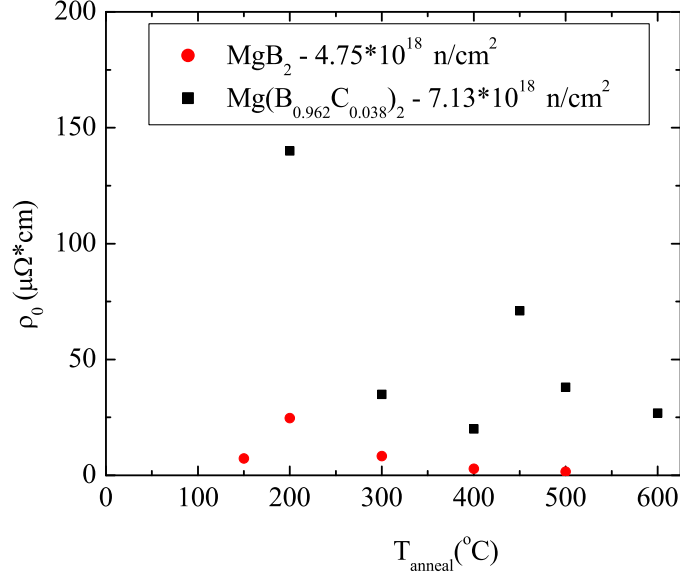


Figure 10.11 Evolution of the normal state resistivity as a function of annealing temperature in neutron irradiated pure and carbon doped MgB_2 filaments.

samples, following the abrupt increase, the normal state resistivity decreases monotonically as a function of annealing temperature. It should be noted however, that, in the case of the carbon doped samples, it is not clear whether or not there exists some correlation between the change in the temperature dependence of the normal state resistivity for the 300 °C and 400 °C anneals and the reduced ρ_0 values for these anneals. That is, rather than the jump in ρ_0 at 450 °C representing an anomalous increase, the ρ_0 values associated with the samples annealed at 300 °C and 400 °C may in fact be anomalously low.

These data, coupled with the analysis of the rate constants, suggest that in the case of neutron irradiated carbon doped MgB_2 samples, there is a different, and higher, energy scale associated with the annealing of defects. This is perhaps not altogether surprising, as it was shown that higher reaction temperatures were necessary to form the carbon doped phase. Whereas pure boron filaments can be fully converted to MgB_2 in as little as 2 hours at 950

$^{\circ}\text{C}$ (67), isothermal reactions required 48 hours at 1200°C to convert carbon doped boron fibers to $\text{Mg}(\text{B}_{1-x}\text{C}_x)_2$, even for doping levels as low as $x=0.004$ (86). Although diffusion of Mg vapor into a carbon doped boron matrix and repair of neutron induced damage are indeed two, rather different, phenomena, this correlation is at least worth noting.

The temperature dependence of the upper critical field shows positive curvature near T_c for samples with a T_c near 26 K and above (Figure 10.9). For the samples annealed for 24 hours at 200°C and 300°C H_{c2} approaches T_c linearly. If the two bands are fully mixed, the temperature dependence of the upper critical field should follow WHH (33) behavior, where $H_{c2}(T=0)$ is given by:

$$H_{c2}(T = 0) = 0.69T_c \frac{dH_{c2}}{dT}. \quad (10.3)$$

Calculating $H_{c2}(T=0)$ using equation 3 for the samples annealed for 24 hours at 200°C , 300°C , and 400°C yields values of 2.4 T, 5.2 T, and 6.5 T. Experimentally, lowest temperature H_{c2} values we could reliably attain from transport measurements for each of these samples were 2.1 T, 6.5 T, and 10 T, occurring at temperatures of 4.2 K, 5.2 K, and 4.6 K respectively. Only for the sample annealed at 200°C does the WHH fit yield an $H_{c2}(T=0)$ value which is consistent with the experimentally observed data. Thus it is likely that only for samples with a T_c below 10 K are the bands fully mixed. Such a result was also obtained in the case of the neutron irradiation on pure MgB_2 (11). This implies that the inter-band scattering rates resulting from defects associated with the neutron irradiation are comparable in both pure and carbon doped samples, suggesting that the scattering associated with the two different sources of defects act independently. This is not altogether surprising as the suppression in T_c for carbon doped samples is believed to result from changes in the Fermi surface, rather than increases in inter-band scattering and scattering associated with carbon doping is believed to be primarily within the π band (3). Thus if inter-band scattering is introduced primarily through defects resulting from neutron damage, and if pure and carbon doped samples have similar initial T_c values, then they should also exhibit fully mixed bands at similar T_c s, which was experimentally observed. A similar result was found in the case of neutron irradiation on

pure MgB_2 filaments, implying that the scattering associated with carbon doping and neutron irradiation act independently.

CHAPTER 11. Conclusions and Future Work

In this thesis I have presented the results of investigations into the changes in the superconducting properties of MgB_2 as a function of carbon doping and neutron irradiation. The goal has been to understand the physics underlying this unique two-gap superconductor as different types of perturbations are made to the system. Such knowledge not only contributes to our understanding of two-gap superconductivity, but could potentially lead to the development of superconducting MgB_2 wires for the use in power applications near 20 K.

Systematic carbon doping of superconducting MgB_2 was achieved by pre-doping boron filaments using carbon and boron containing precursor gases in a chemical vapor deposition system. We have succeeded in synthesizing $\text{Mg}(\text{B}_{1-x}\text{C}_x)_2$ up to $x=0.052$, which results in a more than two fold increase in the upper critical field, up to near 36 T extrapolated to zero Kelvin. Full conversion of the carbon doped fibers into $\text{Mg}(\text{B}_{1-x}\text{C}_x)_2$ required high temperatures and long reaction times, resulting in large grains and poor flux pinning. Tailoring of the reaction time and temperature profile can somewhat reduce this problem.

We have shown that both Ti and C can simultaneously be added to MgB_2 . A sample containing 0.5% Ti and 2.1% C and reacted with excess Mg vapor at 1200 °C showed similar H_{c2} values at low temperatures as a sample doped with 2.1% carbon. TEM images showed the Ti formed TiB_2 precipitates embedded within the MgB_2 matrix. No evidence for the formation of TiC precipitates was seen. The long time and high reaction temperatures necessary to synthesize the fully dense filaments resulted in a coarsening of the precipitates. The precipitates were approximately 50 nm in size, which is too large to be effective in pinning flux and as a result no enhancement in J_c values was observed. It is plausible that Ti additions to carbon doped MgB_2 will lead to both high H_{c2} values, resulting from the carbon doping, and

enhanced in-field J_c values, resulting from increasing pinning associated with the addition of TiB_x pinning centers. However, different synthesis methods, which allow for shorter time and lower temperature reactions needs to be developed.

We have established a method for synthesizing $Mg(B_{1-x}C_x)_2$ using a mixture of distilled magnesium, boron and the binary compound B_4C . Impurities in the starting boron affect T_c and the magnitude of the a-lattice parameter. By tracking $|\Delta a|$ and T_c we were able to show that different boron purities lead to differing $T_c(|\Delta a|)$ manifolds. There appears to be a solubility limit in the carbon content for samples synthesized at 1200 °C and 1 atm near $x \sim 0.07$. Lower purity boron in the starting material results in lower transition temperatures and appears to limit the maximum achievable upper critical field.

Fine grain doped boron powders that are ideally suited for powder-in-tube applications can be synthesized by plasma spray processing. The powders are approximately 50 nm in size and form lacy agglomerates that are as large as 10 μm . The fine grain nature allows for dramatically reduced reaction temperatures relative to fully dense carbon doped fibers. Whereas the 80 μm diameter carbon doped fibers required 48 hours at 1200 °C to be fully converted, conversion of doped powders was achieved in as little as 4 hours at 950 °C. Low temperature reactions lead to superconducting grains that are of order 1 μm in size, which in turn lead to enhanced J_c values, pushing the field at which J_c drops below 10^5 A/cm² at 5 K out to near 5.5 T in the case of a pellet containing 8.1% carbon.

We systematically studied the effects of neutron fluence level, annealing temperature, and annealing time on the superconducting and normal state properties of MgB_2 . As damaged samples showed an anisotropic expansion of the unit cell and a suppression of T_c to below 5 K. Defects introduced by the irradiation process had a low activation energy and hence much of the damage could be repaired by post-exposure annealing. H_{c2} values tended to scale with T_c and the evolution of H_{c2} with ρ_0 was dramatically different than in the case of carbon doping. Lithium produced through nuclear processes appeared to have no significant effects on the superconducting properties. We attribute the changes in the superconducting properties of neutron irradiated samples primarily to an increase in scattering between the two bands.

We have studied superconducting and normal state properties of neutron irradiated carbon doped MgB_2 filaments as a function of post exposure annealing time and temperature. In spite of anomalous behavior in the evolution of the c - lattice parameter and normal state resistivity T_c tended to return towards the undamaged value with increased annealing time and temperature. Upper critical field values were found to approximately scale with T_c and exhibited WHH like behavior, suggesting a complete mixing of the two bands, for samples with T_c near 10 K. Neutron irradiation of pure MgB_2 also led to a complete mixing of the bands near 10 K, suggesting that the scattering associated with carbon doping and neutron irradiation act independently.

The neutron damage experiments discussed in this thesis all involved fluences which fully suppressed or nearly fully suppressed superconductivity. Therefore, many of the sample underwent post exposure annealing. An alternative approach is to lower the fluence levels and investigate superconducting properties of as-damaged samples which exhibit T_c values above 30 K. Other research groups have reported enhanced H_{c2} values for as-damaged samples with only slightly suppressed T_c values. Although these reports use different irradiation conditions (e.g. isotopically enriched ^{11}B , Cd shielding, etc.), the results suggest we may see different behavior for lower fluence levels. Additionally, no direct measurements of the superconducting gaps was performed on any of the neutron irradiated samples. Tunnelling measurements and/or specific heat data are needed to confirm our conjecture regarding the merging of the gaps for a T_c near 10 K.

Much of the work was done on high purity polycrystalline samples made from doped boron wires produced by Chemical Vapor Deposition. Although other groups have been successful in synthesizing small single crystals of carbon doped MgB_2 , the CVD approach has allowed us to add a variety of chemical impurities to bulk samples of MgB_2 and access their physical properties. In addition to providing an avenue to address issues associated with the basic physics of doped MgB_2 samples, the CVD approach, through plasma spray synthesis, may prove to be an important synthesis technique for the production of commercially viable MgB_2 powders for powder-in-tube wire fabrication.

In order to further develop the plasma spray technology, several technical issues need to be addressed. It is desirable to introduce additional pinning centers in carbon doped MgB_2 powders. One possibility is to dope the powders with Ti, which has been shown to form ~ 10 nm sized TiB precipitate for reaction profiles similar to those used in converting the carbon doped boron powders to $\text{Mg}(\text{B}_{1-x}\text{C}_x)_2$. It should be noted that Ti is not the only potential candidate for precipitate formation. Many other transition metals form chlorides which can readily be used in plasma spray synthesis. The thermodynamics of the boride precipitate formation may be more favorable for a different transition metal. The technical problems of how to successfully introduce these transition metals into the B powder need to be solved in order to further investigate precipitate pinning in MgB_2 . Additionally, while the process of reacting pressed pellets to investigate superconducting properties for samples of a given composition is relatively straight forward, scaling the production up to produce long length PIT wires is a non-trivial issue that needs to be addressed. Although many groups have synthesized PIT MgB_2 wires, the unique reaction conditions necessary for optimizing superconducting properties in doped boron powders may require different synthesis conditions and wire architecture.

Bibliography

- [1] J. Nagamatsu, N. Nakagawa, T. Muranaka, Y. Zenitani, and J. Akimitsu, *Nature* 410 (2001) 63.
- [2] D.C. Larbalestier, L.D. Cooley, M.O. Rikel, A.A. Polyanskii, J. Jiang, S. Patnaik, X.Y. Cai, D.M. Feldmann, A. Gurevich, A.A. Squitieri, M.T. Naus, C.B. Eom, E.E. Hellstrom, R.J. Cava, K.A. Regan, N. Rogado, M.A. Hayward, T. He, J.S. Slusky, P. Khalifah, K. Inumaru, M. Haas, *Nature* 410 (2001) 186.
- [3] S.L. Bud'ko, C. Petrovic, G. Lapertot, C.E. Cunningham, P.C. Canfield, M-H. Jung, and A.H. Lacerda, *Phys. Rev. B* 63 (2001) 220503.
- [4] S.L. Bud'ko, V.G. Kogan, and P.C. Canfield, *Phys. Rev. B* 64 (2001) 180506.
- [5] Terry P. Orlando and Kevin A. Delin, *Foundations of Applied Superconductivity*, Addison-Wesley Publishing Company, Reading, 1991.
- [6] M. Eisterer, M. Zehetmayer, and H.W. Weber, *Phys. Rev. Lett.* 90 (2003) 247002.
- [7] P.C. Canfield, D.K. Finnemore, S.L. Bud'ko, J.E. Ostenson, G. Lapertot, C.E. Cunningham, and C. Petrovic, *Phys. Rev. Lett.* 86 (2001) 2423.
- [8] S.L. Bud'ko, G. Lapertot, C. Petrovic, C.E. Cunningham, N. Anderson, and P.C. Canfield, *Phys. Rev. Lett.* 86 (2001) 1877-1880.
- [9] I.I. Mazin, V.P. Antropov, *Physica C* 385 (2003) 49.
- [10] H.J. Choi, M.L. Cohen, and S.G. Louie, *Physica C* 385 (2003) 66.
- [11] M. Tinkham, *Introduction to Superconductivity*, McGraw-Hill, Inc., New York, 1996.

- [12] R.A. Fisher, G. Li, J.C. Lashley, F. Bouquet, N.E. Phillips, D.G. Hinks, J.D. Jorgensen, G.W. Crabtree, *Physica C* 385 (2003) 180.
- [13] R.J. Cava, H.W. Zandbergen, K. Inumaru, *Physica C* 385 (2003) 8.
- [14] M. Angst, S.L. Bud'ko, R.H.T. Wilke, and P.C. Canfield, *Phys. Rev. B* 71 (2005) 144512.
- [15] R. Puzniak, M. Angst, A. Szewczyk, J. Jun, S.M. Kazakov, and J. Karpinski, *cond-mat/0405060*.
- [16] S.L. Bud'ko and P.C. Canfield, *Phys. Rev. B* 65 (2002) 212501.
- [17] L. Lyard, P. Samuely, P. Szabo, T. Klein, C. Marcenat, L. Paulius, K.H.P. Kim, C.U. Jung, H.-S. Lee, B. Kang, S. Choi, S.-I Lee, J. Marcus, S. Blanchard, A.G.M. Jansen, U. Welp, G. Karapetrov, and W.K. Kwok, *Phys. Rev. B* 66 (2002) 180502.
- [18] A.C. Damask and G.J. Dienes, *Point Defects in Metals*, Gordon and Breach, Science Publishers, Inc., New York, 1963.
- [19] J. Bardeen, L.N. Cooper, and J.R. Schrieffer, *Phys. Rev.* 108 (1957) 1175.
- [20] W.L. McMillan, *Phys. Rev.* 167 (1968) 331.
- [21] J. Shelton, H. Ullmaier, and W. Schmatz, *Phys. Status Solidi B* 48 (1971) 619.
- [22] A.L. Fetter and P.C. Hohenberg in; R.D. Parks (Ed.) *Superconductivity*, Marcel Decker, New York, 1969, p. 817.
- [23] V.G. Kogan, *Phys. Rev. B* 31 (1985) 1318.
- [24] E. Helfand and N.R. Werthamer, *Phys. Rev.* 147 (1966) 288.
- [25] M. Suenaga, K. Aihara, and T.S. Luhman, *Advances in Cryogenic Engineering* 26 (1980) 442.
- [26] E.J. Kramer, *J. Appl. Phys.* 44 (1973) 1360.
- [27] A. Gurevich, *Phys. Rev. B* 67 (2003) 184515.

- [28] J.B. Ketterson and S.N. Song, Superconductivity, Canmbridge University Press, Cam-
bridge, 1999.
- [29] S.V. Pokrovsky and V.L. Pokrovsky, Phys. Rev. B 54 (1996) 13275.
- [30] A.A. Golubov and I.I. Mazin, Phys. Rev. B 55 (1997) 15146.
- [31] A.A. Golubov, J. Kortus, O.V. Dolgov, O. Jepsen, Y. Kong, O.K. Andersen, B.J. Gibson,
K. Ahn, and R.K. Kremer, J. Phys.: Condens. Matter 14 (2002) 1353.
- [32] P.G. de Gennes, Phys. Kondens. Mater, 3 (1964) 79.
- [33] N.R. Werthamer, E. Helfand, and P.C. Hohenberg, Phys. Rev. 147 (1966) 295.
- [34] C.P. Bean, Phys. Rev. Lett 8 (1962) 250.
- [35] P.C. Canfield and G.W. Crabtree, Physics Today, March 2003, p.34.
- [36] J.M. An, and W.E. Pickett, Phys. Rev. Lett. 86 (2001) 4366.
- [37] H. Kamerlingh Onnes, Leiden Comm. 120b, 122b, 124c (1911).
- [38] J.R. Gavaler, Appl. Phys. Lett. 23 (1973) 480.
- [39] R.J. Cava, H. Takagi, B. Batlogg, H.W. Zandbergen, J.J. Krajewski, W.F. Peck Jr., R.B.
van Dover, R.J. Felder, T. Siegrist, Nature 367 (1994) 146.
- [40] J.G. Bednorz and K.A. Müller, Z. Phys. B64 (1986) 661.
- [41] S.L. Bud'ko, G. Lapertot, C. Petrovic, C.E. Cunningham, N. Anderson, and P.C. Canfield,
Phys. Rev. Lett. 86 (2001) 1877.
- [42] D.G. Hinks, H. Claus, J.D. Jorgensen, Nature 411 (2001) 457.
- [43] H. Kotegawa, K. Ishida, Y. Kitaoka, T. Muranaka, and J. Akimitsu, Phys. Rev. Lett. 87
(2001) 127001.
- [44] D.G. Hinks, J.D. Jorgensen, Physica C 385 (2003) 98.

- [45] P.C. Canfield, S.L. Bud'ko, and D.K. Finnemore, *Physica C* 385 (2003) 1.
- [46] L.Ya. Vinnikov, J. Karpinski, S.M. Kazakov, J. Jun, J. Anderegg, S.L. Bud'ko, and P.C. Canfield, *Physica C* 385 (2003) 177.
- [47] M.R. Eskildsen, M. Kugler, G. Levy, S. Tanaka, J. Jun, S.M. Kazakov, J. Karpinski, and Ø. Fischer, *Physica C* 385 (2003) 169.
- [48] F. Simon, A. Jánossy, T. Fehér, F. Murányi, S. Garaj, L. Forró, C. Petrovic, S.L. Bud'ko, G. Lapertot, V.G. Kogan, and P.C. Canfield, *Phys. Rev. Lett.* 87 (2001) 047002.
- [49] S.L. Bud'ko, P.C. Canfield, and V.G. Kogan, *AIP Conference Proceedings*, 614 (2002) 846.
- [50] P. Samuely, P. Szabó, J. Kačmarčík, T. Klein, A.G.M. Jansen, *Physica C* 385 (2003) 244.
- [51] H. Suhl, B.T. Matthias, and L.R. Walker, *Phys. Rev. Lett.* 3 (1959) 552.
- [52] V.A. Moskalenko, *Fiz. Metal. Metalloved.* 8 (1959) 503.
- [53] G. Binnig, A. Baratoff, H.E. Hoenig, and J.G. Bednorz, *Phys. Rev. Lett.* 45 (1980) 1352.
- [54] T. Yokoya, T. Kiss, A. Chainani, S. Shin, M. Nohara and H. Takagi, *Science* 294 (2001) 2518.
- [55] P.C. Canfield, D.K. Finnemore, S.L. Bud'ko, J.E. Ostenson, G. Lapertot, C. Petrovic, *Phys. Rev. Lett.* 86 (2001) 2423.
- [56] D.K. Finnemore, J.E. Ostensen, S.L. Bud'ko, G. Lapertot, and P.C. Canfield, *Phys. Rev. Lett.* 86 (2001) 2420.
- [57] Y.B. Kim and M.J. Stevens, in: R.D. Parks (Ed.), *Superconductivity*, Marcel Dekker, New York, 1969, p. 1149.
- [58] *Physica C* 385 (2003), edited by G. Crabtree, W. Kwok, S.L. Bud'ko, and P.C. Canfield.
- [59] R.A. Ribeiro, S.L. Bud'ko, C. Petrovic, P.C. Canfield, *Physica C* 384 (2003) 227.

- [60] M. Avdeev, J.D. Jorgensen, R.A. Ribeiro, S.L. Bud'ko, P.C. Canfield, *Physica C* 387 (2003) 301.
- [61] P. Samuely, Z. Holánová, P. Szabó, J. Kačmarčík, R.A. Ribeiro, S.L. Bud'ko, and P.C. Canfield, *Phys. Rev. B* 68 (2003) 020505.
- [62] A.E. Karkin, V.I. Voronin, T.V. Dyachkova, A.P. Tyutyunnik, V.G. Zubkov, Yu. G. Zainulin, and B.N. Goshchitskii, *JETP Letters* 73 (2001) 570.
- [63] D.K. Finnemore, P.C. Canfield, S.L. Bud'ko, J.E. Ostenson, C. Petrovic, C.E. Cunningham, G. Lapertot, Manufacture of superconducting magnesium diboride objects from boron objects with similar form. U.S. Pat. Nos. 6,591,119 and 6,514,557 (2003)
- [64] P.C. Canfield, D.K. Finnemore, S.L. Bud'ko, J.E. Ostenson, G. Lapertot, C.E. Cunningham, C. Petrovic, *Phys. Rev. Lett.* 86 (2001) 2423.
- [65] R.J. Suplinskas and J.V. Marzik, Boron and Silicon Carbide Filaments, in: J.V. Milewski and H.S. Kats (Eds.) *Handbook of Reinforcements for Plastics*, Van Nostrand Reinhold, New York, 1987.
- [66] "Desk Handbook - Phase Diagrams for Binary Alloys," Hiroaki Okamoto editor, ASM International (2000).
- [67] C.E. Cunningham, C. Petrovic, G. Laperot, S.L. Bud'ko, F. Laabs, W. Straszheim, D.K. Finnemore, and P.C. Canfield, *Physica C* 353 (2001) 5.
- [68] Kenneth S. Krane, *Introduction to Nuclear Physics*, John Wiley & Sons, Inc., New York, 1988.
- [69] M. Paranthaman, J.R. Thompson, D.K. Christen, *Physica C* 335 (2001) 1.
- [70] T. Takenobu, T. Ito, D. H. Chi, K. Prassides, and Y. Iwasa, *Phys. Rev. B* 64 (2001) 134513.
- [71] A. Bharathi, S. Jemina Balaselvi, S. Kalavathi, G.L.N. Reddy, V. Sankara Sastry, Y. Hariharan, T. S. Radhakrishnan, *Physica C* 370 (2002) 211.

- [72] Z.-h. Cheng, B.-g Shen, J. Zhang, S.-y Zhang, T.-y Zhao, H.-w Zhao, J. Appl. Phys. 91 (2002) 7125.
- [73] W. Mickelson, John Cumings, W.Q. Han, and A. Zettl, Phys. Rev. B 65 (2002) 052505.
- [74] Z. Hoľanová, J. Kačmarčík, P. Szabó, P. Samuely, I. Sheikin, R. A. Ribeiro, S. L. Bud'ko and P. C. Canfield, Physica C 404 (2004) 195.
- [75] R.H.T. Wilke, S.L. Bud'ko, P.C. Canfield, D.K. Finnemore, Raymond J. Suplinskas, and S.T. Hannahs, Phys. Rev. Lett. 92 (2004) 217003.
- [76] S. Kirkpatrick, Reviews of Modern Physics 45 (1973) 574.
- [77] S.M. Kazakov, R. Puzniak, K. Rogacki, A.V. Mironov, N.D. Zhigadlo, J. Jun, Ch. Soltmann, B. Batlogg, and J. Karpinski, cond-mat/0405060.
- [78] Y. Zhao, Y. Feng, C.H. Cheng, L. Zhou, Y. Wu, T. Machi, Y. Fudamoto, N. Kosizuka, and M. Murakami, Applied Physics Letters, 79 (2001) 1154.
- [79] N.E. Anderson Jr., W.E. Straszheim, S.L. Bud'ko, P.C. Canfield, D.K. Finnemore, and R.J. Suplinskas, Physica C, 390 (2003) 11-15.
- [80] X.F. Rui, Y. Zhao, Y.Y. Xu, L. Zhang, X.F. Sun, Y.Z. Wang, and H. Zhang, Supercond. Sci. Technol. 17 (2004) 689-691.
- [81] J. Wang, Y. Bugoslavsky, A. Berenov, L. Cowey, A.D. Caplin, L.F. Cohen, J.L. MacManus Driscoll, L.D. Cooley, X. Song, and D.C. Larblestier, Applied Physics Letters 81 (2002) 2026-2028.
- [82] S.X. Dou, S. Soltanian, J. Horvat, X.L. Wang, P. Munroe, S.H. Zhou, M. Ionescu, H.K. Liu, and M. Tomsic, Applied Physics Letters, 81 (2002) 3419.
- [83] R.H.T. Wilke, S.L. Bud'ko, P.C. Canfield, M.J. Kramer, Y.Q. Wu, D.K. Finnemore, R.J. Suplinskas, J.V. Marzik, and S.T. Hannahs, Physica C 418 (2005) 160-167.

- [84] J.V. Marzik, R.J. Suplinskas, R.H.T. Wilke, P.C. Canfield, D.K. Finnemore, M. Rindfleisch, J. Margolies, and S.T. Hannahs, *Physica C* 423 (2005) 83.
- [85] Y. Zhao, D.X. Huang, Y. Feng, C.H. Cheng, T. Machi, N. Koshizuka, M. Murakami, *Appl. Phys. Lett* 80 (2002) 1640.
- [86] R.H.T. Wilke, S.L. Bud'ko, P.C. Canfield, D.K. Finnemore, Raymond J. Suplinskas, and S.T. Hannahs, , *Physica C* 424 (2005) 1.
- [87] A. Serquis, L. Civale, X.Z. Liao, J.Y. Coulter, Y.T. Zhu, M. Jaime, D.E. Peterson, F.M. Mueller, V.F. Nesterenko, and Y. Gu, *Appl. Phys. Lett.* 82 (2003) 2847.
- [88] P. Lezza, V. Abächerli, N. Clayton, C. Senatore, D. Uglietti, H.L. Suo, and R. Flükiger, *Physica C* 401 (2004) 305.
- [89] X.L. Wang, Q.W. Yao, J. Horvat, M.J. Qin, and S.X. Dou, *Supercond. Sci. Technol.* 17 (2004) L21.
- [90] Y. Zhao, Y. Feng, C.H. Cheng, L. Zhou, Y. Wu, T. Machi, Y. Fudamoto, N. Koshizuka, and M. Murakami, *Appl. Phys. Lett.* 79 (2001) 1154.
- [91] R.A. Ribeiro, S.L. Bud'ko, C. Petrovic, and P.C. Canfield, *Physica C* 382 (2002) 194.
- [92] X.L. Wang, S. Soltanian, M. James, M.J. Qin, J. Horvat, Q.W. Yao, H.K. Liu, and S.X. Dou, *Physica C*, 408-410 (2004) 63.
- [93] V. Selvamanickam, P.M. Martin, D.M. Kroeger, and M. Tomsic, *Supercond. Sci. Technol.* 8 (1995) 587.
- [94] R.H.T. Wilke, S.L. Bud'ko, P. C. Canfield, D. K. Finnemore, and S.T. Hannahs, *cond-mat/0507151*
- [95] A. Serquis, L. Civale, D.L. Hammon, X.Z. Liao, J.Y. Coulter, Y.T. Zhu, M. Jaime, D.E. Peterson, F. Mueller, V.F. Nesterenko, and Y. Gu, *App. Phys. Lett.* 82 (2003) 2847.

- [96] A.C. Damask and G.J. Dienes, Point Defects in Metals, Gordon and Breach, Science Publishers, Inc., New York, 1963.
- [97] M. Eisterer, M. Zehetmayer, S. Tonies, H. W. Weber, M. Kambara, N. Hari Babu, D.A. Cardwell, and L.R. Greenwood, Superconductor Science and Technology 15 (2002) L9-L12.
- [98] E. Babic, D. Miljanic, K. Zadro, I. Kusevic, Z. Marohnic, D. Drobac, X.L. Wang, and S.X. Dou, Fizika A 10 (2001) 87-94.
- [99] U.P. Trociewitz, P.V.P.S.S. Sastry, A. Wyda, K. Crockett, and J. Schwartz, IEEE Transactions on Applied Superconductivity 13 (2003) 3320-3323.
- [100] Y. Wang, F. Bouquet, I. Sheikin, P. Toulemonde, B. Revaz, M. Eisterer, H.W. Weber, J. Hinderer, and A. Junod, J. Phys.: Condens. Matter 15 (2003) 883-893.
- [101] M. Zehetmayer, M. eisterer, J. Jun, S.M. Kazakov, J. Karpinski, B. Birajdar, O. Eibl, and H.W. Weber, Phys. Rev. B 69 (2004) 054510.
- [102] M. Putti, V. Braccini, C. Ferdeghini, F. Gatti, P. Manfrinetti, D. Marre, A. Palenzona, I. Pallecchi, C. Tarantini, I. Sheikin, H.U. Aebersold, and E. Lehmann, App. Phys. Lett. 86 (2005) 112503.
- [103] M. Ortolani, D. Di Castro, P. Postorino, I. Pallecchi, M. Monni, M Putti, and P. Dore, cond-mat/0411616.
- [104] M.W. Thompson, Defects and Radiation Damage in Metals, Cambridge University Press, London, 1969.
- [105] A.F. Goncharov and V.V. Struzhkin, Physica C 385 (2003) 117.
- [106] X.H. Zeng, A.V. Pogrebnyakov, M.H. Zhu, J.E. Jones, X.X. Xi, S.Y. Xu, E. Wertz, Qi Li, J.M. Redwing, J. Lettieri, V. Vaithyanathan, D.G. Schlom, Zi-Kui Liu, O. Trithaveesak, and J. Schubert, Appl. Phys. Lett. 82 (2003) 2097.

- [107] S. Deemyad, T. Tomita, J.J. Hamlin, B.R. Beckett, J.S. Schilling, J.D. Jorgensen, S. Lee, and S. Tajima, *Physica C* 385 (2003) 105.
- [108] V.P. Antropov, K.D. Belashchenko, M. van Shilfgaarde, and S.N. Rashkeev, *Studies of High Temperature Superconductors* 38 (2002) 91.
- [109] A.P. Gerashenko, K.N. Mikhalev, S.V. Verkhovskii, A.E. Karkin, and B.N. Goshchitskii, *Phys. Rev. B* 65 (2002) 132506.
- [110] S. Serventi, G. Allodi, C. Bucci, R. De Renzi, G. Guidi, E. Pavarini, P. Manfrinetti, and A Palenzona, *Supercond. Sci. Technol.* 16 (2003) 152-155.
- [111] S.H. Baek, B.J. Suh, E. Pavarini, R.G. Barnes, S.L. Bud'ko, and P.C. Canfield, *Phys. Rev. B* 66 (2002) 104510.
- [112] Z. Hořanová, J. Kačmarčík, P. Szabó, P. Samuely, I. Sheikin, R. A. Ribeiro, S. L. Bud'ko and P. C. Canfield, *Physica C* 404 (2004) 195.
- [113] J. Karpinski, N.D. Zhigald, G. Schuck. S.M. Kazakov, B. Batlogg, K. Rogacki, R. Puzniak, J. Jun, E. Muller, P. Wagli, R. Gonnelli, D. Daghero, G.A. Ummarino, V.A. Stepanov, and P.N. Lebedev, *cond-mat/0411449*
- [114] R.H.T. Wilke, S.L. Bud'ko, P.C. Canfield, J. Farmer, and S.T. Hannahs, *cond-mat/0507185*

Acknowledgements

The body of work presented here is the culmination of hard work and effort by many individuals. I would like to take this opportunity to express my thanks to those who helped me with various aspects of this project: Dr. Paul C. Canfield, Dr. Sergey L. Bud'ko, and Dr. Doug K. Finnemore of Ames Laboratory and Iowa State University, Department of Physics and Astronomy; Dr. Manuel Angst of Ames Laboratory, Dr. Peter Samuely of the Institute of Experimental Physics - Slovak Academy of Sciences, Dr. Scott T. Hannahs of the National High Magnetic Field Laboratory in Tallahassee, Florida; Dr. John Farmer of the Missouri University Research Reactor; Dr. Raymond J. Suplinskas and Dr. James V. Marzik of Specialty Materials, Inc.; Dr. Matthew Rindfleisch and Mike Tomsic of Hyper Tech Research, Inc.; Dr. Joshua Margolies of GE Research, Stephanie Law of Iowa State University, Norman E. Anderson Jr. currently at the University of Florida, and Nathan Kelso currently at the University of California-Berkeley.

Ames Laboratory is operated for the U.S. Department of Energy by Iowa State University under Contract No. W-7405-Eng-82. The United States government has assigned the DOE Report number IS-T 2205 to this thesis. A portion of this work was performed at the National High Magnetic Field Laboratory, which is supported by NSF Cooperative Agreement No. DMR-0084173 and by the State of Florida.

In the course of this work Raymond J. Suplinskas succumbed to a long term illness. Ray's enthusiastic support and collaboration was vital to much of the success of the research presented in this thesis. He will be greatly missed.